

Alma Mater Studiorum – Università di Bologna

DOTTORATO DI RICERCA IN

Chimica

Ciclo XXXI

Settore Concorsuale: 03/C2

Settore Scientifico Disciplinare: CHIM/04

Catalysis for chemicals production from bio-based building blocks: examples of industrial relevance

Presentata da: GIADA INNOCENTI

Coordinatore Dottorato

Prof. ALDO RODA

Supervisore

Prof. FABRIZIO CAVANI

Esame finale anno 2019

Abstract

The research work presented in this PhD thesis is focused on two research topics which aim is to enhance the sustainability of the modern biorefinery. In fact, the production of an advanced biofuel such as 1-butanol is studied in the first part, while the second part deals with the valorisation of glycerol, which is a biodiesel co-product.

Therefore, in the first part of the thesis 1-butanol production by means of the Guerbet reaction is studied. The catalytic synthesis of 1-butanol is more desirable than ABE fermentation because it allows to reach higher productivity, lowering the separation costs. The study is aimed to provide a deeper understanding on the effect of acid and base active sites. Therefore, pure basic alkaline earth metal oxides were synthesized and fully characterized. Afterwards, the oxide which showed the best performance was doped with H_3PO_4 and its catalytic behaviour was studied. Finally, its performance was compared with that one of hydroxyapatite, even with respect to its lifetime.

Dihydroxyacetone, a glycerol derivative, upgrading into lactic acid is the topic of the second part of this work. Glycerol valorisation into chemicals might help to support the economic sustainability of biodiesel production. In fact, its disposal as a waste is expensive and not sustainable according to the biorefinery concept. Therefore, a continuous process aimed at directly upgrading glycerol is highly desirable. The main problem in dihydroxyacetone conversion is the need for water-resistant catalysts. A continuous process is more convenient from both an economical and a technological point of view than a batch one. In this thesis, a thorough study of metal phosphate-based catalysts reactivity in the aqueous phase and in a continuous-feed reactor is presented. The catalysts were fully characterized in order to understand the relationship between their physico-chemical characteristics and catalytic performance.

Table of contents

Chapter 1. Introduction	1
1.1 Bio-Ethanol	5
1.2 Bio-1-butanol	7
1.3 Bio-Diesel (FAME)	9
1.4 Lactic Acid	10
Chapter 2. The Guerbet Reaction: from ethanol to 1-butanol	12
2.1 Introduction	12
2.2 Methods	15
2.2.1 Catalyst syntheses	15
2.2.2 Catalyst characterizations	16
2.2.3 Reactivity Tests	16
2.2.4 In-situ DRIFTS-MS measurements	17
2.3 Basic oxides in the Guerbet Reaction	20
2.3.1 MgO, CaO and SrO characterizion	20
2.3.2 MgO, CaO and SrO reactivities	21
2.3.3 MgO, CaO and SrO DRIFTS	25
2.3.4 Conclusions	28
2.4 How is the addition of phosphate to MgO affecting the Guerbet reaction?	29
2.4.1 H ₃ PO ₄ /MgO catalysts characterization	29
2.4.2 H ₃ PO ₄ /MgO temperature screening	31
2.4.3 5 % w/w H ₃ PO ₄ reactivity study	33
2.4.4 5 % w/w H ₃ PO ₄ /MgO DRIFTS-MS experiments	37
2.4.5 Conclusions	41
2.5 H ₃ PO ₄ /MgO vs Hydroxyapatites in the Guerbet reaction	42
2.5.1 HAP and 5PMgO characterization	42
2.5.2 HAP and 5PMgO reactivity	45
2.5.3 HAP and 5PMgO DRIFTS	50
2.5.4 Conclusions	55
Chapter 3. Dihydroxyacetone upgrading into Lactic Acid	56
3.1 Introduction	56
3.2 Methods	59
3.2.1 Catalyst syntheses	59
3.2.2 Catalyst characterization	59
3.2.3 Catalytic tests	60
3.3 Results and discussion	63

Table of contents

3.3.1	Catalyst structure and compositions.....	63
3.3.2	Phosphate acidity	66
3.3.3	Dihydroxyacetone rearrangement to Lactic acid	67
3.4	Conclusions	73
Overall conclusions.....		75
Appendix A. Ethanol steam reforming		77
A.1	Methods	77
A.2	ZrO ₂ based catalysts	77
A.3	CeO ₂ based catalysts	86
A.4	Conclusions	91
Appendix B. Ethyl lactate oxidation into ethyl pyruvate		92
B.5	Methods	92
B.6	DRIFTS spectra of bare V ₂ O ₅ /TiO ₂	92
B.7	Ethyl Lactate (L) adsorption on VO _x TiO ₂ in absence of O ₂	94
B.8	Ethyl Lactate (L) adsorption on VO _x TiO ₂ in presence of O ₂	96
B.9	Aerobic oxidation of ethyl lactate on mesoV-TiO ₂ at 130 °C	98
B.1	Conclusion	98
Publications		100
References		101

Chapter 1. Introduction

To date, oil, once transformed into fossil fuels, is along with charcoal the main worldwide source of energy. In the last decades, raising concerns about oil source depletion and climate change along with an increase in worldwide energy demand encouraged the research of alternative energy sources and processes.¹⁻³ In this frame, a lot of effort is done by academia, industry and governments to find alternatives that rely on green, sustainable and eco-friendly feedstocks.⁴

The appearance of the concept of sustainability in the '80s highlighted the key role of chemistry in the definition of greener and more sustainable processes.⁴ Chemistry crucial role was finally proclaimed with the Green Chemistry concept and its twelve principles in 1998.⁵ All these principles deal with cutting unnecessary process steps, increasing the intrinsic process safety, and the atomic efficiency which means reducing not only the wastes but even the CO₂ and all the other greenhouse gas emissions.⁶ Biomass and biofuels, which are the answer to the aforementioned problems, have always been known.^{4,7} In fact, wood is considered an energy source from the first man-made fire. Furthermore, biofuels (ethanol and vegetable oils) were used to run the Ford Model T and the diesel engine by Henry Ford and Rudolph Diesel, respectively.⁴ When the technology to produce fossil fuels were implemented and their price dropped, biofuels were set aside.⁴ Nevertheless, in the last decades, even the research on biofuels was strongly affected by oil price variations.⁷ However, the production of biofuels is driven by blending mandates emanated by the main states such as EU, US, Brazil and China. Europe was the first to emanate a blending mandate, which aimed to reach a 10 % biofuel content blend by 2020 but it has been scaled back to 7.5 %.^{8,9} US, China and Brazil set targets are in the range of 15 – 27 % to reach by 2020 – 2022.^a Therefore, in the last years the research attention focused on biomass conversion into biofuels. Biomass are completely renewable feedstocks, more often than not plant-based. Biofuels, according to the biomass from which are derived, can be grouped in 4 categories:

- First generation biofuels produced from corn, wheat, sugarbeets, barley, potato wastes and vegetable oils;⁷
- Second generation biofuels mainly derived from non-edible lignocellulosic biomass (grasses, *Jatropha*, ...), waste vegetable oil and municipal waste;⁷
- Third generation biofuels produced from algae;⁷
- Fourth generation biofuels derived from genetically engineered algae.^{7,10}

Third and fourth generation biofuels are still at the initial research stages. The technology to pretreat algae are expensive and not optimized (lipid extraction and dewatering) as their cultivation.^{7,11}

Biorefineries are the equivalent of the current refinery to produce biofuels instead of oil-based fuels. A biorefinery is defined by the US Department of Energy as a processing plant where biomass feedstocks are converted and extracted into diverse valuable products.¹²⁻¹⁴ The final aim of a biorefinery is to produce fuels, power and chemicals from biomasses.¹⁴ There are three different types of biorefinery depending on the kind of feedstock used, as shown in Figure 1.1. Triglyceride biorefinery and sugar and starchy biorefinery produce mainly first-generation biofuels. In fact, they are well implemented for the use of vegetable oils and food crop such as corn and sugarbeets, respectively. Their main restrictions are the use of arable lands and the “fuel *versus* food” debate.⁷ For example, ethanol from sugarbeets is in competition with sugar production in Brazil while ethanol from corn is subjected to the increase value of food on a world scale. The same restrictions applies to the biodiesel market which is limited by the vegetable oils price.⁷

^a <http://www.biofuelsdigest.com/bdigest/2016/01/03/biofuels-mandates-around-the-world-2016/>

Introduction

Therefore, the interest towards second generation biofuels is growing. The production cost of biofuels is mainly driven by: feedstock cost, processing cost and production scale.¹¹

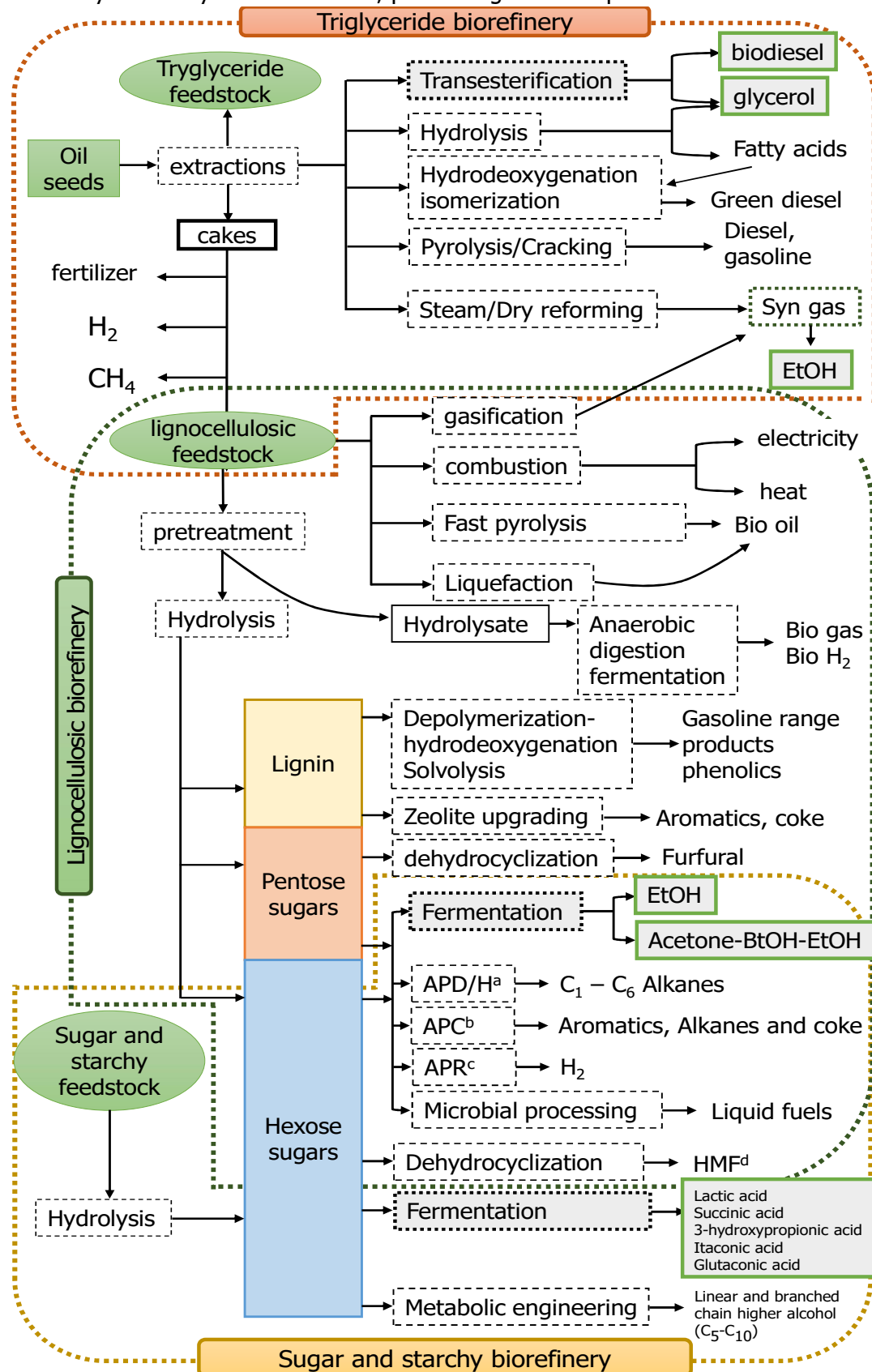


Figure 1.1 Examples of biorefinery as function of the feedstock used. ^aAPD/H = Aqueous phase dehydration/hydrogenation, ^bAPC = Aqueous phase catalysis (Zeolite upgrading), ^cAPR = Aqueous phase reforming, ^dHMF = 5-hydroxymethylfurfural.

Introduction

Usually a triglyceride biorefinery is limited by feedstock costs while the lignocellulosic one relies on cheap but quite chemically complex feedstocks. Therefore, the latter is made expensive by technology cost and limitation.¹¹ In fact, a lignocellulosic biorefinery can be considered sustainable only when it will be possible to completely valorize lignin. Currently, lignin is used as low grade-fuel to generate heat or steam to power the pulping process.¹¹

Nowadays, ethanol is the main biofuel produced. In fact, it is possible to produce ethanol either by sugar or syn gas fermentation or by syn gas catalytic upgrading.^{11,14} Therefore, as highlighted in Figure 1.1, it is possible to produce ethanol from different feedstock sources. Bioethanol leading producers, in 2017, were United states (15800 million gallons (MG)) and Brazil (7060 MG) followed by EU (1415 MG) and China (875 MG).^b A bioethanol production plant from lignocellulosic biomass started-up in Italy in 2013 with a capacity of ~50 million liters (ML) but it was closed in November 2017.⁹ Europe biofuel production in 2017 accounted for the 17% on a worldwide scale, as reported in Figure 1.2.¹⁵ The biggest portion of the 17% is constituted by biodiesel of which Europe is the world's largest producer.⁹ In 2017, Europe produced 14980 ML of biodiesel of which 12397 ML fatty acid methyl esters (FAME) and 2853 ML hydrogenated vegetable oils (HVO).⁹ The production trend of biofuel in Europe from 2011 to 2018 is reported in Figure 1.3. It is possible to notice that FAME production is forecasted to diminish in favor of HVO. Currently, HVO is produced only in six European countries, one of which since 2014 is Italy. Italy yearly produces on average 15% and 5% of the total FAME and HVO produced in the European union, respectively. The HVO production is forecasted to increase even because new HVO plant are opening in France, Italy and Sweden in 2018.⁹ HVO (Green Diesel) and FAME are both produced inside a triglyceride biorefinery (Figure 1.1). It is important to notice that FAME biodiesel produces glycerol as co-product.¹⁴ 126 MG of biodiesel were produced in February 2018 in USA¹⁶, which also co-produced ~12 MG of glycerol. Since this is such a large volume side product, it is considered as a renewable resource.¹⁷ In this frame, glycerol upgrading to high-added value products has gained interest and lactic acid (LA) is considered one of the most promising glycerol derivatives.¹⁷ However, glycerol upgrading directly in the biorefinery would be an economical advantage.

3

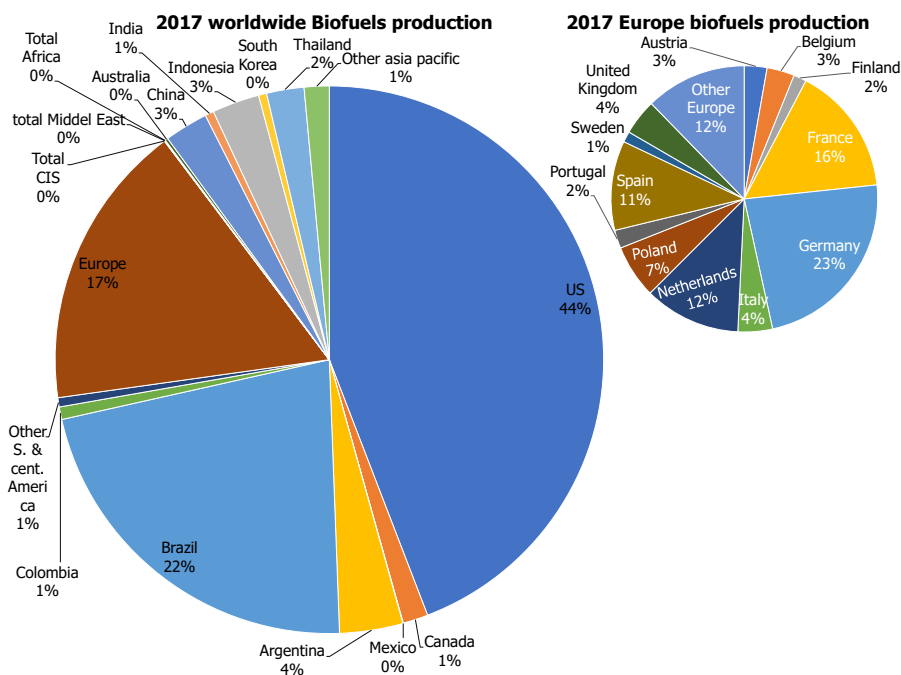


Figure 1.2 2017 worldwide biofuels production.¹⁵ CIS = Commonwealth of Independent States.

^b <https://www.statista.com/statistics/281606/ethanol-production-in-selected-countries/>

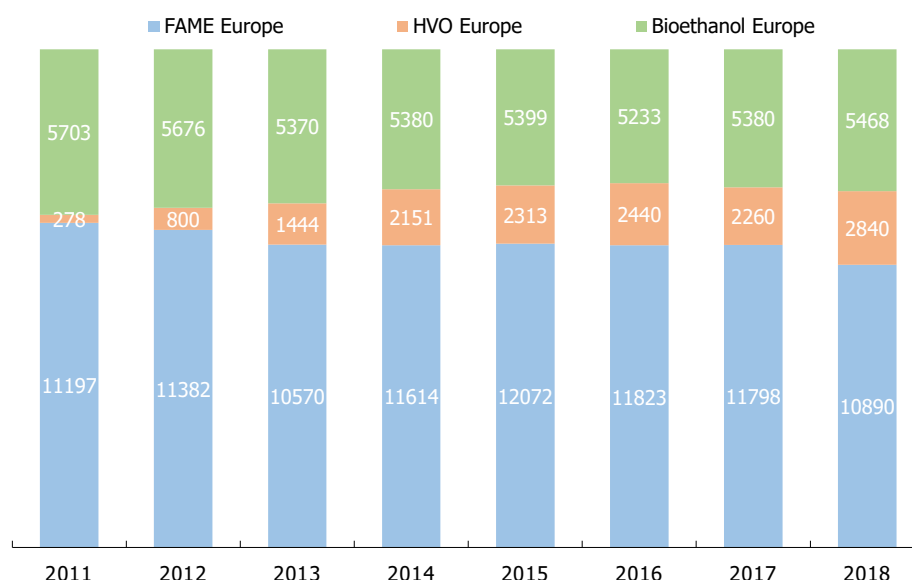


Figure 1.3 Yearly European biofuels production. The value reported for 2017 are estimated, 2018 are forecast while for all the other years are the actual numbers.

HVO is considered by the European union as an advanced biofuel, even if it is not necessarily produced by non-food feedstocks. In fact, the current feedstock in Italy is palm oil and the yearly production in the plant of Venice (by Eni spa) is 320 ML. Its production is forecasted to increase up to 540 ML while the feedstock will include increasing portion of used oils, animal fat and by-products from palm oil production. Moreover, Eni is converting the Gela refinery, in Sicily, into a renewable diesel production facility with a capacity of 680 ML per year. The facility is likely to be operative by the end of 2018.⁹

4

Table 1.1 Comparison among alcohol specifications and fossil fuels.

	Gasoline	Diesel	Ethanol	1-butanol
Molecular formula	C ₄ – C ₁₂	C ₁₂ – C ₂₅	C ₂ H ₅ OH	C ₄ H ₉ OH
Octane number	80 – 99	20 – 30	108	96
Oxygen content (% wt.)	-	-	34.8	21.6
Density	0.72 – 0.78	0.82 – 0.86	0.790	0.808
Autoignition temperature (°C)	~300	~210	434	385
Flash point (°C) at closed cup	-45 to -38	65 - 88	8	35
Latent heating (kJ kg ⁻¹) at 25 °C	380 - 500	270	904	582
Flammability limits (% vol.)	0.6 - 8	1.5 – 7.6	4.3 – 19	1.4 – 11.2
Boiling point (°C)	25 - 212	180 - 370	78.4	117.7
Viscosity (mm ² s ⁻¹) at 40 °C	0.4 – 0.8 (20 °C)	1.9 – 4.1	1.08	2.63

An important emerging fuel, according to the US department of energy, is bio-1-butanol which can be considered an alternative advanced biofuel.^c Bio1-butanol can be produced from the same ethanol feedstocks. Moreover, ethanol producing facilities can be easily retrofitted to produce 1-butanol.¹¹ Currently, it is difficult to make forecast on bio1-butanol since its production has been small and intermittent. In fact, EPA Renewable Identification Number (RIN) data report that approximately 12,000 gallons were produced in 2013, none in 2014 and 2015, and more than 125,000 gallons in 2016.^d 1-butanol possesses some advantages with respect to ethanol. Their physical-chemical properties are compared with fossil fuels in Table 1.1. Ethanol has a number of significant drawbacks: it has lower energy density (70 % that of gasoline), it is corrosive for

^c https://www.afdc.energy.gov/fuels/emerging_biobutanol.html

^d Ibid.

current engine technology and, fuel infrastructure, and it readily absorbs water, which leads to separation and dilution problems in storage tanks. On the contrary, 1-butanol has fuel properties close to gasoline, thus bypassing some of the problems associated to ethanol. In fact, 1-butanol is essentially noncorrosive and immiscible with water. The main 1-butanol disadvantage is that its energy density is lower than the gasoline one (10 % – 20 %) meaning that more fuel is required.^e Bio1-butanol can be used in unmodified conventional engines at 100 % as it was proven by David Ramey that in 2005 was driving his unmodified car across the US fueled only with 1-butanol.¹¹ However, in commerce blends with more than 15% 1-butanol are not available. Furthermore, bio1-butanol has the potential to reduce the emission of 85% with respect to gasoline.^f For all these reasons, 1-butanol is seen as a valid biofuel alternative for the future, even though currently its production via ABE fermentation suffers from several drawbacks that will be highlighted later on in this introduction.¹⁸

In this work, an attempt to address two of the sustainability problems of the biorefinery and of biofuels production was done.

A study on ethanol upgrading into 1-butanol by means of the Guerbet reaction is here reported. 1-Butanol, as previously mentioned, demonstrated to be a suitable advanced biofuel to be used in car engines. Therefore, it is important to find a chemical synthesis alternative to the fermentative process, which is briefly described in this introduction and suffers from low productivity. The Guerbet reaction is discussed in Chapter 2. Here, briefly, the main challenges and the proposed solutions are described. In fact, the Guerbet reaction mechanism is still under debate while the active sites needed to efficiently carry out the reaction in the gas phase still needs to be disclosed. A deeper understanding of acid-base pairs effect needs to be gained. Therefore, the pure basic oxides behavior is studied in section 2.3. MgO, CaO and SrO performances are compared and MgO demonstrated to possess the highest selectivity to 1-butanol. Afterwards, in section 2.4 the catalytic performances of MgO doped with H₃PO₄ are investigated. H₃PO₄ is used as a dopant to simulate the hydroxyapatite with only Mg²⁺ counterions, which to our knowledge has never been tested or synthesized. Afterwards, in section 2.5 the doped MgO performance are directly compared with calcium hydroxyapatite and strontium hydroxyapatite obtaining unexpected results. The other piece of work focuses on dihydroxyacetone upgrading into lactic acid. This reaction represents a possibility to increase glycerol profitability which would improve the profitability of the biodiesel industry. The importance of lactic acid and the reaction studied is discussed in Chapter 3. Briefly, the main challenge in the catalytic upgrade of dihydroxyacetone into lactic acid is the need to find a catalyst resilient in water. Moreover, in the literature there is a lack of studies dealing with the continuous-feed, liquid-phase, which is the simplest reactor set up for the scale up and it is more advantageous even from an economical point of view. Therefore, in this work a thorough study of the phosphate metal performance in the continuous aqueous phase dihydroxyacetone upgrading is reported. In this introduction, the current lactic acid production will be summed up.

1.1 *Bio-Ethanol*

To date, synthetic ethanol, which relies on petrochemical sources, is produced in small amount with respect to bio-ethanol, which relies on biomasses. For example in 2010 only 7% of the global total ethanol production was synthetic.¹⁹ However, ethanol can be produced by ethylene hydration with steam using as catalyst phosphoric acid – silica gel (Figure 1.4). Usually the reaction is carried out using an ethylene - water ratio ranging between 1:0.3 and 1:0.8 at 250 – 300 °C and 6 – 8 MPa. The equilibrium conversion of ethylene is 7 – 22 %, therefore the unconverted

^e <http://bioenergytalk.blogspot.com/2012/10/biobutanol-production-and-properties.html>

^f <https://www.azocleantech.com/article.aspx?ArticleID=408>

Introduction

ethylene is recycled. It is not possible to work at lower temperature because diethyl ether formation is favored while higher pressure must be avoided to limit ethylene polymerization. 10 - 22 wt.% ethanol is recovered and purified by distillation to the azeotropic limit (95%). If higher purity is required, the product are subjected to a further azeotropic distillation to obtain anhydrous ethanol.²⁰

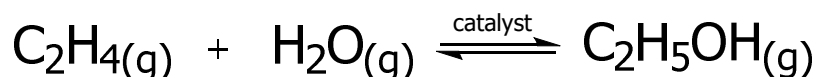


Figure 1.4 Ethylene hydration to ethanol

To date ethanol accounts for 75% of the total biofuels in commerce. It dominates the market with a sale of 58 billion dollars per year. Furthermore, approximately the 50 % of global sugar is used for ethanol production (approximately ~86000 kton year⁻¹).

The most commonly used feedstock to obtain sugar for ethanol fermentation are sugarbeet (Brazil), corn (USA) and grain (EU). The ethanol produced from these crops is known as "first generation ethanol" and it is economically cheaper than the second generation one.^{11,14} These starch-based crops can be upgraded into ethanol by dry- or wet- mill processes. Currently, 90 % of bio-ethanol based on corn is produced by dry milling and the remaining by wet milling.⁹ In the dry mill process the entire corn-kernel is grounded into "meal" and then slurred with water to form a mash. On the contrary, in the wet milling the grain is separated into its basic component by soaking. After steeping, it is processed through grinders to separate the corn germ, which can be refined to corn oil. The gluten component is used to produce animal feed. The dry mill mash and the remaining starch from the wet mill are subjected to the same processing. In fact, the starch is liquefied (dextrines and small amount of glucose) in presence of α -amylase at 90 – 110 °C. Afterwards, the liquefied starch is saccharified at 50 – 60 °C with glucoamylase. At this point the hexose sugars are fermented to ethanol using Baker's yeast.¹¹ The main drawback of these process is ethical and it is due to the feedstock used. Indeed, the use of food-crop makes the ethanol production competitive with food. Furthermore, it prevents from the use of all the herbaceous biomass in which the sugars are aggregated in less accessible and more robust polymer such as cellulose and hemicellulose.

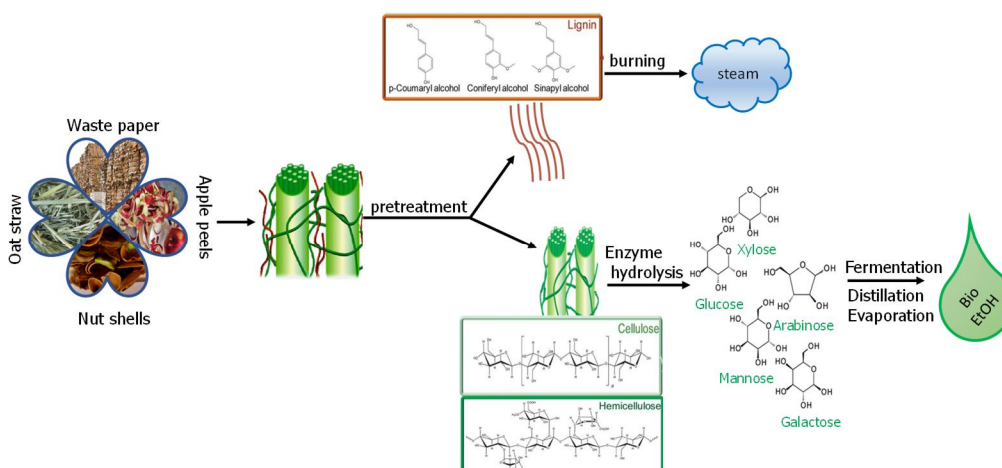


Figure 1.5 Lignocellulosic biomass upgrading into bio-EtOH.

The cost of lignocellulosic ethanol is higher than the food-crop ethanol. In fact, the biomass requires an initial pretreatment to remove lignin and hemicellulose, increase the porosity and

⁹ <https://ethanolrfa.org/how-ethanol-is-made/>

remove the crystallinity of cellulose, which is otherwise unreactive (Figure 1.5). The possible pretreatment methods are: mechanical comminution, steam explosion, hydrothermolysis, NH_3 fiber explosion, treatment with lime or diluted acid. Cellulose is always recovered as solid while hemicellulose or lignin are solubilized or recovered as solid as function of the used pretreatment method. Usually, the pretreatment method is chosen considering the nature and chemical composition of the feedstock, the cost involved and the degree of carbohydrates recoverable.¹¹ After the pretreatment, the solid residue, containing mainly cellulose and some extent of hemicellulose and lignin, is hydrolyzed using cellulase and hemicellulase. The obtained sugar stream is composed by both pentose and hexose. The pentose fermentation is still a challenge even if promising results were obtained with *Candida Shehate*, *Pichia Stipitis* and *Pachysolen Tannophilus*.

However, alcohol concentration in fermentation broth is normally very low (4 – 4.5%). Indeed, the separation is usually expensive, even though the residue after separation, in case of lignocellulosic ethanol, contains unreacted cellulose, hemicellulose and other components which are usually concentrated and used as fuel for the process.

A proper recovery and use of lignin and hemicellulose, using improved microorganism and advance separation processes, can increase the overall economics.

1.2 Bio-1-butanol

Bio-1-butanol, as previously mentioned, is an appealing alternative biofuel. However, 1-butanol, in general, is widely used as solvent in several industrial sectors, such as the painting, the plastics and the cosmetics industries. Nevertheless, it is an intermediate to produce added value products such as maleic anhydride, butadiene or butenes.²¹ 1-Butanol market demand is forecasted to reach 9.9 billion USD in 2020 with a yearly production of 4.5-5.4 million tonnes. Currently, 1-butanol is produced by oxo-synthesis which relies on petrochemical feedstock.²¹ The oxo process generates an aldehyde by reaction of an olefin with syn gas. The synthesized aldehyde is, then, hydrogenated to produce the alcohol. In 1963, the *Shell process* was commercialized and allowed to directly hydrogenate the aldehyde in the oxo reactor using $\text{HCo}(\text{CO})_3\text{PR}_3$ as catalyst under pressure (20 – 30·10⁶ Pa CO/H₂) at 180 °C.^{22,23} 1-butanol can be produced also by *Reppe process*. This process became available on a commercial scale in 1942. In the *Reppe process*, propylene, CO and H₂O are reacted under milder pressure (0.5 – 2·10⁶ Pa CO/H₂) in presence of a tertiary ammonium salt of polynuclear iron carbonyl hydrides at 100 °C.²³

Bio-1-butanol is produced by Acetone 1-butanol Ethanol (ABE) fermentation which was discovered in 1861 by Pasteur.¹⁸ The research on this reaction was established during world war I due to the Britain needs of acetone. After the war, the 1-butanol demands increased, and the first industrial large-scale plants were created in Canada and USA. After 1936 production plants were installed in Soviet Union, Japan, China, South Africa and Egypt. With the advent of oxo-synthesis during the 1950s the ABE fermentation was abandoned and the last factory to be dismissed in 1986 was in South Africa.¹⁸ Currently, several industrial plant^h are working in US (Gevo, Butamax), Brazil, Europe and China.²⁴

This fermentation is done with genetically modified strain of the *Clostridia* specie. These bacteria are rod-shaped, Gram positive and strictly anaerobic. Furthermore, they produce spore if introduced in an unsuitable environment and they are not able to sustain fermentation broth containing more than 2 % solvent. This fermentation is strongly affected by the feedstock chosen to obtain the sugars, as shown in Figure 1.6. To date the most benign feedstock is based on starch, even if the latter is food competitive. In fact, its upgrading process is simpler and

^h <http://www.biobutanol.com/Biobutanol-Producers-Gevo,-Butamax,-Cobalt,.html>

Introduction

economically advantageous with respect the one needed to upgrade lignocellulosic or algae biomasses. In fact, algae biomasses are still limited by technological issue in their cultivation and drying processes, while lignocellulosic feedstocks require expensive and energy demanding pretreatment steps. Starch based feedstocks are widely available and their related food wastes are still rich in starch and usable in the fermentative processes.²¹ Furthermore, the amylase used for their hydrolysis is about 110 times cheaper than cellulase and it does not produce phenolic compounds, acids and furfural which can inhibit the bacteria during the fermentation.²¹ The initial substrate concentration has to be strictly controlled. If sugar concentration is higher than 100 g L⁻¹ it inhibits cell growth while if lower than 40 g L⁻¹ the fermentation yields more acids than solvent inhibiting the cells after 48 h.²¹ Hitherto, the best performance were obtained using *C. acetobutylicum* strain JB200 which produced 20 g L⁻¹ of bio1-butanol and could stand 16 cycles of repeated batch fermentation for 30 days.²⁵ However, the final 1-butanol concentration is still low leading to high energy demanding and expensive separation steps.

The main drawbacks that the ABE fermentation should overcome in order to be competitive with the petrochemical route are:

- The low 1-butanol concentration in the final strain due to bacteria inhibition
- The low 1-butanol yield because of hetero-fermentation
- The expensive separation steps

Furthermore, it is necessary to find non-food competitive, abundant, economic feedstocks which do not produce inhibitory compounds.^{18,21}

For all these reasons, it is necessary to find a viable green and sustainable alternative chemical route to produce bio1-butanol such as the Guerbet reaction, which is discussed in Chapter 2.

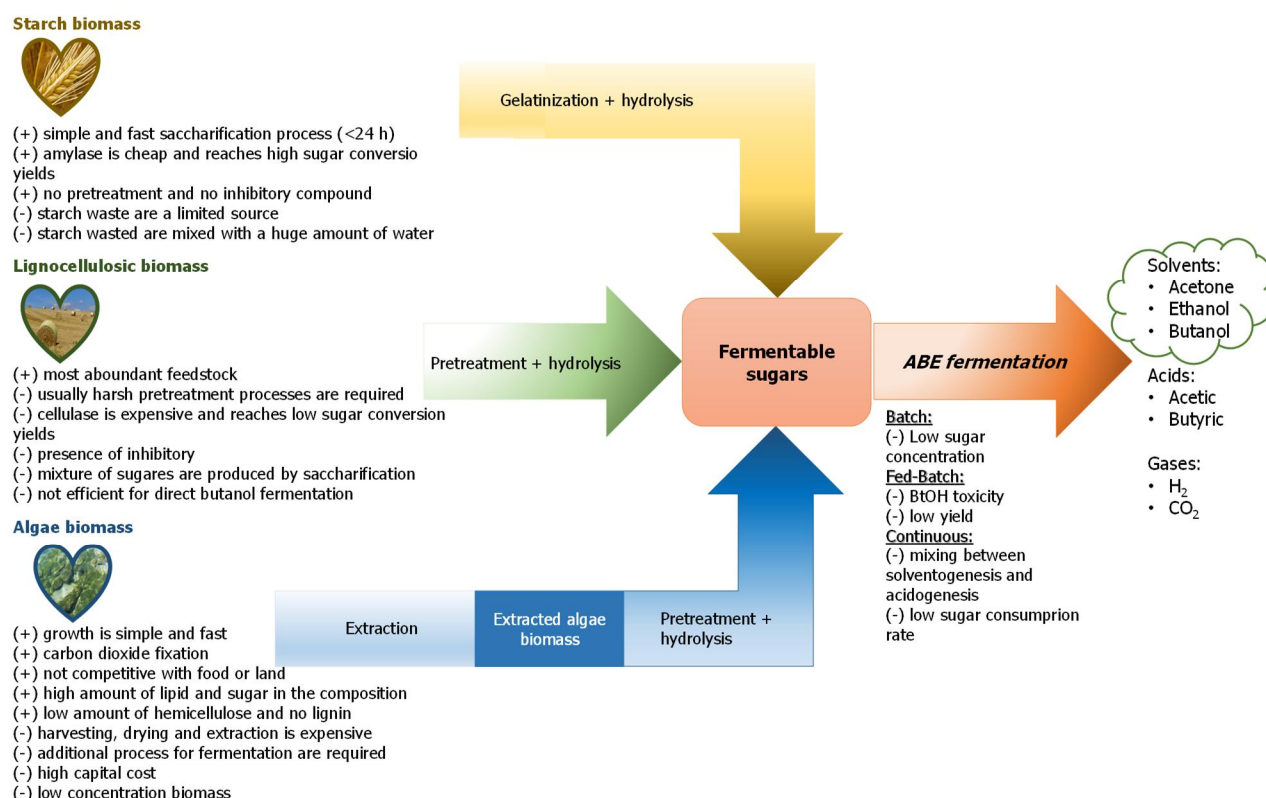


Figure 1.6 ABE fermentation from various feedstock with (+) advantageous and (-) disadvantageous characteristics.²¹

1.3 Bio-Diesel (FAME)

Biodiesel is produced along with glycerol by fatty acid transesterification in the presence of an alcohol and a catalyst, as shown in Figure 1.7. This reaction is sensitive to the feedstock used, which account for the 60 % -80 % of the total process cost.¹⁴ Currently, vegetable oils (soybean oil in the US and rapeseed oil in EU) are the principal feedstocks used for producing biodiesel.^{9,11} The oil used affects the final properties of biodiesel. Indeed, for example the use of soy bean and palm oil is limited in EU because soybean-based biodiesel does not comply with the iodine standard set in DN EN 14214 while the palm oil one does not provide enough winter stability for the northern countries.⁹ However, it is possible to meet the required standard using a mixed feedstock (soybean, palm and rapeseed oil).⁹ The feedstock quality, which is determined by the amount of Free Fatty Acids (FFA) and water contained in the 'crude' oil, is directly proportional to its cost.²⁶ Furthermore, the purity of the feedstock can affect the transesterification process which can be carried out using base, acid and enzymatic catalysts.²⁶

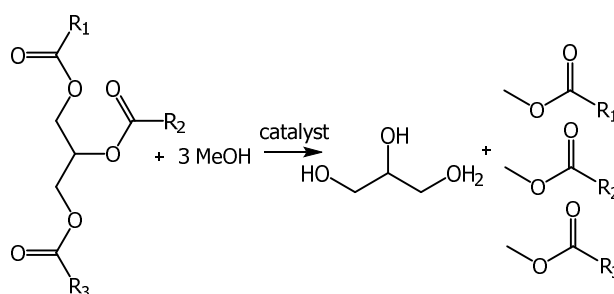


Figure 1.7 Transesterification reaction scheme.

Currently, the biodiesel production mostly proceeds through homogeneous base (alkali) catalysis. In fact, the use of sodium hydroxide or potassium hydroxide allows to reach high yields (98%) using mild reaction conditions (50 °C – 60 °C, 1.4 bar) in a short time.¹⁴ The first reaction step, as shown in Figure 1.8, is the reaction between methanol (in excess) and the vegetable oil in presence of the catalyst. The reaction mixture is then let to settle down for 1h to 8h. Afterwards, glycerine is separated from the methyl esters which are neutralized with mineral acids and washed producing two different streams. One of which is sent to an evaporator unit which further purifies the biodiesel (98%).²⁶ The glycerol obtained from the low pressure transesterification processes has an high salt content (2 – 5%) and its concentration is 90 – 92 %.²⁷ From the glycerol refining unit there are three outputs: glycerol, water, dissolved salts and unreacted MeOH, which is recycled back to the reactor, and the fatty acids.²⁶

The use of base catalysis is limited by the presence of free fatty acids (FFA). In fact, FFA oil content higher than 2 wt.% provoke soap formation, reducing biodiesel yield and increasing the difficulties in the separation step (due to emulsions formation).²⁶ Usually non-edible oils, animal fats and waste cooking oils contain high FFA percentage and are unsuitable for alkali processes.¹⁴ In these cases an acid catalysis is necessary. In fact, acid catalysts are practically insensitive to FFA and water content. The homogeneous acid process is more economical than the alkali one. However, the reaction rate is slower, the use of acids such as HCl or H₂SO₄ can lead to corrosion problems on reactor and pipelines walls and the separation step is not simple.²⁶ On the contrary, the use of heterogeneous catalysts would solve all these issues. However, the process is more energy intensive requiring higher reaction temperatures. Finally, the enzymes (i.e. *Mucor miehei*, *C. antarctica*, *Bacillus subtilis*) are insensitive to FFA and water content, work at low temperature and require only simple purification steps. However, other than being really expensive, they can undergo deactivation in the presence of MeOH and the reaction rate is slow.²⁶

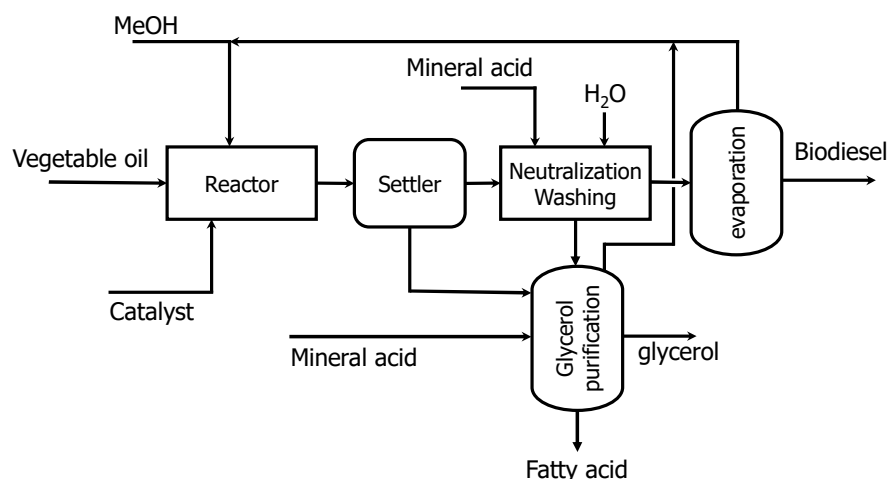


Figure 1.8 Homogeneous catalyst biodiesel production plant.²⁶

Usually, 100 units of feedstock react with 10 unit of MeOH in the presence of a catalyst producing 10 units of glycerine and 100 units of biodiesel.ⁱ Considering that the world biodiesel production is forecasted to reach 10.3 billion gallons by 2024, it is crucial to enhance glycerol profitability to increase the biodiesel industry viability.^{17,28}

1.4 Lactic Acid

Lactic acid finds its application in food industry (as pH regulator, preservative, bacterial spoilage inhibitor), in cosmetics industry (as moisturizing agent) and in textile industry (as mordant).²⁹ Moreover, lactic acid can be used to produce the bio-polymer poly-lactic acid (PLA). PLA is the most interesting lactic acid application because it has been widely used for medical purposes and, thanks to its biodegradability, by the packaging industry.^{30,31} In 2013, the global demand for lactic acid was estimated to be 714 kilo tons. It is expected to reach 1960 kilo tons by 2020 and a global market size of USD 9.8 billion by 2025.^{29,32}

Lactic acid started to be produced synthetically during the 1960s. The industrial process is based on the reaction of acetaldehyde with hydrogen cyanide and a successive hydrolysis of the resultant lactonitrile.³³ However, it is since 1995 that about 90% of the worldwide lactic acid production is mainly performed *via* fermentation, which allows to reach high chiral purity.^{33,34}

The fermentative production of lactic acid relies on hexose sugars derived from starch-based biomass. During the fermentation the broth pH is controlled between 5.0 and 6.5. Calcium hydroxide or calcium carbonate or ammonium hydroxide are used to neutralize the produced lactic acid, which can deactivate the microorganisms diminishing the pH. Therefore, the final product is a lactic acid salt. The fermentation is performed using *Lactobacillus*, *bacillus* bacteria and *Rizopus* fungal strains. The latter tends to give lower lactic acid yield and works in aerobic conditions. On the contrary, the bacteria strains need an anaerobic environment. The process yields 85-95% of lactic acid as function of the sugar used. Usually, by-products (formic acid and acetic acid) are formed in concentration lower than 0.5 %.³³

The main advantage of this technology is that it is possible to produce optically pure LA, depending on the chosen microbe. However, this process suffers from several drawbacks such as low productivity, complex and expensive purification steps, expensive enzymes and the production of several wastes.^{29,35} Furthermore, to date it works only if edible sugars are used as starting substrate even if currently several efforts are done to make the conversion of lignocellulosic hexose and pentose sugars sustainable and viable.^{29,34,36}

ⁱⁱ <http://www.eubia.org/cms/wiki-biomass/biofuels/biodiesel/>

Introduction

Therefore, a chemo catalytic alternative is necessary. Indeed, glycerol upgrading into lactic acid can be the desired alternative and it can be performed as one-pot reaction or in two steps. In this work the second reaction of the two-step approach will be investigated (Chapter 3). In fact this process involves a first step in which glycerol is oxidized to triose sugars (dihydroxyacetone or glyceraldehyde), which undergo rearrangement into lactic acid.¹⁷

Chapter 2. The Guerbet Reaction: from ethanol to 1-butanol

2.1 Introduction

In the last decades, ethanol production has become more and more important to the point that it is nowadays considered one of the most important building blocks for green chemistry.^{37,38} In fact, it is already produced in large amount from renewable feedstocks such as starch and sugars. However, these first-generation biomasses are food competitive, therefore other alternatives have been sought.^{39–42} In fact, research focuses on the exploration of low-cost and non-food competitive biomass sources to produce ethanol. In this context, cellulosic (second-generation) and algal (third-generation) feedstocks are promising alternatives.^{43–45} Furthermore, syngas, containing mainly CO, H₂O, CO₂ and H₂, can be fermented to ethanol.⁴⁶

In a few years, ethanol has become one of the principal sources of bio-based carbon to produce chemicals and fuels. Moreover, due to its potential use as a renewable fuel its production has increased from 46.3 million cubic meters in 2000 (of which 17.1 for fuel use only) up to 216.1 million cubic meters in 2017 (98.9 for fuel use only), and it is expected to increase further.^j The main bio-ethanol producers are United States and Brazil, as shown in Figure 2.1. In Europe the bioethanol leading producer is France, followed by Germany and Spain.^k

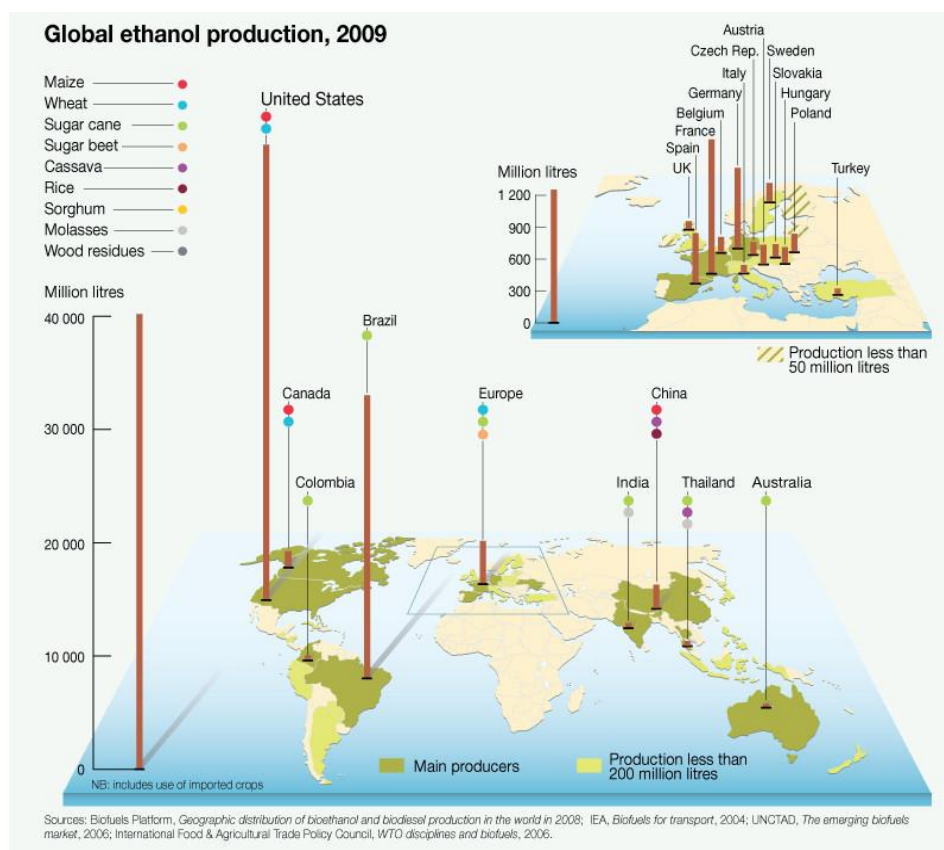


Figure 2.1 Global ethanol production in 2009.

^j <https://www.statista.com/statistics/274142/global-ethanol-production-since-2000/>

^k <https://www.grida.no/resources/6208>

However, ethanol is considered a building block also due to the possibility of upgrading it into added value products such as 1-butanol, diethyl ether, butadiene, butenes, H_2 and acetonitrile.⁴⁷ In the present work, ethanol upgrading into 1-butanol is studied.

1-Butanol is an interesting product since it can be transformed in several higher value products such as butenes and maleic anhydride.^{48,49} It can be also used as an additive in several products of everyday use such as paints or skincare lotions but the main potential use is as biofuel.^{18,23,50,51}

Bio-1-butanol has fuel properties closer to gasoline than ethanol.^{18,41} In fact, it possesses an high energy density (90 % of gasoline one), is non corrosive and immiscible with water and for this reason it can be blended with gasoline in higher concentration (85 %) than ethanol.^{18,41} Another, not negligible advantage is the possibility of using 1-butanol without substantial modification of nowadays car engines, which are instead required if ethanol is used.¹⁸

Around 1912, 1-butanol was produced industrially for the first time by fermentation of carbohydrates to give mainly acetone and 1-butanol along with some ethanol (ABE process). After 1950s the industrial production plants were dismissed because 1-butanol production by oil-based route was more convenient.^m

Nowadays, 1-butanol is produced by an oil-based chemical route: oxo-synthesis. This process consists in the addition of CO and H_2 to a C=C bond in presence of a Co, Rh or Ru based catalyst in liquid phase to form an aldehyde with one more C atom than the original olefin. The produced aldehyde is then hydrogenated to obtain the desired alcohol.²³ In the recent years, ABE fermentation gained interest again because of the necessity to find green and sustainable alternatives to the oil-based processes. Unfortunately, as all the fermentative processes it needs to overcome some intrinsic limitations such as the diluted concentration in the fermentation broth, the low productivity, and complex separation procedures.^{18,51} Despite all these drawbacks, Green Biologics, Butamax Advanced Biofuels and Gevo converted some pilot plants for ethanol production *via* fermentation to produce 1-butanol. Another interesting pilot plant was proposed by Abengoa but it exploits a green chemical route. In fact, in 2013 they announced that they were able to produce 1-butanol with 99.8 % purity through Guerbet reaction.ⁿ

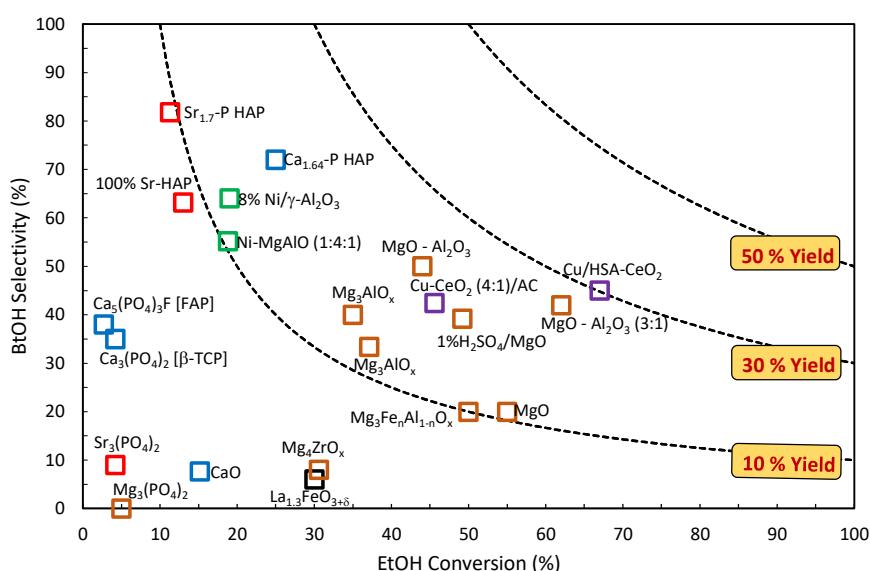


Figure 2.2 Catalyst tested in the Guerbet coupling of ethanol in gas phase.

The Guerbet reaction is the subject of this chapter, it is named after Marcel Guerbet who proposed this reaction for the first time in 1899.⁵² This reaction is a condensation between two

^l <http://www.etipbioenergy.eu/value-chains/products-end-use/products/biobutanol>

^m <https://ihsmarket.com/products/chemical-technology-pep-reviews-biobutanol-2007.html>

ⁿ <http://www.etipbioenergy.eu/value-chains/products-end-use/products/biobutanol>

alcohol molecules to release another alcohol with the chain elongated of one C atom coproducing water. This reaction can be performed both in liquid and gas phase.⁵³

The number of catalysts and literature related papers is huge and for this reason in this introduction only the main gas phase results will be discussed. Figure 2.2 plots the main catalysts tested in the gas phase.^{54–70} The graph clearly shows that reaching both high selectivity and high conversion is not possible, yet. In fact the best result in terms of selectivity was obtained by Ogo et al^{66,67} with Sr-substituted hydroxyapatite (over 80 %) at 11 % conversion. A better compromise between selectivity (45 %) and ethanol conversion (67 %) was obtained using Cu supported on CeO₂ while carrying out the reaction in supercritical CO₂.⁶² Despite this catalyst showed the highest yield ever reached under the specified reaction conditions, it is not the most suitable for industrialization due to the high pressure required.

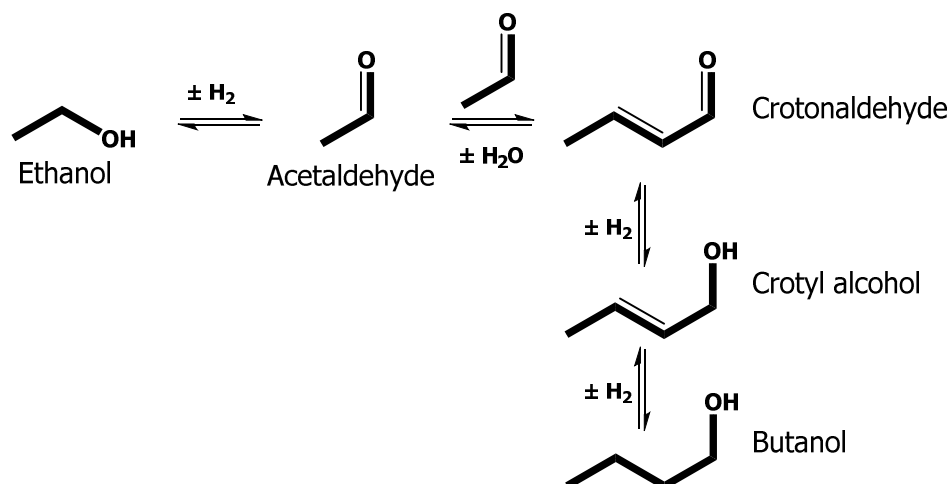


Figure 2.3 Most accredited Guerbet reaction mechanism to convert ethanol into 1-butanol.

It is possible to notice that different mixed oxides were tested in order to tune the acid base properties and some authors tried to add some dehydrogenating/hydrogenating metal such as Ni or Cu. In fact, it is thought that a fine tuning of acid base properties along with the presence of a dehydrogenating/hydrogenating agent is the key to enhance 1-butanol productivity. In this regard, it was found that a higher acid-base ratio (R_{AB}) in hydroxyapatite promotes the Guerbet side products such as ethylene and diethyl ether while a lower R_{AB} favors 1-butanol production.⁵⁹ Similar findings are valid also for mixed metal oxides.⁵³ It is worth noting that recently Mg₃(PO₄)₂ was tested and showed the behavior of an acidic catalyst leading to 52 % and 36 % selectivity to ethylene and diethyl ether, respectively. In the same work, Ca and Sr phosphates were tested and were found not so effective for 1-butanol production, even if calcium phosphate was able to reach a 35 % selectivity to 1-butanol thanks to its medium strength Lewis acid sites furnished by Ca²⁺ cations.⁶¹

Anyway, to date it is still not clear which is the acid or basic strength needed to carry out this reaction efficiently. Moreover, there is a general lack of study of catalyst stability over time in ethanol condensation to 1-butanol.⁷¹

All of these properties are important if the reaction mechanism is considered. In fact, the most accepted reaction mechanism involves ethanol dehydrogenation to acetaldehyde which undergoes aldol condensation followed by a hydrogenation step. The hydrogenation step is thought to occur either through a Merweein-Pondorf-Verlain (MPV) mechanism (consuming a sacrificial ethanol) or thanks to the H₂ produced in the first step. This reaction mechanism, reported in Figure 2.3, has been recently discarded on MgO and basic zeolites.^{72,73} As alternative, Chierigato et al⁷² proposed a direct condensation of two ethanol molecules through a carbanion intermediate whose

existence was proven by Diffuse Reflectance Infrared Fourier Transform Spectroscopy (DRIFTS) and Density Functional Theory (DFT) calculation.

Recently, Young et al⁷⁴ studied the hydrogenation properties of hydroxyapatite and magnesium oxide. According to their study, hydroxyapatite and MgO are not able to hydrogenate (in presence of H₂) neither ethene nor acetone. The latter is hydrogenated through H-transfer (MPV mechanism). The absence of evidence for C=C hydrogenation allowed them to hypothesize that the hydrogenation step proceeds through MPV H-transfer, likely followed by a double bond shift to form an enol species which tautomerizes to a carbonyl moiety. Moreover, they found out that the benzyl alcohol dehydrogenation rate on HAP was lower than the ethanol coupling rate. This observation led to the conclusion that the hydrogenation step on HAP is a H-transfer reaction. The authors also mentioned that this step is coherent with an autocatalytic reaction. Overall, the Guerbet reaction mechanism in gas phase is still far from being understood.

The main idea of the present work is to address the problem of the acid-base sites role. The catalytic performance of basic oxides in the Guerbet reaction was investigated and the different intermediates formed on the catalyst surface were studied by means of DRIFTS. The aim was to gain a complete understanding on basicity strength effect. Afterwards, MgO was impregnated with H₃PO₄, since PO₄ groups might be responsible for the unprecedented selectivity of hydroxyapatite catalysts and a better understanding of their role is crucial. The last part of this work is a comparison of the performance of impregnated catalysts with that one of Ca and Sr hydroxyapatite (HAP). In order to better highlight the differences, in this work the stability of these catalysts over time was also studied. Furthermore, to our knowledge this work is the first one to study the catalytic performance of hydroxyapatite in the Guerbet reaction over the mid-term time.

2.2 Methods

15

2.2.1 Catalyst syntheses

MgO was prepared by controlled pH precipitation synthesis. A solution of Na₂CO₃ of desired concentration was prepared and warmed up to 60 °C under constant stirring. Then, a nitrate solution of the corresponding metal was added dropwise. Throughout the precipitation process, the pH was kept stable at 10.5 using 3 M NaOH solution. The precipitate obtained was filtrated, washed with excess of lukewarm distilled water and dried in the oven at 120 °C overnight.

CaO and **SrO** were synthesized with a similar procedure but instead of Na₂CO₃ a solution of NaOH 3M was used. Moreover, the reaction was kept under nitrogen atmosphere in order to avoid carbonation due to CO₂ in the atmosphere. After filtration and washing with lukewarm water, the wet powder was dried under vacuum at 70 °C overnight. The catalysts were kept under N₂ atmosphere in a desiccator.

The obtained dried Mg(OH)₂, Ca(OH)₂, and Sr(OH)₂ powders were calcined at 450 °C, 700 °C and 900 °C for 3 h to obtain the respective oxides. SrO was also purchased from *Sigma-Aldrich* (99.9 % purity) and it was used as received. It will be named SrO_CS.

Part of a batch of MgO possessing a surface area higher than 160 m² g⁻¹ was used as support to produce **H₃PO₄/MgO**. This catalyst was synthesized by incipient wetness impregnation (IWI). Some aliquots (5 g) of MgO (with a surface area higher than 150 m² g⁻¹) were impregnated with a H₃PO₄ solution. The H₃PO₄ solution concentration was changed to obtain 0.5 %, 1 % and 5 % (w/w) H₃PO₄ on MgO. The wet powder was dried in an oven at 120 °C and then calcined at 450 °C. A small amount of the powder calcined at 450 °C was successively calcined at 550 °C. The catalysts will be named 0.5PMgO, 1PMgO and 5PMgO, respectively. This synthesis procedure is

strongly affected by the initial MgO surface area and by the different operator who performs the impregnation.

Ca-hydroxyapatite (HAP) was synthesized according to the procedure reported by Tsuchida et al.⁶⁴. In a typical procedure, a solution of $\text{Ca}(\text{NO}_3)_2$ 0.6 M was added dropwise to a 0.4 M $(\text{NH}_4)_2\text{HPO}_4$ solution, under stirring and keeping the pH constant to 10.5. The precipitate solution was left aging for 24 h at 60 °C under reflux. Then, the precipitate was filtrated, washed with lukewarm water and dried in an oven at 140 °C overnight.

SrHAP was obtained with the same procedure but instead of a $\text{Ca}(\text{NO}_3)_2$ solution a solution 0.6 M of $\text{Sr}(\text{NO}_3)_2$ was used.

The obtained powders were calcined to 600 °C for 2h.

2.2.2 Catalyst characterizations

X-ray diffraction (XRD) patterns were recorded in the range of $10^\circ < 2\theta < 80^\circ$ with a Philips PW 1050/81 apparatus controlled by a PW 1710 unit ($\lambda = 0.15418$ nm (Cu), 40 kV, 40 mA). The scanning rate was $0.05^\circ 2\theta \text{ s}^{-1}$ and the step time 1 s. The XRD phase was assigned using the "Search and match!" option of X'Pert Highscore Plus and the ICSD database.

The specific surface area was measured by applying the single-point Brunauer-Emmet-Teller (BET) theory.⁷⁵ The instrument used was a Carlo Erba Sorptly 1700. Around 0.15 g of sample was placed inside a sample holder. Prior to analysis, the sample was heated at 150 °C under vacuum in order to release all the possibly adsorbed molecules.

Attenuated Total Reflectance (ATR) spectra of the materials were recorded at room temperature with an ALPHA-FTIR instrument at a resolution of 2 cm^{-1} .

Temperature programmed desorption (TPD) of NH_3 or CO_2 measurements were obtained with a TPD/TPR/TPO Micromeritics instrument. About 150 mg of catalysts were pre-treated at the calcination temperature for 1 h under a He flow. After cooling down to 50 °C (or 100 °C), NH_3 was adsorbed by flowing the catalysts under a 10 % NH_3/He gas mixture for 30 min (30 mL min^{-1} , NTP), with subsequent He treatment at 50 °C for 15 min to remove physisorbed NH_3 . Afterwards, the samples were heated under He flow (30 mL min^{-1} , NTP) up to 450 °C at a heating rate of $10^\circ \text{C min}^{-1}$. The experiments with CO_2 followed the same procedure but instead of NH_3/He , CO_2/He was dosed and the temperature programmed desorption experiments started at 40 °C.

Raman spectroscopy measurement were performed using a Renishaw Raman System 1000 equipped with a confocal microscope Leica DMLM with lens 5x, 20x and 50x and color video camera. The laser used was the green with Ar ions at 514 nm and 25 mW of power. The system can reach resolution up to $0.5 \mu\text{m}$.

ThermoGravimetric Analysis (TGA) was carried out using a TA Instrument SDT-Q600 apparatus. To decide the sample calcination temperature, the weight loss was evaluated under N_2 flow (100 mL min^{-1}). In a typical experiment 15-30 mg of catalyst were thermally treated in N_2 from room temperature to 1000 °C at $10^\circ \text{C min}^{-1}$.

2.2.3 Reactivity Tests.

The catalytic activity was studied in a gas phase continuous-flow quartz reactor working at atmospheric pressure. In a typical reaction, the amount of catalyst, loaded as pellet (30-40 mesh), was varied between 0.5 and 2 g according to the necessities, unless otherwise specified. The activity was studied as a function of both temperature and residence time. The inlet gas feed varied according to the experiment between 2 and 15 mol % EtOH in He.

The outlet gas stream was analyzed by an online Agilent 6890A gas-chromatograph. The latter was equipped with two TCD detectors and the products were separated using a PLOT-Q (30 m x 0.32 mm x 20 mm) and a FFAP (50 m x 0.32 mm x 0.52 mm) columns. The main products that might derive from the reaction were calibrated while all the uncalibrated peaks were considered using a common calibration curve. The unknown and uncalibrated peaks are grouped as Others_NID. On the contrary, Others_ID groups compounds that are known and quantified using their specific calibration curve, but their amount is almost negligible if considered as single. Unless otherwise specified, Others_ID value is given by the yield sum of acetone, diethyl ether, butanal, butenes, ethyl acetate, crotonaldehyde and crotyl alcohol.

The conversion, yields, selectivities and the carbon loss were calculated as follow:

$$\begin{aligned}\chi &= \frac{\text{mol}_{\text{EtOH}}^{\text{in}} - \text{mol}_{\text{EtOH}}^{\text{out}}}{\text{mol}_{\text{EtOH}}^{\text{in}}} \\ Y_p &= \frac{C_{\text{atom}}^p \cdot \text{mol}_p^{\text{out}}}{C_{\text{atom}}^{\text{EtOH}} \cdot \text{mol}_{\text{EtOH}}^{\text{in}}} \\ S_p &= \frac{Y_p}{\chi} \\ C_{\text{loss}} &= \chi - \sum_i Y_{p_i}\end{aligned}$$

Residence time was calculated as the ratio between the mass of catalyst loaded in the reactor (g) and the total volumetric gas flow (ml · min⁻¹):

$$\tau = \frac{m_{\text{catalyst}}}{\dot{V}_{\text{total}}}$$

2.2.4 *In-situ DRIFTS-MS measurements.*

The IR apparatus used was a Bruker Vertex 70 equipped with a Pike DiffusIR cell attachment. Spectra were recorded using an MCT detector after 128 scans and 4 cm⁻¹ resolution. The coupled mass spectrometer was an EcoSys-P from European Spectrometry Systems.

In all cases, samples were pre-treated at 450 °C under a He flow (10 mL min⁻¹) for 30 min to remove any adsorbed molecules on the material surface. Then, the sample was cooled down to 50 °C, and an ethanol pulse was fed and vaporized. Subsequently, helium was left flow until weakly adsorbed ethanol was evacuated. The temperature was raised to 450 °C at 5 °C min⁻¹, a spectrum was recorded every 50 °C. In another set of experiments, after the pre-treatment, the temperature was raised to 350 °C and kept for 180 min without stopping the ethanol flow. The reaction evolution was followed with a spectrum every 10 min. The following selected mass spectroscopy signals (m/z) were monitored continuously with time (and temperature): 2, 16, 25, 28, 29, 30, 31, 40, 41, 43, 44, 45, 56, 58, 59, 60, and 61.

When pyridine was used as probe molecule, the samples were pretreated till 450 °C for 30 min. Afterwards, 1 µl of pyridine was injected at 50 °C. After 30 minutes, when the physisorbed pyridine had been removed by the He flow (8 mL min⁻¹), the temperature was raised to 300 °C and after 10 min it was decreased to 50 °C, again. The spectra were collected at 50 °C before and after the temperature raise to evaluate if strong Lewis or Brønsted acid sites were present on the catalyst surface.

Ethanol adsorption

Ethanol adsorption on different metal oxides can lead to various adsorbed species depending on the surface properties of the material studied. Table 2.1 shows the main surface species which can be formed after ethanol adsorption and their characteristic infrared bands.^{72,76–91} However, some differences in wavenumbers are due to a different interaction between the catalyst and the adsorbed molecule. Moreover, both species formed, and their transformation pathways are strictly related to the surface chemistry of each catalyst.

Table 2.1 Characteristic bands of common surface species derived from Ethanol adsorption.

Species		Characteristic wavenumber (cm ⁻¹)	
H-bonded molecular ethanol	$\begin{array}{c} \text{CH}_3\text{CH}_2\text{O} \\ \\ \text{H} \\ \downarrow \\ \text{---} \end{array}$	3700-3000 1380 1500-1200	$\nu(\text{OH})$ $\delta(\text{CH}_3)$ $\delta(\text{CH}_3)$
O-bonded molecular ethanol	$\begin{array}{c} \text{CH}_3\text{CH}_2 \quad \text{H} \\ \diagdown \quad \diagup \\ \text{O} \\ \downarrow \\ \text{---} \end{array}$	3700-3000 1380 1270	$\nu(\text{OH})$ $\delta(\text{CH}_3)$ $\delta(\text{CH}_3)$
Ethoxide	$\begin{array}{c} \text{CH}_3\text{CH}_2 \\ \\ \text{O} \\ \downarrow \\ \text{---} \end{array}$	2970 2930 2875 1107 1065 875	$\nu_{\text{as}}(\text{CH}_3)$ $\nu_{\text{as}}(\text{CH}_2)$ $\nu_{\text{s}}(\text{CH}_3)$ $\nu(\text{CO})_{\text{monodentate}}$ $\nu(\text{CO})_{\text{bidentat}}/\nu(\text{CC})$ $\nu(\text{CC})$
η^1 -Acetaldehyde	$\begin{array}{c} \text{CH}_3\text{CH} \\ \\ \text{O} \\ \downarrow \\ \text{---} \end{array}$	1700-1650 1407-1449 1366-1386 1344	$\nu(\text{C=O})$ $\delta_{\text{as}}(\text{CH}_3)$ $\delta(\text{CH})$ $\delta_{\text{s}}(\text{CH}_3)$
η^2 -Aldehyde	$\begin{array}{c} \text{H} \\ \\ \text{CH}_3-\text{C}-\text{O} \\ \diagup \quad \diagdown \\ \text{---} \quad \text{---} \end{array}$	2755 1348 1275 1148 972	$\nu(\text{CH})$ $\delta(\text{CH}_3)$ $\nu(\text{CO})$ $\nu(\text{CC})$ $\rho(\text{CH}_3)$
Acyl	$\begin{array}{c} \text{CH}_3 \\ \\ \text{C}=\text{O} \\ \\ \text{---} \end{array}$	2978 2901 1636	$\nu_{\text{as}}(\text{CH}_3)$ $\nu_{\text{as}}(\text{CH}_2)/\nu_{\text{s}}(\text{CH}_3)$ $\nu(\text{C=O})$
Acetate	$\begin{array}{c} \text{CH}_3 \\ \\ \text{C} \\ / \quad \backslash \\ \text{O} \quad \text{O} \\ \quad \\ \text{---} \quad \text{---} \end{array}$	1547 1445 1338	$\nu_{\text{as}}(\text{OCO})$ $\nu_{\text{s}}(\text{OCO})$ $\delta(\text{CH}_3)$
Carbonate	$\begin{array}{c} \text{O} \quad \text{O} \\ \backslash \quad / \\ \text{C} \\ \\ \text{O} \\ \\ \text{---} \end{array}$	1558 1506 1445 1300 1336 1425	$\nu_{\text{as}}(\text{OCO})_{\text{bidentate}}$ $\nu_{\text{as}}(\text{OCO})_{\text{monodentate}}$ $\nu_{\text{as}}(\text{OCO})_{\text{polydentate}}$ $\nu_{\text{s}}(\text{OCO})_{\text{bidentate}}$ $\nu_{\text{s}}(\text{OCO})_{\text{monodentate}}$ $\nu_{\text{s}}(\text{OCO})_{\text{polydentate}}$

Acetone	$\begin{array}{c} \text{CH}_3\text{CCH}_3 \\ \parallel \\ \text{O} \\ \downarrow \\ \hline \end{array}$	1735 – 1723 1437/1365 1225 – 1207	$\nu(\text{CO})$ $\delta_{\text{as}}(\text{CH}_3)/\delta_{\text{s}}(\text{CH}_3)$ $\nu(\text{CC})$
Crotonaldehyde	$\begin{array}{c} \text{CH}_3\text{CH}=\text{CHCH} \\ \parallel \\ \text{O} \\ \downarrow \\ \hline \end{array}$	1713-1670 1640-1600 1454 – 1039 1190 – 1156 1080 971	$\nu(\text{C}=\text{O})$ $\nu(\text{C}=\text{C})$ $\delta(\text{CH})$ $\gamma(\text{CH})$ $\nu(\text{CHO})$ $\nu(\text{CC})$
Crotyl alcohol	$\begin{array}{c} \text{CH}_3\text{CH}=\text{CHCHO} \\ \parallel \\ \text{H} \\ \downarrow \\ \hline \end{array}$	1674-1602 1450-1364 1218-1113 1077-1000 965	$\nu(\text{C}=\text{C})$ $\delta(\text{CH})$ $\gamma(\text{CH})$ $\nu(\text{CO})$ $\nu(\text{CC})$

The m/z signals followed during the analyses are reported in Table 2.2. The m/z value specific for each molecule was chosen according to the statistical weight of the fragment in the mass spectrum. Then, weighted contributions of other fragments at the same m/z were subtracted to obtain molecule-specific signals, using the following equation:

$$I_{X,mol_1} = I_X - \sum_i W_{X,mol_i} \cdot \frac{I_{Y,mol_i}}{W_{Y,mol_i}}$$

Where X = m/z assigned to mol_1 , Y = m/z assigned to mol_i , mol_1 = molecule of interest, mol_i = interfering molecules, W = statistical weight of fragment X

19

Table 2.2 m/z signal followed during DRIFTS-MS experiments.

m/z	Compound identified	Interferences
2	H ₂	
18	H ₂ O	
26	Ethylene	
29	Acetaldehyde	Ethanol, Diethyl ether
31	Ethanol	Diethyl ether
41	Butenes	Butyraldehyde, Crotonaldehyde, Crotyl Alcohol
43	Ethyl Acetate	Butyraldehyde, Crotyl Alcohol, Acetone
54	1,3-Butadiene	
56	1-butanol	
57	Crotyl Alcohol	Butyraldehyde
58	Acetone	
59	Diethyl ether	
70	Crotonaldehyde	Ethyl Acetate
72	Butyraldehyde	Crotyl Alcohol

2.3 Basic oxides in the Guerbet Reaction

2.3.1 *MgO, CaO and SrO characterization*

BET analysis after calcination showed that only MgO possessed a relatively high surface area, even after the thermal treatment (Table 2.3). All the other catalysts presented very low surface area. The first column reports the code given to each catalyst that will be respected from now on, throughout this thesis.

Table 2.3 Catalyst specific surface area.

Catalyst	Surface Area $\text{m}^2 \cdot \text{g}^{-1}$
MgO	127
CaO	< 5
Ca(OH) ₂	< 5
SrO	< 5
SrO_CS	< 5

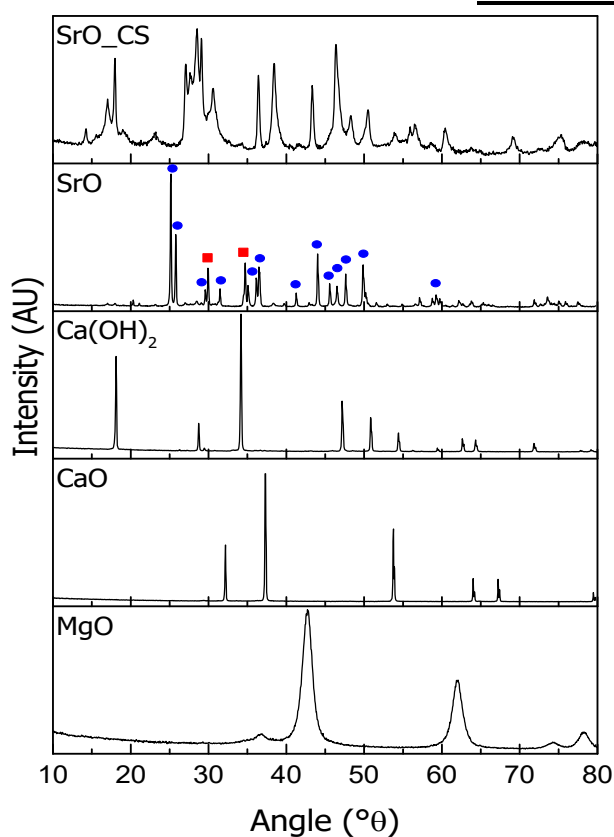


Figure 2.4 XRD patterns for MgO, CaO, Ca(OH)₂, SrO and SrO_CS.

MgO, CaO, SrO, and SrO_CS diffraction patterns are reported in Figure 2.4. MgO (Ref. Code: 01-089-7746) was obtained without any impurity. The broad reflection indicates that the sample was not as crystalline as CaO and SrO. CaO was highly crystalline and it showed sharp reflections typical of lime (CaO) (ref. 01-077-2376). On the contrary, the synthesized strontium oxide presented a high crystalline degree while the commercial one was less crystalline, as shown by reflections width. Moreover, none of them was a pure SrO phase (ref. 00-048-1477). In fact, some SrO reflections were shown by the synthesized samples (red square) but also those of SrCO₃ were present (ref. 00-005-0418, blue circle). Surprisingly, the commercial SrO was characterized only by the presence of Sr(OH)₂ (ref. 01-074-0407). The SrO pattern indicates its high affinity for both water and CO₂ demonstrating that it is difficult to obtain and maintain a pure SrO phase. A second batch of CaO was synthesized and used without calcination. Its XRD pattern is reported in Figure 2.4 and showed the presence of highly crystalline Ca(OH)₂ (Ref. 00-001-1079).

A TGA analysis was performed on Ca(OH)₂ in order to determine at which temperature this compound shows the weight loss. This analysis was used to decide the pretreatment temperature to apply before running the reaction. Figure 2.5 shows that the sample underwent two weight losses: one at 450 °C due to H₂O release and another smaller one (around 1 %) at 650 °C due to CO₂ loss. This second weight loss was related to a minor sample carbonation. 500 °C was pointed out as the best temperature to carry out the catalyst pretreatment inside the reactor.

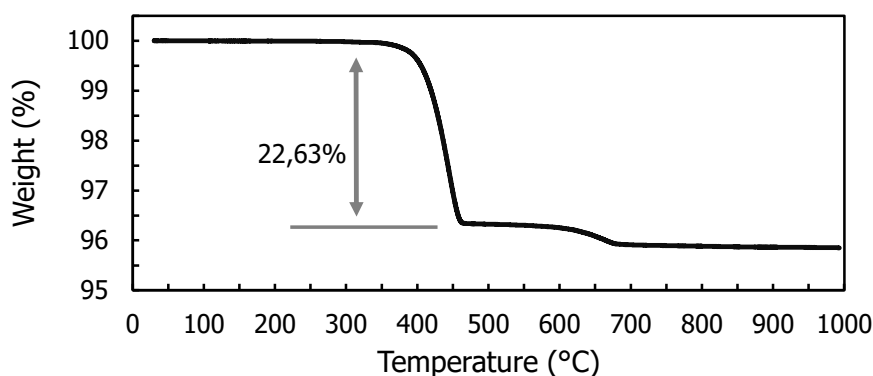


Figure 2.5 Ca(OH)_2 TGA analysis.

2.3.2 MgO, CaO and SrO reactivities

All the reactivity plots, shown in the following sections, have two vertical axes. All the dashed lines, that usually represent conversion and carbon loss, are referred to the dashed left axis while the solid axis, on the right, shows the scale for all the solid yield lines. If a yield line is dashed in a specific plot then, only in that plot, this specific yield is scaled towards the left dashed axis. In this section the butenes yield was not considered in others_ID but it was considered along with butadiene yield.

Temperature effect

In general, catalyst activity increased when temperature was raised. However, on one side a high temperature may facilitate the desired reaction while on the other one it can enhance the contribution of side-reactions. The described effect is one of the main problems which one has to deal with when the reaction network is complex as in the Guerbet reaction. For this reason, catalyst performances were evaluated as a function of temperature with the aim of enhancing 1-butanol yield and limiting side-products formation. The products distribution as a function of temperature is reported in Figure 2.6. Ethanol conversion (black dashed line) increased along with the temperature rise and reached its maximum value (57 %) at 450 °C. Likewise, all the products yields and the C_{loss} (violet dashed line) were increasing. 1-Butanol yield (green solid line) was the highest from 300 °C to 400 °C. At 450 °C, it reached a plateau. In fact, at such temperature 1-butanol might undergo either successive condensation forming longer chain alcohols, as suggested by the increase of others_NID yield (orange solid line), or degradation reactions, i.e., dehydration into butenes or oxidation into butyraldehyde which reached 1 % yield at 450 °C (red solid line in Figure 2.6). Acetaldehyde yield (blue solid line in Figure 2.6) was increasing along with the temperature raise and it was always one of the main reaction products. After 350 °C, several secondary reactions started to be significant as demonstrated by ethylene (gray solid line), C_4 olefins (red solid line), Others_ID and Others_NID yields. Moreover, the C_{loss} reached 20 % at 450 °C meaning that a lot of coke was formed at such temperature. It is worth noting that at 450 °C ethylene showed the highest yield (7 %). Ethylene, usually, is a typical product derived from ethanol dehydration on acidic solid catalysts. It is obvious that on MgO its formation is not due to the presence of acidic sites, therefore it is following a different chemistry. In fact, if acidic sites were present diethyl ether should have been formed also, but this compound was not detected at any temperature, as shown in Figure 2.6. Ethylene formation might be due to the carbanion decomposition on basic sites at high temperature, on MgO.⁷² Then, the best temperature to carry out the Guerbet reaction on MgO is 350 °C, because 1-butanol yield was 2 % at 8 % conversion and the other product yields were close to or less than 1 %.

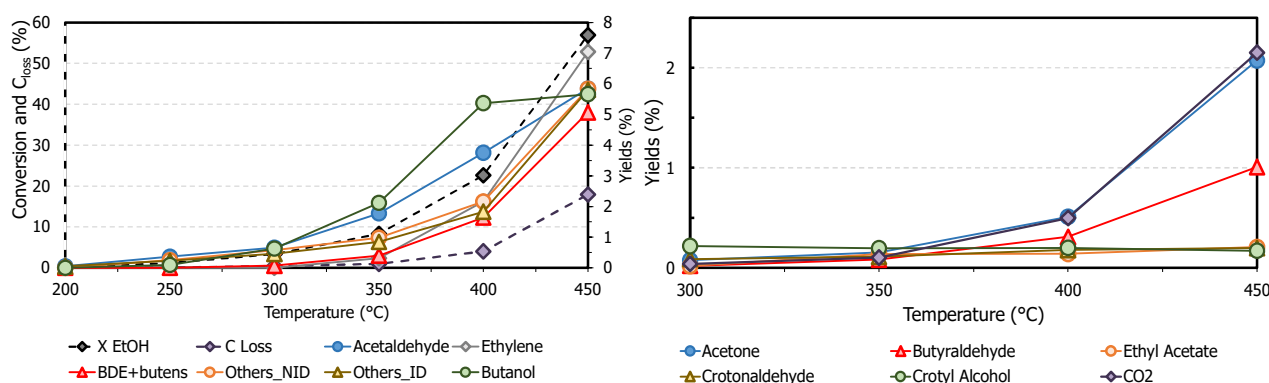


Figure 2.6 MgO product distribution as temperature function, on the left. Minor products grouped in Others_ID, on the right Reaction conditions: $\tau = 0.5 \text{ g} \cdot \text{s} \cdot \text{mL}^{-1}$, $m_{\text{cat}} = 0.5 \text{ g}$, 5 % EtOH in He.

$\text{Ca}(\text{OH})_2$ and CaO were tested in the reactor after 1h of pre-activation at 500 °C in He. This pre-treatment should enhance selectivity by removing carbonate species from catalyst surface.

The product distributions for $\text{Ca}(\text{OH})_2$ and CaO are reported in Figure 2.7 on the left and on the right-hand side, respectively. It is worth to notice that the activity of the two catalysts was not dramatically different. The conversion (black dashed line) was increasing with temperature and the same occurred also for acetaldehyde (light blue solid line) and ethylene yields (gray solid line). The main difference between the two samples was that $\text{Ca}(\text{OH})_2$ showed 2 % 1-butanol yield at 450 °C while with CaO 1-butanol yield was lower than 0.5 % even at 500 °C. Others_ID formation was increasing with the temperature raise because of acetone yield, which reached 1.5 % at 450 °C on $\text{Ca}(\text{OH})_2$, and 3.5 % at 500 °C on CaO, respectively. At 500 °C on CaO, Others_NID yield was increasing, as well.

This difference in activity shown by the two samples can be explained with their diverse hydroxylation. In fact, Petitjean et al.⁹² observed that in order to use CaO as a basic catalyst, the key parameter to optimize is the hydroxylation degree. They stated that the hydroxylation degree has to be low enough in order to maintain the CaO phase while avoiding $\text{Ca}(\text{OH})_2$ formation, but high enough to have many reactive surface hydroxyl groups.

Therefore, it is possible that the *in situ* calcination favored the basic reactivity of CaO in the completely dehydroxylated CaO. However, 1-butanol was not among the main reaction products at any temperature. In fact, the best temperature for the Guerbet reaction on $\text{Ca}(\text{OH})_2$ is 450 °C, since at the latter temperature 1-butanol yield was 2 % at 15 % conversion.

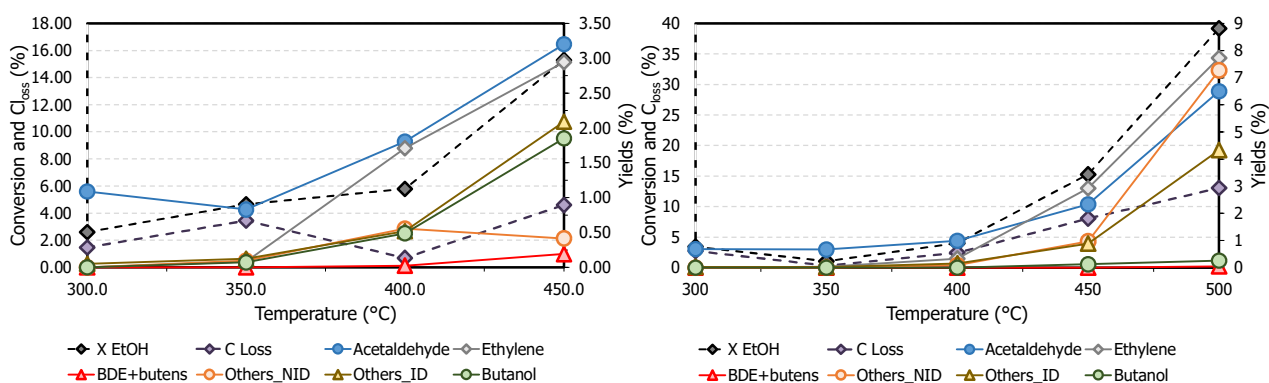


Figure 2.7 $\text{Ca}(\text{OH})_2$ (on the left) and CaO (on the right) product distributions as temperature function. Reaction conditions: $\tau = 0.5 \text{ g} \cdot \text{s} \cdot \text{mL}^{-1}$, $m_{\text{cat}} = 0.5 \text{ g}$, 5 % EtOH in He.

Finally, the reactivity of the two SrO samples was evaluated, results are reported in Figure 2.8. It is possible to notice that SrO_CS, that contained mainly $\text{Sr}(\text{OH})_2$, was slightly more active than SrO. In fact, the conversion at 500 °C was around 20 % and 10 % for SrO_CS and SrO,

respectively, with acetaldehyde as the main product (yield 14 % and 9 %, respectively). 1-Butanol yield was around 1 % on SrO_CS at 500 °C while it was lower than 0.5 % at every temperature on SrO. All in all, these samples resulted to be quite inactive for 1-butanol production. On the other hand, they were quite active in ethanol dehydrogenation to acetaldehyde. All the other products showed yield lower than 1 % with SrO, while for SrO_CS the highest yield was shown by Others_ID, close to 4 % because of acetone production. It is possible that the hydration degree plays a crucial role even on this system as it was for CaO, but to our knowledge the hydration effect for SrO has not been studied, yet.^{92,93}

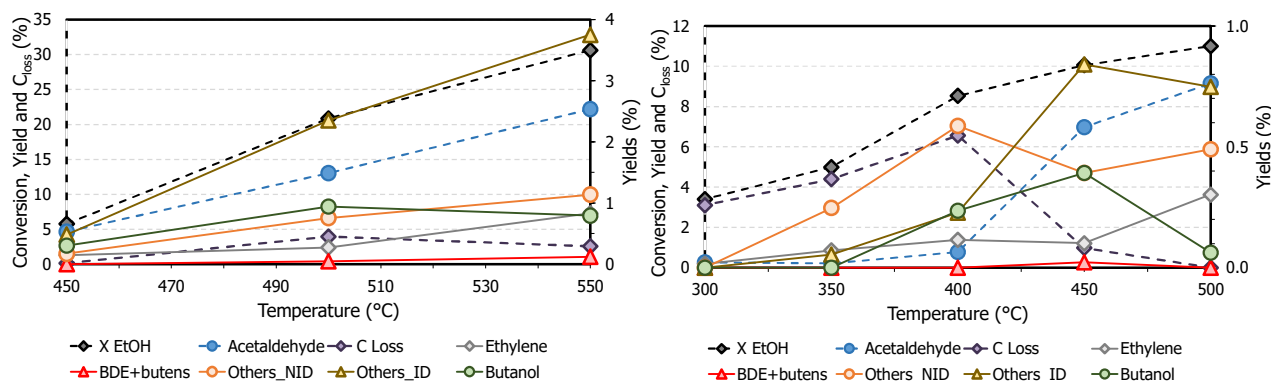


Figure 2.8 SrO_CS (on the left) and SrO (on the right) product distributions as temperature function. Reaction conditions: $\tau = 0.5 \text{ g} \cdot \text{s} \cdot \text{mL}^{-1}$, $m_{\text{cat}} = 0.5 \text{ g}$, 5 % EtOH in He.

It is possible to notice that 1-butanol yield was decreasing with the increase in basicity⁹⁴, in fact the yield to 1-butanol can be ranked as follows: $\text{MgO} > \text{CaO} > \text{SrO}$.

Contact time effect

A contact time screening was carried out at the best temperature chosen. However, Sr oxide samples showed a low mechanic resistance, and catalyst pellets tended to pulverize during reaction bringing to reactor clogging and dangerous pressure raise. Therefore, this catalytic system was discarded from further reactivity investigations even in light of its low activity in 1-butanol formation. In order to carry out these catalytic tests, the catalyst load was varied, and the inlet flow rate was kept constant.

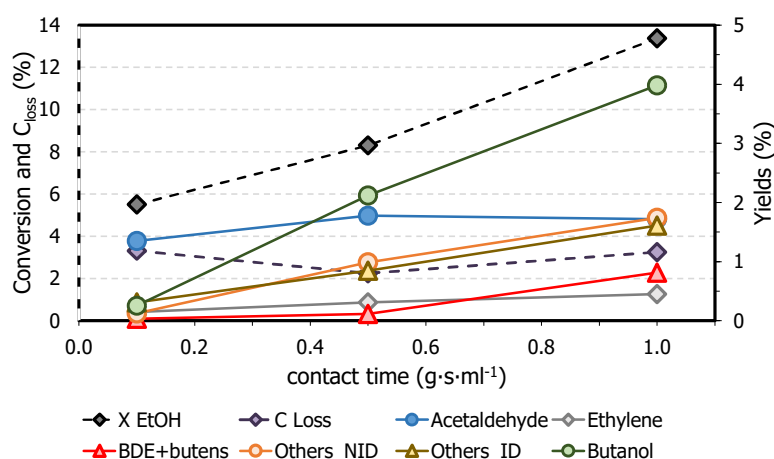


Figure 2.9 MgO product distribution with respect to residence time. Reaction conditions: 350 °C, $\dot{V}_{\text{tot}} = 60 \text{ mL min}^{-1}$, $m_{\text{cat}} = 0.1 \div 1.0 \text{ g}$.

Ethanol conversion increased from 6 % (at $0.1 \text{ g} \cdot \text{s} \cdot \text{mL}^{-1}$) up to 13 % (at $1 \text{ g} \cdot \text{s} \cdot \text{mL}^{-1}$) when the contact time was increased; 1-butanol yield was equal to 0.3 % and 4 %, respectively, as shown

in Figure 2.9. On the contrary, acetaldehyde yield slightly decreased from $0.5 \text{ g}\cdot\text{s}\cdot\text{mL}^{-1}$ to $1 \text{ g}\cdot\text{s}\cdot\text{mL}^{-1}$ while others_ID and others_NID increased along with C_4 olefins yield. A competition between the generally accepted mechanism and the carbanion mechanism is reasonable, since 1-butanol seemed to be a primary product and it did not reach a plateau. Moreover, a higher contact time allowed a prolonged interaction between the adsorbed molecule and the catalyst, so favoring secondary products, such as C_4 olefins and Others_ID (aldol condensation intermediates, i.e., crotonaldehyde), and side products, such as Others_NID.

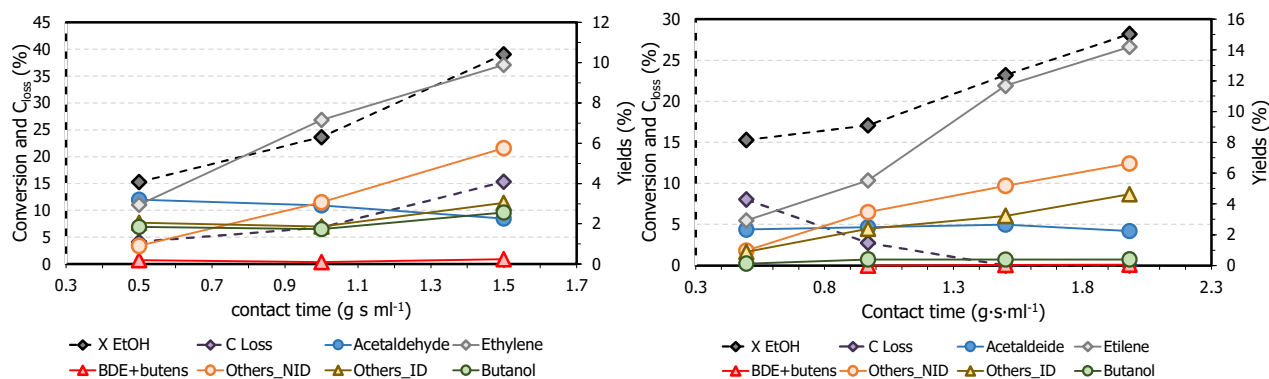


Figure 2.10 $\text{Ca}(\text{OH})_2$ (on the left) and CaO (on the right) product distribution with respect to residence time. Reaction conditions: 450°C , $\dot{V}_{\text{tot}} = 60 \text{ mL min}^{-1}$, $m_{\text{cat}} = 0.1 \div 1.0 \text{ g}$.

The effect of contact time for $\text{Ca}(\text{OH})_2$ and CaO is reported in Figure 2.10. As already seen from the temperature screening, $\text{Ca}(\text{OH})_2$ was more active in 1-butanol formation reaching a 3 % yield at $1.5 \text{ g}\cdot\text{s}\cdot\text{mL}^{-1}$ while 1-butanol yield was negligible with CaO even at higher contact time. The main product for these two catalysts was ethylene, whose yield was steeply increasing along with contact time reaching 10 % at $1.5 \text{ g}\cdot\text{s}\cdot\text{mL}^{-1}$ and 14 % at $2.0 \text{ g}\cdot\text{s}\cdot\text{mL}^{-1}$ for $\text{Ca}(\text{OH})_2$ and CaO , respectively. Acetaldehyde yield was decreasing in favor of Others_ID and Others_NID with both catalysts. These results can be explained assuming a competition between the two hypothesized reaction mechanisms. In fact, it is possible that on CaO , which possesses a higher basicity than MgO , the formed carbanion is not sufficiently stabilised by the weakly acidic metal cation (Ca^{2+}) promoting ethylene production *via* carbanion dehydration. In fact, it is likely that on increasing the O^{2-} basicity, the counterion acidity becomes correspondingly weaker. For this reason, on one side the catalyst can be more effective in forming the carbanion but on the other one it is less efficient in building up the right interaction needed for 1-butanol formation.

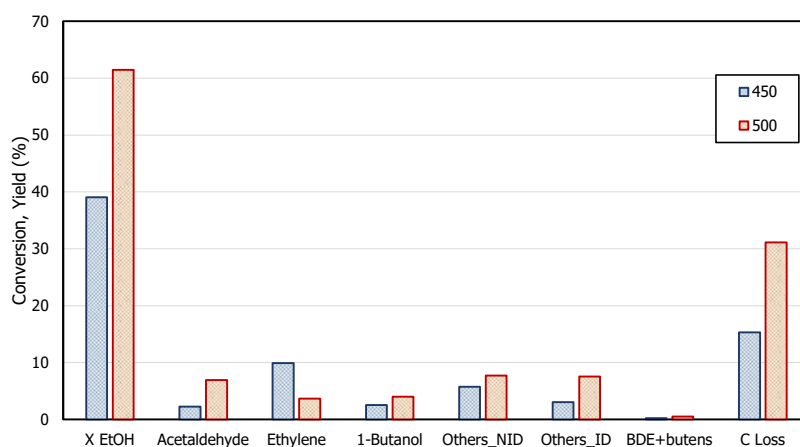


Figure 2.11 Comparison between $\text{Ca}(\text{OH})_2$ reactivity at 450°C and 500°C at $1.5 \text{ g}\cdot\text{s}\cdot\text{mL}^{-1}$.

In order to understand if it is possible to further enhance 1-butanol yield with $\text{Ca}(\text{OH})_2$, a further test at $1.5 \text{ g}\cdot\text{s}\cdot\text{mL}^{-1}$ and 500°C was carried out; the results are reported in Figure 2.11. 1-butanol

yield slightly increased from 3 % to 4 % along with acetaldehyde, Others_ID and C_{loss} yields. The latter was the dominant “product” at such temperature and contact time. These results might suggest that 1-butanol was produced on CaO *via* aldol condensation. In fact, its yield slightly increased while acetaldehyde and crotonaldehyde yields doubled (from 2 % to 7 % and from 0.03 % to 0.2 %, respectively). The temperature was not further raised because of the poor carbon balance shown.

Overall, this part of the work showed that the most active catalyst in 1-butanol formation is MgO, which gave 4 % yield at 350 °C and $1.0 \text{ g}\cdot\text{s}\cdot\text{mL}^{-1}$. The same 4 % 1-butanol yield was reached with CaO also, at 550 °C and $1.5 \text{ g}\cdot\text{s}\cdot\text{mL}^{-1}$ but with poor carbon balance. The different reaction conditions required can be explained by a different reaction mechanism occurring with the two catalysts. In fact, it is likely that with CaO 1-butanol production occurs *via* aldol condensation while with MgO 1-butanol is produced *via* carbanion. It can be hypothesized that the carbanion formation is responsible for the high ethylene yield observed with CaO and SrO. In fact, the basicity of these two catalysts is higher than that one of MgO.⁹⁴ Moreover, the very weak Lewis metal acidity can be ranked as follows: $\text{Mg}^{2+} > \text{Ca}^{2+} > \text{Sr}^{2+}$ and it is possible to hypothesize that Ca and Sr acidity is too weak to interact efficiently with the carbanion CH_2^- . To corroborate this hypothesis some DRIFTS tests were carried out and the results are reported in the next section.

2.3.3 *MgO, CaO and SrO DRIFTS*

MgO DRIFT

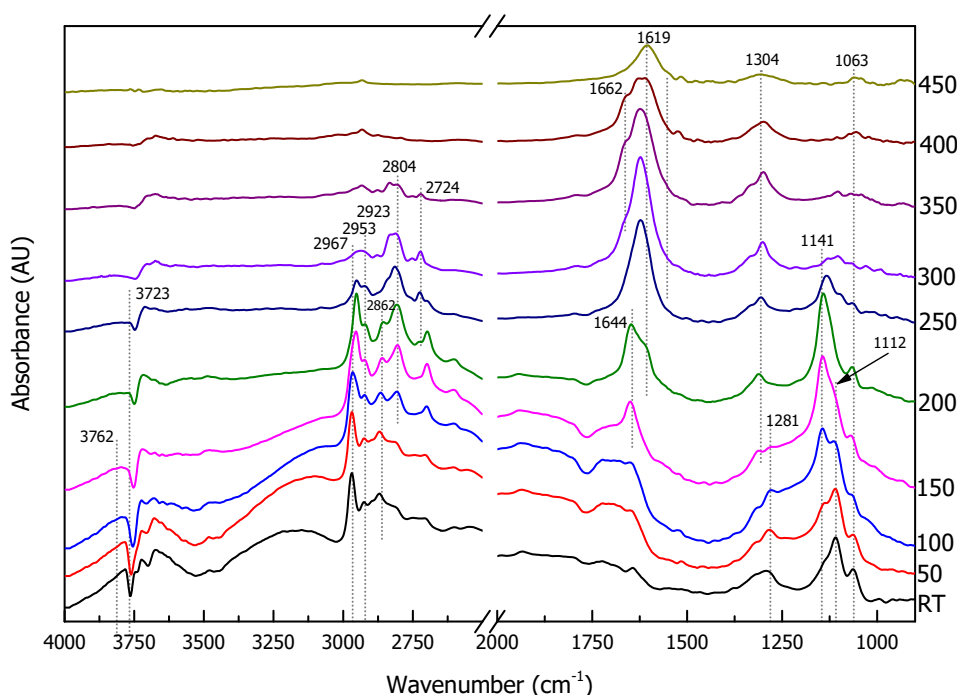


Figure 2.12 Ethanol adsorption and intermediate evolution with temperature followed by DRIFTS.

Figure 2.12 shows the DRIFT spectra of ethanol adsorbed on MgO, during the stepwise temperature-programmed desorption experiment (STPD). The spectra are shown in the order of raising temperature, from the bottom to the top of the graph.

At RT, the observed bands correspond to adsorbed un-dissociated (H-bonded and O-bonded) ethanol as well as ethoxide (product of ethanol dissociative adsorption). The broad band between 3000 and 3500 cm^{-1} was due to OH stretching, while the weak band at 1281 cm^{-1} was assigned to the OH bending mode of molecular ethanol. The bands at 2967 cm^{-1} , 2923 cm^{-1} and 2862 cm^{-1}

were attributed to $\nu_{\text{as}}(\text{CH}_3)$, $\nu_{\text{as}}(\text{CH}_2)$ and $\nu_{\text{s}}(\text{CH}_3)$ stretching modes of adsorbed ethoxide.⁷² Additionally, also bands at 1063 cm^{-1} and 1112 cm^{-1} were associated to the ethoxide species $\nu(\text{C-O})$ adsorbed as monodentate and bidentate, respectively.⁹¹ At 1141 cm^{-1} a small shoulder was present due to a peculiar C-O stretching, as recently proposed by Chieragato et al.⁷², that was attributed to the carbanion intermediate.

A temperature raise caused an increase of the intensity of the band at 1141 cm^{-1} which reached its maximum value at $200\text{ }^\circ\text{C}$. After this temperature, one C-H vibration band underwent a red-shift (namely, from 2967 towards 2953 cm^{-1}). The carbanion main band disappeared at $350\text{ }^\circ\text{C}$. Another peak that emerged at elevated temperatures was shown at 1304 cm^{-1} , reaching its maximum intensity at $350\text{ }^\circ\text{C}$. It could be assigned to $\nu_{\text{s}}(\text{OCO})$ of monodentate carbonates that are formed on the surface.⁹⁵ Complementary evidence for surface carbonates might be the broadening of the band at around 1600 cm^{-1} .^{72,79} Another band at 1619 cm^{-1} , ascribable to crotyl alcohol, seemed to increase when temperature was raised and this could be tentatively correlated with the decrease of ethanol and ethoxy specific bands (1063 cm^{-1} , 1112 cm^{-1} and 1281 cm^{-1}), suggesting the transformation of ethanol into crotyl alcohol at $T > 150\text{ }^\circ\text{C}$.⁷² This band remained visible in the spectrum even when the temperature was increased up to $450\text{ }^\circ\text{C}$. At 1662 cm^{-1} , the detected shoulder was assigned to a crotonaldehyde precursor, while the band at 1644 cm^{-1} was reported to be characteristic of the C=O stretch of acyl or acetyl species.⁷² Acetyl species, at high temperature, may decompose into CO and methyl, which might further form acetone explaining its presence among the reaction products.⁷² In the middle range of temperatures ($100 - 350\text{ }^\circ\text{C}$) bands typical for aldehydes were noticed at 2804 cm^{-1} and 2724 cm^{-1} .⁹⁶ In the high wavenumbers region, the bands at 3723 cm^{-1} and 3762 cm^{-1} were attributed to OH stretching modes. The former was assigned to the formation of new superficial OH groups while the latter (negative) was due to the interaction of the OH group already present on the catalyst surface with other adsorbed molecules.

To sum up, presented results have shown noticeable coherence with literature and experimental reactivity data. It was confirmed that the direct condensation mechanism on MgO could proceed through a carbanion intermediate and might be the favored one. At low temperature, acetaldehyde was not detected in our experiments, and for this reason it is hard to confirm the competition between the two mechanisms.

Ca(OH)₂ and CaO

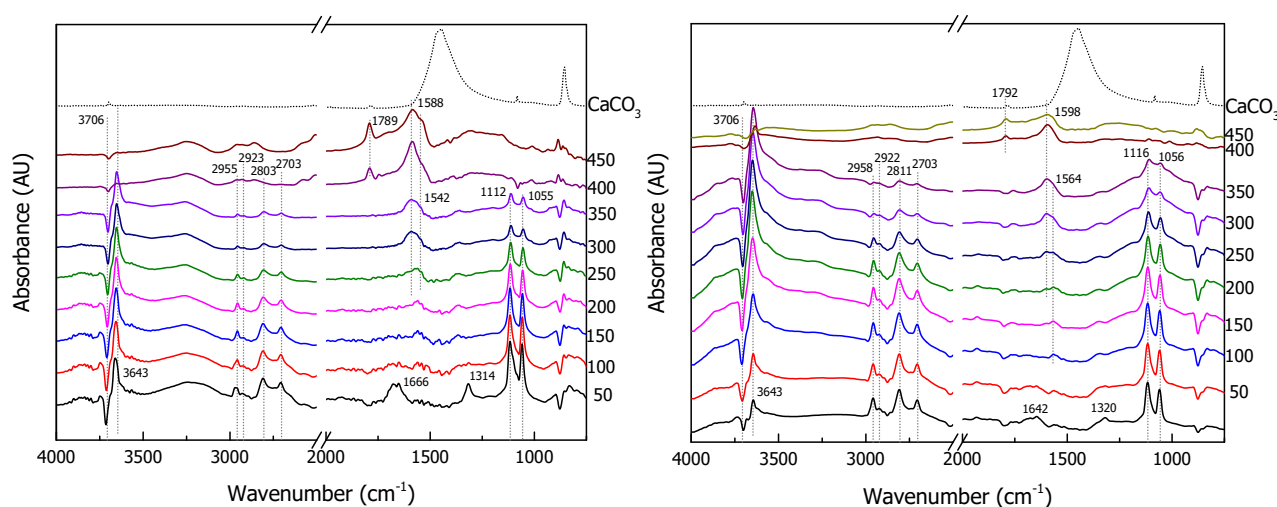


Figure 2.13 Ethanol adsorption and intermediates evolution followed by DRIFTS on CaO (left) and Ca(OH)₂ (right).

CaO and Ca(OH)₂ DRIFTS spectra as function of temperature, recorded after ethanol adsorption, are reported in Figure 2.13 on the left and on the right-hand side, respectively.

The ethanol spectral features were quite similar on the two samples and then a common elaboration will be reported herein, highlighting the small differences between the two samples. At the lowest temperature (spectrum in black), on both samples it was possible to detect the ethoxy transitions: 1056 cm^{-1} and 1116 cm^{-1} assignable to monodentate and bidentate adsorbed ethoxy $\nu(\text{C-O})$, respectively.⁹¹ Correspondingly, it was possible to observe the CH_3 and CH_2 stretching between 3000 cm^{-1} and 2800 cm^{-1} along with the $\nu(\text{OH})$ at 3643 cm^{-1} .⁷² The negative band at 3706 cm^{-1} was ascribed to $\nu(\text{OH})$ of the terminal OH present on the catalyst surface before ethanol adsorption. Other two low intensity bands were visible at 1642 cm^{-1} and 1320 cm^{-1} , attributed to η^1 -acetaldehyde $\nu(\text{C=O})$ and $\delta(\text{CH}_3)$.⁷⁷ The monodentate (1056 cm^{-1}) and bidentate (1116 cm^{-1}) ratio (M/B) was equal to 1 and 0.84 for CaO and $\text{Ca}(\text{OH})_2$, respectively. Increasing the temperature, acetaldehyde bands vanished and new lower intensity bands at 1564 cm^{-1} and 1368 cm^{-1} started to be visible and were ascribed to either acetate or carbonate $\nu_{\text{as}}(\text{OCO})$ and $\nu_{\text{s}}(\text{OCO})$, respectively. Ethanol bands vanished completely at $400\text{ }^\circ\text{C}$. At such temperature a new band at 1790 cm^{-1} started to be detectable and it was ascribed to a complete catalyst surface carbonation. In fact, this band was well visible in CaCO_3 ATR spectrum (from RRUFF database), reported as dotted spectrum in the graph.⁹

According to this experiment, it is not possible to correlate the higher $\text{Ca}(\text{OH})_2$ reactivity to a specific intermediate species. The $\text{Ca}(\text{OH})_2$ higher activity might be due to the lower interaction with acetaldehyde and the lower attitude to transform adsorbed ethanol into carbonates. On this catalyst surface, no evidence for carbanion formation was shown. This difference can be correlated with its lower activity in 1-butanol formation. It is reasonable to hypothesize that this catalyst is following the classic reaction mechanism. Probably, the carbanion, if formed, is highly unstable on this catalyst surface and soon “decomposes” forming ethylene and water, in agreement with reactivity results.

SrO_CS and SrO

27

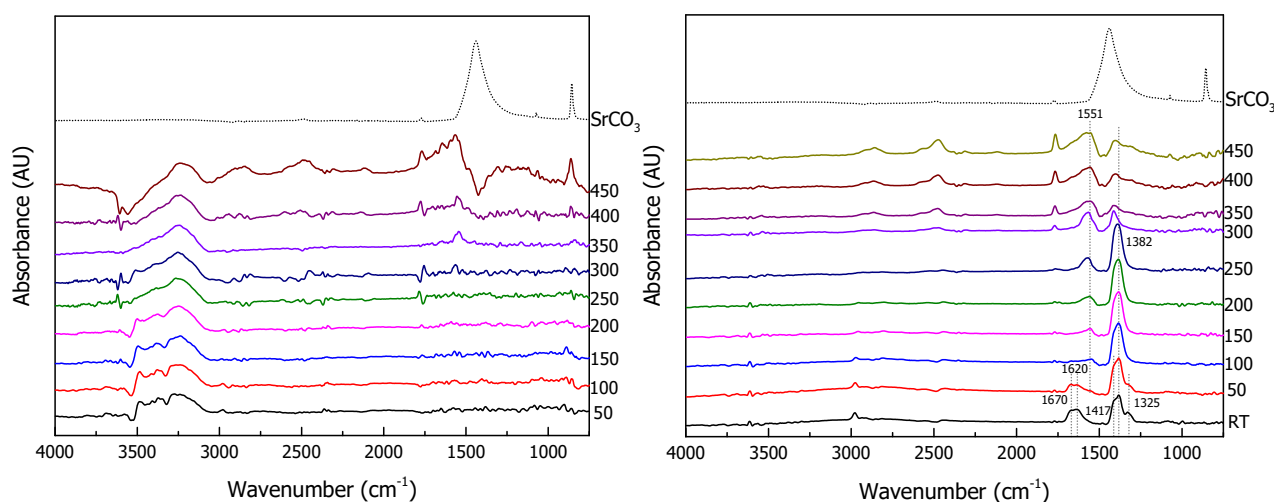


Figure 2.14 Ethanol adsorption and intermediate evolution on SrO (left) and SrO_CS (right) followed by DRIFTS.

SrO , whose spectra after ethanol adsorption are reported on the left-hand side of Figure 2.14, seemed not to interact with ethanol. Anyway, it is possible to hypothesize a weak interaction with the ethoxy species that was released as acetaldehyde. This hypothesis is in good agreement with the catalytic tests and with the broad band, centred at 3500 cm^{-1} , assignable to the newly formed

⁹ <http://rruff.info/Calcite/R050128>

surface OH. Some new bands appeared at 450 °C and were assigned to catalyst carbonation in agreement with the SrCO₃ reference (from RRUFF database), reported as dotted spectrum.^p

The interaction with ethanol shown by the commercial sample was different and it was in agreement with its higher activity in ethanol conversion. In fact, two bands at 1670 cm⁻¹ and 1620 cm⁻¹ were assigned to $\nu(\text{C}=\text{O})$ of η^1 -acetaldehyde and acyl species.^{72,77,82,89} The bands at 1417 cm⁻¹, 1382 cm⁻¹ and 1325 cm⁻¹ were related to $\delta_{\text{as}}(\text{CH}_3)$, $\delta(\text{CH})$ and $\delta_{\text{s}}(\text{CH}_3)$ vibrations of acetaldehyde.^{77,97} Upon increasing the temperature, acetaldehyde was released while acyl was probably converted into acetate species as suggested by the appearing of the band at 1551 cm⁻¹ assignable to $\nu_{\text{as}}(\text{OCO})$, while the band at 1382 cm⁻¹ is now associated to acetate $\nu_{\text{s}}(\text{OCO})$. A further temperature increase brought to a blue shift of the symmetric stretching along with the appearance of a band at 1750 cm⁻¹ ascribed to SrCO₃. Then, it was possible to see that after 350 °C carbonates are the sole specie present on the catalyst surface.

The catalyst ability to dehydrogenate ethanol increased in the following order: SrO>CaO>CaO. It is possible to say that the higher the basicity, the higher the dehydrogenation efficiency. Moreover, the higher basicity seemed to favour the aldol condensation mechanism over the direct ethanol condensation.

2.3.4 Conclusions

In this section the catalytic performances of basic oxides were studied. MgO had the highest surface area while the other two oxides showed a comparable surface area, lower than 5 m² g⁻¹. Therefore, it is not surprising that MgO showed the highest catalytic activity in terms of both 1-butanol yield and ethanol conversion.

MgO at 400 °C and 0.5 g·s·mL⁻¹ yielded 6 % 1-butanol, 4 % acetaldehyde, 2 % ethylene at 23 % ethanol conversion. CaO gave similar 1-butanol yield (4 %) at 500 °C and 1.5 g·s·mL⁻¹ along with 4 % ethylene, 7 % acetaldehyde at 61 % conversion. However, the high temperature used for CaO caused a relevant C loss of 31 %. Finally, SrO at 550 °C and 0.5 g·s·mL⁻¹ yielded 1 % 1-butanol, 23 % acetaldehyde, 1 % ethylene at 30 % conversion. The optimal temperature was increasing along with the basic strength increase. Moreover, 1-butanol yield decreased when the basicity was increased, while acetaldehyde yield increased. Furthermore, ethylene yield was the highest with CaO. These results suggest a competition between the aldol condensation mechanism and the direct condensation. The carbanion formation was verified only on MgO along with ethanol chemisorbed and adsorbed as ethoxide. CaO presented ethoxide and acetaldehyde on its surface while on SrO only acetaldehyde was detected. These results confirmed the increase in dehydrogenation efficiency occurring with the increase of basicity. Moreover, their combination with reactivity tests allowed to hypothesize that Mg²⁺ ion were weak acid sites but strong enough to interact with the carbanion so to allow it to undergo direct condensation. On the contrary, if the carbanion was formed on CaO, Ca²⁺ ions were not able to efficiently interact with the carbanion that being a highly unstable specie underwent dehydration to ethylene. Finally, it is reasonable that the carbanion was formed in negligible amount on SrO, as demonstrated by the low ethylene yield.

All in all, it was seen that the stronger is the basicity, the lesser is the efficiency in stabilizing the carbanion. For this reason, it is possible to hypothesize that 1-butanol is formed on MgO *via* both mechanisms reported in the literature while on CaO and SrO it is formed mainly by aldol condensation, explaining the low 1-butanol yields. On these two catalysts, if the carbanion is formed, it evolves to the formation of ethylene.

^p <http://rruff.info/Strontianite/R040037>

2.4 How is the addition of phosphate to MgO affecting the Guerbet reaction?

This work was done in a collaboration with prof. I. Rossetti, University of Milan. In fact, the experimental data reported in section 2.4.3 will be used to perform a kinetic study aimed at the design of a plant for this process.

2.4.1 H_3PO_4 /MgO catalysts characterization

Three MgO batches were impregnated with different H_3PO_4 solutions in order to obtain three different catalysts, as reported in section 2.2.1. These samples were calcined to 450 °C and part of the already calcined sample was further calcined at 550 °C. In this paragraph the characterization of these samples is reported.

The surface area decreased with H_3PO_4 concentration for the samples calcined at 450 °C, as shown in Table 2.4, while the sample containing 1 % w/w H_3PO_4 showed the lowest surface area among the samples calcined at 550 °C.

The XRD patterns of samples, shown in Figure 2.15, presented only MgO diffraction. These results evidenced that the bulk phase was not affected by the impregnation and that H_3PO_4 was well dispersed on the catalyst surface.

Table 2.4 Surface area and total acid site concentration for the samples calcined at different temperature.

Catalyst	SA ^{a,b} m ² g ⁻¹	SA ^{a,c} m ² g ⁻¹	Total acid site concentration ^{d,b}		Total acid site concentration ^{d,c}	
			μmol g ⁻¹	μmol m ⁻²	μmol g ⁻¹	μmol m ⁻²
MgO	161	-	-	-	-	-
0.5PMgO	133	81	24	0.180	24	0.296
1PMgO	114	46	40	0.351	20	0.435
5PMgP	78	71	75	0.962	51	0.718

^a SA = Surface Area, evaluated by BET

^b samples calcined at 450 °C

^c samples calcined at 550 °C

^d calculated by TPD-NH₃

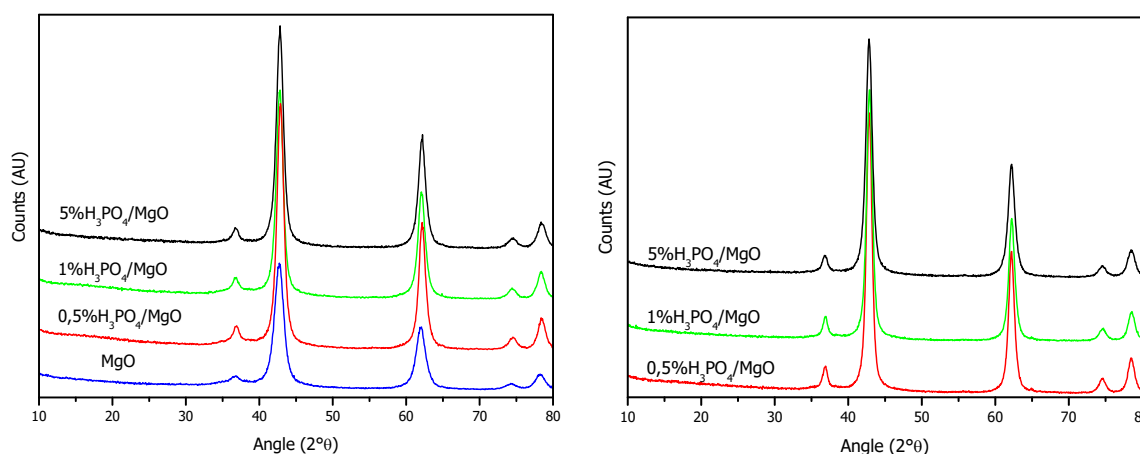


Figure 2.15 H_3PO_4 /MgO sample diffraction patterns calcined at 450 °C (left) and 550 °C (right).

The presence of phosphate groups was confirmed by Raman spectroscopy. The Raman spectra are reported in Figure 2.16, in the left figure for samples calcined at 450 °C while on the right-hand side, samples calcined at 550 °C. In all cases, it was possible to appreciate two PO_4^{3-} vibrations: the ν_3 (due to asymmetrical stretching of P–O bond) and the ν_2 (due to in plane PO_4^{3-}

bending vibration).^{98–100} In fact, the bands at 1084 cm^{-1} and 1045 cm^{-1} were assigned to ν_3 while the band at 445 cm^{-1} was due to ν_2 .^{98–100} The attribution of the band at 971 cm^{-1} was not unambiguous, in fact it could be either assigned to a degenerative band of ν_3 or to ν_1 (symmetrical stretching) whose width may be increased by a certain degree of carbonation of the surface.¹⁰¹ In the spectrum there was no evidence of carbonate presence⁹⁸, therefore this band width could not be attributed to carbonation.¹⁰² It is possible that it started to be visible because of the increase in PO_4^{3-} content. Therefore, it was tentatively attributed to ν_1 , in agreement with previous assignments for this sample.^{98,103} The calcination at higher temperatures removed the vibrational mode degeneration for all samples and only the main ν_3 and ν_2 bands were still visible at 1087 cm^{-1} and 442 cm^{-1} , respectively.

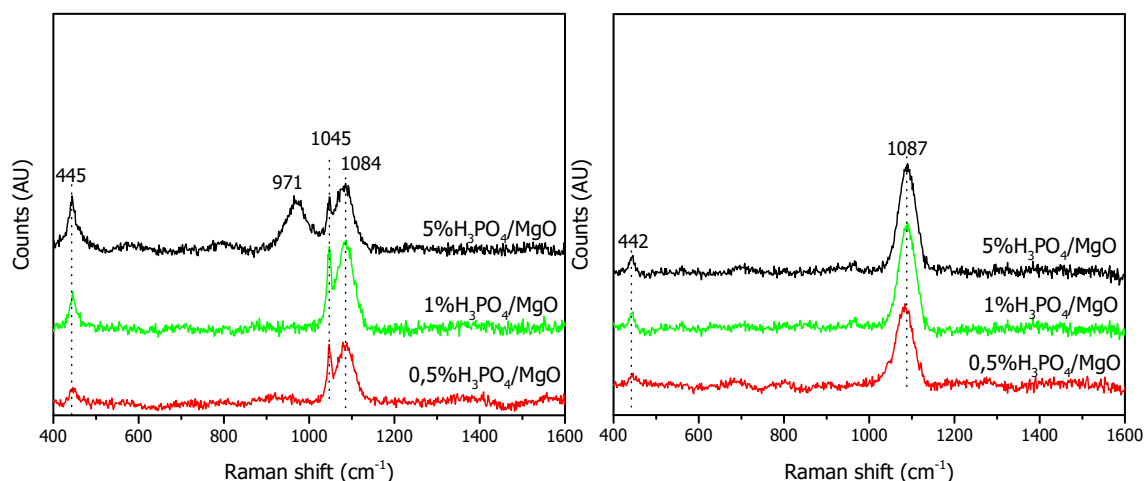


Figure 2.16 $\text{H}_3\text{PO}_4/\text{MgO}$ catalysts Raman spectra. The sample calcined at $450\text{ }^\circ\text{C}$ are on the left-hand side while the calcined at $550\text{ }^\circ\text{C}$ one on the right-hand side.

The acidity of samples was measured by means of TPD- NH_3 . NH_3 desorption profiles for the samples calcined at $450\text{ }^\circ\text{C}$ are reported on the left-hand side of Figure 2.17 while the total acid site concentration is reported in Table 2.4. The acid sites, in this work, are divided in 3 categories: weak, medium and strong according to the desorption temperature (under $200\text{ }^\circ\text{C}$, between $200\text{ }^\circ\text{C}$ and $300\text{ }^\circ\text{C}$ and, over $300\text{ }^\circ\text{C}$, respectively). The total acidity concentration was in excellent agreement with the increase of PO_4^{3-} weight content. The ammonia desorption profile for 0.5PMgO, 1PMgO and 5PMgO was centred at $162\text{ }^\circ\text{C}$, $131\text{ }^\circ\text{C}$ and $155\text{ }^\circ\text{C}$, respectively. According to the desorption range previously mentioned, the small and Gaussian-shaped desorption profile of 0.5PMgO was in the region of weak acid strength, with some contribution of medium strength sites. On the contrary, 1PMgO and 5PMgO presented broad desorption profiles. 1PMgO distribution was centred at $131\text{ }^\circ\text{C}$ and it was mainly characterized by weak and some medium strength acid sites. Instead, 5PMgO possessed the broadest desorption profile centred at $155\text{ }^\circ\text{C}$ and it was characterized by weak and medium acid sites, but it possessed also some strong acid sites.

The desorption profiles for catalysts calcined at $550\text{ }^\circ\text{C}$ are reported on the right side of Figure 2.17. In this case, total acidity, normalized with respect to the catalyst mass and reported in Table 2.4, was not in good agreement with the PO_4^{3-} concentration. In order to obtain values that can be correlated with PO_4^{3-} content, it was necessary to refer values to the surface area of samples. However, a small total acidity concentration decrement was detected using the higher calcination temperature, along with a general increase of acid sites strength. In fact, for 0.5PMgO the ammonia desorption profile was centred at $162\text{ }^\circ\text{C}$, for 1PMgO at $163\text{ }^\circ\text{C}$ and for 5PMgO at $171\text{ }^\circ\text{C}$. 0.5PMgO and 1PMgO were mainly characterized by medium strength acid sites with small

number of strong sites. On the contrary, 5PMgO was mainly characterized by medium strength acid sites with contribution of weak and strong acid sites.

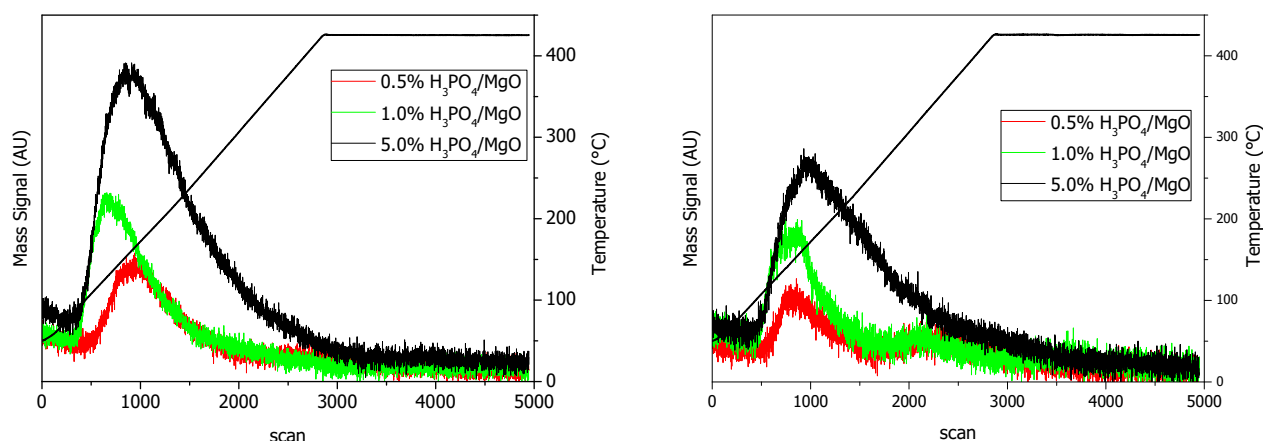


Figure 2.17 TPD-NH₃ profiles for H₃PO₄/MgO calcined at 450 °C (on the left) and 550 °C (on the right).

2.4.2 H₃PO₄/MgO temperature screening

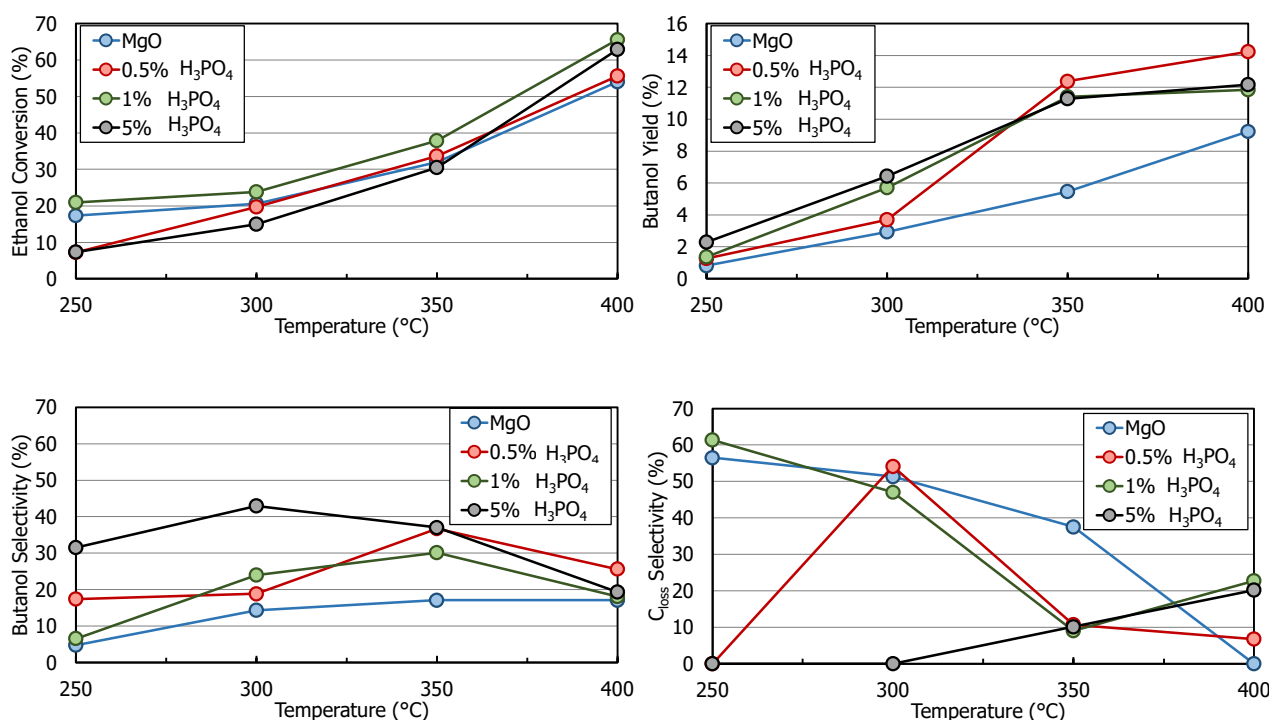


Figure 2.18 Ethanol conversion, 1-butanol yield and selectivity, C_{loss} selectivity for H₃PO₄/MgO samples as function of temperature. Reaction conditions: 2 % EtOH in He, $V_{tot} = 30 \text{ mL min}^{-1}$, $\tau = 1 \text{ g} \cdot \text{s} \cdot \text{mL}^{-1}$.

The catalysts calcined at 450 °C were tested in function of temperature. It was observed that even a small addition of H₃PO₄ to magnesium oxide increased 1-butanol yield, as shown in Figure 2.18. For all samples both conversion (from 10-20 % to 55-65 %) and 1-butanol yield (from 1-2 % to 9-14 %) increased with an increase of temperature. With MgO, the selectivity (blue line) reached a plateau (18 %) after 350 °C. Instead, all the other catalysts showed a maximum at 350 °C probably because at 400 °C 1-butanol underwent side reactions. In fact, the C_{loss} selectivity increased from 350 °C to 400 °C.

Catalysts were calcined at higher temperature (550 °C) to determine if this parameter affects catalyst performance. As expected, conversion (shown in Figure 2.19) was negatively affected by calcination at high temperature. In fact, it decreased from an average value of 35 %, for the

catalyst calcined at 450 °C, down to 25 % at 350 °C, when the catalyst was calcined at 550 °C. The 1-butanol yields slightly decreased by the 2 %. On the contrary, the selectivity was comparable, and all the impregnated catalysts showed close values for 1-butanol selectivity. Another positive effect of the calcination at the higher temperature was the decrease of the C_{loss} values at 250 °C and 300 °C, by the 20 % and 10 %, respectively.

Since the catalyst performances were not significantly improved by the higher calcination temperature, those samples were discarded from further examination. On the other hand, a catalyst from the 450 °C series was chosen to carry out a complete reactivity study.

The best temperature chosen for the reaction was 350 °C, at which the best catalyst yielded ~12 % 1-butanol at ~32 % ethanol conversion, with a good carbon balance.

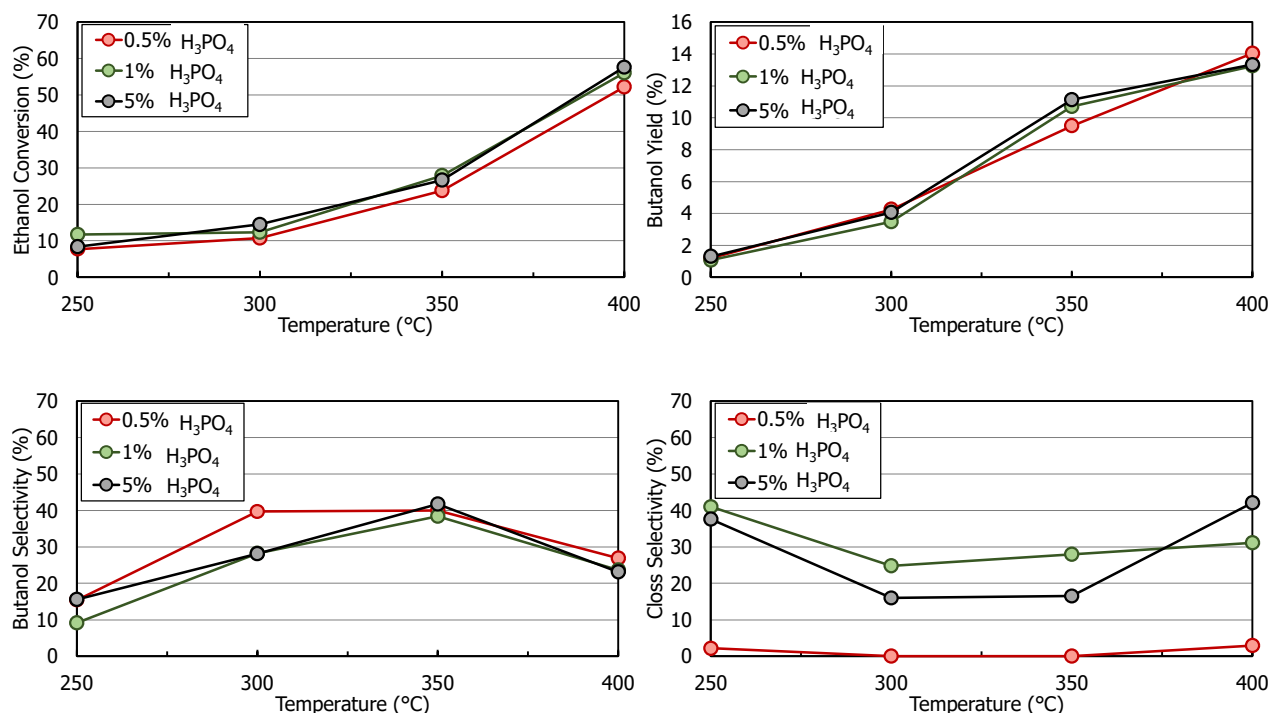


Figure 2.19 Ethanol conversion, 1-butanol yield and selectivity, C_{loss} selectivity for the H_3PO_4 /MgO samples as function of temperature. Reaction conditions: 2 % EtOH in He, $V_{tot} = 30 \text{ mL min}^{-1}$, $\tau = 1 \text{ g} \cdot \text{s} \cdot \text{mL}^{-1}$.

The products distributions at 350 °C are compared in Figure 2.20. MgO showed the highest acetaldehyde yield (3 %) and C_{loss} (12 %) at 32 % conversion. The carbon loss decreased by the 9 % after phosphate addition. 0.5PMgO yielded 11 % 1-butanol, 4 % butadiene, 9 % Others_NID and 3 % Others_ID. In this case, Others_ID comprised: ethylene, crotonaldehyde, crotyl alcohol, diethyl ether and ethyl acetate. 1PMgO yielded 11 % 1-butanol showing the highest Others_NID yield (13 %) at 38 % ethanol conversion. Finally, 5PMgO yielded 11 % 1-butanol and 6 % Others_NID at 31 % conversion.

1PMgO showed the lowest 1-butanol selectivity (Figure 2.18). Therefore, it was discarded from further investigation. Since the final aim of this work was to carry out a complete kinetic study, it is necessary to be completely aware of all the possible side reactions. 0.5PMgO and 5PMgO were not so different in terms of both 1-butanol selectivity and conversion. The known side reactions were the discriminant to decide which catalyst use to carry out the kinetic study. 5PMgO was chosen as the best catalyst because it showed a lower C_{loss} and others_NID yield compared to 0.5PMgO. This is a great advantage because at the end it will be simpler to model the reaction scheme.

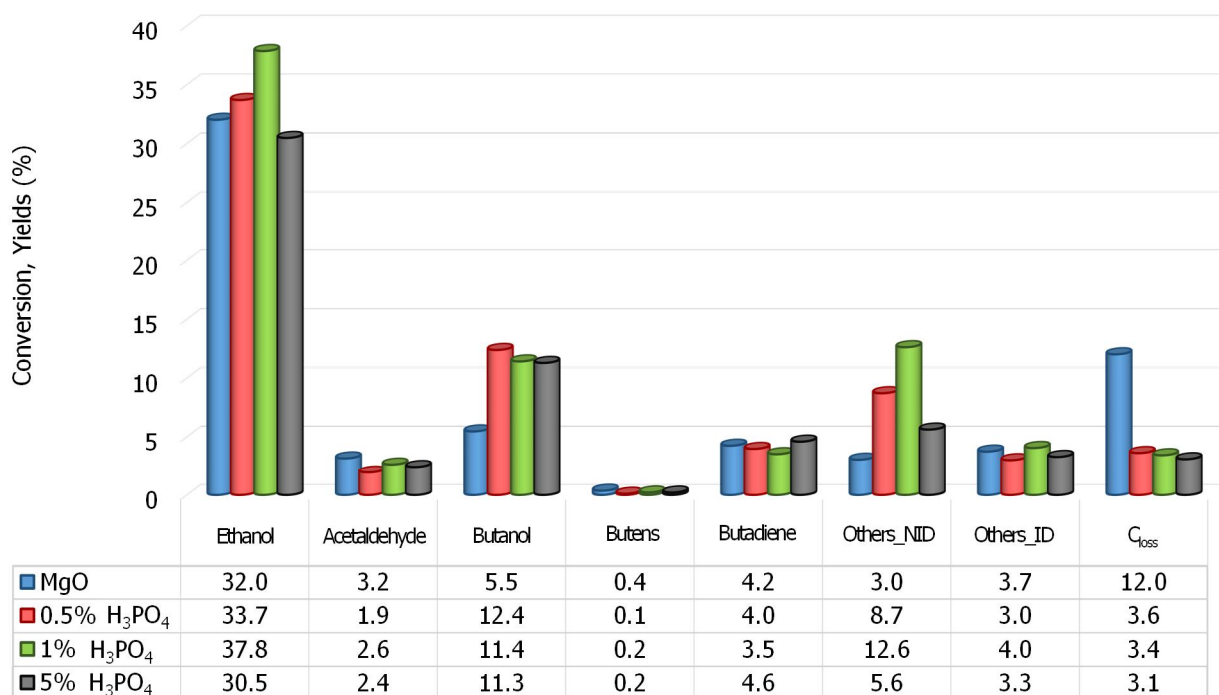


Figure 2.20 Catalyst performances at 350 °C, $\tau = 1 \text{ g s mL}^{-1}$, $V_{\text{tot}}=30 \text{ mL min}^{-1}$ and 2 % EtOH in He.

2.4.3 5 % w/w H₃PO₄ reactivity study

The experimental work was aimed at finding the optimal conditions to carry out the reaction. Hence, several tests were conducted changing both catalyst amount and temperature. The reaction parameters and the results which showed a conversion of about 50 % were chosen as the central point for a square test. The square test was necessary in order to understand how small variations in reaction parameters affected the reaction kinetics. This piece of information is needed to carry out a complete kinetic study, whose results will be reported somewhere else.

Catalyst stability over time on stream

Since the catalyst synthesis is not simple, as also explained in section 2.2.1, the catalyst was tested during a short lifetime test in order to check if deactivation was a relevant phenomenon. The ethanol conversion (black dashed line in Figure 2.21) dropped from 70 % to 30 % within the first 4 h of reaction. Subsequently, it stabilized around 25 % conversion. After the first 2 h 1-butanol yield was 10 %, then it slightly decreased to reach a stable 9 % yield in 9 h. In 18 h of reaction 1-butanol yield decreased by only 1 %. For this reason, deactivation can be considered negligible. Along with a slight decrease of 1-butanol yield, a slow increase of acetaldehyde yield (blue line) was also detected. This result suggests that 1-butanol formation is somehow related to acetaldehyde. Therefore, it is possible that the direct condensation and the aldol condensation are competing mechanisms. All tests reported from now on have been carried out for 5 h. Moreover, the experiments as a function of temperature were performed using the same catalyst. In fact, the temperature increase was enough to remove the coke formed at low temperature and restore the catalytic activity. However, in some tests reported in this section, a regenerated catalyst was used. The regeneration was carried out by calcination of the used catalyst in a muffle at 450 °C for 5 h, to remove coke. This step did not negatively affect the catalytic performance.

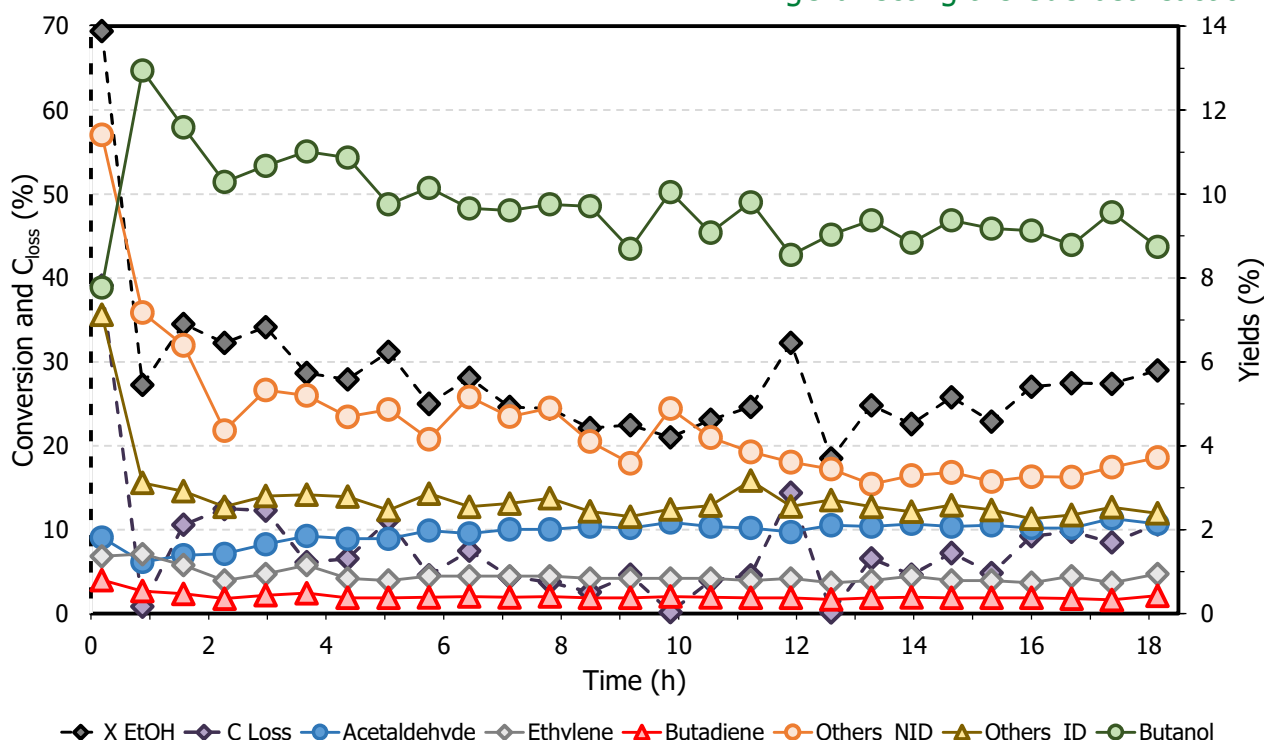


Figure 2.21 Ethanol conversion and product distribution for 5PMgO respect time on stream. Reaction conditions: 350 °C, $\tau = 1 \text{ g s mL}^{-1}$, $V_{tot} = 30 \text{ mL min}^{-1}$, 2 % EtOH in He, $m_{cat} = 0.5 \text{ g}$, 30-40 mesh.

Mass transfer limitations

Mass transfer limitations can significantly affect the reaction rate. The apparent reaction rate can be altered by diffusion. In fact, the reactant has to diffuse through the layer surrounding the catalyst particle (external diffusion limitation), then inside the catalyst pore to reach the active sites and later, the products have to counterdiffuse outside the pore (internal diffusion limitation).¹⁰⁴ In order to experimentally test the external mass transfer limitation, the total volumetric flow (at constant contact time) was decreased, while in order to test the internal diffusion the particle size (at constant temperature, total flow and contact time) was diminished. In this set of experiments, instead of halving the total flow, the latter was doubled because of instrumental limitations. In fact, the mass flow instrument used was not able to maintain a stable He flow at 15 ml min^{-1} . In this work both the external and internal mass transfer limitations were excluded because the conversion fluctuated within the experimental error by varying both the flow and the particle size, as shown in Figure 2.22.

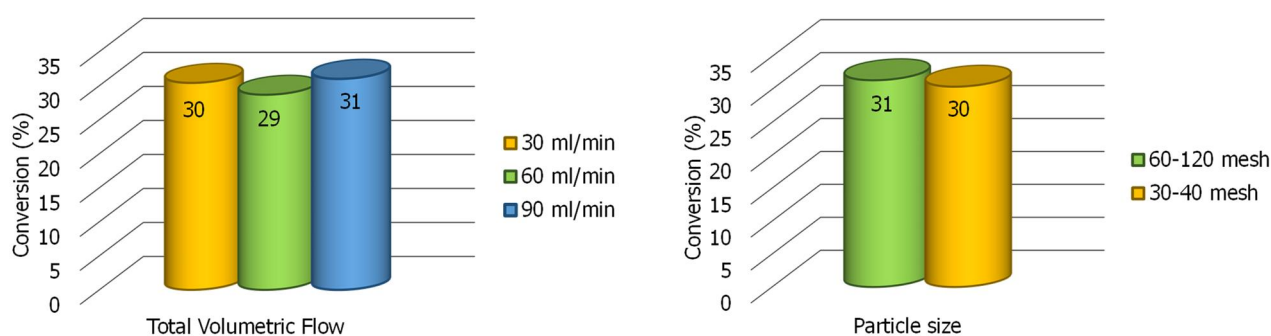


Figure 2.22 Limiting external (on the left) and internal (on the right) mass transfer limitations. Reaction conditions: 350 °C, 2 % EtOH in He. External mass transfer: $m_{cat} = 0.5, 1.0, 1.5 \text{ g}$, 30 -40 mesh. Internal mass transfer: $m_{cat} = 0.5 \text{ g}$, $V_{tot} = 30 \text{ mL min}^{-1}$.

Contact time screening

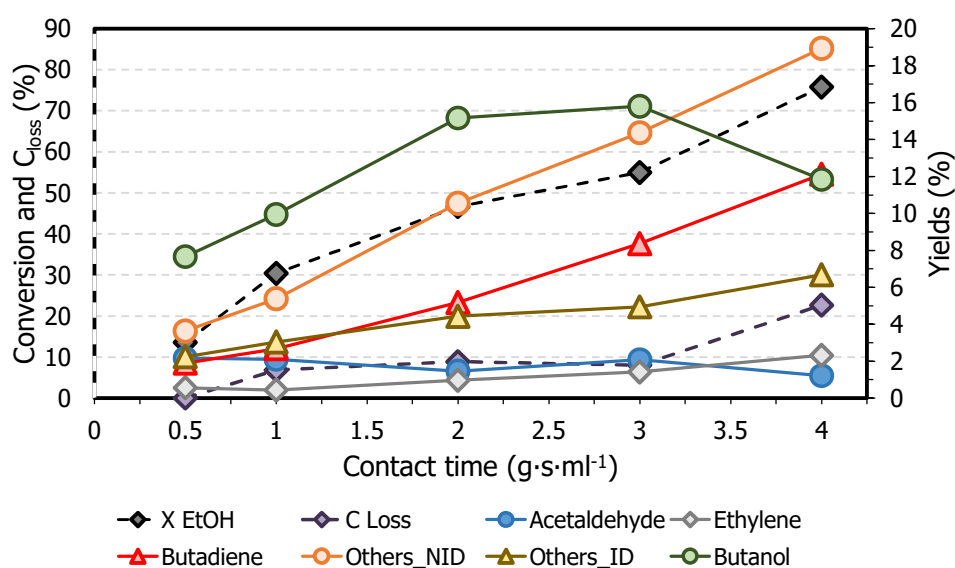


Figure 2.23 Ethanol conversion and product distribution respect contact time. Reaction conditions: 350 °C, $V_{tot} = 30 \text{ mL min}^{-1}$, $m_{cat} = 0.25 \div 2.00 \text{ g}$

A contact time screening was carried out in order to identify the reaction network. The conversion (black dashed line in Figure 2.23) increased from 14 % to 76 % while raising the contact time. Butadiene (red solid line) and others_NID (orange solid line) yields steeply raised (from 2 % to 12 % and from 4 % to 19 %, respectively) when contact time was increased. Others_ID (yellow solid line) and ethylene (grey solid line) yields slowly increased from 2 % to 7 % and from 0.6 % to 2 %. Acetaldehyde yield (blue solid line) was constant around 2 % until 4 g s mL⁻¹. Finally, 1-butanol yield (green solid line) steeply increased from 8 % to 15 % until 2 g s mL⁻¹, reaching 16 % at 2.5 g s mL⁻¹ and then dropped down to 12 % at 4 g s mL⁻¹. The C_{loss} (violet dashed line) was around 10 % from 1 g s mL⁻¹ up to 2 g s mL⁻¹ but it doubled at 4 g s mL⁻¹. These results showed that both acetaldehyde and 1-butanol are kinetically primary products since both of them showed a positive slope interpolating their yield to nil contact time. The C_{loss} increase shown at the highest contact time along with butadiene, Others_ID and Others_NID yields increase pointed out that at such contact time the contribution of side reactions occurring on butanol raised. In fact, butanol yield drop can be easily correlated to Others_NID increase. It is likely that others_NID is mainly composed of heavy products the formation of which is favoured by secondary condensations. Moreover, it is possible that some of them are trapped in the catalyst pore favouring the C_{loss} increase along with coke formation. On the other hand, it is possible to correlate acetaldehyde yield drop to others_ID increase at longer contact time. In fact, Others_ID lumps all the products derived from aldol condensation, such as crotonaldehyde, crotyl alcohol and butyraldehyde.

The experiment at 2 g s mL⁻¹ was chosen as central point to carry out the investigation on temperature effect because even if butanol yield was not the highest, however, the amount of side products, such as Other_NID, were still low.

Temperature screening

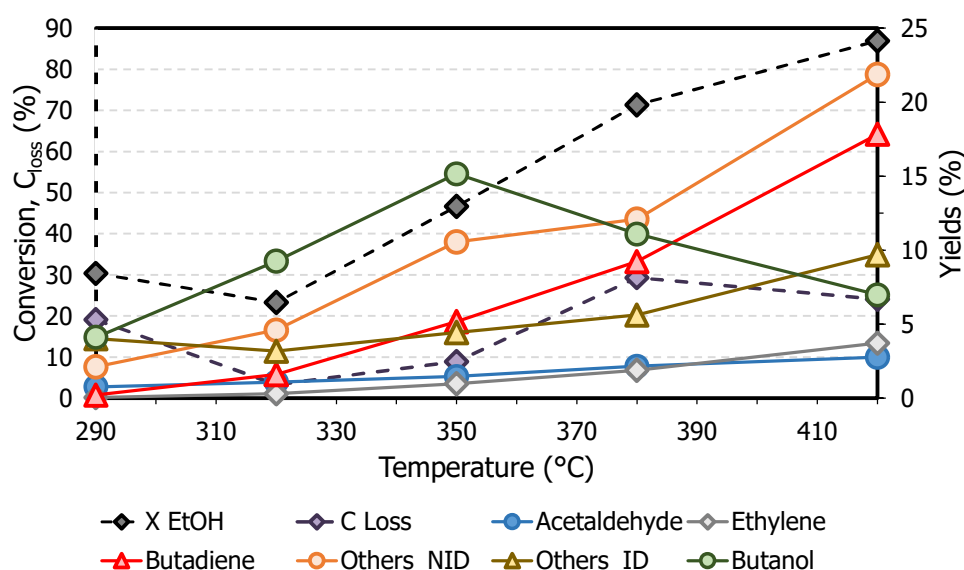


Figure 2.24 Product distribution as temperature function. Reaction parameters: $\tau = 2 \text{ g s mL}^{-1}$, $V_{\text{tot}} = 30 \text{ mL min}^{-1}$, 2 % EtOH in He, $m_{\text{cat}} = 1.0 \text{ g}$, 30-40 mesh.

5PMgO started to be active in the Guerbet reaction at 320 °C. In fact, the C_{loss} (20 % yield at 30 % conversion) was the main product at 290 °C, as shown in Figure 2.24. The conversion, as usual, increased along with the temperature raise. Interestingly, acetaldehyde and other_ID yields slowly increased and the same occurred for butadiene and Others_NID. The latter were the main products at 420 °C along with butadiene. On the contrary, 1-butanol yield showed a maximum centred at 350 °C, which resulted to be the optimal temperature to carry out the Guerbet reaction. In fact, at higher temperatures the activation energy for side reactions, such as the successive condensation, was overcome, as shown by the steep increase of Others_NID formation.

Square test

According to the previous results, the central point for the square test was chosen at 2 g s mL^{-1} and 350 °C. In order to study the variation of products distribution occurring with small changes of the reaction parameters, we decided to carry out four tests more by varying the temperature of $\pm 30 \text{ °C}$ and the contact time of $\pm 1 \text{ g s mL}^{-1}$. Butanol yield increased from 8 % to 13 % at 320 °C while it decreased from 12 % down to 3 % at 380 °C, as shown in Figure 2.25 and Figure 2.26, respectively. 1-Butanol was the main product at low contact time and 320 °C, while at 380 °C the main products were others_ID, which also included butadiene. The secondary reactions were accelerated when the contact time was increased at both temperatures, as also shown by the raising slope of C_{loss} . The C_{loss} increase at 320 °C can be justified by hypothesizing that some Others_ID compounds underwent secondary reactions, so enhancing the formation of heavy products. On the contrary, all the products (1-butanol, Others_ID and Others_NID) at 380 °C underwent side-reactions to form coke or heavy compounds. This observation was suggested by the highest yield shown by all products at contact time 2 g s mL^{-1} . In fact, both coke and heavy compounds are included in the C_{loss} , that showed a dramatic increase.

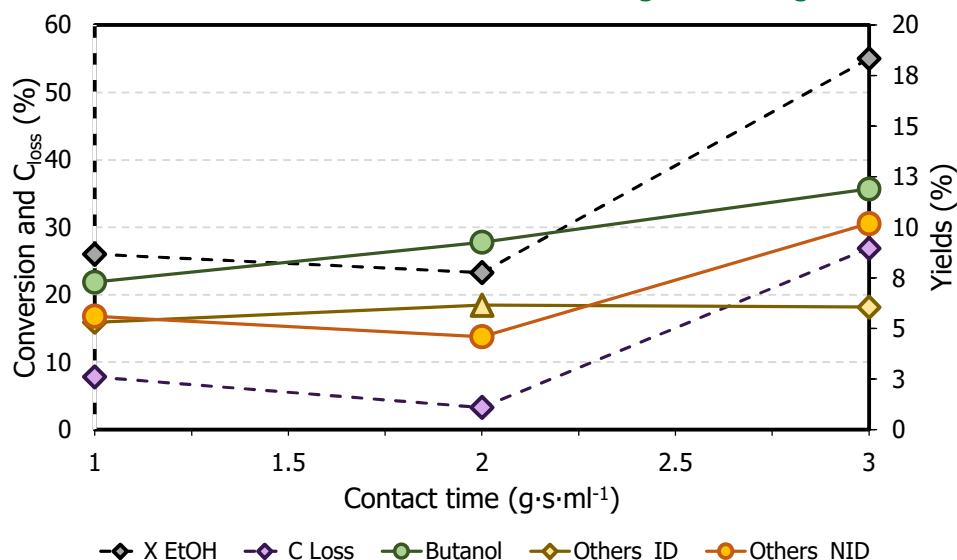


Figure 2.25 Square test results at 320 °C. reaction conditions: $m_{cat} = 0.5, 1.0, 1.5$ g, $V_{tot} = 30$ mL min⁻¹, 30-40 mesh.

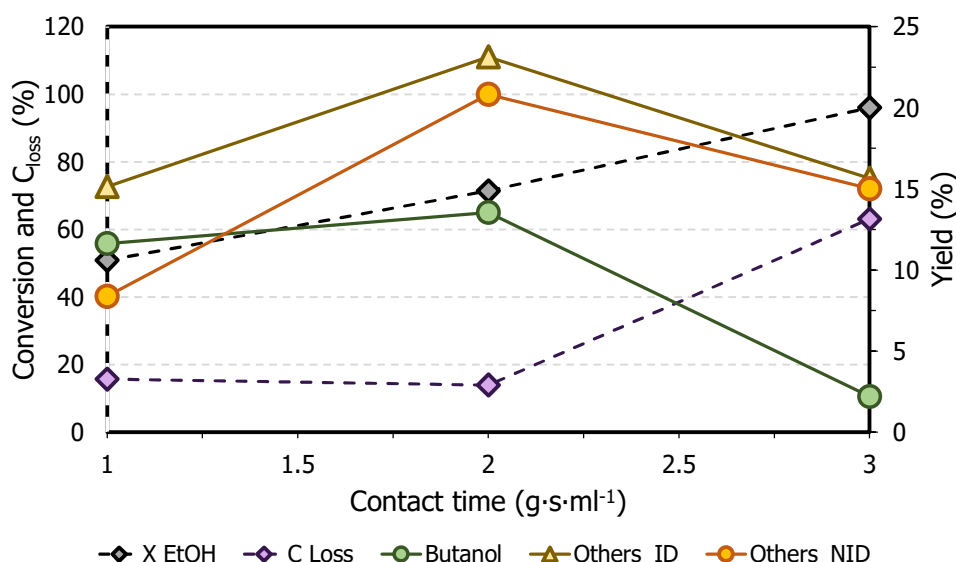


Figure 2.26 Square test results at 380 °C. reaction conditions: $m_{cat} = 0.5, 1.0, 1.5$ g, $V_{tot} = 30$ mL min⁻¹, 30-40 mesh.

2.4.4 5 % w/w H₃PO₄/MgO DRIFTS-MS experiments

Ethanol temperature programmed desorption with 5PMgO catalyst, followed by DRIFTS

Ethanol was adsorbed on the catalyst surface with the final aim of discriminating between the mechanisms occurring either *via* aldol condensation or *via* carbanion. In this case, it was not possible to detect any band below 1250 cm⁻¹, as shown in Figure 2.27, because the phosphate strong absorption covered all the bands of interest in this spectral region. Therefore, it was not possible to observe neither the carbanion transitions nor the ethoxide ones. Anyway, the test gave some useful information on ethanol adsorption and activation on 5PMgO.

At 50 °C, several adsorption bands were detected. The broad absorption band which raised the spectrum baseline until 200 °C can be attributed to undissociated ethanol $\nu(\text{OH})$.⁷² The presence of ethanol adsorbed as ethoxy species was demonstrated by the presence of $\nu_{as}(\text{CH}_3)$, $\nu_{as}(\text{CH}_2)$ and $\nu_s(\text{CH}_2, \text{CH}_3)$ at 2965 cm⁻¹, 2927 cm⁻¹ and 2872 cm⁻¹, respectively.^{72,78,81,91} Also the band at 1378 cm⁻¹ was assigned to $\delta(\text{CH}_3)$ vibration of ethoxy species.⁹¹ The band at 1635 cm⁻¹ was

assigned to $\nu(\text{C}=\text{O})$ of acetaldehyde whose presence was confirmed by the band at 2812 cm^{-1} $\nu(\text{CH})$.^{72,83} The peak at 1264 cm^{-1} was assigned to a twisting (τ) mode of ethoxy species while the band at 1285 cm^{-1} was related to $\rho_w(\text{CHO})$.^{83,105} A temperature increase up to $150\text{ }^\circ\text{C}$ brought to a blue-shift to 1657 cm^{-1} of acetaldehyde band $\nu(\text{C}=\text{O})$. At such temperature, acetaldehyde mass slightly increased indicating that some aldehyde was desorbed. At $250\text{ }^\circ\text{C}$, a band at 1623 cm^{-1} appeared along with some red-shift of $\nu_{\text{as}}(\text{CH}_3)$ and $\nu_{\text{s}}(\text{CH}_3)$. The band at 1623 cm^{-1} was related to $\nu(\text{C}=\text{C})$ of crotonaldehyde.^{83,88} A further temperature increase made visible a small shoulder at 1673 cm^{-1} attributed to crotonaldehyde $\nu(\text{C}=\text{O})$. A peak in 1-butanol, butyraldehyde and crotyl alcohol m/z trend was observed at $350\text{ }^\circ\text{C}$. On the other hand, crotonaldehyde trend did not show any peak of intensity at such temperature, supporting its presence on the catalyst surface. At $450\text{ }^\circ\text{C}$ a peak at 1602 cm^{-1} was clearly visible along with a shoulder at 1673 cm^{-1} . These bands could be attributed to either crotonaldehyde or crotyl alcohol precursor or to some polycondensation product strongly adsorbed on the catalyst surface. Interestingly, this catalyst did not promote neither acetate nor carbonate formation as instead MgO did (section 2.3.3).

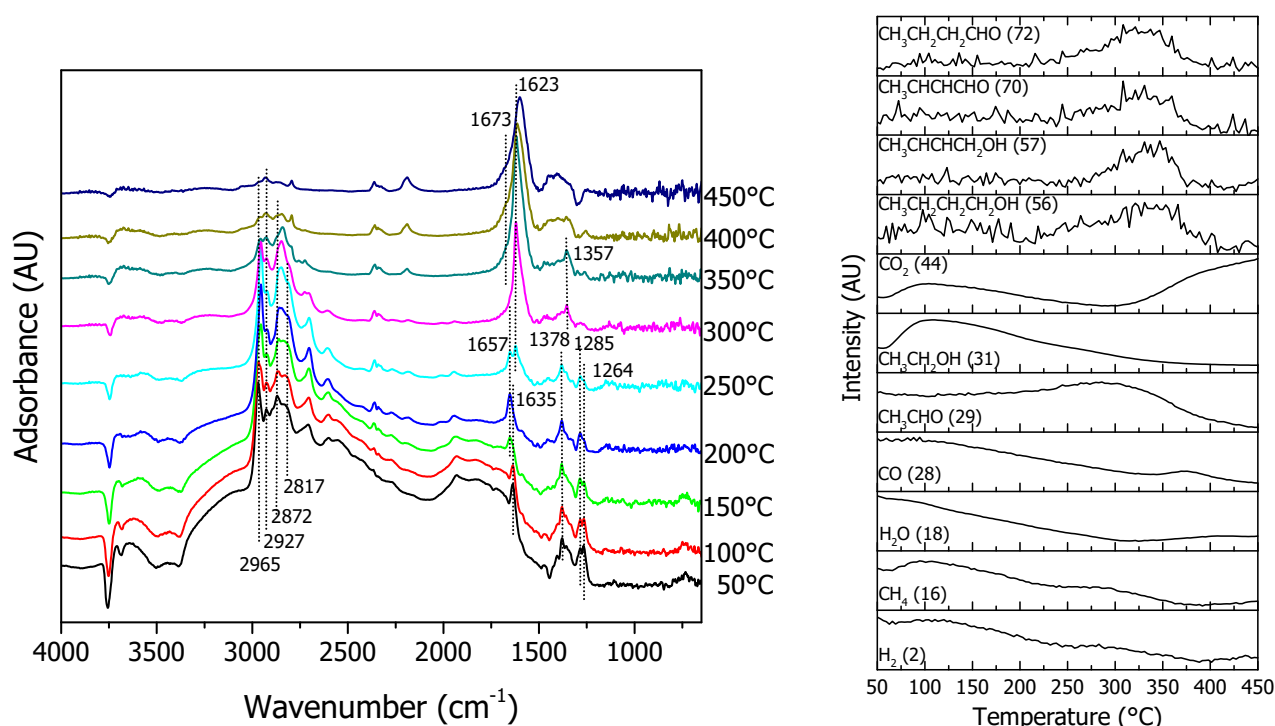


Figure 2.27 Ethanol adsorption and activation on 5PMgO followed by DRIFT-MS. On the left the DRIFTS spectra recorded respect temperature are reported while on the right some product m/z signals are reported.

Comparison of MgO and 5PMgO ethanol activation at $350\text{ }^\circ\text{C}$

DRIFTS experiments were carried out during ethanol reaction on MgO and 5PMgO in order to understand the reason for the different selectivity to 1-butanol shown. In these two experiments ethanol was continuously fed on the catalysts. The identification of reaction intermediates under these conditions can be a hard task, but spectra turned out to be similar to those detected at lower temperature in the TPD mode.

At the beginning of the reaction ($t = 0\text{ min}$), MgO (spectra reported in Figure 2.28), showed bands at 1059 cm^{-1} , 1128 cm^{-1} and 1620 cm^{-1} ascribed to the bidentate ethoxy, carbanion and acyl, respectively.^{72,83,88} The peaks at 2960 cm^{-1} , 2923 cm^{-1} and 2850 cm^{-1} were assigned to the ethoxy species $\nu_{\text{as}}(\text{CH}_3)$, $\nu_{\text{as}}(\text{CH}_2)$ and $\nu_{\text{s}}(\text{CH}_3, \text{CH}_2)$.⁷² Both ethoxy and carbanion band intensity increased over time until 110 min and 150 min (Figure 2.29), respectively. Finally, the intensity of both

ethoxy and carbanion bands started to decrease in favor of the peak at 1620 cm^{-1} . This latter band broadened over time and shifted slowly towards 1600 cm^{-1} at 130 min. A band at 1205 cm^{-1} started to be visible after 100 min. Both this new band and the broadening of the band at 1600 cm^{-1} were associated to the possible presence of carbonates on the catalyst surface.⁷⁹ The formation of carbonates was supported even by the band at 2181 cm^{-1} ascribed to physisorbed CO_2 .⁷⁹ In fact, the intensity of this band started to raise after 20 min reaching a maximum at 100 min. Afterwards, it decreased over time probably in favor of carbonates formation. Furthermore, a small shoulder at 1669 cm^{-1} started to be detectable at 180 min and it could be related to $\nu(\text{C}=\text{C})$ or $\nu(\text{C}=\text{O})$ of either some crotonaldehyde precursor or polycondensation products.^{72,76,83} The ethoxy band seemed to decrease over time faster than the carbanion one, suggesting a competition between the two reaction mechanisms.

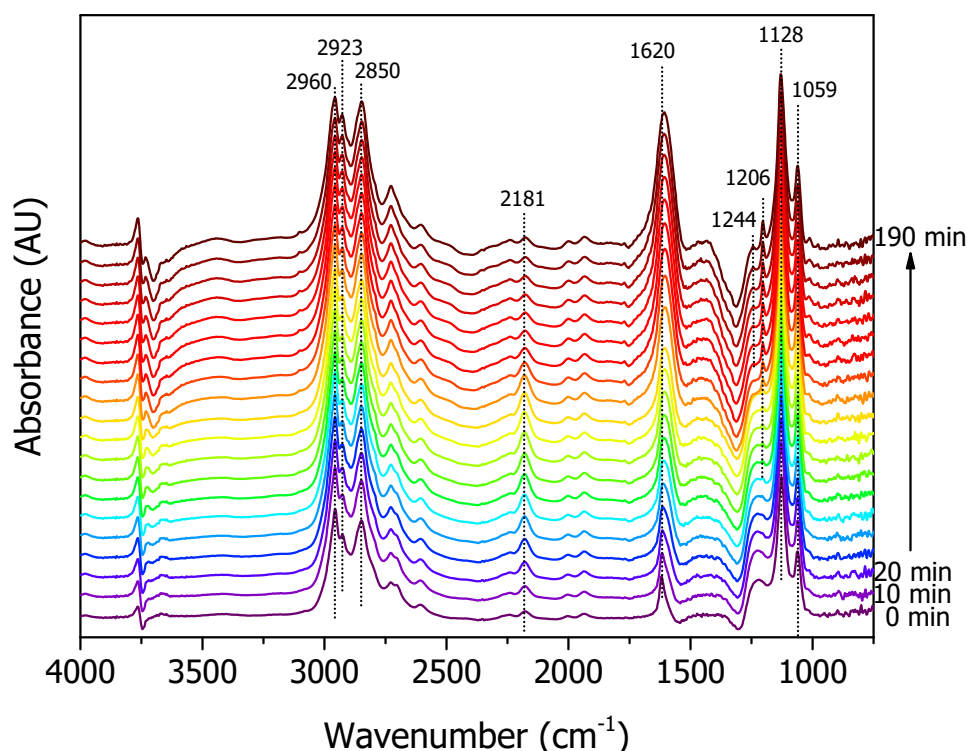


Figure 2.28 DRIFTS spectra over the time during ethanol reaction on MgO at $350\text{ }^{\circ}\text{C}$.

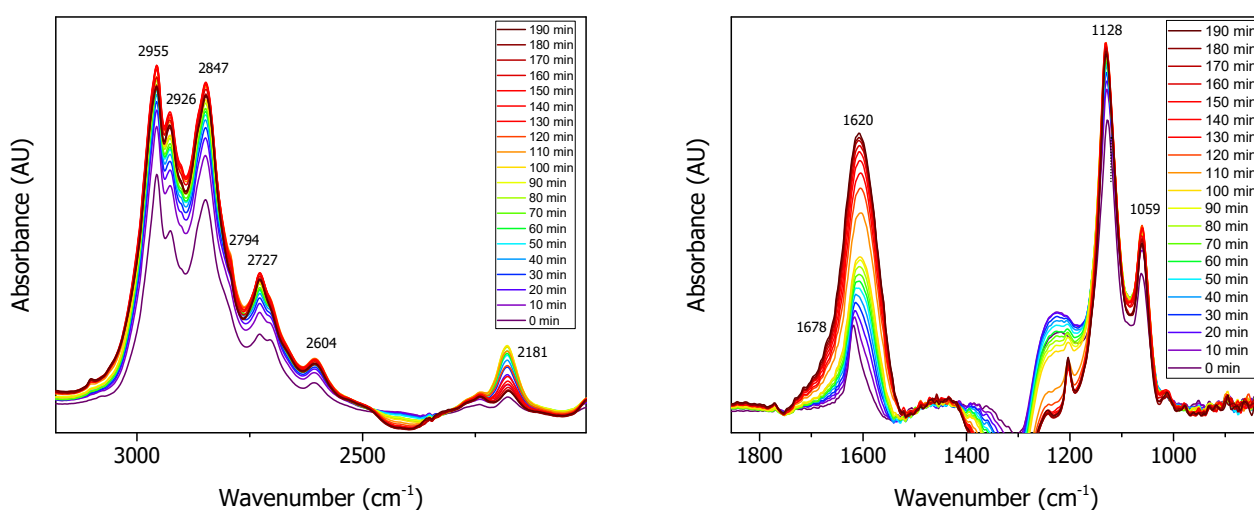


Figure 2.29 Zoom in of ethanol reaction on MgO.

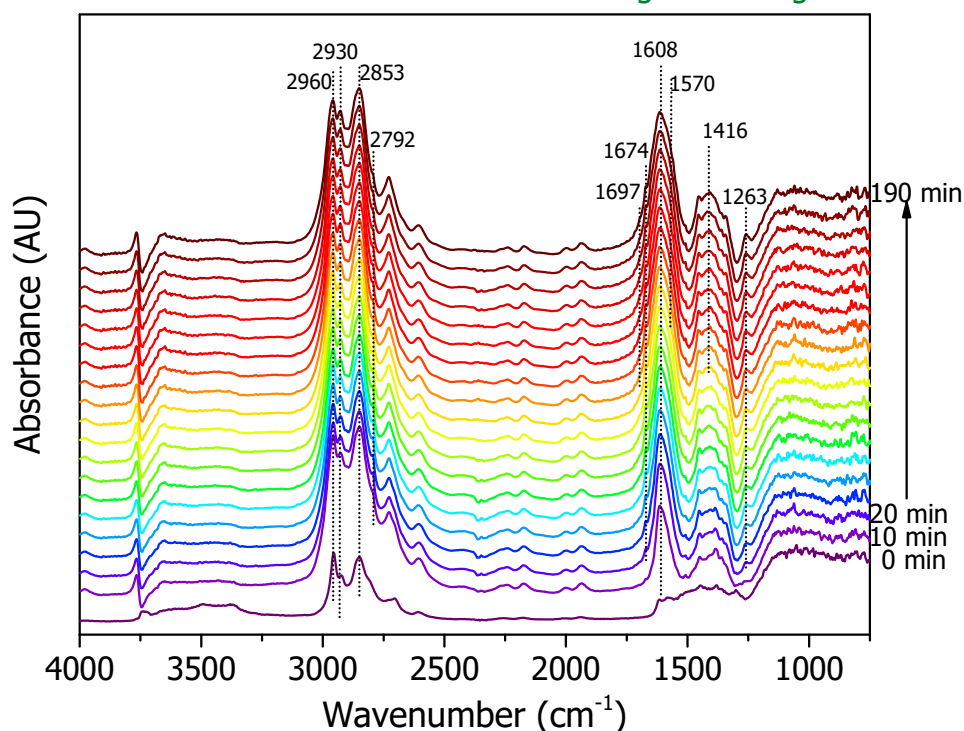


Figure 2.30 DRIFTS spectra recorded over the time during ethanol reactivity on 5PMgO.

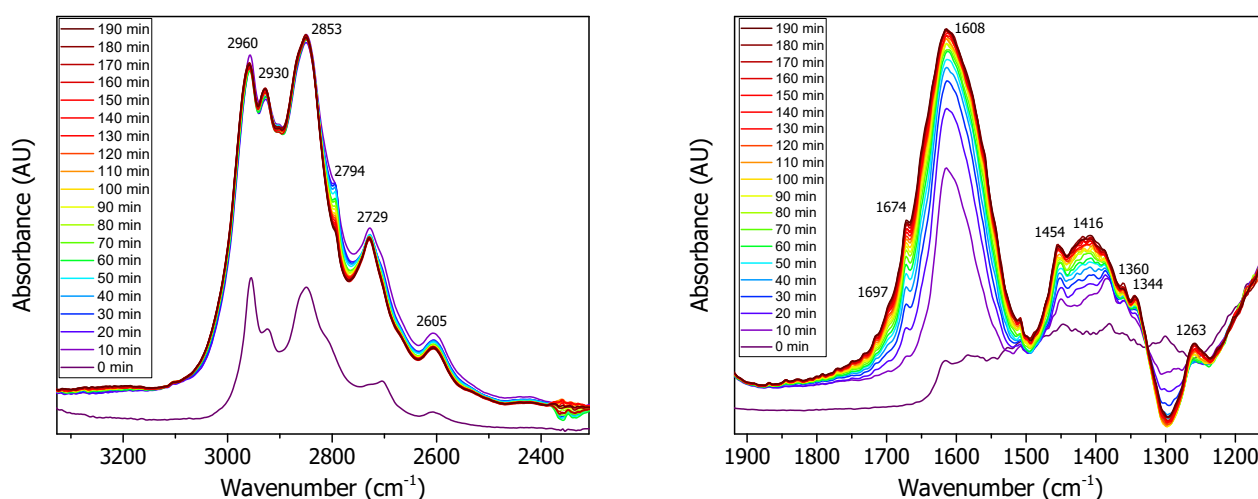


Figure 2.31 5PMgO Ethanol reactivity zoom in.

Both the carbanion and the ethoxy adsorption on 5PMgO were confirmed by the presence of C-H stretching ($\nu_{\text{as}}(\text{CH}_3)$ 2960 cm^{-1} , $\nu_{\text{as}}(\text{CH}_2)$ 2930 cm^{-1} and $\nu_{\text{s}}(\text{CH}_3, \text{CH}_2)$ 2853 cm^{-1}) even at the very beginning of the experiment, as it is possible to notice in Figure 2.30. After 10 min a band at 1608 cm^{-1} assignable to either $\nu(\text{C}=\text{O})$ or $\nu(\text{C}=\text{C})$ appeared. Along with this band, other bands appeared at 1263 cm^{-1} , 1380 cm^{-1} and 1450 cm^{-1} attributed to $\delta(\text{CHO})$, $\delta_{\text{s}}(\text{CH}_3)$ and $\delta_{\text{as}}(\text{CH}_3)$.⁸³ These bands suggest the presence of acetaldehyde on the catalyst surface after 10 min. Anyway, the presence of the band at 1674 cm^{-1} ($\nu(\text{C}=\text{O})$) and 1360 cm^{-1} ($\delta(\text{CH}_3)$), both clearly detectable after 20 min, proved the formation of crotonaldehyde.⁸³ The peaks at 1608 cm^{-1} and 1416 cm^{-1} broadened over time, and after 90 min they were likely due to some adsorbed carboxylate species. The latter can be a reaction intermediate or a side product strongly adsorbed on the catalyst surface. However, these catalysts, as shown in the lifetime reactivity tests, did not undergo deactivation. Therefore, the attribution of the mentioned bands to some reaction intermediates is more likely. After 120

min a small band at 1674 cm^{-1} started to be detectable and it was ascribed to some polycondensation product.

The analysis of the *operando* test is not straightforward since reaction intermediates can be rapidly desorbed from the catalyst surface. Anyway, some differences between MgO and 5PMgO were highlighted. 5PMgO C-H stretching band intensity was not diminishing over time suggesting that alcoholic or aldehydic species are always present on its surface; conversely, with MgO the intensity of C-H stretching band started to decrease after 130 min. At the same time, some carbonates were detected on MgO. With 5PMgO it was not possible to discriminate between the two mechanisms, while it was possible to detect a possible competition between the aldol condensation and the mechanism *via* carbanion on MgO. However, it is likely that the same competition was in action on 5PMgO also.

2.4.5 Conclusions

MgO was impregnated with H_3PO_4 . It was demonstrated that the presence of PO_4 groups strongly affected MgO reactivity in the Guerbet reaction, doubling the selectivity to 1-butanol even with the addition of a small amount of it.

5 % w/w $\text{H}_3\text{PO}_4/\text{MgO}$ was found to be the best catalyst amongst those synthesized since it presented the lowest carbon loss along with a small production of unidentified products. This catalyst yielded 15 % butanol at 45 % conversion at $350\text{ }^\circ\text{C}$ and 2 g s mL^{-1} .

The activation of ethanol on 5PMgO was investigated by means of DRIFT spectroscopy. The presence of acetaldehyde was shown already at low temperature while carbonate or acetate formation was not appreciated. The reactivity of ethanol at $350\text{ }^\circ\text{C}$ with MgO and 5PMgO was compared through an *in operando* DRIFTS experiment, which highlighted that 5PMgO is not subjected to carbonation as for MgO within 190 min reaction time. Moreover, crotonaldehyde vibrational transitions were detected on 5PMgO after 20 min while it was necessary to wait 180 min to detect some crotonaldehyde or crotyl alcohol characteristic band with MgO. All these observations seemed to suggest that PO_4 is inhibiting catalyst carbonation. Unfortunately, it was not possible to detect any carbanion characteristic band on 5PMgO. Therefore, it was not possible to conclude whether the higher selectivity shown by this catalyst was due to a specific reaction pathway.

2.5 $\text{H}_3\text{PO}_4/\text{MgO}$ vs Hydroxyapatites in the Guerbet reaction

In this chapter the catalytic performance of $\text{H}_3\text{PO}_4/\text{MgO}$ (5PMgO) is compared with that one of Ca- and Sr-hydroxyapatites (CaHAP and SrHAP). 5PMgO was a newly synthesized batch and the MgO used as support in this case had a surface area of $186 \text{ m}^2 \text{ g}^{-1}$.

2.5.1 HAP and 5PMgO characterization

The hydroxyapatite samples presented a smaller surface area compared to 5PMgO (See Table 2.5.). This difference can be related to the calcination temperature used, which was 600°C for the hydroxyapatite and 450°C for 5PMgO, because higher temperatures might cause the synthering of MgO particles.

Table 2.5 Catalysts surface area and total acid and basic sites concentration.

Catalyst	Surface area ^a	Total acid site concentration ^b		Total basic site concentration ^c	
	$\text{m}^2 \cdot \text{g}^{-1}$	$\mu\text{mol} \cdot \text{g}^{-1}$	$\mu\text{mol} \cdot \text{m}^{-2}$	$\mu\text{mol} \cdot \text{g}^{-1}$	$\mu\text{mol} \cdot \text{m}^{-2}$
5PMgO	101	29.92	0.30	169.38	1.68
CaHAP	57	158.05	2.77	118.90	2.09
SrHAP	38	113.50	2.99	121.23	3.19

^a evaluated by BET

^b evaluated by TPD- NH_3

^c evaluated by TPD- CO_2

The XRD pattern reported in Figure 2.32 showed that the desired hydroxyapatite phase had been obtained (Figure 2.32, Left). For CaHAP the crystalline phase was $\text{Ca}_5(\text{PO}_4)_3(\text{OH})$ (ref. 01-086-1199), while for SrHAP was $\text{Sr}_5(\text{PO}_4)_3(\text{OH})$ (ref. 01-070-1511). The XRD pattern of 5PMgO did not evidence any crystalline phase other than MgO. All samples showed a high cristallinity.

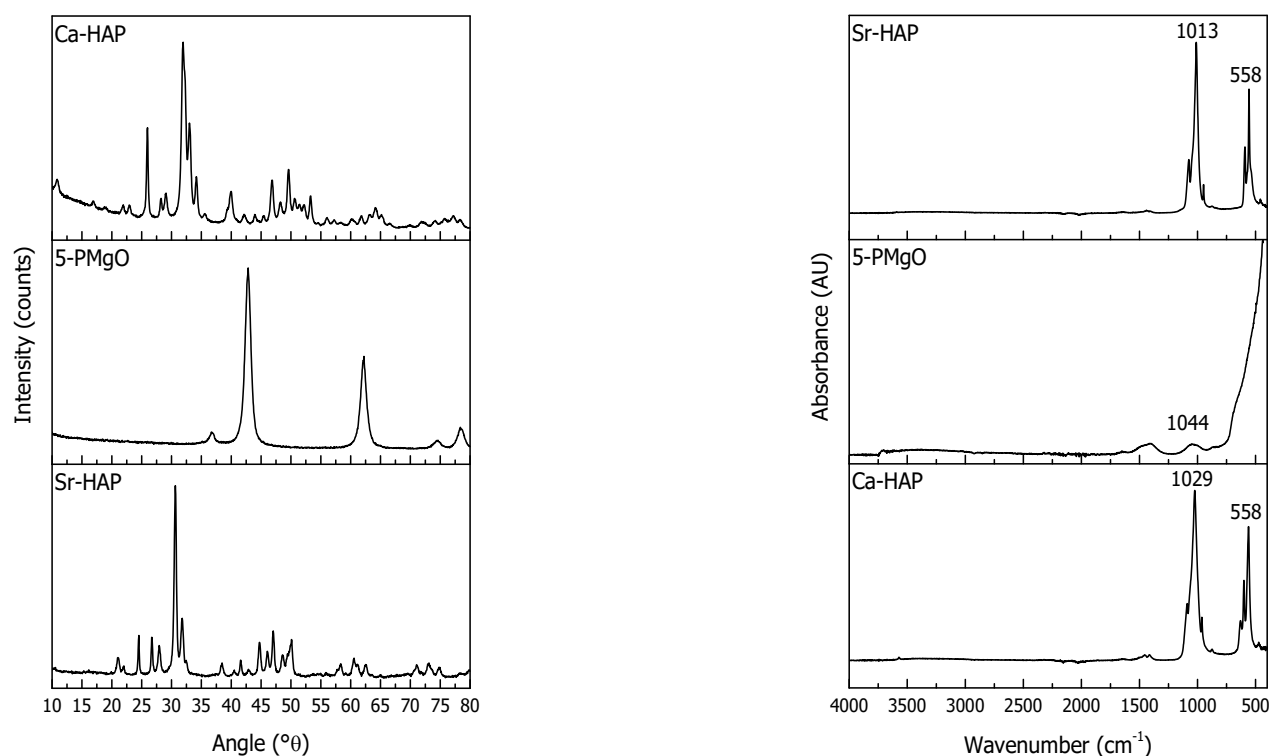


Figure 2.32 Hydroxyapatite and 5PMgO XRD, on the left-hand side, and ATR, on the right-hand side.

ATR analysis was used to both confirm the presence of phosphate groups on the surface of 5PMgO and characterize HAP samples (Figure 2.32, Right). The most intense phosphate adsorption was the antisymmetric stretching of P-O bond (ν_3) which was detected at 1044 cm^{-1} , 1029 cm^{-1} and 1013 cm^{-1} for 5PMgO, CaHAP and SrHAP, respectively.^{59,101} It is worth notice that this absorption underwent a red-shift with increasing the cation ionic radius (Mg 173 pm, Ca 231 pm and Sr 255 pm), suggesting an increase in the ionicity of M- PO_4 bond. The HAP samples presented also the $\nu_4(\text{PO}_4)$ bending mode at 558 cm^{-1} , that in the case of 5PMgO was covered by the strong Mg-O adsorption.^{106,107} Furthermore, all the samples showed minor adsorption bands at around 1400 cm^{-1} related to CO_3^{2-} presence.¹⁰¹

Basicity characterization

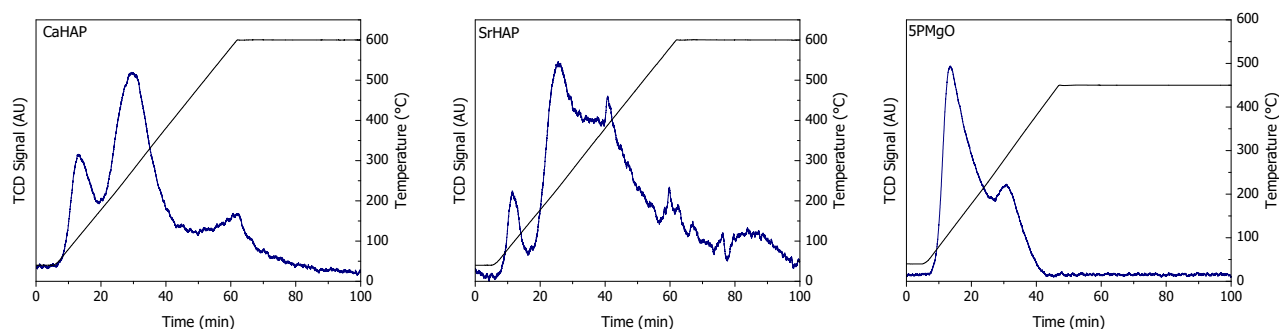


Figure 2.33 CO_2 Temperature programmed desorption for HAPs and 5PMgO.

The density of basic sites was evaluated by means of CO_2 temperature programmed desorption. According to the results reported in Table 2.5, SrHAP possessed the highest basicity followed by CaHAP and 5PMgO. Alongside, the basic site strength was correlated to the desorption temperature range as follows: CO_2 desorption below $200\text{ }^\circ\text{C}$ is indicative of weak basic sites, between $200\text{ }^\circ\text{C}$ and $300\text{ }^\circ\text{C}$ of medium strength sites, between $300\text{ }^\circ\text{C}$ and $400\text{ }^\circ\text{C}$ of strong sites and over $400\text{ }^\circ\text{C}$ of very strong sites. The same classification will be used for the acid sites strength determination, reported in the following sections.

As observed in Figure 2.33, all catalysts showed more than one CO_2 desorption peak: 5PMgO showed two sites with different basic strength, centred at $115\text{ }^\circ\text{C}$ (with a higher area in the TPD profile) and $288\text{ }^\circ\text{C}$. Therefore, it can be stated that this catalyst possessed mainly weak basic sites with the presence of some medium strength sites. CaHAP also showed two main peaks centred at $110\text{ }^\circ\text{C}$ and $277\text{ }^\circ\text{C}$, but with opposite intensity compared with respect to 5PMgO. Indeed, CaHAP possessed mainly medium strength basic sites and some weak sites. SrHAP showed a distribution similar to CaHAP. In fact, SrHAP major peak was centred at $234\text{ }^\circ\text{C}$ indicating that this catalyst possessed mainly medium strength basic sites, along with some weak and strong basic ones (peaks centred at $95\text{ }^\circ\text{C}$ and $392\text{ }^\circ\text{C}$, respectively). The small peak at $600\text{ }^\circ\text{C}$ detected in both CaHAP and SrHAP desorption profiles was related to some structural H_2O contribution as it was also observed in the NH_3 TPD (Figure 2.34).

Acidity characterization

CaHAP and SrHAP possessed a comparable total acid site density, as reported in Table 2.5. However, these samples presented a different NH_3 desorption profile (shown in Figure 2.34). In fact, CaHAP was characterized by a broad desorption profile with two peaks centred at $199\text{ }^\circ\text{C}$ and $321\text{ }^\circ\text{C}$, which can be attributed to weak and strong acid sites. In contrast, SrHAP showed only one defined peak at $196\text{ }^\circ\text{C}$, which is related to weak acid sites. Finally, 5PMgO, which possessed the lowest total acid site density, was characterized by a quite broad desorption profile centred at

189 °C. However, it is not possible to exclude the presence of some medium strength acid site on the three catalysts.

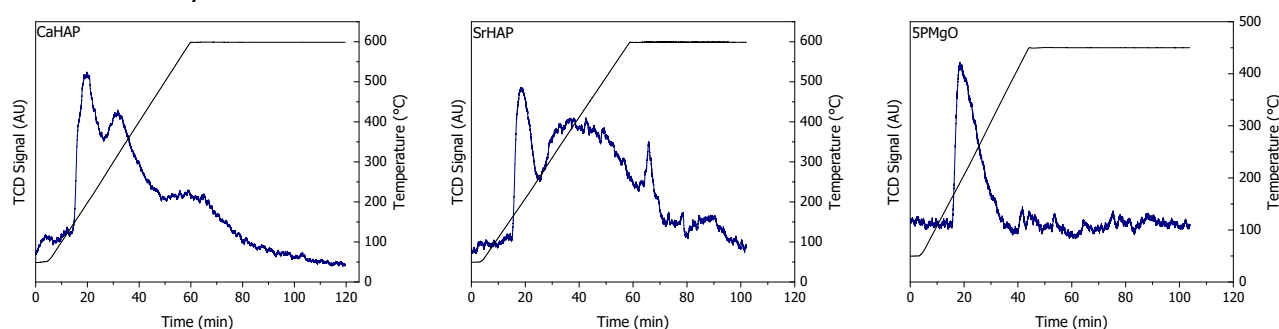


Figure 2.34 NH_3 Temperature programmed desorption for HAPs and 5PMgO

To discriminate the type of acid sites DRIFTS tests were performed by adsorbing pyridine. In fact, pyridine can adsorb on acid sites mainly in three different modes:

- forming a new coordination bond by pyridine N electron lone pairs interaction with a Lewis acid site (coordinatively unsaturated metal cation);
- pyridinium ion formation by strong interaction of pyridine with a terminal O-H group on the catalyst surface,
- H bond interaction, if pyridine is only physisorbed on the catalyst surface.

The Lewis sites are characterized by the band at 1450 cm^{-1} while the Brønsted sites by the band at 1540 cm^{-1} .¹⁰⁸

The Lewis or Brønsted acid sites strength is evaluated by considering the temperature at which the bands attributed to adsorbed pyridine are still detectable on the catalyst surface. In this case, it was evaluated how increasing the temperature from 50 to 300 °C affected the intensity of the bands related to Lewis and Brønsted acid sites.

All the catalysts showed only the pyridine vibration related to Lewis acid sites, as shown in Figure 2.35. This band was still visible and intense after heating at 300 °C, thus demonstrating that these Lewis sites are strong.

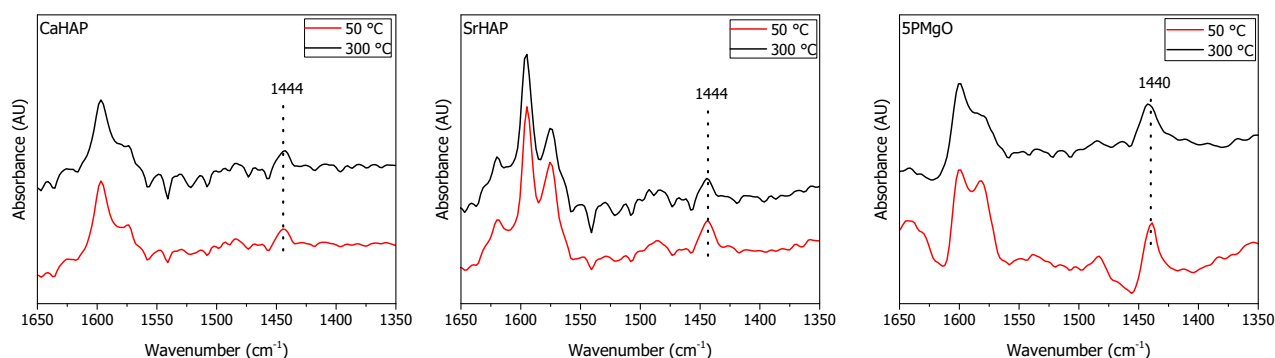


Figure 2.35 Pyridine adsorption followed by DRIFTS for 5PMgO and HAP

2.5.2 *HAP and 5PMgO reactivity*

All the catalytic tests reported in the present paragraph were carried out by feeding 5 % EtOH in He.

Temperature effect

HAPs and 5PMgO catalytic properties were studied in function of temperature in the range 250-450°C. With both catalysts, ethanol conversion increased when raising the temperature. Nevertheless, 1-butanol yield presented a different behavior depending on the catalyst used. For CaHAP, the maximum 1-butanol yield (14%) was recorded at 350°C whereas at higher temperatures yield decreased with an increase of both other unidentified products (Others_NID) and carbon loss. The latter reached 52 % at 450 °C probably due to coke deposition. Furthermore, ethylene and butadiene yields increased up to 6 and 9 %, respectively, when raising the temperature until 450°C.

SrHAP showed a similar products distribution, as reported in Figure 2.37. In fact, the conversion increased up to 85 % at 450 °C. 1-Butanol was the main product until 350 °C. At such temperature 1-butanol yield showed a maximum of 3 % at 11 % conversion. Afterwards, its yield decreased while butadiene, ethylene and acetaldehyde yields increased up to 10, 57, and 5 %, respectively. Ethylene yield increased, becoming the predominant product (it is important to note that ethylene (grey dashed line) in this graph is referred to the axis on the left-hand side of the figure).

After these tests, the temperature to carry out the reaction using the hydroxyapatites (HAPs) was set at 350 °C because at this temperature 1-butanol yield was the highest and carbon balance was higher than 90 %.

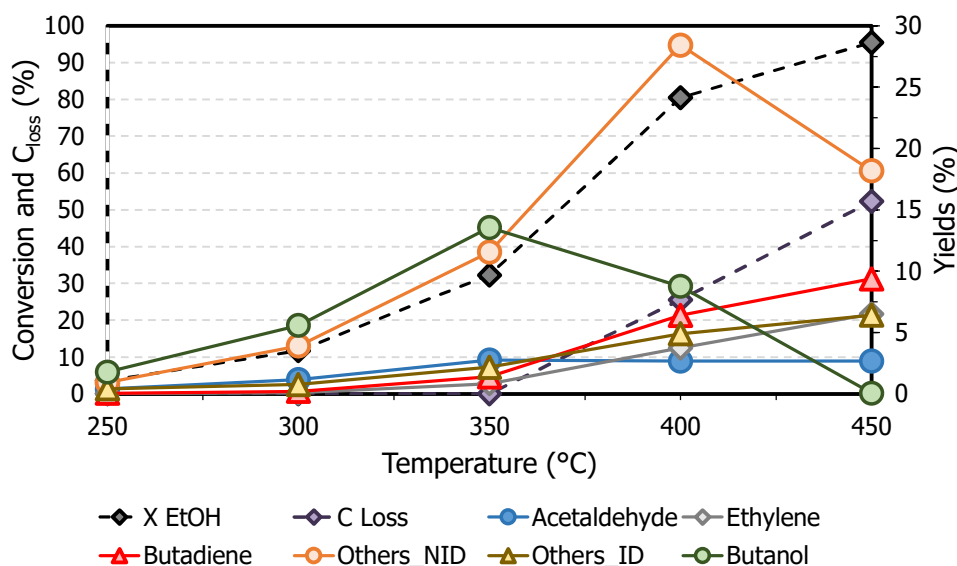


Figure 2.36 CaHAP product distribution as function of temperature. Reaction conditions: 5 %EtOH in He, $V_{\text{tot}} = 60 \text{ mL min}^{-1}$, $m_{\text{cat}} = 0.5 \text{ g}$, 30-40 mesh

5PMgO showed a different products distribution compared to the HAPs. In fact, ethanol conversion and 1-butanol yield increased along with the temperature raise, reaching the highest value at 450°C. However, at this temperature there were also several secondary products such as ethylene, butadiene and "others" (14 %, 9 % and 13 % yield, respectively). Thus, the best temperature to carry out the reaction using 5PMgO was 400 °C, because 1-butanol yield was 8 % while yields to all the other products were lower than 4 %.

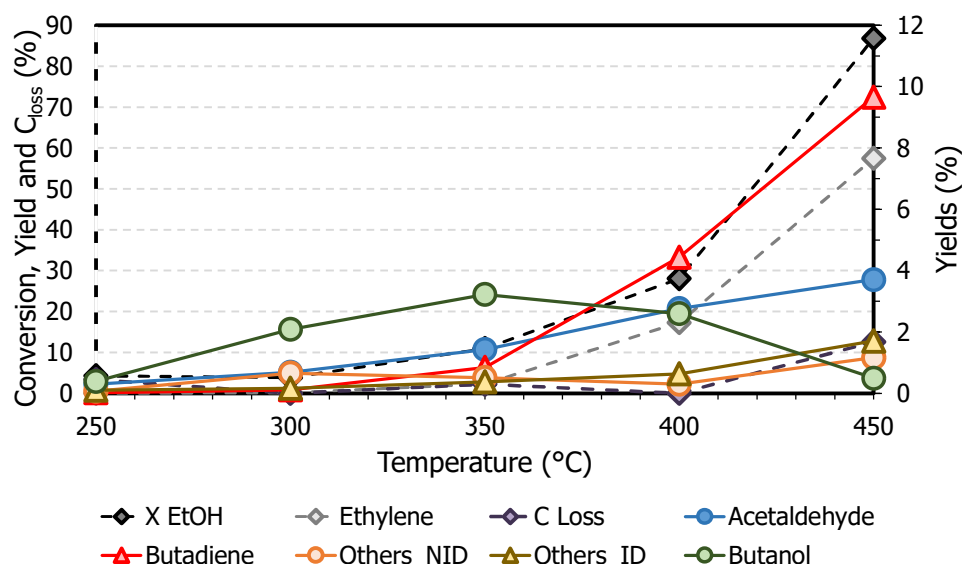


Figure 2.37 SrHAP product distribution as function of temperature. Reaction conditions: 5 %EtOH in He, $V_{\text{tot}} = 60 \text{ mL min}^{-1}$, $m_{\text{cat}} = 0.5 \text{ g}$, 30-40 mesh

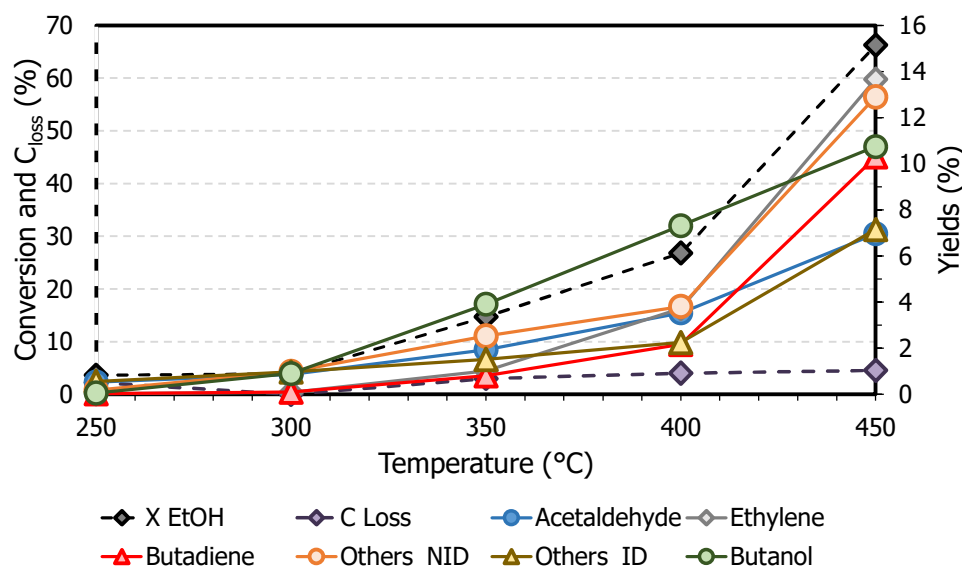


Figure 2.38 5PMgO product distribution as function of temperature. Reaction conditions: 5 %EtOH in He, $V_{\text{tot}} = 60 \text{ mL min}^{-1}$, $m_{\text{cat}} = 0.5 \text{ g}$, 30-40 mesh

In general, high temperatures ($>350 \text{ }^{\circ}\text{C}$) favored heavy coke (polyaromatic) formation while low temperatures might promote some soft coke (derived mainly by condensation).¹⁰⁹ Besides the reaction temperature, the presence of strong acid sites might be responsible of coke formation.^{109,110} It is worth to notice, that CaHAP was the catalyst which showed the highest acid site density and the highest amount of strong acid sites (area of the NH_3 desorption second peak) and its reactivity at high temperature was characterized by a poor carbon balance. Indeed, the C_{loss} reached 50 % at $450 \text{ }^{\circ}\text{C}$. On the other hand, SrHAP and 5PMgO which possessed only weak (and some medium) acid sites showed an increase in ethylene and butadiene yield. In fact, butadiene is produced by the Lebedev reaction which also requires acid sites¹¹¹⁻¹¹³ while ethylene is produced by dehydration on acid sites¹¹⁴⁻¹¹⁶. It is reasonable to hypothesize that HAPs reactivity is dominated by their acid sites over $350 \text{ }^{\circ}\text{C}$. On the other hand, 5PMgO reactivity is strongly influenced by these sites only at $450 \text{ }^{\circ}\text{C}$. Moreover, the presence of weak acid sites promoted the formation of ethylene and butadiene while strong acid sites seemed to promote coke formation.

Contact time effect

The contact time tests are used to discriminate primary from secondary (consecutive) products according.

For CaHAP, ethanol conversion increased from 20 % to 96 % while raising the contact time whereas 1-butanol yield increased from 8% (at 0.2 g s mL⁻¹) to 14% (at 0.5 g s mL⁻¹), then it reached a steady value which drastically dropped at the contact time of 2.0 g s mL⁻¹ (Figure 2.39), probably due to the consecutive formation of other unidentified products (by condensation) and coke. In fact, Others_NID yield and C_{loss} increased from 5 % and 3 % to 31 % and 47 %, respectively. The presence of strong acid sites along with a long contact time catalyzed the formation of heavy coke while the formation of soft coke or Others_NID can be attributed to the medium strength basic sites. In fact, the latter promote successive condensation reaction producing heavy compounds, especially at long contact time.

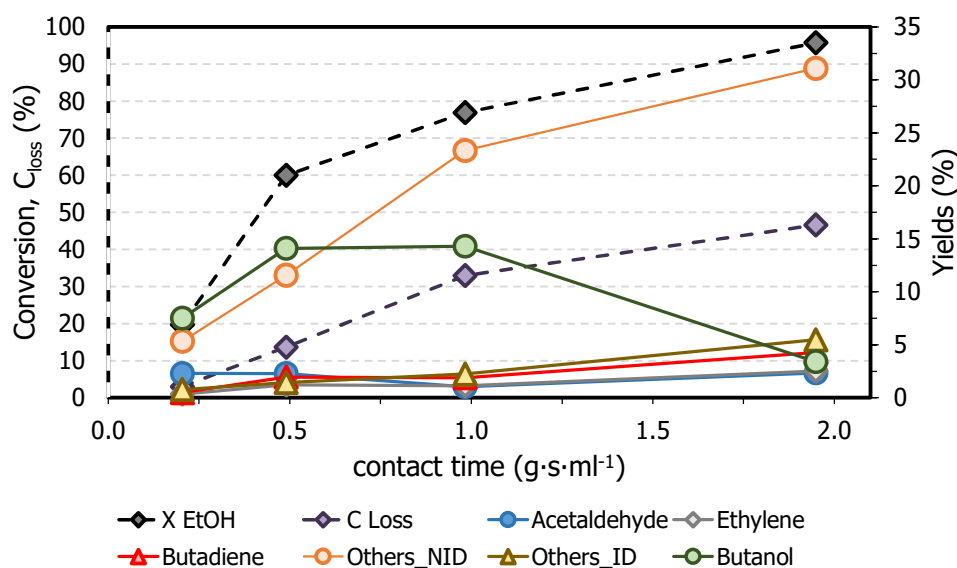


Figure 2.39 CaHAP product distribution with respect to contact time. Reaction conditions: 350 °C, 5 % EtOH in He, $V_{tot} = 60 \text{ mL min}^{-1}$, 30 - 40 mesh.

The SrHAP sample (Figure 2.40) showed an ethanol conversion that increased steeply from 6 % at low contact time (0.2 g s mL⁻¹) to 36 % at 1.0 g s mL⁻¹, but then it remained almost constant. As regards the 1-butanol yield, it sharply increased up to 16 % at 1.0 g s mL⁻¹ but afterwards it decreased slightly in favour of C_{loss} (5 %).

5PMgO (Figure 2.41) showed a conversion that increased from 21 % (at contact time 0.2 g s mL⁻¹) to 61 % (at 2.0 g s mL⁻¹). Acetaldehyde yield varied around 4 % while 1-butanol yield increased up to 13 % at 1.0 g s mL⁻¹. Afterwards, 1-butanol yield decreased by 2 % in favor of Others_NID and C_{loss}.

In all cases, the extrapolation of 1-butanol yield at nil contact time that this compound is a kinetically primary product, since its slope at short contact time seemed to be higher than zero. Thus, it is reasonable to hypothesize that the carbanion mechanism proposed for the MgO (where 1-butanol is a primary and not a secondary product) might be possible even with HAP catalysts. For all catalysts, a contact time of 0.5 g s mL⁻¹ allowed to obtain the highest selectivity to 1-butanol: SrHAP (51 %) > 5PMgO (28 %) > CaHAP (24 %). Under these conditions the yield can be ranked as follows: CaHAP (14 %) > SrHAP (8 %) > 5PMgO (7 %).

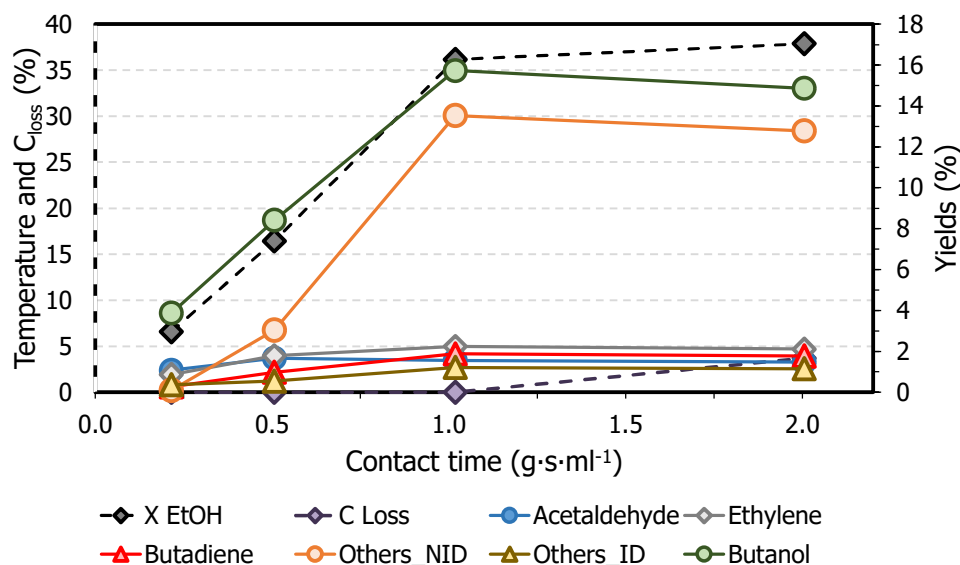


Figure 2.40 SrHAP product distribution with respect to contact time. Reaction conditions: 350 °C, 5 % EtOH in He, $V_{tot} = 60 \text{ mL min}^{-1}$, 30 - 40 mesh.

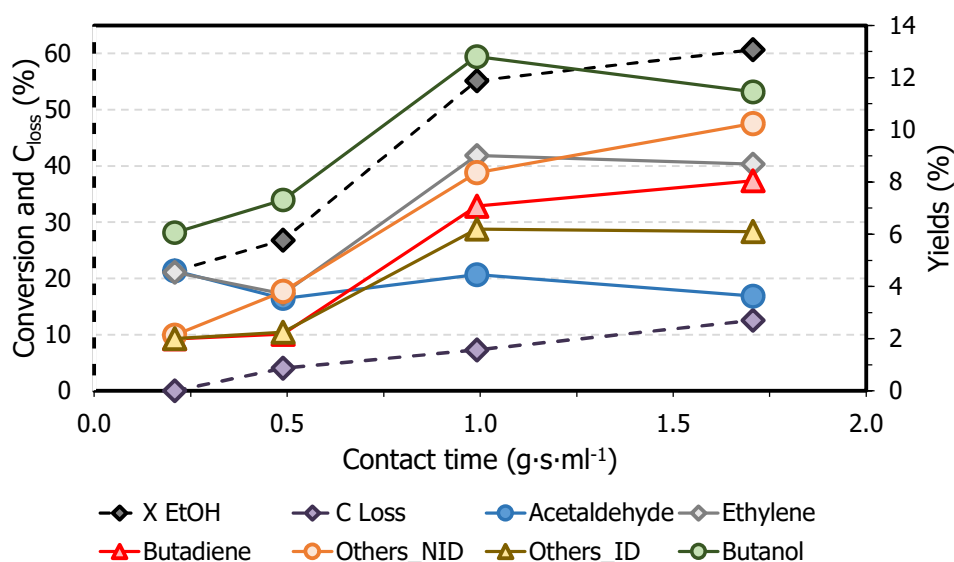


Figure 2.41 5PMgO product distribution with respect to contact time. Reaction conditions: 400 °C, 5 % EtOH in He, $V_{tot} = 60 \text{ mL min}^{-1}$, 30 - 40 mesh.

Another interesting observation is that for the HAPs, the consecutive condensation products (others_NID) were among the main products at all contact times tested. This might be correlated to the presence of medium strength basic sites. On the other hand, it was observed that strong acid sites (as those present in CaHAP) were detrimental for 1-butanol selectivity. These observations are supported by the coke yield which was lower than 10 % even at high contact time on SrHAP and 5PMgO (samples which do not possess strong Lewis acid sites). Moreover, 5PMgO which is the catalyst showing a lower acid sites density and strength, showed a 1-butanol yield two times higher than others_NID (from 0.2 g s mL⁻¹ to 1.0 g s mL⁻¹). These observations are in good agreement with those reported by Davis and coworkers⁶¹ about alkali metal phosphate catalysts. At this point, it seems reasonable to hypothesize that the ideal catalyst should possess weak basic sites able to assist the condensation (either aldolic or direct) to 1-butanol avoiding the

consecutive condensation as much as possible, and weak Lewis acid sites able to assist the dehydration step without promoting coke formation.

Deactivation study

In order to have a complete understanding of the different behavior of HAPs and 5PMgO, their performances were evaluated in function time-on-stream (short lifetime experiments). The reactions were performed at 0.2 g s mL⁻¹ contact time in order to get a lower conversion and thus better highlight any eventual catalyst deactivation.

CaHAP performance over time is shown in Figure 2.42. Ethanol conversion dropped from 60 % (after 8 min of reaction) to 16 % (after 2 h of reaction), which was then the average value of conversion for the successive 16 h of reaction. Interestingly, 1-butanol yield slowly decreased over time from 14 % (8 min) down to 7% (2h) and 3 % (18 h). Perez-Ramirez and coworkers¹¹⁷ reported that CaHAP performance were stable for 15 h in propanal condensation after a small conversion decrement within the first 2 h. Their observation is in agreement with the conversion trend reported in this work. The slight decrease in selectivity to 1-butanol indicates that the Guerbet reaction is affected by coke formation over time that progressively covers the active sites necessary to produce 1-butanol. In fact, Weckhuysen and coworkers¹¹⁸ reported that CaHAP is subjected to hard coke formation (detected by different spectroscopic techniques) in the case of propanal condensation.

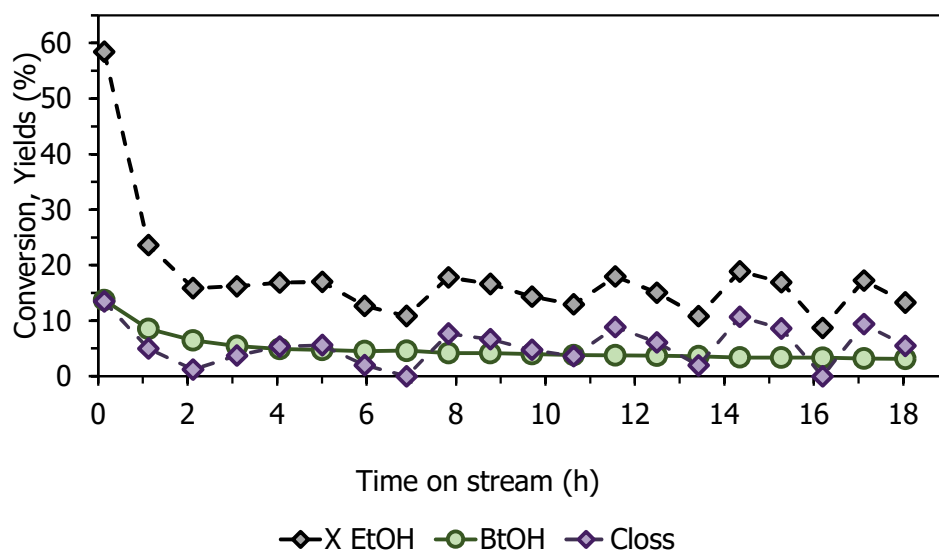


Figure 2.42 CaHAP ethanol conversion, 1-butanol yield and C_{loss} over the time of reaction. Reaction conditions: m_{cat} : 0.2 g, 30 - 40 mesh, V_{tot} = 60 mL min⁻¹, 350 °C

SrHAP showed a dramatic deactivation within the first 2 h of reaction, as shown in Figure 2.43. In fact, ethanol conversion for this catalyst decreased from 30 % down to 5%, which was the average conversion for the successive 16 h of reaction; 1-butanol yield decreased from 15 % to less than 1 % in three hours.

Surprisingly, 5PMgO showed the most stable performance over time. In fact, ethanol conversion decreased within 1 h of reaction from 28 % to 20 %, which thereafter was the steady state conversion for at least 17 h. At the same time, 1-butanol yield only decreased over 18 h from 7 % to 5 %.

The Guerbet Reaction: from ethanol to 1-butanol $\text{H}_3\text{PO}_4/\text{MgO}$ vs Hydroxyapatites in the Guerbet reaction

Therefore, it is possible to correlate the predominance of medium strength basic sites on HAP samples with their deactivation due to soft coke formation (caused by successive condensation). In contrast, 5PMgO, possessing mainly weak basic sites, underwent less deactivation.

In conclusion, the presence of strong acid sites promotes the formation of hard coke with CaHAP whereas the presence of mainly medium strength basic sites also catalyzes the soft coke formation with both HAP samples.

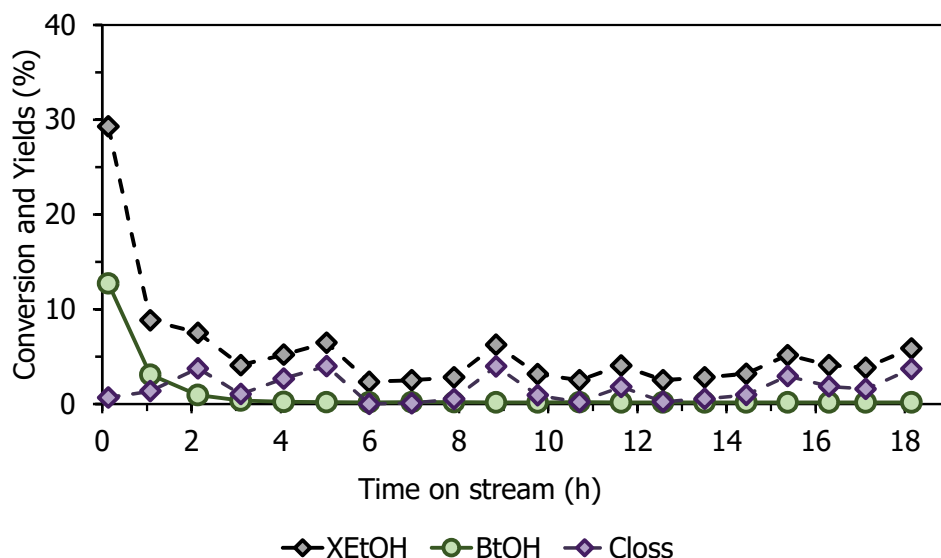


Figure 2.43 SrHAP ethanol conversion, 1-butanol yield and C_{loss} over the time of reaction. Reaction conditions: m_{cat} : 0.2 g, 30 - 40 mesh, V_{tot} = 60 mL min⁻¹, 350 °C

50

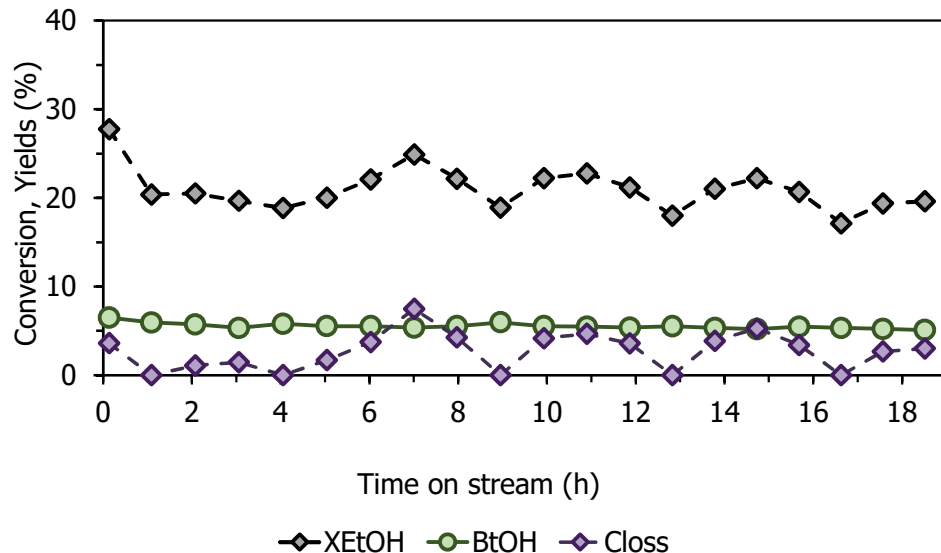


Figure 2.44 5PMgO ethanol conversion, 1-butanol yield and C_{loss} over the time of reaction. Reaction conditions: m_{cat} : 0.2 g, 30 - 40 mesh, V_{tot} = 60 mL min⁻¹, 400 °C

2.5.3 HAPs and 5PMgO DRIFTS study

The hydroxyapatite DRIFT spectra herein reported were recorded by diluting the sample with KBr (1:5) in order to reduce the strong phosphate absorption which completely saturates the C-O stretching region (1100-1000 cm⁻¹). Furthermore, with the aim to minimize the phosphate absorption, all spectra were recorded using a reduced interferogram intensity (integrating sphere height at 4 mm instead of 3.5 mm). Despite these operations, all the spectra reported are blind

with respect to the C-O ethanol stretching because of the strong phosphate group adsorption in such region.

CaHAP DRIFTS study

CaHAP DRIFT spectra, reported in Figure 2.45, showed some transitions in the C-H and O-H stretching region ascribable to adsorbed ethanol, after a pulse of ethanol at 50 °C. In fact, the broad transition centred at 3300 cm^{-1} was ascribed to H-bonded ethanol.⁷² On the contrary the bands at 2977 cm^{-1} ($\nu_{\text{as}}(\text{CH}_3)$), 2937 cm^{-1} ($\nu_{\text{as}}(\text{CH}_2)$) and 2901 cm^{-1} ($\nu_{\text{s}}(\text{CH}_3, \text{CH}_2)$) were ascribed to ethoxy species (dissociated ethanol) on the catalyst surface.⁸⁹ The broad transition centered at 1642 cm^{-1} was a convolution of at least two peaks and this is consistent with the observation of Young et al⁷⁶ on the same catalyst. It is reasonable to assign these bands in the C=C and C=O stretching region to the presence of aldehyde species, such as acetaldehyde and crotonaldehyde. Ethoxy, aldehydes and H-bonded ethanol peaks vanished at 200 °C. Only a band at 1587 cm^{-1} was detected at such temperature and it could be assigned either to acetate/carbonate like $\nu_{\text{as}}(\text{COO})$ or to some $\nu(\text{C}=\text{C})$ belonging to a coke precursor.^{91,118} Either way, the fast desorption of ethanol and its products can explain the higher activity shown by this catalyst at the first stages of reaction time. At the same time the presence of some coke precursor on the catalyst surface can explain the decrease in 1-butanol yield observed over a mid-term time scale.

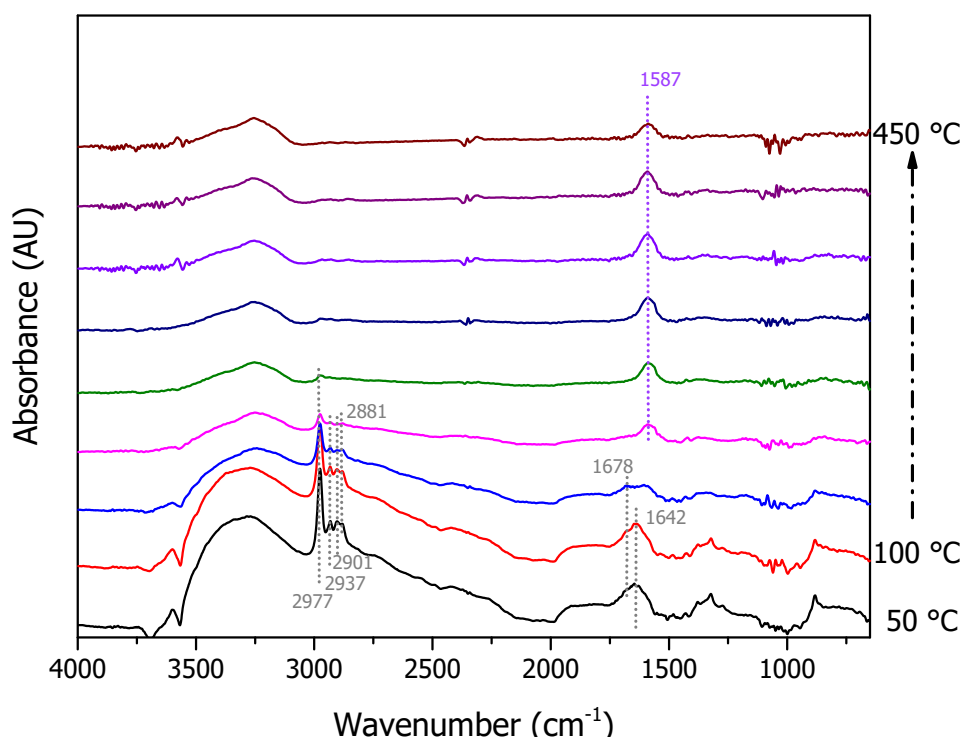


Figure 2.45 CaHAP DRIFTS spectra registered after an ethanol pulse.

SrHAP DRIFTS study

SrHAP ethanol adsorption at 50 °C was similar to CaHAP adsorption, as reported in Figure 2.46. In fact, the broad band due to the H-bonded ethanol and the ethoxy antisymmetric and symmetric CH_3 and CH_2 stretching (2981 cm^{-1} , 2933 cm^{-1} and 2901 cm^{-1}) were detected on SrHAP surface. At the same time, three peaks were observed in the C=O stretching area: 1698, 1639 and 1622 cm^{-1} (shoulder). These were associated to acetaldehyde and crotonaldehyde adsorbed on the catalyst surface.⁸³ As for the ethanol bands, these spectral features completely vanished at 200 °C. At this temperature, as observed with CaHAP, the only visible transition was at 1587 cm^{-1} and it was

The Guerbet Reaction: from ethanol to 1-butanol $\text{H}_3\text{PO}_4/\text{MgO}$ vs Hydroxyapatites in the Guerbet reaction

related to some coke precursor such as acetate/carbonate or $\nu(\text{C}=\text{C})$ of an enolate specie.^{83,89,95,118} The acetate presence is confirmed by the small band visible at 1420 cm^{-1} which could be ascribed to $\nu_s(\text{COO})$. However, on this catalyst two additional bands were detected at low temperature, one at 1143 cm^{-1} and another at 1377 cm^{-1} . Interestingly, such transitions have been correlated to a carbanion intermediate previously observed by Chiericato et al⁷² on MgO. The authors mentioned that such species should be characterized by a particular $\nu(\text{C}-\text{O})$ stretching at 1140 cm^{-1} and a second transition at 1380 cm^{-1} due to the carbanion OH wagging vibration that they did not observe on MgO. Thus, the two bands observed on SrHAP can be correlated with these specific vibrational carbanion modes.

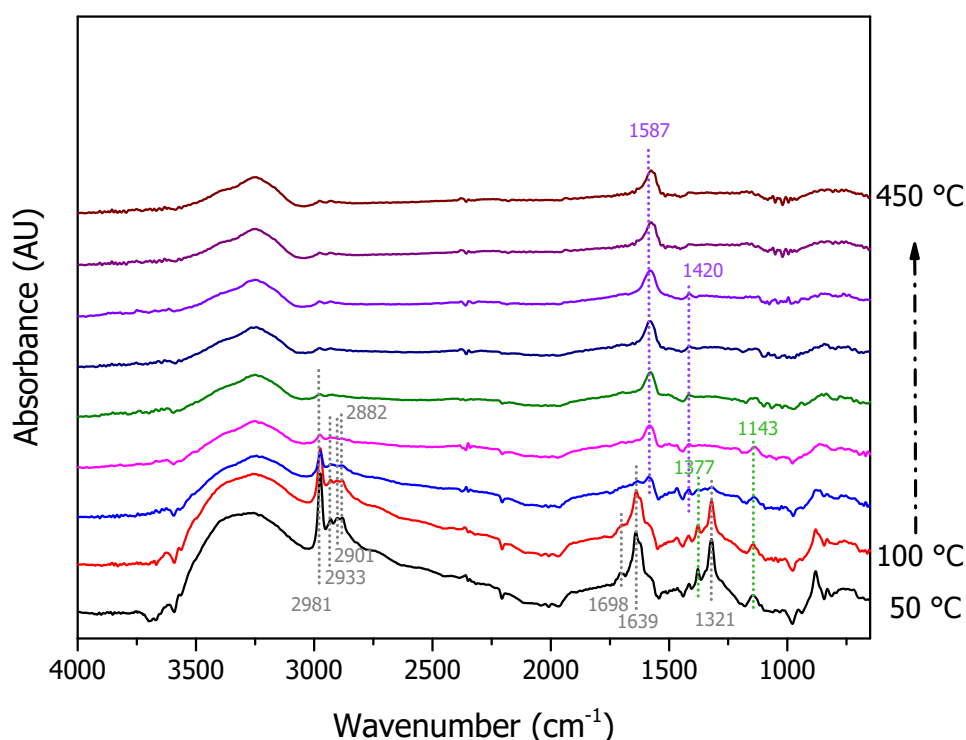


Figure 2.46 SrHAP DRIFTS spectra registered after an ethanol pulse.

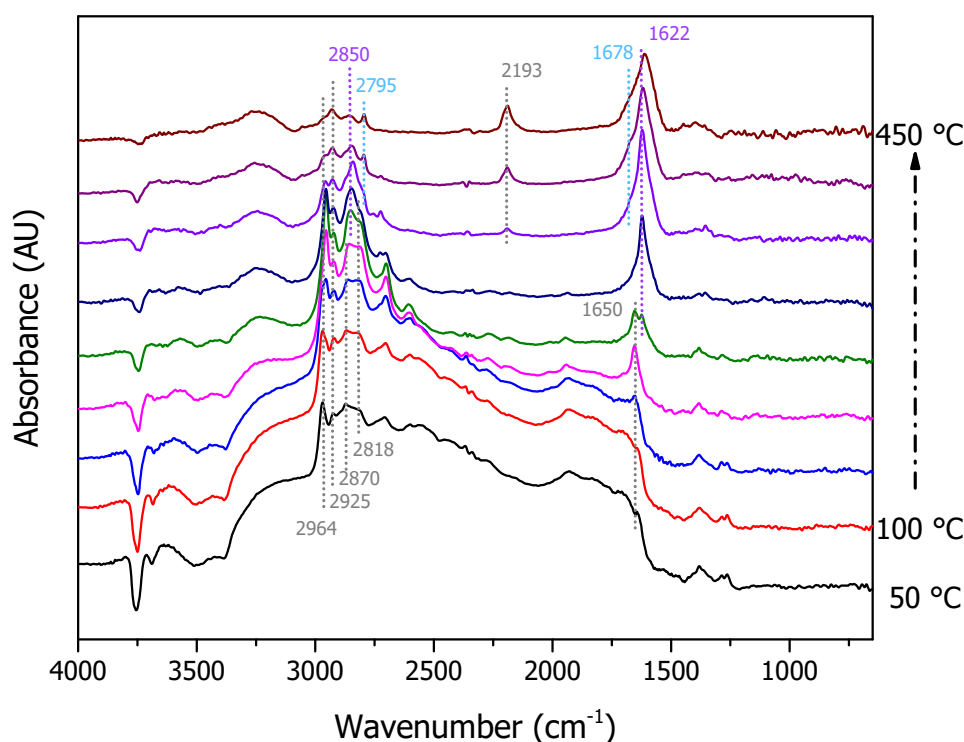
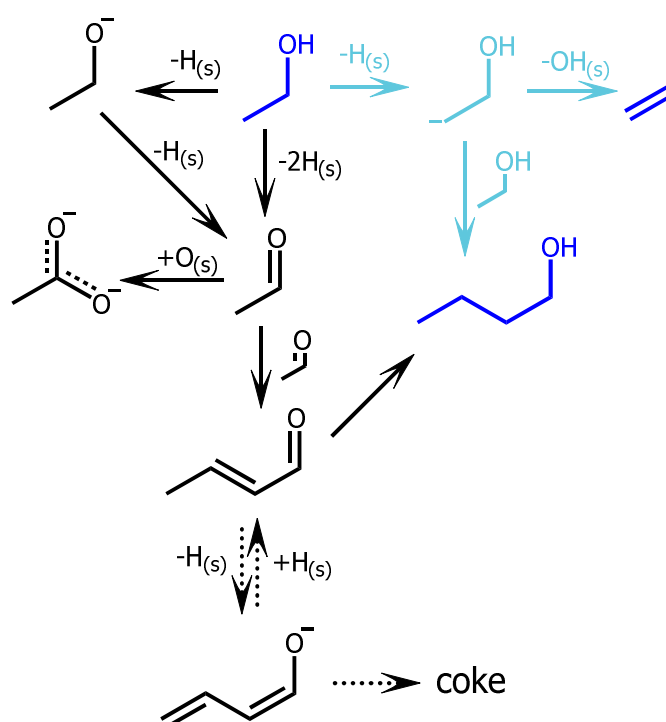


Figure 2.47 5PMgO DRIFTS spectra registered after an ethanol pulse.

The spectra reported in Figure 2.47 are similar to those reported in Figure 2.27. Therefore, the spectra elaboration is the same. However, a brief description will be reported. At low temperature, the broad band over 3000 cm^{-1} and the bands at 2964 cm^{-1} , 2925 cm^{-1} , 2870 cm^{-1} confirmed the presence of H-bonded undissociated ethanol and ethoxy species.^{72,78,81,91} It was not possible to detect the carbanion specific transition due to the strong phosphate adsorption. The band at 1650 cm^{-1} was assigned to acetaldehyde $\nu(\text{C}=\text{O})$.^{72,83} H-bonded ethanol peaks vanished at 250 °C while another band at 1622 cm^{-1} started to be detectable. This was related to the presence of some $\text{C}=\text{C}$ bond probably due to crotyl alcohol or crotonaldehyde.^{83,88} This band underwent a small red-shift with increasing temperature while a shoulder at 1678 cm^{-1} started to be detectable. The latter peak along with the band at 2795 cm^{-1} was related to some crotonaldehyde precursor adsorbed on the catalyst surface.^{83,88} The band at 2193 cm^{-1} was assigned to physisorbed CO_2 .⁶¹



2.5.4 Conclusions

In the present work, 5PMgO performance was compared with hydroxyapatites to understand the role of the acid base strength in the Guerbet reaction.

5PMgO showed performance comparable to hydroxyapatites, requiring slightly higher reaction temperature (50 °C). The selectivity to 1-butanol decreased in the following order SrHAP (51 %) > 5 PMgO (28 %) > CaHAP (24 %). However, SrHAP conversion (16 %) was too low to be considered for an industrial application. 5PMgO and CaHAP showed reasonably higher conversion, 26 % and 60 % at 0.5 g s mL⁻¹. 5PMgO yielded 13 % 1-butanol at 55 % conversion, at 400 °C and 1 g s mL⁻¹.

A comparison of the three catalytic systems with respect to the reaction time highlighted the fast deactivation of the HAPs samples. In contrast, 1-butanol yield decreased by 1 % only within 18 h with 5PMgO.

To our knowledge, this is the first time that hydroxyapatites performance was evaluated with respect to reaction time in the Guerbet reaction. Even though they are the most selective catalysts to 1-butanol, they are not suitable for an industrial application.

Their fast deactivation was related to the prevailing presence of medium strength basic sites which promoted consecutive condensations producing coke on the catalyst surface. Moreover, the presence of strong acid sites considerably affected CaHAP reactivity. In fact, C_{loss} reached 50 % at 450 °C. On the other hand, 5PMgO showed the smallest concentration of weak acid sites (29.92 μmol g⁻¹) along with the highest one of weak basic sites (169.38 μmol g⁻¹). Indeed, it is possible to conclude that the selectivity to 1-butanol is driven by the strength of the acid and basic sites and not only their ratio. Therefore, weak acid and basic sites are a requirement for the selective production of 1-butanol, avoiding a rapid coke formation. In this work, a valid alternative to the hydroxyapatite samples was proposed.

Chapter 3. Dihydroxyacetone upgrading into Lactic Acid

The work reported in this chapter was performed during the period spent in Sievers' research group at Georgia Institute of Technology.

3.1 Introduction

In the last ten years, a lot of scientific literature has been published on lactic acid (LA) production using glycerol as substrate.¹⁷ This reaction is often carried out as one-pot selective oxidation using supported metal catalysts. Alternatively, a cascade reaction in which glycerol is first converted into dihydroxyacetone (DHA) by aerobic catalytic oxidation or fermentation and then further converted into LA is possible.¹¹⁹ The second processing step of this cascade scheme is an area of continuing investigation and the focus of the proposed research.^{120–124}

In 2005, Hayashi et al¹²⁵ published the first paper about DHA upgrading into LA. They reached about 80 % alkyl lactates in alcoholic media using homogeneous Lewis acidic Sn salt at 90 °C for 3 h.

The catalytic performances of Brønsted acids, such as H_2SO_4 ^{122,126}, HCl ^{122,126}, and H_3PO_4 ^{122,127} were studied, and it was observed that, for those catalytic systems, the main product was pyruvaldehyde (PVA) with trace amounts of LA. These results show that Brønsted acid sites are required to produce PVA but are not involved in lactic acid formation. The main drawbacks of homogeneous catalysis are separation issues and harsh reaction conditions, making a heterogeneous process highly desirable.

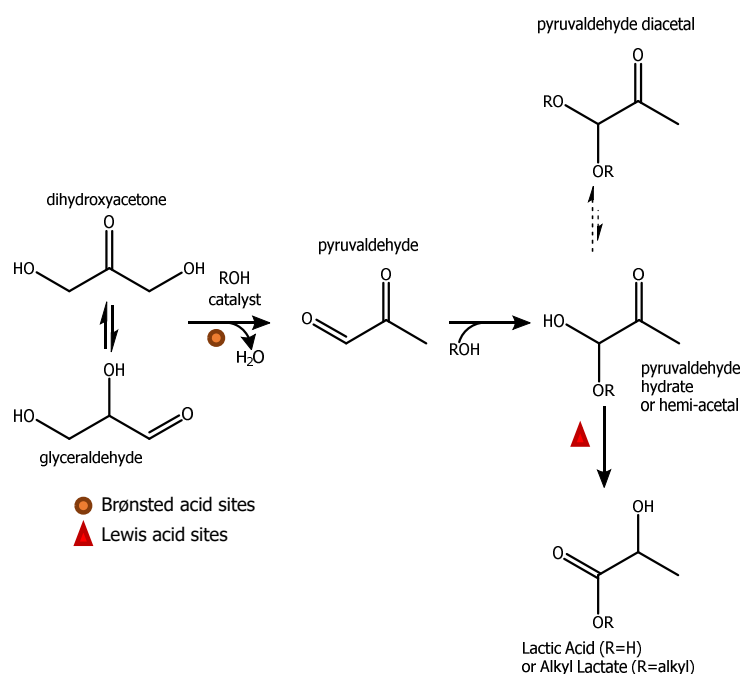


Figure 3.1 DHA upgrading mechanism into LA or alkyl lactate in aqueous ($R=H$) or alcoholic ($R=alkyl$) solvent, respectively.

The reaction mechanism hypothesized for homogeneous catalysis, reported in Figure 3.1, is equally valid for heterogeneous catalysts. It is generally accepted that glyceraldehyde (GLA) isomerizes on Lewis acid sites to DHA, which is the most stable isomer.¹²⁸ This hypothesis is supported by the low concentration of glyceraldehyde detected in the product mixture when DHA

is used as substrate.¹²⁶ It is still not clear if glyceraldehyde or dihydroxyacetone undergo dehydration by means of mild Brønsted acidity.¹²⁹ The dehydration can be assisted even by Lewis acid sites, but it occurs more efficiently in presence of Brønsted acidity.¹³⁰ Finally, PVA is converted into LA or alkyl lactate over Lewis acid sites via the Cannizzaro reaction. If an alcoholic solvent is used instead of water alkyl lactates are produced, and the presence of strong Brønsted acid sites leads to PVA diacetal formation as side product.¹³¹

According to the active site requirements, the ideal heterogeneous catalyst possesses tunable and specific Brønsted and Lewis acid sites. In fact, it is no coincidence that in 2007 Sels and coworkers¹³², publishing the first paper about heterogeneous catalysis, carried out a screening of FAU zeolites to catalyze DHA conversion into alkyl lactates with 59 % yield in 6 h at 90 °C using CBV-600. In 2010, West et al.¹³³ studied the catalytic performance of H-USY-6 (FAU) in a batch and continuous liquid phase set-up. In the continuous liquid phase tests, H-USY-6 showed continuous deactivation when H₂O was used as solvent while its stability in this set-up increased using MeOH. The deactivation was attributed to both carbon deposition and framework degradation. A catalyst able to work in water without strongly deactivating is highly desirable since water is the greenest and cheapest solvent.¹³⁴ Moreover, if an alcoholic solvent is used the final product is an alkyl lactate which needs to be converted in lactic acid in a successive step.^{123,135} In this case, the use of water allows to directly produce lactic acid reducing the reaction steps.

Since Sn resulted to be an optimal Lewis acid center in homogeneous catalysis a lot of researcher tested Sn-containing solids such as Sn-zeolites^{121,136-138}, Sn-Al₂O₃¹³⁹, Sn-silica mesoporous material (MSM-41)¹⁴⁰, Sn-Porous Carbon Silica Material (CSM)¹²³, Sn-hydroxyapatite¹⁴¹, and Sn-montmorillonite¹⁴², modified Sn-phosphates^{127,143}. It is well known, that zeolites, and similar materials, suffer from limited hydrothermal stability. For example, USY in presence of LA in aqueous environment could undergo irreversible framework damages such as loss of pore volume, surface area and acidity, but when MeOH is used as solvent only minor damage was observed.¹³⁰

Simpler tin-based catalytic systems were proposed since porous material syntheses are sometimes not easily scalable and expensive.¹⁴⁴ Wang et al.¹²⁷, in 2015, obtained 96 % lactic acid yield, at 140 °C in ca. 4 h, using SnP-PEG2000. The recycles, for 1 h reactions, showed that even if the DHA conversion was reproducible the LA yield slightly decreased from the first reuse. A variation in DHA concentration affected LA yield while it did not affect the conversion. These observations point to a first order reaction for the conversion of DHA to PVA. Furthermore, they observed that higher amounts of black insoluble compounds were more likely formed at higher DHA concentrations. The same authors tested the catalytic performances of siliceous-tin phosphate catalysts, in 2016. The obtained results were comparable with the previously reported for SnP-PEG2000 in terms of both activity and deactivation.¹⁴³ SnPO, along with ZrPO, is object of a Chinese patent application for C3 and C6 sugar conversion into lactic acid.¹⁴⁵ Metal phosphates are interesting for dihydroxyacetone upgrading in water thanks to their well know water tolerance.¹³⁴ Furthermore, the use of ZrPO, NbPO and SnPO is well documented to carry out reactions requiring both Brønsted and Lewis acid sites such as sugars conversion into HMF.¹⁴⁶⁻¹⁴⁸ Phosphates showed reproducible performances (small decrease in conversion at constant yield) in sugars conversion up to 5 reuses.

According to Perez-Ramirez and coworkers the main drawbacks of tin containing materials for its industrial application are: tin scarce worldwide availability, and typically, complex and lengthy syntheses procedures.^{120,149,150}

Recently, Wang et al.¹⁵¹ attempted to address the problem of the synthesis procedure proposing a SnO₂ – doped NbOPO₄ - CTAB synthesized by sol-gel. This system, in a batch reactor, yielded to

92 % LA at complete conversion at 160 °C in 20 min. The authors observed a sensible decrement in LA yield (about 20 %) within 6 reuses. This productivity decrement was mainly attributed to a 1.2 % and 14.8 % loss of metal content and total acid site, respectively. Furthermore, the presence of carbonaceous deposit was found on the catalyst surface.

As alternative tin-free material desilicated zeolites,¹⁴⁹ Ga-zeolites,^{120,150} Nb-zeolites,¹³⁵ Pt(dppe) supported on montmorillonite,¹⁵² ZrO₂ based mixed oxide¹⁵³, and deformed orthorhombic phase Nb₂O₅¹²⁴ were proposed as catalyst in batch configurations.

A batch process is less appealing for industrialization since the scale up is less obvious than for a flow reactor.¹⁵⁴ In fact, the mixing in flow reactors is well characterized with respect to the batch set up one. In general, flow reactors present an increased surface area to volume ratio enhancing the heat and mass transfer and requiring smaller spaces. The precise control of the reaction parameters such as temperature allows to reduce unwanted side-reactions. Moreover, a flow reactor allows a continuous production, with an evident economical advantage since it requires less programmed stops and can facilitate the product transportation. In fact, a batch process handles a bulk load of material and it is not possible to transform the next load of material until the first reaction is over. The handling of lower amount of reactant and solvents reduces the process waste and increase the general process safety. Furthermore, it is simpler to enhance flow reactor productivity by their coupling with other technologies such as microwave irradiation and ultrasound.^{155,156} Even from a lab-scale point of view the flow reactors are more efficient in obtaining reaction kinetic information and produce more accurate data. In fact, if a metal leaches from the catalyst, it is removed from the reaction environment continuously while in a batch reactor it would act as an homogeneous catalyst.¹⁵⁷ A major use of continuous flow processes is auspicious for the future in the academic laboratories since it is simpler to model the mass transfer and it is easier to scale up for biomass valorization. Nevertheless, the flow set up is the preferred configuration for petrochemical processes¹⁵⁴ and their application in biomass valorization would make easier the conversion of refineries into bio-refineries.

Mylin et al.¹⁵³ studied the activity of amphoteric ZrO₂-based mixed oxide both in batch and continuous flow setups. ZrO₂-TiO₂ (1:3) in a continuous flow system yielded to 90 % ethyl lactate at 140 °C, 1.0 MPa, and LHSV=2.2 h⁻¹. DHA conversion was stable for 7 h, while the ethyl lactate yield decreased by 15 % over the time. A comparison between the autoclave and the continuous flow results showed that the reaction under flow conditions allows to reach higher yields. Anyway, the authors did not dig up into this performance enhancement and since the contact time in a flow reactor is shorter than in an autoclave a deeper understanding on this observation is necessary.

However, studies performed using continuous flow set-ups remain rare.^{158–160} Moreover, a cheap, easy synthesizable and water-tolerant catalytic system needs to be developed. La, Zr and Nb phosphates are reported among the water-tolerant solid acid catalysts.¹³⁴ To our best knowledge their catalytic activity in DHA conversion to LA in continuous liquid flow reactor still needs to be disclosed.

In this contribution, we investigate Nb, Zr and La phosphates for LA production from DHA in a continuous liquid phase setup using water as solvent. The materials were fully characterized in terms of specific surface area, porosity and acidity. Their performances as function of temperature, contact time, and time on stream were evaluated. The roles of mass transfer and intrinsic kinetics were fully understood for these catalysts.

3.2 Methods

3.2.1 Catalyst syntheses

Three different metal phosphate catalysts (ZrPO, LaPO, NbPO) were synthesized by coprecipitation using methods adapted from the literature.^{161–164}

LaPO was synthesized by slowly dropping a 0.8 M $\text{La}(\text{NO}_3)_3 \cdot 6\text{H}_2\text{O}$ aqueous solution (130 mL) into a 1.2 M H_3PO_4 solution (130 mL) under stirring. Then, pH was adjusted to 7 using NH_4OH and the precipitate was aged under ambient condition for 2 h. This was then filtrated, washed and dried at 80 °C overnight.¹⁶¹

ZrPO synthesis followed a similar procedure. In fact, 1 M $\text{ZrOCl}_2 \cdot 8\text{H}_2\text{O}$ solution (64 mL) was added dropwise to a solution 1 M of $\text{NH}_4\text{H}_2\text{PO}_4$ (128 mL). In this case, the pH was not adjusted and after the aging the precipitate was filtered, washed and dried at 80 °C overnight.^{163,164}

NbPO was synthesized with a slightly different procedure. In fact, a templating agent was used to enhance its surface area. In a typical procedure, 100 mL of 0.4 M H_3PO_4 ethanol solution was added dropwise to 100 mL of 0.2 M NbCl_5 ethanol solution, the mixture was stirred vigorously for 30 minutes, after the pH was adjusted to 2.6 with NH_4OH obtaining a white precipitate. The precipitate was filtered, washed, and added to a 0.6 M hexadecylamine solution. The new slurry was aged for 30 min under stirring and then the pH was adjusted to 3.5 with 85 % w/w H_3PO_4 . The obtained gel was aged in a Teflon autoclave for 2 days at 65 °C. Finally, the precipitate was filtered, washed, and dried in an oven overnight.¹⁶²

LaPO, ZrPO, and NbPO, after drying, were calcined at 550 °C¹⁶⁴, 400 °C¹⁶³, and 800 °C, respectively.

NbPO calcination temperature is the minimum necessary to completely remove the templating agent. Such temperature was chosen with a trial and error approach. In fact, it was the minimum temperature at which the catalyst resulted white and not full of coke from the templating agent burning.

3.2.2 Catalyst characterization

X-ray diffraction (XRD) patterns were recorded in the range of $10^\circ < 2\theta < 80^\circ$ with a Philips PW 1050/81 apparatus controlled by a PW1710 unit ($\lambda = 0.15418$ nm (Cu), 40 kV, 40 mA). The scanning rate was $0.05^\circ 2\theta \text{ s}^{-1}$ and the step time 1 s. The XRD phase was assigned using the "Search and match!" option of X'Pert Highscore Plus and the ICSD database.

Nitrogen physisorption measurements were performed using a Micromeritics ASAP 2020 physisorption analyser. The catalysts were degassed at 200 °C for 4 h prior to measurement. Surface areas and mesopore volumes were calculated based on the BET method⁷⁵ and BJH method¹⁶⁵, respectively.

Attenuated total reflectance spectra of the materials, without any pre-treatment, were recorded at room temperature with an ALPHA-FTIR instrument at a resolution of 2 cm^{-1} after 64 scans. The spectrometer was equipped with a DLaTGS and a single reflection diamond.

MAS ^{31}P NMR spectra were measured with a Bruker Avance III HD 300 solids spectrometer at a sample spinning rate of 10 kHz and a time delay of 5 s. Chemical shifts were referenced with respect to ammonium-dihydrogen-phosphate at 0 ppm. The used pulse length was 1 μs and the spectra were acquired after 256 scans. A rotor with a nominal 4 mm outer diameter and 16 mm length was used to load the sample and measure the spectrum.

Catalyst total acid site strength and concentration were determined by NH₃ temperature-programmed desorption (NH₃-TPD) using a Micromeritics Autochem II 2920. Typically, 50 mg of powder sample was placed in a U-shaped fixed-bed reactor, preheated at 400 °C for 1 h, and cooled to 100 °C. Then, gaseous NH₃ was injected to saturate the sample, followed by introduction of a He carrier gas to purge the excess of NH₃. After stabilization for 1 h, the sample was heated to 700 °C at a ramping rate of 10 °C min⁻¹. NH₃ desorption profile in the temperature range of 100 – 700 °C was measured using a thermal conductivity detector (TCD).

The Brønsted and Lewis acidity were evaluated by pyridine adsorption followed by Fourier Transform Infrared (FTIR) Spectroscopy. The experiments were performed using a Nicolet 8700 FTIR spectrometer with an MCT/A detector. Each sample was loaded into a vacuum transmission cell as self-supported wafer (diameter 1.25 cm). The sample was activated at 450 °C for 1 h under high vacuum. A background spectrum was recorded at 150 °C. Then, pyridine (0.1 mbar) was dosed for 30 mins. Subsequently, the cell was evacuated for 1 h to remove physisorbed pyridine. To determine the strength of acid sites a temperature programmed desorption was carried out. The sample was heated to 250 °C, 350 °C and 450 °C for 1 h, and each 'high temperature' spectrum was taken at 150 °C. The concentration of Lewis and Brønsted acid sites was determined using the Lambert–Beer equation:

$$C_w = \frac{A_{peak} \cdot S}{W \cdot \varepsilon}$$

Where C_w (μmol g⁻¹), W (g), S (cm²), and ε (cm² μmol⁻¹) indicate weight-based concentration, sample weight, sample disk area and the integrated molar extinction coefficient as reported by Tamura et al., respectively.¹⁶⁶

The elements (from Na to U, O percentage is obtained by difference) present in the samples¹⁷ were detected by Particle Induced X-ray Emission (PIXE) analysis, performed by Elemental Analysis Inc.

60

X-Ray Fluorescences analysis (XRF) were used to evaluate the catalyst leaching. A PANalytical Axios Advanced dispersive wavelength spectrometer, equipped with 4kW power rhodium tube, was used for analysis.

3.2.3 Catalytic tests

Catalytic conversion of dihydroxyacetone was studied in an up-flow fixed bed reactor (1/4 in Swagelok 316 stainless steel tube). Quartz wool was used in both ends of the reactor to keep the catalyst bed in place. The reactor temperature was varied between 90 °C and 150 °C, and the pressure was set at 10 bar using an Equilibar EB1LF2 back pressure regulator with a PTFE/glass diaphragm. A 0.4 M dihydroxyacetone aqueous solution was pumped by an Agilent 1100 Series HPLC pump at a flow rate of 0.2 mL min⁻¹ (except where otherwise noted). In a typical experiment 200 mg of catalyst (90 – 212 μm) were loaded, and the reaction products were collected periodically (every 30 min) for 6 h with the aid of an automatic Valco selector valve. All the collected samples were filtered using a 0.45 μm polypropylene membrane prior to analysis. The system requires about 1.5 h to reach a steady state.

All aliquots were analyzed by high performance liquid chromatography (HPLC) in an Agilent 1260 Infinity HPLC equipped with a refractive index detector (RID). A Rezex ROA-H⁺ column was used at 60 °C in isocratic elution mode with a 0.0025 mol L⁻¹ H₂SO₄ solution as mobile phase at a flow rate of 0.6 mL min⁻¹. RID temperature was kept at 50 °C.

¹⁷ <http://www.elementalanalysis.com/pixe.html>

To determine any external mass transfer limitations, the flow rate was varied ($0.1 \div 0.3 \text{ mL min}^{-1}$), and the amount of catalyst in the reactor was adjusted to maintain constant space-time. To evaluate potential pore diffusion limitations, the catalyst particle size was varied from $38 - 75 \mu\text{m}$ to $355 - 425 \mu\text{m}$.

Since the apparent density varies among the three catalyst, the space time is expressed as follow:

$$\tau = \frac{m}{\dot{V}_{tot}}$$

Where m is the loaded catalyst mass in the reactor and \dot{V}_{tot} is the total volumetric flow expressed in g and mL s^{-1} , respectively.

Dihydroxyacetone conversion (X_{DHA}), products selectivities (S_p) and yields (Y_p) were determined using the following equations:

$$X_{DHA} = \frac{C_{DHA}^{in} - C_{DHA}^{out}}{C_{DHA}^{in}} \cdot 100 \%$$

$$Y_p = \frac{C_p^{out} \cdot CA_p}{C_{DHA}^{in} \cdot CA_{DHA}} \cdot 100 \%$$

$$S_p = \frac{Y_p}{X_{DHA}} \cdot 100 \%$$

Where C_{DHA}^{in} is the initial DHA number of moles, C_{DHA}^{out} is the final DHA number of moles, C_p^{out} is the product of interest number of moles while CA_p and CA_{DHA} are the carbon atom number of the product of interest and DHA, respectively. The carbon loss was evaluated as difference between the conversion and the sum of the yields of detected products. For this reason, if a carbon loss resulted negative it was forced to zero imposing the yield sum equal to the conversion. This mathematical imposition was necessary only at low temperature ($90 \text{ }^\circ\text{C}$) probably because the catalysts were not completely active, yet.

Rate constant (k) and reaction rate for DHA conversion into PVA were evaluated assuming a first order reaction according to the following equations:

$$k = \frac{1}{1 - X_{DHA}} \cdot \frac{1}{\tau}$$

$$r_{DHA} = k \cdot C_{DHA}$$

The (apparent) activation energies (E_a) for each catalyst was evaluated using the Arrhenius equation:

$$\ln(r_{DHA}) = -\frac{E_a}{RT} + \ln(A)$$

Where A is the pre-exponential factor and the linear plot intercept in the Arrhenius plot, R is the ideal gas constant.

Since two out of three catalysts were found to be partially external mass transfer limited, the mass transfer coefficient (k_c) was evaluated through a linear plot of k_{obs}^{-1} against the reciprocal of the square root of fluid speed inside the reactor ($v^{-1/2}$) and compared to the surface rate constant (k_s) to evaluate the limitation entity. This was possible because k_{obs} , obtained by using the experimental data, is related to k_c and k_s by the following equation:

$$\frac{1}{k_{obs}} = \frac{1}{k_c} + \frac{1}{k_s}$$

The mass transfer coefficient is related to a species diffusivity (D_{AB}) and the particle radius (R_p) as expressed by the Sherwood number (Sh). If the particle is assumed to be spherical, Sh is related to the Schmidt number (Sc) and the Reynolds number (Re):

$$Sh = 2 + 0.6 Re^{1/2} Sc^{1/3}$$

Finally, based in this equation, it is possible to find the correlation between k_c and the liquid reactant speed (v) inside the reactor:

$$k_c \propto \frac{(D_{AB})^{2/3} v^{1/2} \rho^{1/6}}{(R_p)^{1/2} (\bar{\mu})^{1/6}}$$

Where ρ is the fluid density and $\bar{\mu}$ is the average viscosity.¹⁶⁷

On the other hand, the catalyst that was not externally limited showed a peculiar conversion change varying the particle size. Therefore, it was decided to evaluate the internal mass transfer limitation calculating for this sample the Thiele modulus (ϕ) and the effectiveness factor (η), assuming a spherical particle size:

$$\phi = R_p \sqrt{\frac{k}{D_{TA}^e}}$$

$$\eta = \frac{\tanh(\phi)}{\phi}$$

Where, R_p , k and D_{TA}^e are the particle size radius, the observed reaction rate constant and the effective transition diffusivity, respectively.¹⁶⁷ As D_{TA}^e was used the glycerol diffusion coefficient glycerol in water ($9.36 \cdot 10^{-6}$).¹⁶⁸ If the reaction is severely mass transfer limited η is approximated by the inverse of ϕ . A small value of Thiele modulus (generally, $\phi < 1$) results from a low diffusional resistance, and the effectiveness factor is close to 1.¹⁶⁷

3.3 Results and discussion

3.3.1 Catalyst structure and compositions

The catalyst surface properties such as pore size, pore volume and surface area were evaluated by N₂-physisorption. All the catalysts showed a type IV hysteresis curve characteristic of mesoporous materials as shown in Figure 3.2. LaPO is the catalyst which presented the lowest surface and the larger mesopore width, as reported in Figure 3.2. On the contrary, ZrPO possessed the highest surface area and a mesopore distribution shifted towards the micropore region, while NbPO showed the lowest cumulative pore volume and the smaller average mesopore width.

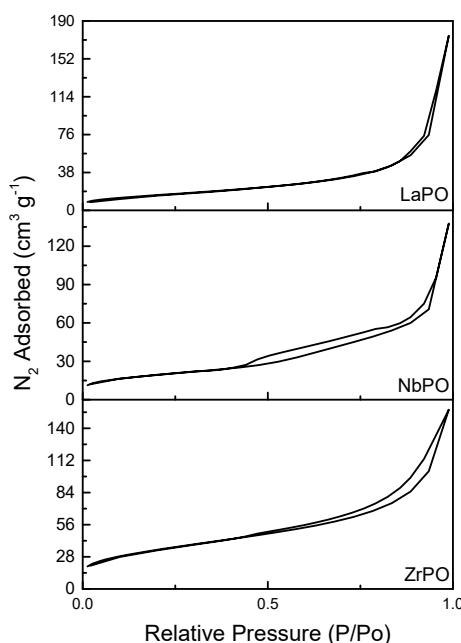


Figure 3.2 N₂ - physisorption isotherms.

The catalysts were analyzed by PIXE analysis to detect all the possible contaminant present and to evaluate the M/P ratio. LaPO contained only Na (0.29 mol%) in terms of impurities. Si (0.11 mol%), Cl (0.09 mol%), Ni (0.0004 mol%), Ce (0.01 mol%) and Hf (0.06 mol%) were detected in ZrPO. NbPO contained S (1.04 mol%), Ca (0.02 mol%), Fe (0.001 mol%), Zn (0.0003 mol%) and Ta (0.001 mol%). The M/P ratio was 0.80, 0.31, 0.62 for LaPO, ZrPO and NbPO, respectively.

Table 3.1 BET surface area (S_{BET}), BJH desorption cumulative pore volume (BJH_{DPV}), BJH desorption average pore width (BJH_{DPW}) and total concentration of acid sites determined by NH₃-TPD.

Entry	Catalyst	S_{BET} $\text{m}^2 \text{g}^{-1}$	BJH_{DPV} $\text{cm}^3 \text{g}^{-1}$	BJH_{DPW} nm	NH ₃ -TPD	
					$\mu\text{mol m}^{-2}$	$\mu\text{mol g}^{-1}$
1	ZrPO	122	0.175	9.48	5.20	634
2	NbPO	69	0.144	7.97	4.07	281
3	LaPO	56	0.177	14.07	4.80	269

In Figure 3.3 on the left, the catalyst XRD patterns are reported. The plots show that NbPO and ZrPO were almost completely amorphous, while LaPO was semi-crystalline. According to the XRD patterns, the LaPO phase is LaPO₄ (Ref. 00-032-0493), as expected. This result is in agreement with the La/P ratio (0.80) of the sample. The intense diffraction at 20.56 °θ in the X-ray diffractogram of NbPO might be assigned to the most intense diffraction of Nb_{1.91}P_{2.82}O₁₂ (Ref. 00-051-1738) or NbPO₅ (Ref. 00-019-0868). The second phase is discarded since the Nb/P ratio of

0.62 is in excellent agreement with the Nb/P theoretical ratio (0.67) of $\text{Nb}_{1.91}\text{P}_{2.82}\text{O}_{12}$ phase. At the same time the broad diffraction around 20° was found in agreement with the most intense diffraction of $\text{Zr}_2\text{O}(\text{PO}_4)_2$ (Ref. 00-037-0155). Unfortunately, the Zr/P ratio of this phase was not in agreement with Zr/P ratio (0.31) obtained by PIXE analysis. For this reason, it is not possible to assign a phase to ZrPO at this time.

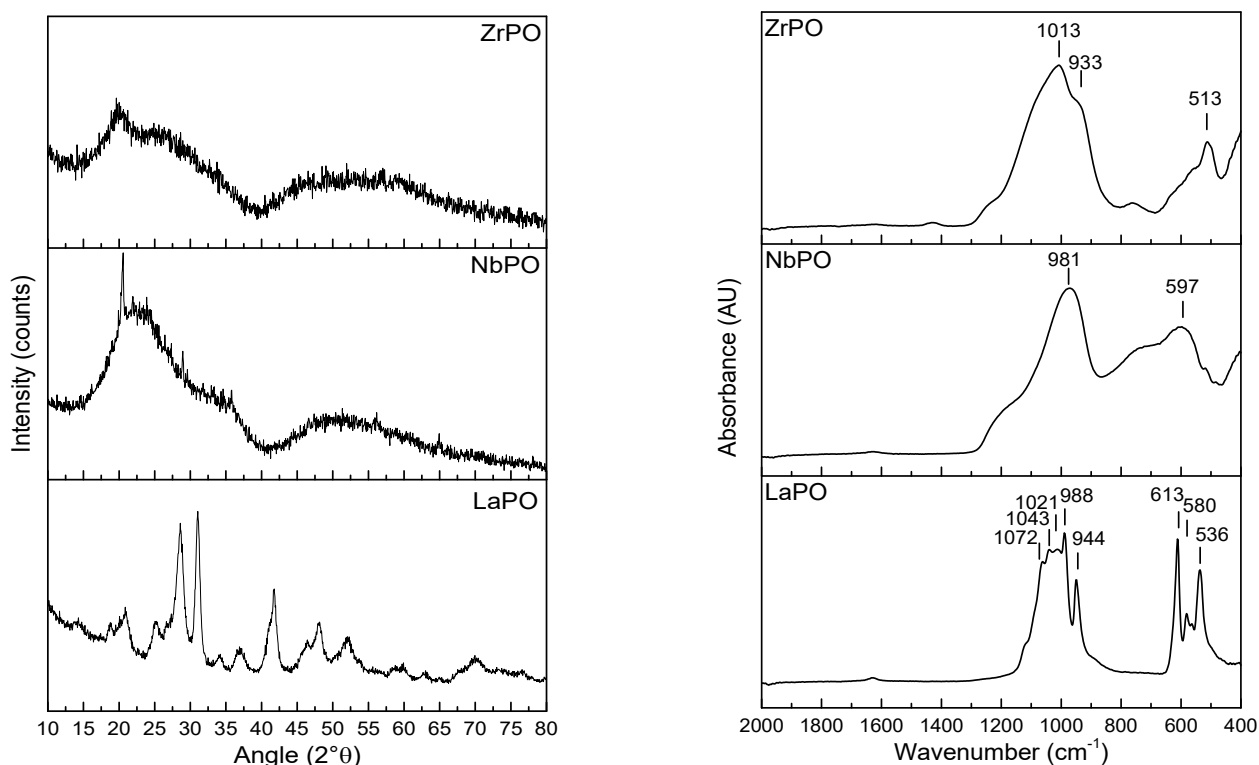


Figure 3.3 XRD pattern for LaPO, ZrPO and NbPO on the left; LaPO, ZrPO, NbPO surface ATR-IR spectra on the right.

Since two catalysts out of three were characterized by major amorphous domain, they were studied also by means of ATR-FTIR spectroscopy to obtain some information about the P-O bonds present.

The ATR spectra are reported in Figure 3.3. Broad phosphates bands (around 1000 cm^{-1} , P-O asymmetrical stretching vibration, and $500\text{--}600\text{ cm}^{-1}$, PO_4 deformation modes) further evidenced the amorphous character of NbPO and ZrPO. Additionally, the high sharp and multiplied lines present in LaPO ATR spectrum confirmed its high crystallinity.¹⁶¹ In fact, the strong crystal field of LaPO splits the asymmetrical P-O stretching (ν_3) into four bands detectable at 1072 cm^{-1} , 1043 cm^{-1} , 1021 cm^{-1} , 988 cm^{-1} and the deformation vibration (ν_4) into three peaks at 613 cm^{-1} , 580 cm^{-1} , 536 cm^{-1} , respectively.^{169–172} Thanks to the high LaPO crystal field, it is possible to appreciate even the symmetrical stretching vibration (ν_1) at 944 cm^{-1} , that should be infrared forbidden.¹⁷¹ The broad band around 750 cm^{-1} in NbPO and ZrPO is attributed to P-O-P vibration of diphosphate groups.¹⁷³ The ZrPO band at 933 cm^{-1} was already observed in α -zirconium hydrogen phosphate FTIR spectrum.¹⁷³ The peak position of asymmetric P-O stretching vibrations usually increases in energy with increasing ionic radius of the cation, which is in good agreement with our experimental results ($\text{Nb (215 pm)} < \text{Zr (230 pm)} < \text{La (250 pm)} \rightarrow 981\text{ cm}^{-1} < 1013\text{ cm}^{-1} < 1072\text{ cm}^{-1}$, respectively). The increase in P-O vibration frequency means that ionic character of the M- PO_4 bond is increasing.

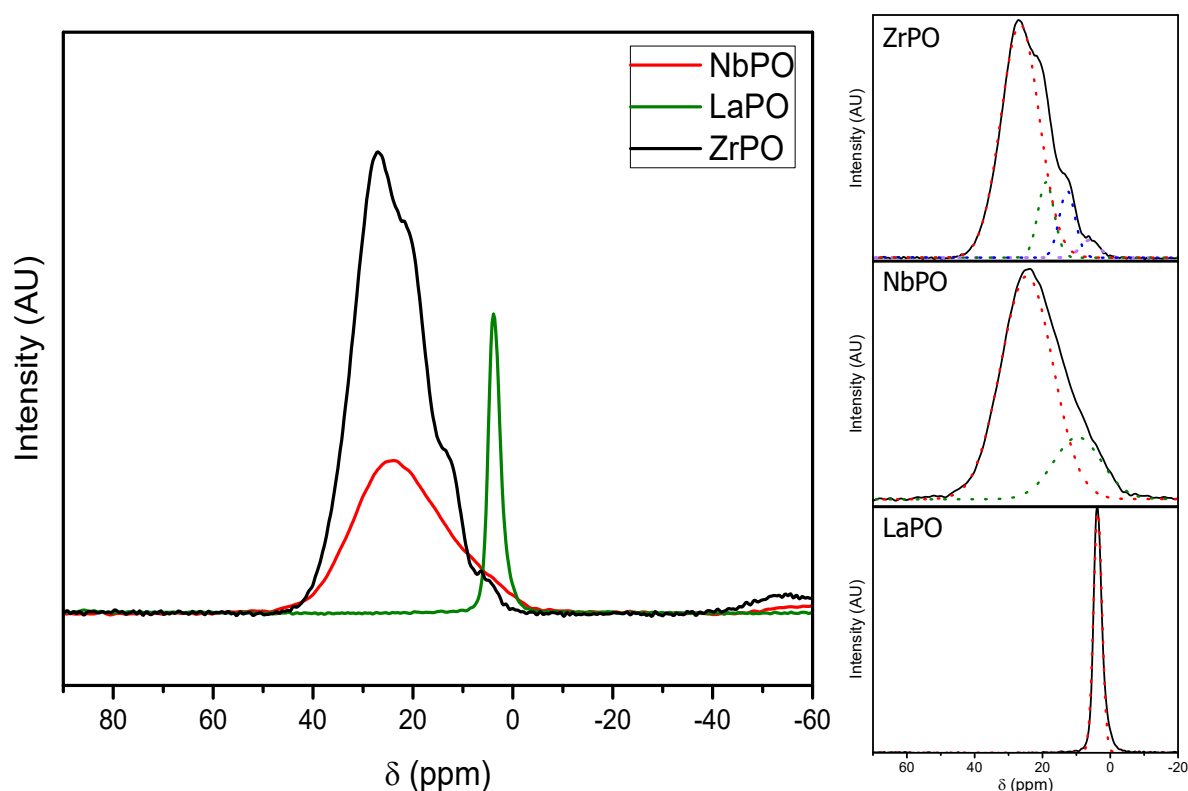


Figure 3.4 ^{31}P -MAS NMR for NbPO, LaPO and ZrPO (on the left) and their peak deconvolutions (on the right).

^{31}P -MAS NMR was used to gain further information on P position and bonds in the amorphous samples. In general, the number of lines in ^{31}P MAS NMR spectra for orthophosphates is equivalent to the number of non-equivalent P atom in the catalyst structure.¹⁷⁴ The nomenclature for phosphate connectivity into solids depends on the number of PO_4 bridging oxygen, n . In phosphate case there are five possibilities from Q^0 (no M-O-P bond is present) to Q^4 (all the oxygen atoms are involved in M-O-P bonds).¹⁷⁵ It was possible to deconvolute the ZrPO, NbPO and LaPO using 4, 2 and 1 Gaussian curves, as shown in Figure 3.4 on the right. The LaPO resonance at 4.0 ppm was attributed to tetrahedral PO_4 connected to two La atoms (Q^2 topology).¹⁷⁴ This assignment is consistent with the monoclinic P21/n, 14 space group characteristic for the LaPO_4 phase. The chemical shifts for the resonance of NbPO were 9.3 ppm and 24.6 ppm. The peak at 24.6 ppm can be assigned to a Q^4 topology, since it is thought that the octahedral NbO_6 and the tetrahedral PO_4 share all the vertices. Therefore, every oxygen atom is linked to a Nb and a P atom in the $\text{Nb}_{1.61}\text{P}_{2.8}\text{O}_{12}$ phase.¹⁷⁶ The resonance at 9.3 ppm is assignable to some defects that decrease the number of bridging oxygen.¹⁷⁷ The ^{31}P MAS NMR spectrum of ZrPO contained four signals at 26.7 ppm, 21.0 ppm, 12.4 ppm and 5.4 ppm. In this case, it was possible to attribute the signals at 26.7 ppm, 21.0 ppm and 12.4 ppm to Q^4 , Q^3 and Q^2 topology of zirconium hydrogen phosphate (HPO_4).¹⁷⁵ The peak at 9.3 ppm in the spectrum of NbPO and that at 5.4 ppm in the spectrum of ZrPO were tentatively assigned to a Q^2 topology of PO_4 . This assignment is in good agreement with the correlation between the electronegativity of the metal center and the isotropic chemical shift. In fact, decreasing the metal electronegativity, P is able to attract more electron density strengthening the P-O bond and causing an upfield chemical shift motion.¹⁷⁵ The electronegativity is 1.6, 1.3, 1.1 for Nb, Zr and La, respectively. Moreover, in light of this result and the ATR IR spectra, it is possible to hypothesize that ZrPO phase is α -zirconium phosphate ($\text{Zr}(\text{HPO}_4)_2 \cdot n \text{H}_2\text{O}$), which has a Zr/P ratio closer to the one obtained from the PIXE analysis (0.31). Moreover, one of the most intense diffraction of this phase XRD pattern (Ref. 00-019-1489) is located at 20.1° .

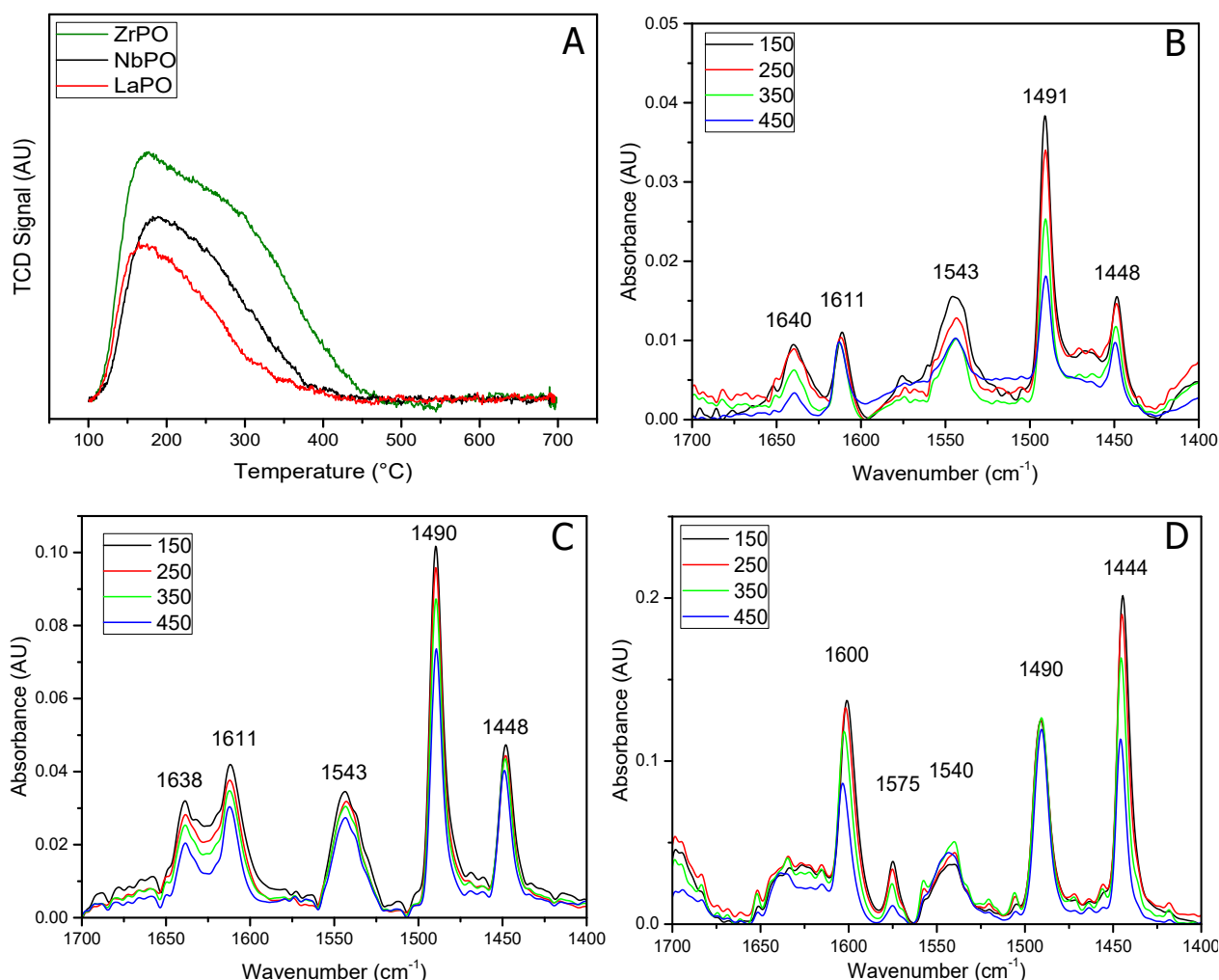
3.3.2 *Phosphate acidity*

Figure 3.5 Acidity characterization. A: NH₃-TPD profiles, B: ZrPO pyridine FTIR desorption, C: NbPO pyridine FTIR desorption, D: LaPO pyridine FTIR desorption.

The acid site concentration on the catalysts was evaluated by NH₃-TPD. In this chapter, the acid sites are defined weak, medium and strong according to the following NH₃ desorption temperature partition: under 200 °C, between 200 °C and 300 °C, and over 300 °C, respectively. ZrPO possessed the highest total acidity (Table 3.1) and showed a very broad desorption peak (from 100 °C to 450 °C), shown in Figure 3.5 A, which can be attributed to the presence of weak, medium and strong acid sites. It presented an absolute maximum around 180 °C and a visible and defined shoulder centered around 290 °C in the medium/strong acid sites transition area. On the contrary, NbPO showed the lowest total acidity and a broad desorption profile (from 100 °C to 400 °C). In this case, the peak maximum is at 190 °C (transition area between weak and medium strength acid sites) and the distribution is mainly centered on medium strength acid sites. Anyway, the contribution of weak and strong acid sites is not neglectable. The desorption curve for LaPO had a maximum centered around 160 °C that can be associated mainly to weak acid sites, but it is not possible to exclude a contribution of medium strength acid sites.

It is possible to order the catalyst in terms of total acidity as follows: ZrPO > LaPO > NbPO.

Since the reaction under investigation is well known for being driven by the different type of acid sites, pyridine adsorption was studied to discriminate the types of acid sites and their relative strength. Figure 3.5 B, C and D show the infrared spectra obtained during the pyridine desorption

for ZrPO, NbPO and LaPO, respectively. The vibrations of pyridine adsorbed on Lewis acid sites were detectable at 1448 cm^{-1} , 1490 cm^{-1} , 1575 cm^{-1} (only on LaPO), and 1610 cm^{-1} . The peaks of the pyridinium ion, which is formed when pyridine is protonated on a Brønsted acid sites, were at 1490 cm^{-1} , 1540 cm^{-1} , 1575 cm^{-1} (only LaPO), 1640 cm^{-1} (only ZrPO and NbPO).

Brønsted acid sites are due to P-OH groups and some contribution of M-OH. Instead the Lewis sites are related to coordinatively unsaturated M^{n+} sites. The ratio between the concentrations of Brønsted and Lewis acid sites on phosphate catalysts is usually determined by the amount of chemisorbed water. In fact, a Lewis acid site can be converted into a Brønsted one by water coordination or water dissociative adsorption on unsaturated M^{n+} .¹⁶¹

The variation of concentrations of Brønsted and Lewis acid sites is reported in Figure 3.6. It was possible to observe that all the catalyst samples possessed both Brønsted and Lewis acidity. The concentration of Lewis acid sites was evaluated integrating the peak around 1445 cm^{-1} while the Brønsted one integrating the peak around 1545 cm^{-1} . At the same time, the concentration of weak, medium, strong and very strong acid sites was evaluated considering the peak areas at 150 °C , 250 °C , 350 °C and 450 °C , respectively. In fact, the higher the temperature of pyridine desorption the stronger is its interaction with the acid site. LaPO showed the lowest Brønsted acid sites concentration that is almost constant increasing the temperature. NbPO had the highest concentration of medium (250 °C), strong (350 °C) and very strong (450 °C) Brønsted acid sites. The distribution of Brønsted acid sites in ZrPO was different. In fact, it showed the highest concentration of Brønsted acid sites, but their concentration decreased steeply from 150 °C ($45\text{ }\mu\text{mol g}^{-1}$) to 450 °C ($16\text{ }\mu\text{mol g}^{-1}$).

As far as the Lewis acid sites concentration is concerned, the three catalysts showed a similar strength distribution. NbPO possessed the highest number of Lewis acid sites at every temperature and the concentration of weak Lewis sites was practically neglectable. On the contrary, ZrPO and LaPO Lewis acid sites concentration were comparable in terms of strong and very strong acid sites, while ZrPO possessed a slightly higher amount of weak and medium strength Lewis acid sites.

The total amount of Brønsted and Lewis acid sites can be ordered as $\text{ZrPO} \approx \text{NbPO} \gg \text{LaPO}$ and $\text{NbPO} > \text{ZrPO} > \text{LaPO}$, respectively. The infrared results showed an acidity trend that is opposite with respect to M- PO_4 bond ionic character ($\text{NbPO} < \text{ZrPO} < \text{LaPO}$) but in good agreement with the metal electronegativity.¹⁷⁸

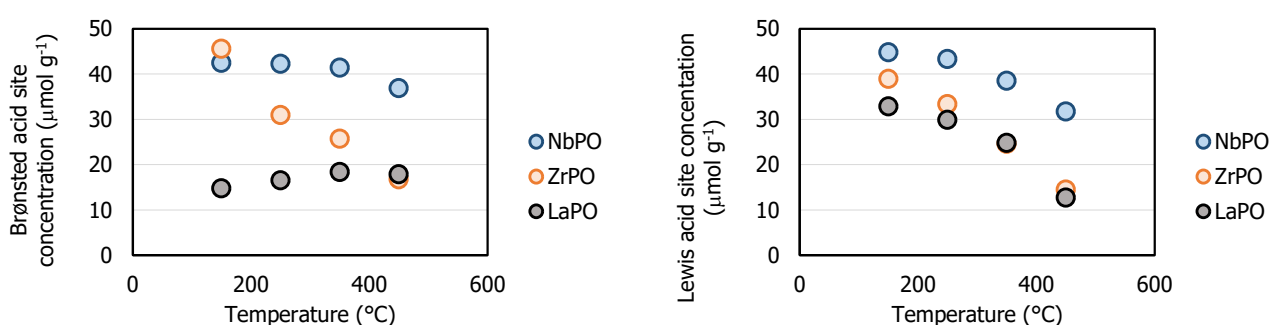


Figure 3.6 Brønsted and Lewis acid sites concentration variation with temperature, on the left and on the right respectively

3.3.3 Dihydroxyacetone rearrangement to Lactic acid

The leaching for the metal phosphate catalysts was evaluated in batch configuration at 90 °C for 4h. The catalyst substrate ratio was 1.5 and the DHA solution concentration was 0.2 M . XRF

analyses were done on the final reaction solution and no metal traces were detected, while the amount of phosphorous revealed was negligible (<0.008 mol%).

Mass transfer limitation check

The mass transfer limitations can affect the reaction rates, the catalyst selectivities and even the reaction mechanism. They can be internal or external, this means that the reagent or product flows are encountering some physical resistance in flowing through the catalyst pore or the boundary layer at the catalyst surface, respectively.¹⁵⁷

The external diffusion limitations were studied running tests, in which the total liquid flow rate and the catalyst mass in the fixed bed were varied by the same factor. Thus, the experiments were performed with constant contact time, and all other parameter were kept constant. On the other hand, the internal diffusion limitations were probed by varying only the catalyst particle size.

It was decided to evaluate the mass transfer phenomena on all the catalysts, since ZrPO showed the highest surface area, LaPO possesses the larger mesopores, while NbPO was the most active towards lactic acid. Often, the higher the surface area, the higher is the activity and for this reason, usually, the transport phenomena are checked just for the most active catalyst.

The external mass transfer limitations were excluded for ZrPO because the dihydroxyacetone conversion only varied within the experimental error when the flow rate was changed (Figure 3.7 (left)). The internal diffusion limitations were evaluated from a theoretical point of view, as explained in section 3.2.3, because the conversion varied by up to 10 % without a clear trend with changing particle size (Figure 3.7). It was possible to exclude the limiting regime in the operative condition chosen because the effectiveness factor was close to one from $75 - 38 \mu\text{m}$ to $212 - 90 \mu\text{m}$, as reported in Table 3.2. It is possible that $212 - 90 \mu\text{m}$ started to be slightly mass transfer limited since its effectiveness factor was 0.91. On the other hand, the biggest particle size used were strongly mass transfer limited ($\eta = 0.58$)

68

Table 3.2 Thiele modulus and effectiveness factor for ZrPO

Particle size μm	k s	Thiele modulus (ϕ)	Effectiveness factor (η)
38-75	$1.42 \cdot 10^{-2}$	0.22	0.98
75-90	$1.13 \cdot 10^{-2}$	0.29	0.97
90-212	$1.19 \cdot 10^{-2}$	0.54	0.91
355-425	$1.55 \cdot 10^{-2}$	1.59	0.58

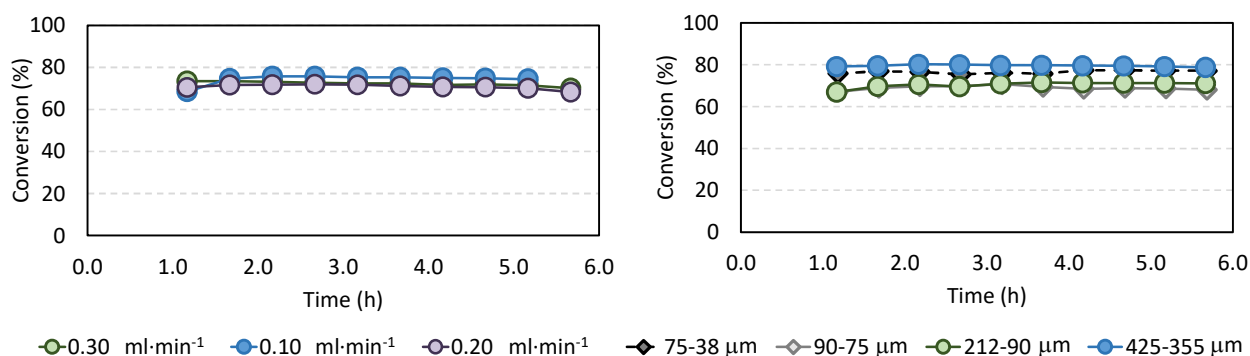


Figure 3.7 ZrPO external (left) and internal (right) diffusion limitation checks

LaPO was not mass transfer limited (Figure 3.8) under the reaction conditions used here (0.2 mL min^{-1} total flow and $212 - 90 \mu\text{m}$ particle size at 150°C). Anyway, the DHA conversion became smaller decreasing the total flow to 0.1 mL min^{-1} and using the biggest particle size ($425 - 355 \mu\text{m}$).

NbPO, as the other two catalyst, is not suffering from internal mass transfer limitation (Figure 3.9 on the right), but it suffered from external limitations as it is visible in the same figure on the left. Specifically, the conversion increases, raising the total flow.

In order to understand the entity of the limited transportation regimes, k_c and k_s were evaluated for LaPO and NbPO, as explained in 3.2.3 section.

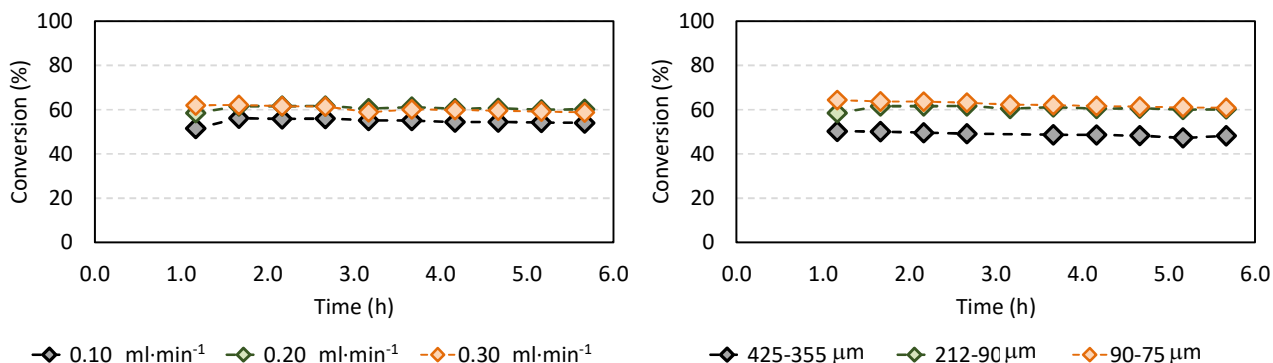


Figure 3.8 LaPO external (left) and internal (right) diffusional limitation checks

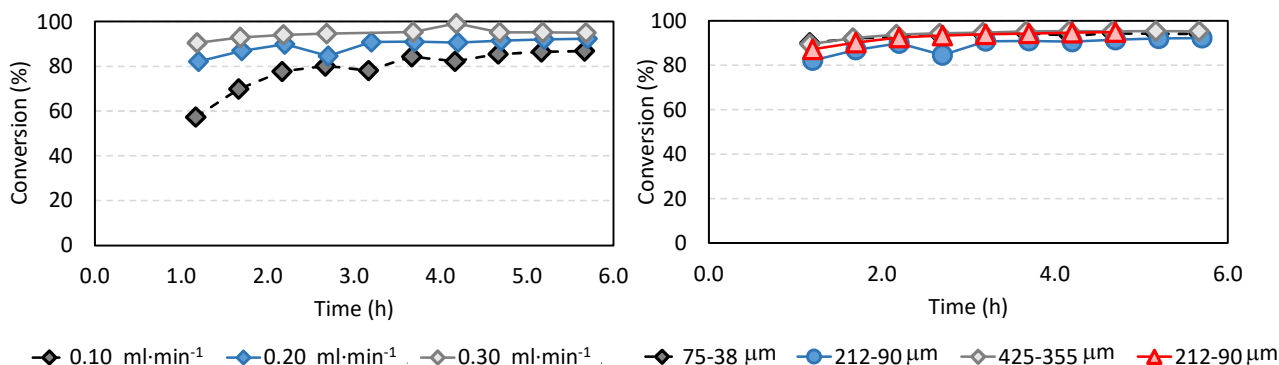


Figure 3.9 NbPO external (left) and internal (right) diffusional limitation checks

The impact of external mass transfer limitations can be evaluated comparing k_c and k_s values. In fact, if the kinetic regime is the dominant phenomenon it means that the contribution of k_c to k_{obs} value is negligible because k_s value is lower than k_c .

Table 3.3 Mass transfer coefficient and kinetic constant evaluated at different flows for LaPO and NbPO. Reaction conditions: 150 °C, 10 bar, 100 - 300 mg catalyst, [DHA] = 0.4 M

v cm min ⁻¹	\dot{V} mL min ⁻¹	NbPO			LaPO		
		k_{obs} s ⁻¹	k_c s ⁻¹	k_s s ⁻¹	k_{obs} s ⁻¹	k_c s ⁻¹	k_s s ⁻¹
0.43	0.1	$1.33 \cdot 10^{-2}$	$1.99 \cdot 10^{-2}$		$1.06 \cdot 10^{-2}$	$2.52 \cdot 10^{-2}$	
0.85	0.2	$1.53 \cdot 10^{-2}$	$2.82 \cdot 10^{-2}$	$3.82 \cdot 10^{-2}$	$1.28 \cdot 10^{-2}$	$3.56 \cdot 10^{-2}$	$1.87 \cdot 10^{-2}$
1.28	0.3	$1.89 \cdot 10^{-2}$	$3.45 \cdot 10^{-2}$		$1.27 \cdot 10^{-2}$	$4.36 \cdot 10^{-2}$	

The values reported in Table 3.3 clearly show that k_c and k_s are comparable, in particular for LaPO at 0.1 mL min⁻¹. Thus, neither external mass transfer nor intrinsic kinetics are completely dominant. Raising the flow rate, the value of k_c increased, and its contribution to k_{obs} diminished. On the contrary, NbPO k_c is lower than k_s at all the used flows meaning that the rate of external mass transfer is the most significant contribution. Anyway, at 0.3 mL min⁻¹, k_s and k_c value are close enough to be considered competitive phenomena. These results illustrate the fact that mass transfer limitations are not neglectable, but the limitation is not dramatic because the order of

magnitude of the constant is the same at every flow rate. Moreover, these results are important because they show that with the reactor set up used it is not possible to work in a strictly microkinetic regime. In fact, the isothermal zone of the oven is 5 cm long, while the NbPO bed height is 3.5 cm using 0.3 mL min⁻¹ flow. Even an increase of the flow to 0.4 mL min⁻¹ would not completely remove the external mass transfer limitation, but it would require a catalyst bed height of 4.5 cm that is too close to the length of the isothermal zone.

Another interesting aspect is that the apparent activation energy for NbPO and LaPO, that are suffering from external limiting diffusion, are 33.9 KJ mol⁻¹ and 59.2 KJ mol⁻¹, respectively. Usually, the activation energy magnitude is around 10 KJ mol⁻¹ in presence of such limitation.¹⁷⁹

These high activation energy values can be justified assuming that probably the adsorption enthalpy is positive for the studied system. In fact, in liquid phase a reactant can be adsorbed only after the displacement of another molecule (solvent, product, reactants) from the catalyst surface.¹⁵⁷ Therefore, the driving force of adsorption in liquid phase is given by several contribution such as: the adsorption enthalpy of the adsorbate onto a surface, the desorption enthalpy of previously adsorbed species, the enthalpy due to interaction among the adsorbed and desorbed species both in solution and on the surface and to the interaction among different sorbed species.¹⁵⁷ Therefore, the activation energy that we calculate is a sum between the actual activation energy (E_a^{true}) and the enthalpic contribution (ΔH) multiplied by the reaction order (n)¹⁸⁰:

$$E_a^{app} = E_a^{true} + \sum n_i \Delta H_i$$

This phenomenon is well known to happen on the zeolites.^{157,180,181} The materials used in this work, if crystalline, show a structure that is similar to the zeolite ones¹⁸² and for this reason assuming that the positive adsorption enthalpy contribution is not negligible for these materials is reasonable.

70

Performance of catalysts in continuous reactions

The temperature effect has been evaluated for all the catalysts at constant contact time and the results are reported in Table 3.4. All the catalytic reactions reached a steady state within 2 h and were not subjected to any measurable deactivation during 6 h, as the conversion trends (black dashed lines) shown in Figure 3.10. All the data reported in Table 3.4 are calculated ignoring the first 1.5 h of reaction since this first three collected samples can be affected by flow or temperature stabilization. For these reasons, all the graph as function of time reported from now on will start at about 2 h.

NbPO and ZrPO were the most active catalysts, showing 38 % and 28 % conversion at 90 °C, respectively, while LaPO was almost inactive until 130 °C. From 90 °C to 130 °C, the PVA yield increased for NbPO and ZrPO, decreasing at 150 °C because of PVA conversion into LA started to be significantly fast. On the contrary, LaPO PVA yield increased over the whole temperature range. The LA yield increase was neglectable for LaPO. On the other hand, ZrPO and NbPO reached 28 % and 36 % LA yield at 150 °C. The GLA yield was below 1.5 % at every temperature for ZrPO and NbPO, while LaPO showed an increasing GLA trend with the temperature. The carbon loss increased with increasing temperature. The solution at 90 °C was transparent, while with increasing the temperature it started to become yellowish to reach at 150 °C an orange-brownish color. This color change was detected even using tin phosphate catalyst, and it was attributed to the formation of polycondensation products including humins.¹²⁷ The pyruvaldehyde and lactic acid yield increased in the following order NbPO > ZrPO > LaPO at each temperature and this trend is

in perfect agreement with the catalyst order obtained for Brønsted and Lewis acid sites, respectively. Ultimately, this is not surprising, since it is well known that Brønsted acid sites are involved in the first dehydration step to produce PVA, while medium strong Lewis acid sites favour PVA Cannizzaro rearrangements into LA.¹⁵⁸ These results further confirm the possibility of dehydrate DHA on Lewis acid sites and that these sites are less efficient than the Brønsted ones.

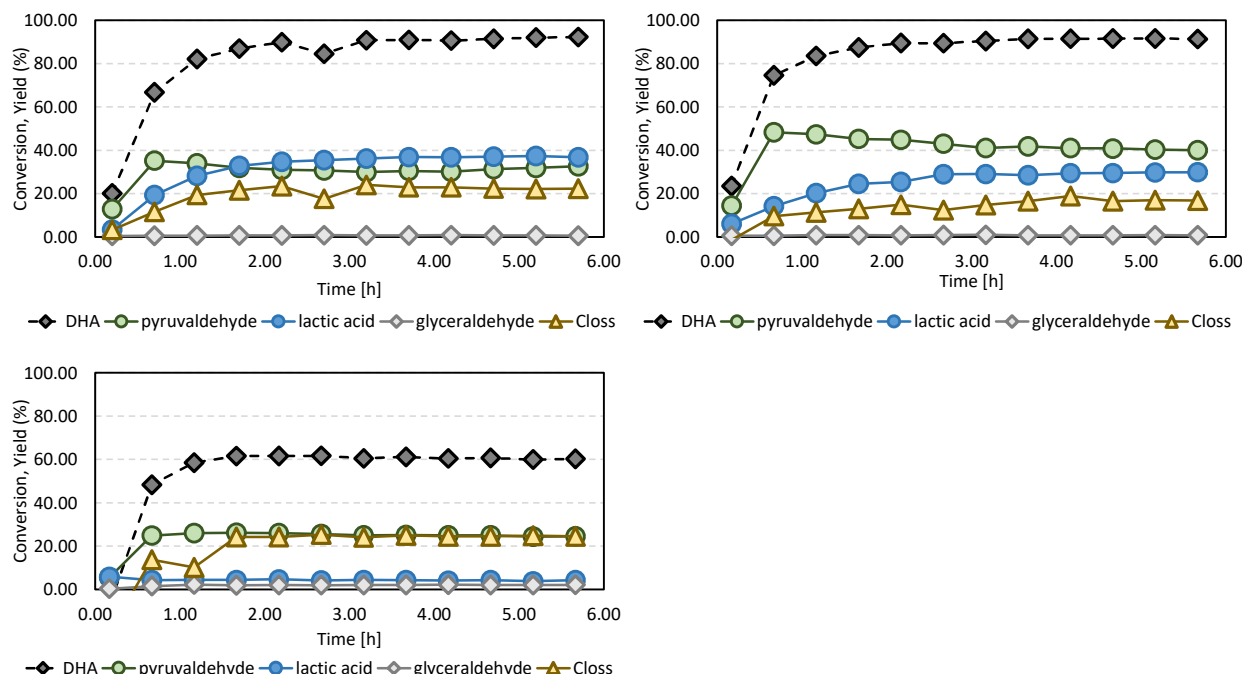


Figure 3.10 Conversion and Yield as time function for NbPO, ZrPO, LaPO. Reaction conditions: $T = 150\text{ }^{\circ}\text{C}$, $p = 10\text{ bar}$, catalyst 200 g, DHA total flow 0.2 mL min^{-1} .

71

Figure 3.11 contains a comparison among the Arrhenius plots used to evaluate the apparent activation energy (E_a) for the three catalysts for DHA conversion into PVA. The apparent E_a values were 33.9 kJ mol^{-1} , 43.6 kJ mol^{-1} and 59.2 kJ mol^{-1} for NbPO, ZrPO and LaPO, respectively. The small limiting mass transfer regime observed in the previous section is confirmed by the slope of NbPO (black line) and ZrPO (green line) Arrhenius plot at low temperatures. On the contrary, LaPO (orange line) slope is closer to a catalyst working in a kinetic regime.¹⁶⁷

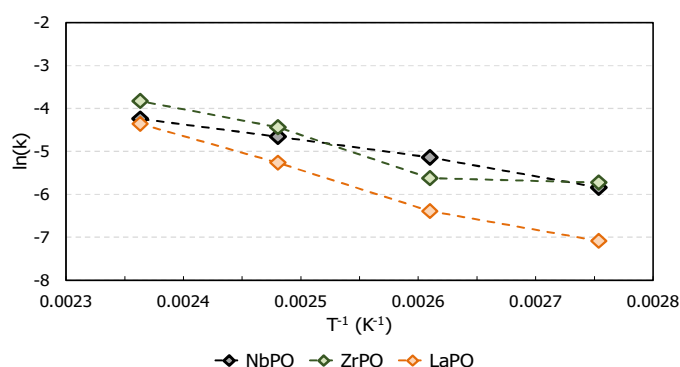


Figure 3.11 Temperature dependence considering Arrhenius plot for LaPO, NbPO and ZrPO.

NbPO was found to be the most active catalyst for lactic acid production. Therefore, its performances were studied with the aim of understanding if it undergo deactivation over a longer time scale. This test is of crucial importance since water is used as solvent. In fact, water is the

greenest and most sustainable solvent but, in general, it can strongly affect the catalyst life-time.¹³⁴

Table 3.4 Catalytic performances of NbPO, ZrPO and LaPO. Reaction parameters: 200mg catalyst, 0.2 mL min⁻¹ DHA flow, [DHA] = 0.4 M, temperature 90÷150 °C, pressure 10 bar, 6h time on stream. DHA = dihydroxyacetone, GLA = glyceraldehyde, PVA = pyruvaldehyde, LA = Lactic Acid, others = pyruvic acid (PA) and glyceric acid (GA), k = rate constant, r_a = dihydroxyacetone conversion rate

Catalyst	Temperature °C	X _{DHA} %	Y _{GLA} %	Y _{PVA} %	Y _{LA} %	Y _{others} %	C _{loss} %	k s ⁻¹	r _a mol l ⁻¹ s ⁻¹
NbPO	90	38.4	0.7	34.5	1.9	1.5	0.0	2.91E-3	7.4E-4
	110	60.6	1.0	51.7	5.0	1.5	1.4	5.86E-3	9.2E-4
	130	77.2	0.9	55.0	13.3	1.8	6.2	9.51E-3	8.7E-4
	150	90.0	0.7	31.1	36.0	3.2	18.9	1.44E-2	5.8E-4
ZrPO	90	28.7	1.0	19.2	2.9	1.6	4.0	3.26E-3	9.3E-4
	110	43.1	1.4	35.4	3.9	1.7	0.6	3.62E-3	8.2E-4
	130	70.4	1.4	52.3	9.9	2.3	4.5	1.19E-2	1.4E-3
	150	89.8	0.8	42.6	27.5	3.7	15.2	2.18E-2	8.9E-4
LaPO	90	5.9	0.4	3.5	1.8	0.1	0.0	8.37E-4	3.2E-4
	110	11.5	1.74	8.0	1.4	0.2	0.2	1.68E-3	5.9E-4
	130	31.43	2.64	16.8	1.8	0.4	9.8	5.18E-3	1.4E-3
	150	60.63	2.10	25.3	4.2	5.0	24.0	1.28E-2	2.0E-3

Catalyst deactivation over time.

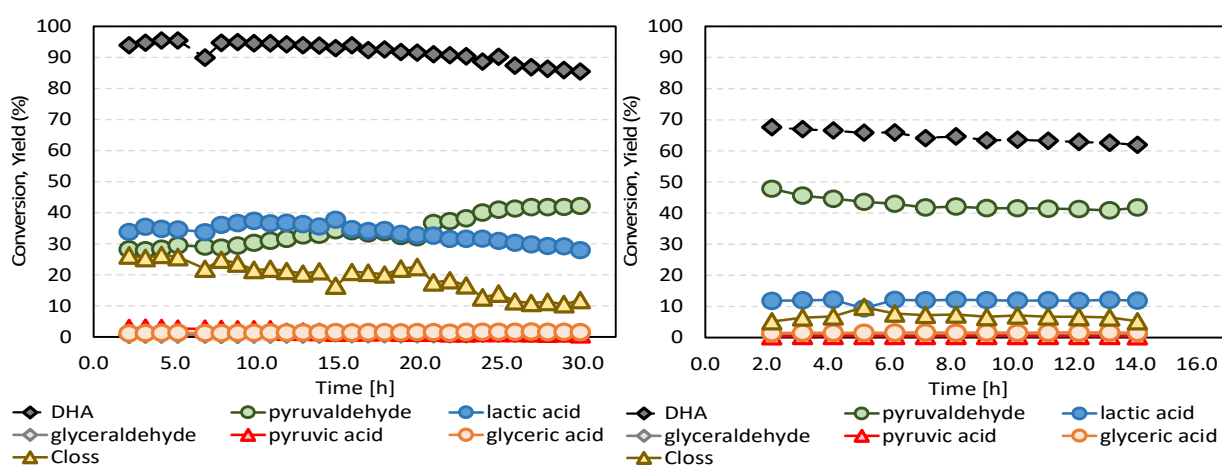


Figure 3.12 NbPO product distribution over time. Reaction conditions: on the left: 150 °C, 200 mg catalyst, 0.2 mL min⁻¹, 425-355 μm particle size, 10 bar; on the right: 130 °C, 200 mg catalyst, 0.2 mL min⁻¹, 90-212 μm, 10 bar.

In Figure 3.12, the conversion (black) slowly decreased over time, indicating that the catalyst is deactivating. The conversion at 150 °C in 15 h shows a 3 % decrease, while in the same time at 130 °C the decrease is of 6 %. The diminution in temperature highlights the deactivation phenomena because high conversions can cover the rate constant decrease. The product yields in the graph at 130 °C, reported in Figure 3.12 on the right, were not affected by the deactivation within 15 h except for pyruvaldehyde whose yield decreased within the first 5 h of 10 %. Afterwards, it was stable around a 40 % yield. On the contrary, the product distribution observed at 150 °C, graph on the left in Figure 3.12, is more interesting. The lactic acid yield was the highest after 15h before it started to decrease. The pyruvaldehyde trend (green line) is opposite with respect to lactic acid. This observation is suggesting a selective slow deactivation of the Lewis acid sites necessary to convert the pyruvaldehyde into lactic acid. C_{loss} trend (yellow line) was

diminishing with the lactic acid yield. This result suggests that probably the C_{loss} is mainly driven by lactic acid polymerization side-products. Probably, the C_{loss} can be enhanced by reducing the initial dihydroxyacetone concentration to have more diluted final lactic acid concentration. However, a reduction in DHA concentration would increase the costs of the process requiring more expensive separation steps.

Contact time effect

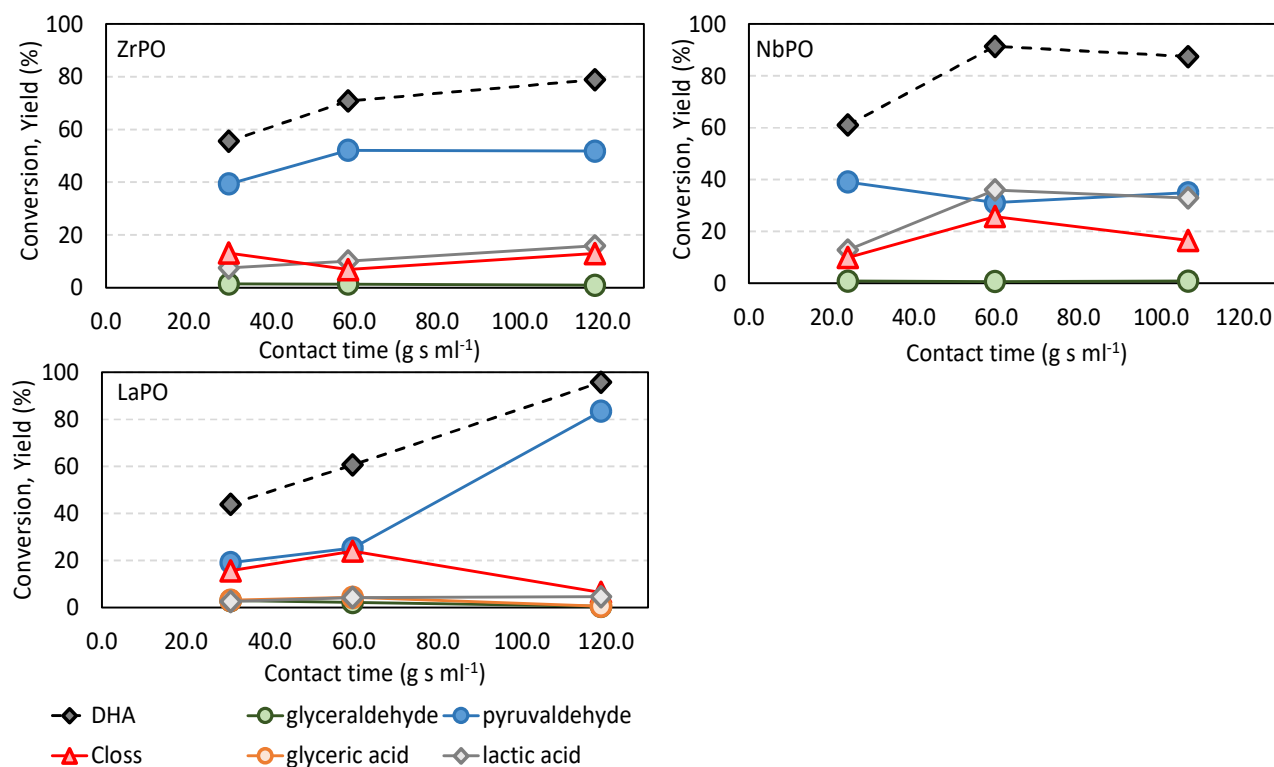


Figure 3.13 Product distribution as function of contact time for ZrPO, LaPO and NbPO. Reaction conditions: 150 °C (LaPO and NbPO) or 130 °C (ZrPO), 10 bar, 0.1-0.3 mL min⁻¹, 100-300 mg catalyst, 90-212 μm.

In Figure 3.13, the product distributions for ZrPO, NbPO and LaPO are reported. The conversion over LaPO increased steeply with increasing contact time. On the other hand, the conversion raised of 20 % and 40 % until 60 g s mL⁻¹ for ZrPO and NbPO, respectively. NbPO conversion reached a plateau while ZrPO one increased of another 8 %. The product distributions varied accordingly with the conversion. In fact, for ZrPO pyruvaldehyde, lactic acid and C_{loss} yields increased with raising the contact time. The product trends are more interesting for LaPO since at long contact time it reached complete conversion and 80 % pyruvaldehyde yield. Contemporary the lactic acid yield slightly increased (from 3 % to 5 %) while the C_{loss} dropped to 5 %. It is not possible to exclude that a further increase of contact time might favour lactic acid yield over the pyruvaldehyde one. Anyway, lactic acid showed a yield that is comparable to the glycer aldehyde and glyceric acid ones at low contact time. Those two last compound yields dropped from ~5 % to ~0.5 %. Since the highest contact time point was reached decreasing the speed of the liquid to 0.1 mL min⁻¹, NbPO was strongly mass transfer limited explaining why the conversion is slightly decreasing.

3.4 Conclusions

NbPO, ZrPO and LaPO were synthesized, characterized and tested in dihydroxyacetone upgrading into lactic acid. All the catalysts showed both Brønsted and Lewis acidic sites, which are

fundamental for the reaction in object. LaPO possesses only one kind of P site, while NbPO and ZrPO have 2 and 4 not-equivalent P in their structures as pointed out by ^{31}P -NMR. This difference in number of P species can be correlated to the differences in Brønsted strength, which are mainly due to the presence of terminal P-OH. In fact, LaPO which possesses only P in Q^2 topology showed a Brønsted acidity which is not affected by the temperature as NbPO which presented mainly P in Q^4 and Q^2 topology. The small decrement in Brønsted acidity strength detected for NbPO might be attributed to the possible presence of some terminal Nb-OH. On the contrary, ZrPO showed a sensible decrease in Brønsted acidity with raising the temperature which can be attributed to presence of HPO_4 in Q^3 and Q^2 topology. Furthermore, the strength and the amount of Lewis acid sites was found in good agreement with the M^{n+} electronegativity. The higher the electronegativity the stronger the Lewis acid site.

NbPO was the most active catalyst reaching a 36 % lactic acid yield at 90 % DHA conversion at 150 °C. ZrPO showed slightly worse yield (28 %), while LaPO required long contact time even to be active towards DHA dehydration to pyruvaldehyde. Thus, the stronger acidic sites in NbPO can be correlated to the highest activity towards lactic acid.

The transport limitations over these catalysts were studied in detail. NbPO and LaPO suffered from external mass transfer limitations. LaPO was not mass transfer limited under the experimental conditions reported in this work. Instead, ZrPO showed an almost negligible internal mass transfer limitation in the operative conditions ($\eta = 0.91$) which became dramatic increasing the particle size. On the contrary, NbPO was slightly externally limited even if its apparent activation energy suggests that it was working within the kinetic regime. This discrepancy between the adsorption energy value and the experimental results was related to a possible positive adsorption enthalpy.

NbPO performance were tested over 30 h of reaction at 150 °C and a slow deactivation over the time was observed. Furthermore, after 15 h of reaction an inversion in PVA and LA trend was observed. This inversion was ascribed to a deactivation of the active site (Lewis acid site) necessary to produce LA. The deactivation resulted to be significant at 130 °C. In fact, the conversion decreased by 10 % in 15 h.

Overall conclusions

In the present work two important reactions, such as ethanol upgrading into 1-butanol and dihydroxyacetone conversion into lactic acid, were studied.

The first part of the work dealt with ethanol upgrading into 1-butanol, known as Guerbet reaction. In the literature, it is reported that the reaction occurs in presence of acid-base sites along with dehydrogenation/hydrogenation ones. However, the most selective catalysts (Sr and Ca hydroxyapatite) ever reported do not possess dehydrogenating sites. Indeed, the active sites required for this reaction are still under debate. Therefore, the work was aimed to gain a deeper understanding on the role of acid-base active sites.

Firstly, the basicity role was investigated evaluating MgO, CaO and SrO performances in the Guerbet reaction. The optimal temperature to carry out the reaction raised along with the basicity, which increased with M^{2+} ionic radius. The three catalysts showed a diverse product distribution. In detail, MgO produced the highest amount of 1-butanol, CaO showed a maximum in ethylene while the principal product for SrO was acetaldehyde. Ethanol interaction with the catalyst surfaces was evaluated by DRIFTS. MgO is not selective to a specific ethanol adsorption mode, in fact ethanol was detected as carbanion, ethoxy and undissociated ethanol. CaO selectively adsorbed ethanol only as ethoxide. Finally, SrO adsorbed ethanol as acetaldehyde, which was the only intermediate detected on its surface. The results herein reported suggest that the dehydrogenation efficiency increased with the basicity. Therefore, it was possible to hypothesize that Mg^{2+} ion are weak acid sites able to enhance the carbanion lifetime on the catalyst surface. Indeed, the direct condensation is the most favorable surface pathway to produce 1-butanol on MgO. On the contrary, Ca^{2+} ions are not able to efficiently interact with the carbanion that, being a highly unstable specie, undergo dehydration. In fact, ethylene formation is favored with CaO. The carbanion formation is less favorable with SrO as suggested by the low 1-butanol and ethylene yields suggesting the predominance of aldol condensation mechanism. Therefore, it is reasonable to conclude that a mild basicity is necessary to efficiently carry out the Guerbet reaction.

To study the acidity role, MgO, which possessed the "optimal" basicity, was doped with H_3PO_4 to synthesize a Mg based hydroxyapatite-like catalyst. In fact, to our knowledge, Mg-hydroxyapatite has never been synthesized or tested in the Guerbet reaction. The presence of PO_4^{3-} moieties on MgO strongly affected its performance in the reaction under investigation. In fact, 1-butanol selectivity was doubled even with small H_3PO_4 addition (0.5 wt. %). The PO_4^{3-} concentration effect, on MgO catalytic performance, was studied from 0.5 to 5 wt.%. The best performance were obtained with 5 wt.%. In fact, it showed the lowest carbon loss along with the smallest yield of unidentified products. Moreover, 5 wt.% H_3PO_4 /MgO yielded to 15 % of 1-butanol at 350 °C and 2 g s mL⁻¹. MgO and 5 wt.% H_3PO_4 /MgO performances in the Guerbet reaction were investigated with an *in operando* DRIFTS study at 350 °C. The study highlighted that MgO undergo carbonation while 5 wt.% H_3PO_4 /MgO do not within 190 min. Crotonaldehyde specific bands were detected on 5 wt. % H_3PO_4 /MgO after 20 min while it was necessary to wait 180 min to detect some crotonaldehyde or crotyl alcohol spectral features on MgO. These observations suggest that PO_4^{3-} presence inhibits catalyst carbonation or coke formation enhancing the production of intermediate species.

Finally, 5 wt.% H_3PO_4 /MgO performance were compared with Ca and Sr hydroxyapatite ones. The selectivity to 1-butanol can be ranged as SrHAP (51 %) > 5 wt. % H_3PO_4 /MgO (28 %) > CaHAP (24 %). Furthermore, the catalyst performance were compared with respect to the time of reaction (18 h). To our knowledge, it is the first time that hydroxyapatite lifetime is evaluated in the Guerbet reaction. Hydroxyapatite samples showed a rapid deactivation within the first 3 h. In

Overall conclusions

contrast, 5 wt. % $\text{H}_3\text{PO}_4/\text{MgO}$ showed only a small decrement in 1-butanol (2 %) in 18h. Hydroxyapatite systems rapid deactivation was related to the presence of mainly medium strength basic sites which promoted consecutive condensation reactions, producing coke on the catalyst surface. Moreover, CaHAP reactivity was strongly affected even by the presence of strong acid sites which promoted a 50 % of coke at 450 °C.

Therefore, it was proven that the selectivity to 1-butanol is driven by the strength of the acid and basic sites and not only by their ratio. Weak acid and basic sites are required to be selective to 1-butanol avoiding a rapid coke formation.

Metal (Zr, Nb, La) phosphate performances in continuous liquid phase conversion of dihydroxyacetone into lactic acid was the topic of the second part of this work. In the literature there is a lack of continuous liquid feed studies, even if their scale up is simpler and economical advantageous with respect to a batch set-up. Furthermore, an acidic catalytic system able to work in aqueous environment without severe damages still need to be disclosed. Addressing to this problem would improve biodiesel production profitability, offering a continuous process to upgrade the glycerol coproduced. NbPO, LaPO and ZrPO were studied in continuous feed upgrading of dihydroxyacetone since they are reported among the water-tolerant acid catalysts.

In fact, all of them possessed both Lewis and Brønsted acid sites whose strength varied accordingly to the metal electronegativity. The mass transfer limitations were thoroughly investigated. Indeed, NbPO was found to be slightly externally limited in the operative conditions. On the contrary, ZrPO, whose mesopore distribution was shifted towards micropores, showed a negligible internal mass transfer limitation (efficiency factor = 0.91). LaPO, which possessed a mesopore distribution shifted towards the macropores, was not mass transfer limited. All the catalysts showed apparent activation energies characteristic of a kinetic regime. This effect was related to the possible positive adsorption enthalpy due to the multiple interactions which a molecule undergoes during the adsorption and desorption phenomena in liquid phase. Despite the limiting regime, NbPO yielded to 36 % lactic acid while ZrPO showed a 28 % lactic acid yield. LaPO was the least active catalyst, requiring high contact time even to be active towards pyruvaldehyde. NbPO higher acid sites amount and their superior strength were related to its catalytic performance. NbPO activity was studied with respect to reaction time. The test, carried out at 150 °C, highlighted a slow deactivation over the time. Furthermore, after 15 h of reaction pyruvaldehyde yield increased at the expense of lactic acid one. This behaviour change was ascribed to a deactivation of the active site (Lewis acid site) necessary to produce lactic acid. A kinetic modelling is required to understand which active site undergoes deactivation.

Appendix A. Ethanol steam reforming

This work was done in a collaboration with C. Pizzolitto in M. Signoretto's research group at Università di Venezia - Ca' Foscari. This section is referred to a paper that was accepted by *ACS Sustainable Chemistry & Engineering* while another paper is in preparation.¹⁸³

The aim of this work was to understand the diverse ethanol adsorption on Ni-ZrO₂ (Ni-Zr), Ni-CeO₂ (Ni-Ce) and La₂O₃ doped Ni-ZrO₂ (Ni-Lac-Zr) and Ni-CeO₂ (Ni-Lac-Ce). In the case of CeO₂ the main aim was to understand if NiO is reduced because of ethanol or because of the H₂ produced. As far as ZrO₂ support is concerned, the principal aim was to understand the difference in the ethanol adsorption and modification on the catalyst surface to discriminate the intermediates that promote a different coke formation. The fresh and spent catalyst characterization and the reactivity data are reported in Cristina Pizzolitto master thesis and the published paper.^{183,184}

A.1 Methods

A Bruker Vertex 70 equipped with a Pike Diffuse IR cell attachment and an MCT detector was used to perform infrared analysis. The spectra were recorded after 128 scans and 4 cm⁻¹ resolution. The IR apparatus was in line with a mass spectrometer, EcoSys-P from European Spectrometry Systems.

During a standard measurement, the sample was pretreated at 500 °C in He flow (8 mL/min) for 60 min, to remove any molecule adsorbed on the material. Then, IR backgrounds were collected every 50 °C from 500 °C to 50 °C and, then, at room temperature (RT). Afterwards, ethanol was fed at 0.6 μL min⁻¹, and, as the ethanol mass signal started to raise, the RT spectrum was recorded. Sample temperature was then increased by 5 °C min⁻¹ and spectra were collected every 50 °C. Once the temperature of 500 °C was reached the sample behavior in presence of ethanol stream was evaluated for 60 min recording a spectrum every 2.5 min. During the overall IR analyses several mass signals (m/z) were monitored continuously: 2, 4, 16, 18, 26, 27, 28, 29, 30, 31, 39, 41, 42, 43, 44, 45, 53, 54, 55, 56, 57, 58, 59, 69, 70, 71, 72, 74.

These test for ZrO₂ based catalyst were carried out also feeding EtOH/H₂O mixture with a mass ratio 1:5.

A.2 ZrO₂ based catalysts

DRIFTS-MS feeding Ethanol on Ni-Zr

In Figure A.1, the spectra recorded at different temperatures, feeding ethanol on Ni-Zr catalyst are reported. At room temperature, absorption bands due to the presence of H-bonded ethanol, ethoxy species and η²-acetaldehyde were shown.

The bands at 1067 cm⁻¹ and 1109 cm⁻¹ were attributed to the C-C-O bond asymmetric stretching (ν_{as}) of bidentate and monodentate ethoxide, respectively.⁸⁸ The peaks at 1395 cm⁻¹ and 1451 cm⁻¹ were related to the symmetric and asymmetric vibration deformation of CH₃ group (δ_{CH3}), respectively. The transition visible at 1479 cm⁻¹ was due to the deformation of CH₂. At higher wavenumber, it was possible to observe the C-H symmetric and asymmetric stretching (ν_{as}(CH₃) 2974 cm⁻¹, ν_{as}(CH₂) 2932 cm⁻¹, ν_s(CH₂) was seen as shoulder 2898 cm⁻¹ and ν_s(CH₃) 2873 cm⁻¹).⁹¹ The broad and low intensity peak from 3060 cm⁻¹ and 3461 cm⁻¹ was attributed to the presence of H-bonded undissociated ethanol.⁸²

The presence of η²-acetaldehyde was revealed by the bands at 1157 cm⁻¹ (ν_{C-C}), 1273 cm⁻¹ (ν_{C-O}) e 2714 cm⁻¹ (ν_{C-H}).^{82,89} As far as the 1273 cm⁻¹ peak is concerned, it was not possible to exclude the contribution of the δ(OH) vibrational mode of undissociated adsorbed ethanol.⁸² Hence, the assignation of this band might be doubtful. However, considering that it was still present when the

H-bonded ethanol vanished around 200 °C, it is likely to assign it to η^2 -acetaldehyde even though some H-bonded ethanol adsorptions contribution might be present under such temperature. η^1 -acetaldehyde bands were not observed in these spectra suggesting that acetaldehyde is preferentially interacting with this catalytic system with two atoms, as shown in Table 2.1.

The negative bands found in the spectra were related to the superficial OH interaction with the adsorbed molecules. In fact, two negative adsorptions at 3740 cm^{-1} e 3688 cm^{-1} were due to the terminal and tribridged (OH bonded to three Zr atoms) OH stretching, respectively.¹⁸⁵ At the same time, the negative band at 1600 cm^{-1} was attributed to $\delta(\text{OH})$ of crystallization water.

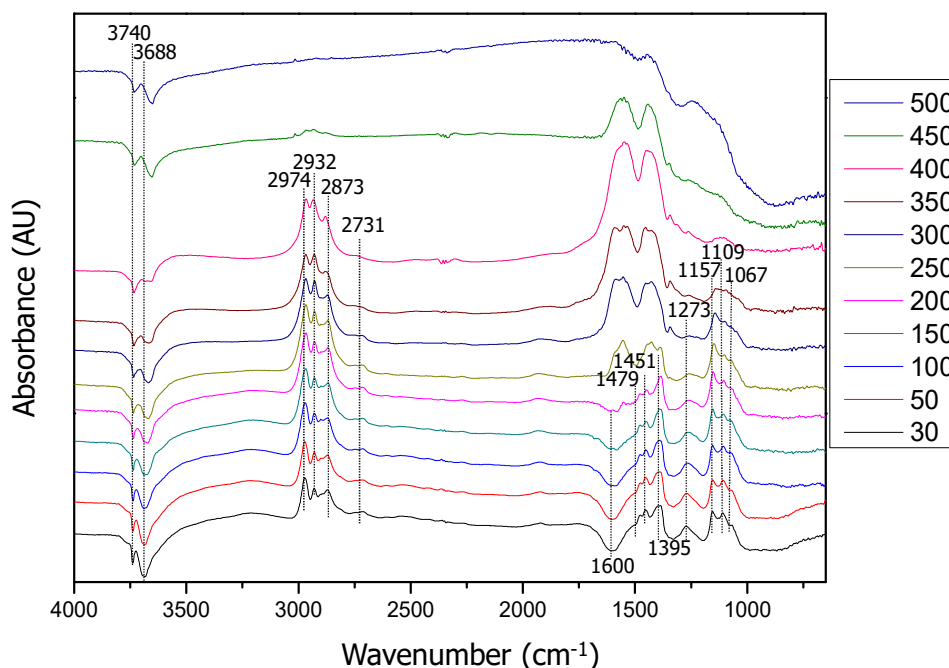


Figure A.1 DRIFTS feeding ethanol of Ni-Zr.

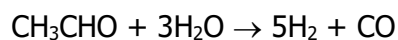
The ethanol, ethoxy and acetaldehyde band intensities decreased with increasing the temperature. However, thanks to the continuous ethanol stream, it was possible to observe the presence of these species on the catalyst surface up to 200 °C for undissociated ethanol, 400 °C for ethoxy and 350 °C for η^2 -acetaldehyde.

New bands at 1554, 1426 started to be detectable and were related to acetate $\nu_{\text{as}}(\text{COO})$ and $\nu_{\text{s}}(\text{COO})$ at 200 °C. These bands were present up to 450 °C. In fact, acetate presence even at high temperature was further supported by the band at 1350 cm^{-1} related to acetate $\delta(\text{CH}_3)$. It was possible to hypothesize the coexistence of acetate and carbonate on the catalyst surface from 350 °C, since these transitions broadened raising the temperature.⁹¹ However, in this wavenumber area it is possible to detect $\nu(\text{C}=\text{C})$ bond due to coke formation.¹¹⁸

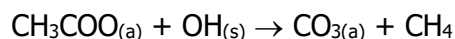
It is possible to note that at 450 °C the continuum line of the spectrum under 1300 cm^{-1} underwent a change which became dramatic at 500 °C. This change in the continuum was attributed to a change in oxidation state which can be attributed to the reduction of NiO to Ni^0 .^{186,187} In fact, the bare catalyst spectrum, recorded when NiO was not reduced, was subtracted to the spectrum recorded under the operative conditions.

The ethanol signal followed by MS increased till 100 °C, as reported in Figure A.2. At 250 °C the catalyst started to be active in converting ethanol as evidenced by the decreasing slope. All the signals under 250 °C were strongly influence by ethanol trend. Therefore, it was not possible to detect any significant information. However, from 250 °C acetaldehyde and ethylene intensities increased along with H_2 and H_2O , suggesting that ethylene and acetaldehyde were produced by ethanol dehydration and oxidative dehydrogenation, respectively. Since the slope of H_2O trend was slightly higher than the H_2 one, it might be hypothesized that more ethylene than

acetaldehyde was released. This hypothesis is reasonable since acetaldehyde was strongly adsorbed on this catalyst till 350 °C as shown by the DRIFTS experiment. CO and CO₂ intensities started to increase at 350 °C. Their production was attributed to acetaldehyde decomposition in presence of water:



Acetaldehyde decomposition reactions were supported by η^2 -acetaldehyde band intensity decrease in the DRIFTS spectra. At 350 °C, CH₄ might be formed by decomposition of acetates to carbonates on the catalyst surface:



Where (s) indicate a catalyst moiety while (a) a specie adsorbed on the catalyst surface.

At 400 °C ethylene and acetaldehyde reached their maximum in intensity while CO, CH₄, CO₂ and H₂ intensity slopes became steeper. This increment might be due not only to the decomposition reaction or the side reaction of ethylene, acetaldehyde and ethanol but to all the reaction that might be involved in the Ethanol Steam Reforming (ESR) process, such as methanation, WGS and Boudouard, combined with the following surface reactions:

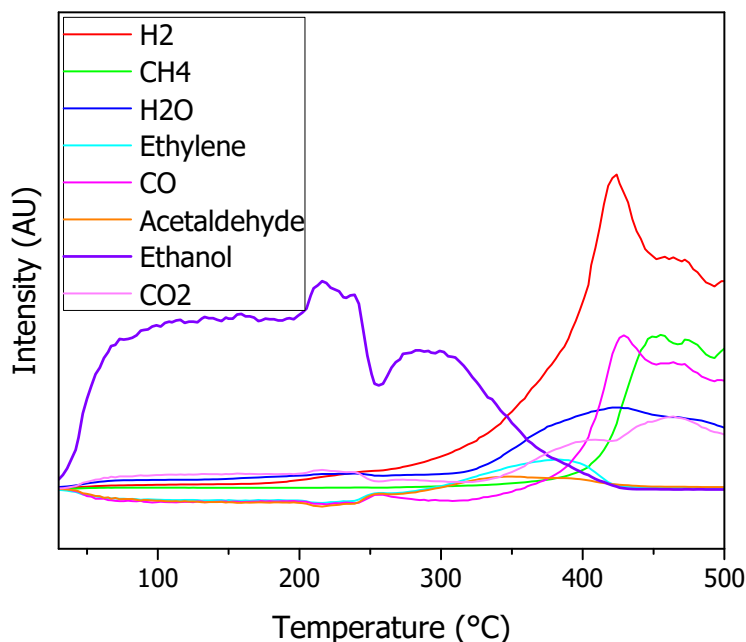
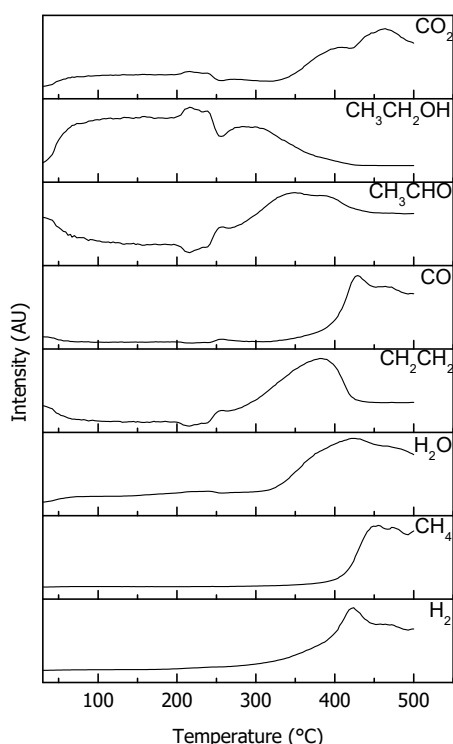
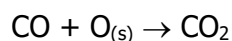
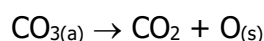
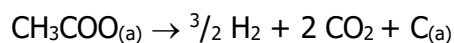
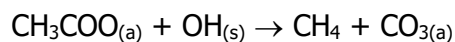


Figure A.2 Mass Ni-ZrO₂ feeding EtOH.

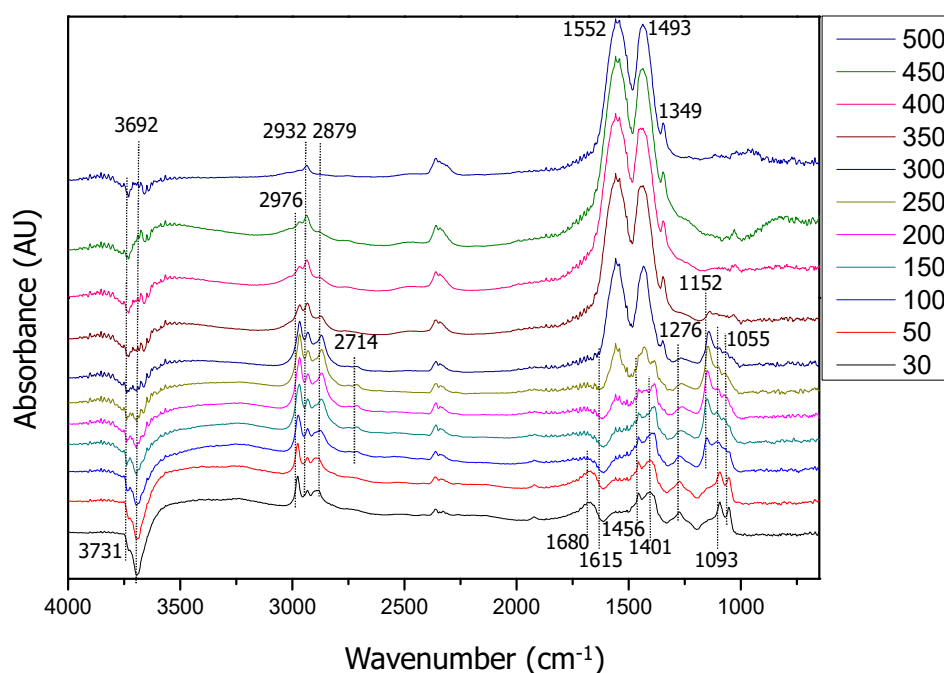


Figure A.3 DRIFTS Ni-Zr feeding ethanol/H₂O continuously as a function of temperature.

In Figure A.3 are reported the Ni-Zr DRIFTS obtained by co-feeding continuously a mixture of ethanol/H₂O. The presence of water vapor in the atmosphere decreased the Signal to Noise Ratio (SNR) of the spectra but these did not show significant differences with the ones reported in Figure A.1.

80

From room temperature to 100 °C it was possible to detect on the catalyst surface only three species: ethoxy, H₂O and undissociated ethanol.

Ethoxy presence was related to the presence of the following bands: 2976 cm⁻¹ ($\nu_{as}(\text{CH}_3)$), 2932 cm⁻¹ ($\nu_{as}(\text{CH}_2)$), shoulder at 2898 cm⁻¹ ($\nu_s(\text{CH}_2)$), 2879 cm⁻¹ ($\nu_s(\text{CH}_3)$), 1456 cm⁻¹ ($\delta_{as}(\text{CH}_3)$), 1401 cm⁻¹ ($\delta_s(\text{CH}_3)$), 1093 cm⁻¹ ($\nu_{as}(\text{C-O})_{\text{monodent}}$), 1055 cm⁻¹ ($\nu_{as}(\text{C-O})_{\text{bident}}$).

The presence of adsorbed water was proven by the broad and quite intense band centered at 1680 cm⁻¹ assignable to the $\delta(\text{OH})$ of H₂O.

Undissociated ethanol was ascribed to the band at 1276 cm⁻¹ $\delta(\text{OH})$ and the broad adsorption between 3089-2585 cm⁻¹ $\nu(\text{OH})$.

At 100 °C, the adsorbed water vanished while a band appeared at 1152 cm⁻¹ as well as a band at 2714 cm⁻¹, these were related to the presence of adsorbed η^2 -acetaldehyde and corresponds to $\nu(\text{C-C})$ and $\nu(\text{C-H})$ respectively.

The band evolution shown at increasing temperature was coherent with the observation done in the experiments with ethanol. For this reason, the evolution of the bands will not be described in this section. It is worth noting a difference, in this case it was possible to detect the bands between 2250 cm⁻¹ and 2500 cm⁻¹ due to gas phase CO₂.⁸⁰

The most important difference to note is that in this case no continuum change was detected. Therefore, it is reasonable to hypothesize that water might compete with ethanol to interact with the active sites. NiO was not reduced neither after 60 min of contact with ethanol, as shown in Figure A.4. In fact, it was possible to appreciate a marginal diminution of the base-line after 2.5 min but no dramatic drop was observed.

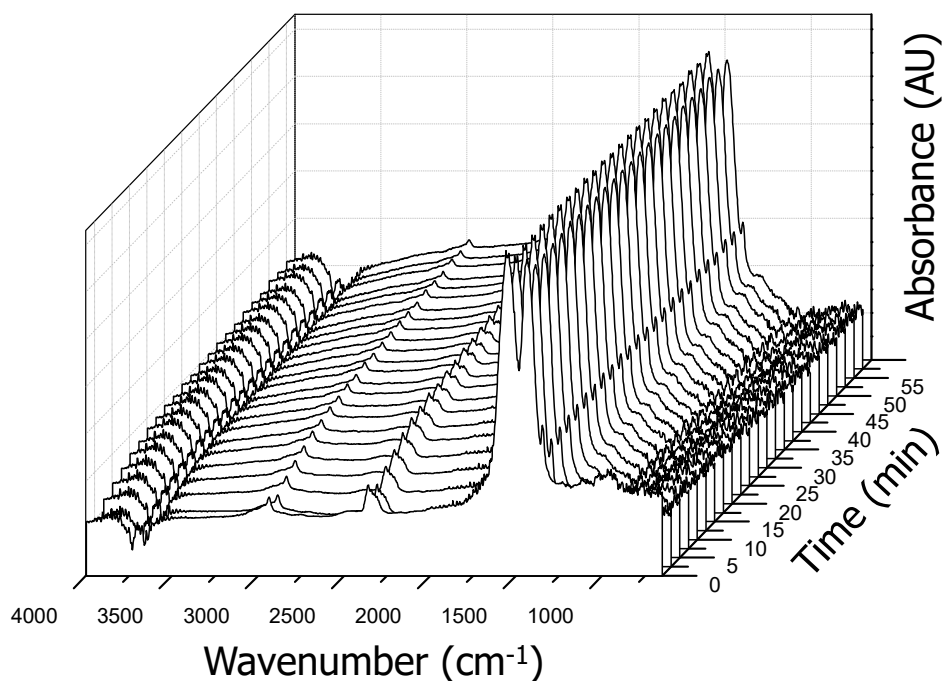


Figure A.4 DRIFTS at 500 °C feeding ethanol/H₂O on Ni-Zr catalyst.

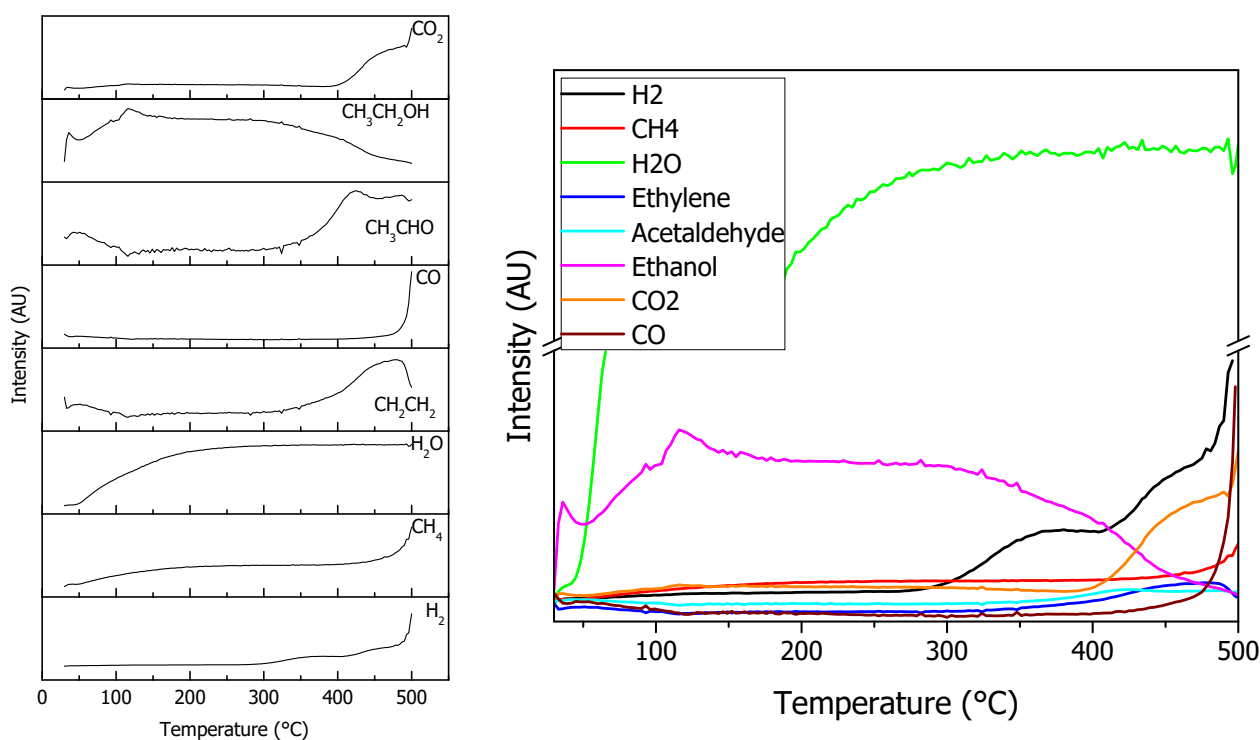


Figure A.5 MS feeding EtOH/H₂O for Ni-Zr.

The mass results, in Figure A.5, as the DRIFTS one, are comparable with those reported in the previous paragraph in Figure A.4. The main difference is that all the phenomena observed were shifted of ~ 50 °C. In fact, EtOH intensity started to decrease after 300 °C. Ethylene and acetaldehyde m/z signal increased after 350 °C. The m/z trend of CO₂ and CH₄ differ from the ones obtained feeding only ethanol, their signal steeply increased at 400 °C. H₂ signal started to increase at 300 °C to steeply raise after 450 °C. The small amount of H₂ released before 450 °C might be due to the oxidative dehydrogenation of ethanol. From 300 °C to 450 °C, oxidative dehydrogenation and dehydration might start to be relevant as well as both acetaldehyde and

ethanol decomposition. In this range of temperatures CH_4 might be formed partially also by surface acetates decomposition. At 450 °C, CO slope increased as CO_2 and CH_4 also did. This increment might be due not only to the decomposition reaction or the side reaction of ethylene, acetaldehyde and ethanol but to all the reaction that might be involved in the ESR process like methanation, WGS, and Boudouard, combined with the surface reactions.

DRIFTS-MS feeding Ethanol on Ni-Lac-Zr

The spectrum at room temperature for Ni-Lac-Zr (Figure A.6) did not diverge from the one reported in the case of Ni-Zr, so the bands at 1068 cm^{-1} , 1102 cm^{-1} , 1389 cm^{-1} , 1451 cm^{-1} , 1479 cm^{-1} , 2881 cm^{-1} , 2930 cm^{-1} and 2974 cm^{-1} were related to ethoxy species.^{91,188,189} η^2 -acetaldehyde presence was demonstrated by the bands at 1150 cm^{-1} , 1255 cm^{-1} and 2718 cm^{-1} .⁹¹ The negative bands were due to the stretching and the bending modes of the OH surface group, as already explained in the previous paragraphs. Ethoxy and acetaldehyde band intensity decreased increasing the temperature. Even though at 50 °C, the intensity of the ethoxy bands increased because of gas phase contribution. In fact, the mass reported a maximum of ethanol and as consequence a minimum of ethylene and acetaldehyde at 50 °C (Figure A.7). This overfeeding was due to a fluctuation of the pump used. In this case, η^2 -acetaldehyde $\nu(\text{C-C})$ was lower in intensity with respect to $\nu(\text{CCO})$ of ethoxy species, this suggests that Ni-Lac-Zr was less oxidizing than Ni-Zr at this temperature. At higher temperature, this difference was not visible and the ethoxy bands were stable on the catalyst surface till 400 °C. Acetaldehyde was also visible on the catalyst till the same temperature.

The bands related to acetates appeared at 250 °C: 1567 $\nu_{\text{as}}(\text{OCO})$, 1452 $\nu_{\text{s}}(\text{OCO})$, 1386 $\delta(\text{CH}_3)$.¹⁹⁰ Also on this catalyst, the broad shape of COO stretchings suggested that carbonates can be present along with acetates. At 450 °C, the drop down of the spectrum at low wavenumber suggested a change in the catalyst background that might be due to the reduction of NiO. This hypothesis was then confirmed by the total change of the spectrum at 500 °C.

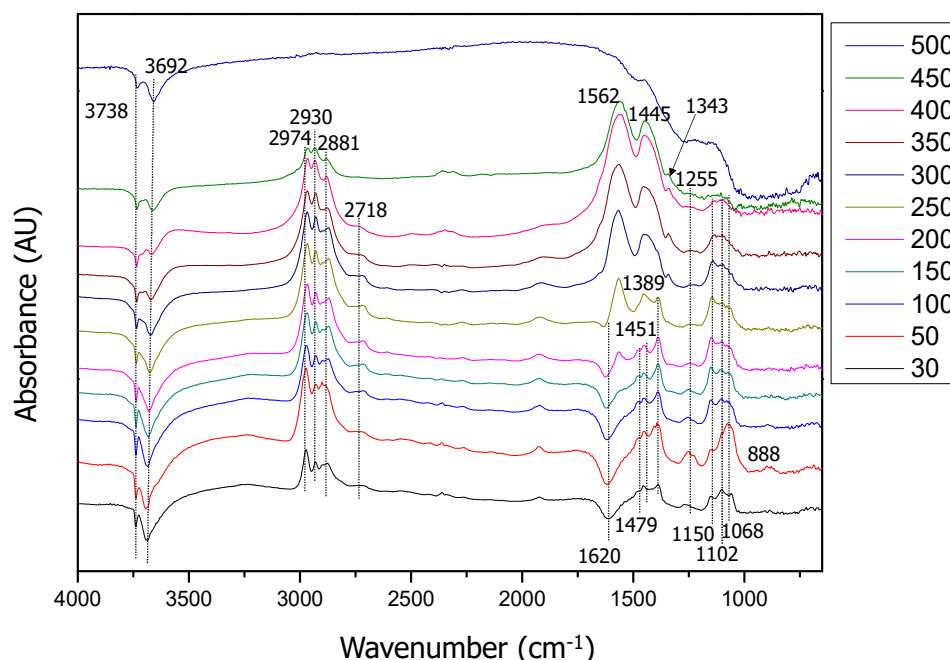


Figure A.6 DRIFTS feeding ethanol on Ni-Lac-Zr.

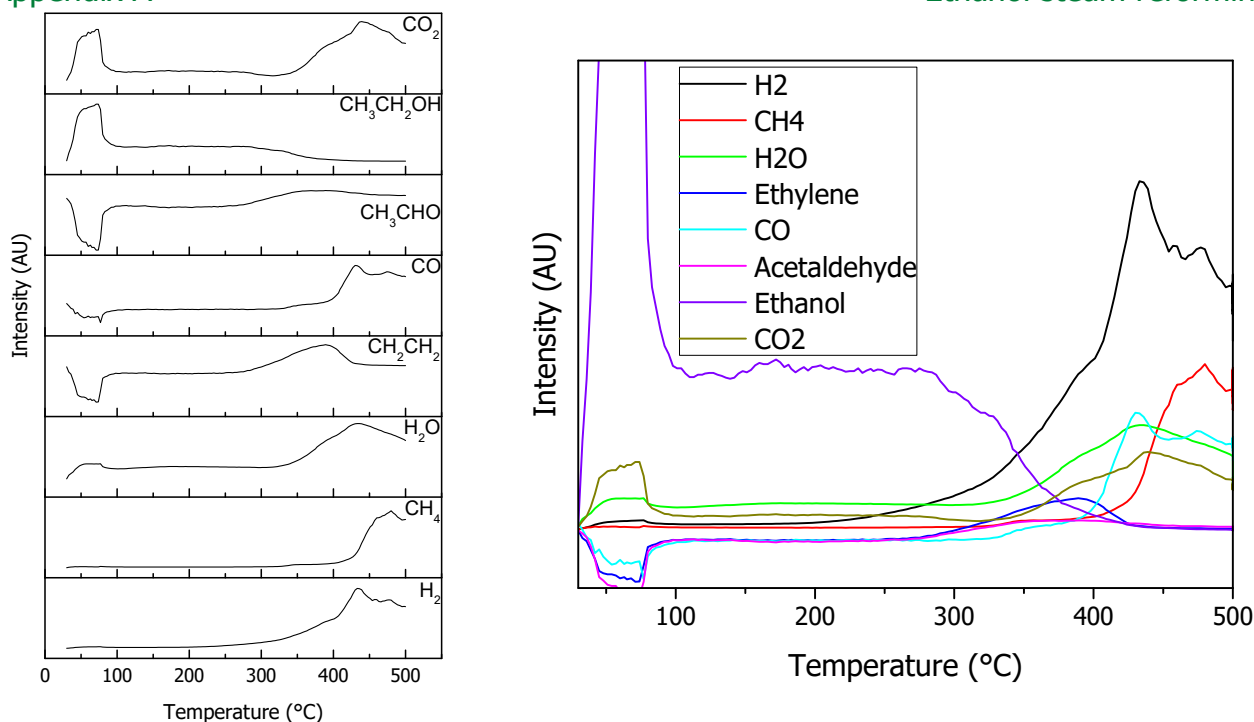


Figure A.7 MS feeding EtOH for Ni-Lac-Zr.

The mass signal, reported in Figure A.7, before 100 °C are not considered because the intensity was saturated by ethanol, as previously explained. Ethanol trend started to decrease slowly after 250 °C and its consumption steeply increased after 300 °C. Ethylene and acetaldehyde started to be produced from 250 °C as indicated by their MS trends. However, it is reasonable to hypothesize that at the beginning acetaldehyde was the favored product since water trend started to raise only at 300 °C while H₂ at 250 °C. From 300 to 400 °C, CH₄ and CO might be formed by surface acetaldehyde or acetates decomposition while CO₂ and H₂ might be produced by ethanol decomposition or surface acetates decomposition. After 400 °C, ethylene intensity started to decrease to vanish at 450 °C. From 400 °C, CO slope increased steep as H₂, CH₄ and CO₂ ones. This increment might be due not only to the decomposition reaction or the side reaction of ethylene, acetaldehyde and ethanol but to all the reactions that might be involved in the ESR process like methanation, WGS and Boudouard combined with the surface reactions.

83

DRIFTS-MS feeding Ethanol/water mixture on Ni-Lac-Zr

Ni-Lac-Zr performance was tested also in presence of H₂O, reported in Figure A.8, and the main effect of water was spectra SNR decrement. Since the obtained spectra are not so different from all the other previously discussed, ethanol adsorption and its evolution with the temperature will be briefly discussed.

At RT and 50 °C the surface presented the bands relative to:

- adsorbed ethoxyde ($\nu_{\text{as}}(\text{CCO})_{\text{bident}}$ 1060 cm⁻¹, $\nu_{\text{as}}(\text{CCO})_{\text{monodent}}$ 1100 cm⁻¹, $\delta_{\text{s}}(\text{CH}_3)$ 1387 cm⁻¹, $\delta_{\text{as}}(\text{CH}_3)$ 1451 cm⁻¹, $\delta(\text{CH}_2)$ 1483 cm⁻¹, $\nu_{\text{as}}(\text{CH}_3)$ 2878 cm⁻¹, $\nu_{\text{as}}(\text{CH}_3)$ 2922 cm⁻¹, $\nu_{\text{s}}(\text{CH}_2)$ 2932 cm⁻¹ (shoulder), $\nu_{\text{s}}(\text{CH}_3)$ 2973 cm⁻¹);
- η^2 -acetaldehyde ($\nu(\text{CC})$ 1150 cm⁻¹, $\nu(\text{CO})$ 1265 cm⁻¹, $\nu(\text{CH})$ 2718 cm⁻¹);
- undissociated H-bonded ethanol ($\delta(\text{OH})$ 1265 cm⁻¹ and $\nu(\text{OH})$ 3053 cm⁻¹ – 3545 cm⁻¹).

The negative band at 1590 cm⁻¹ was ascribed to $\delta(\text{OH})$ of water present on the catalyst while the bands at 3736 cm⁻¹ and 3679 cm⁻¹ were due to the terminal and tribridged OH stretching, respectively. $\nu(\text{CC})$ η^2 -acetaldehyde increased its intensity with respect to $\nu(\text{CCO})_{\text{monodent}}$ while $\nu(\text{CCO})_{\text{monodent}} / \nu(\text{CCO})_{\text{bident}}$ ratio remained constant raising the temperature.

Acetate $\nu_{\text{as}}(\text{COO})$ at 1569 cm^{-1} started to be detectable at $150\text{ }^{\circ}\text{C}$. At $200\text{ }^{\circ}\text{C}$, the acetate presence was corroborated by the growth of the bands at 1569 cm^{-1} , 1452 cm^{-1} $\nu_{\text{s}}(\text{COO})$, 1387 cm^{-1} $\delta(\text{CH}_3)$. Raising the temperature, the intensity of the acetate bands increased, and their shape broadened at $300\text{ }^{\circ}\text{C}$ probably because they were partly oxidized to carbonates.

At $350\text{ }^{\circ}\text{C}$, in the region between $2250\text{--}2500\text{ cm}^{-1}$, it was possible to detect the gas phase CO_2 adsorption bands.

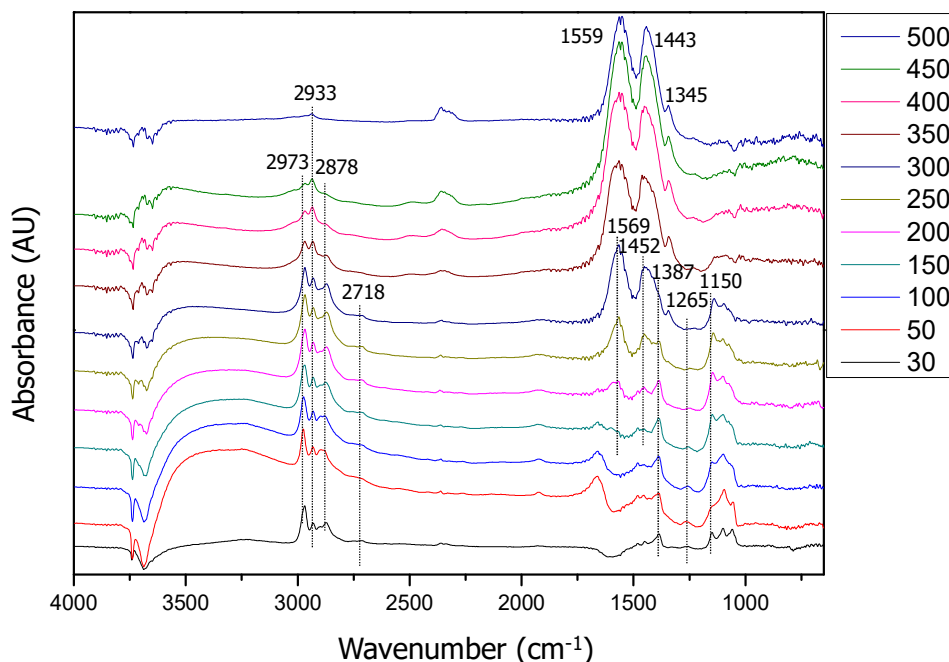


Figure A.8 DRIFTS feeding EtOH-H₂O mixture on Ni-Lac-Zr.

In this case, NiO reduction started at $500\text{ }^{\circ}\text{C}$ as it was possible to appreciate from the slight drop down of the baseline at lower wavenumber and it became more evident looking at the spectra during time, reported in Figure A.9. Ni-Lac-Zr was almost completely reduced during the course of the first hour, as it was possible to hypothesize comparing the spectrum in Figure A.9 on the left with the one reported on the right. It was then, reasonably, hypothesized that the presence of Lanthanum in the catalyst structure increased NiO reducibility.

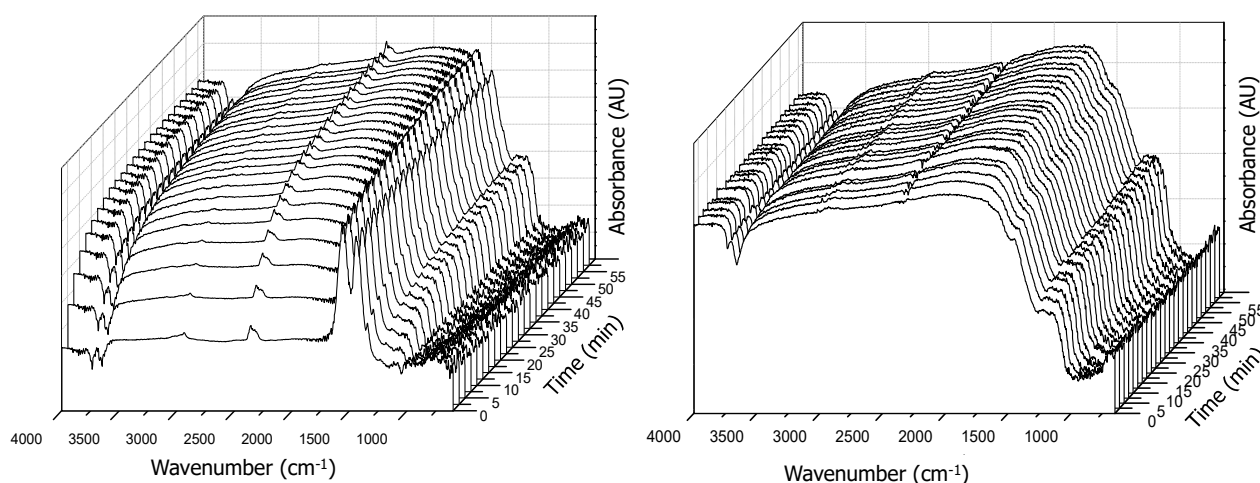


Figure A.9 DRIFTS at $500\text{ }^{\circ}\text{C}$ feeding ethanol/H₂O (left) and EtOH (right) on Ni-Lac-Zr catalyst.

Ethanol intensity rose up to $150\text{ }^{\circ}\text{C}$ while its consumption started at $250\text{ }^{\circ}\text{C}$, as shown in Figure A.10. Acetaldehyde and H_2 started to be detected from $250\text{ }^{\circ}\text{C}$ pointing out that ethanol is consumed in the oxidative dehydrogenation reaction. During the oxidative dehydrogenation H_2

was formed as acetaldehyde co-product (from 250 °C). Ethylene started to be produced at 300 °C reaching its maximum at 400 °C. CO₂ trend started to increase at 350 °C and its formation was attributed to the decomposition of ethanol or acetaldehyde (whose trend started to slightly decrease). After 400 °C no ethylene or acetaldehyde was produced in significant amounts. On the other hand CO₂, CO, CH₄ and H₂ trend steeply raised at such temperature. Methane can be produced along with CO₂ because of surface acetate decomposition. Acetaldehyde after 400 °C diminished because it started to decompose producing CH₄ and CO. These products might both react with water producing H₂ explaining their slight intensity decrease at 500 °C. The CO₂, CO, H₂ and CH₄ slope increment, detected from 400 °C, might be due not only to the decomposition reaction or the side reaction of ethylene, acetaldehyde and ethanol but to all the reactions that might be involved in the ESR process like methanation, WGS and Boudouard combined with the surface reactions.

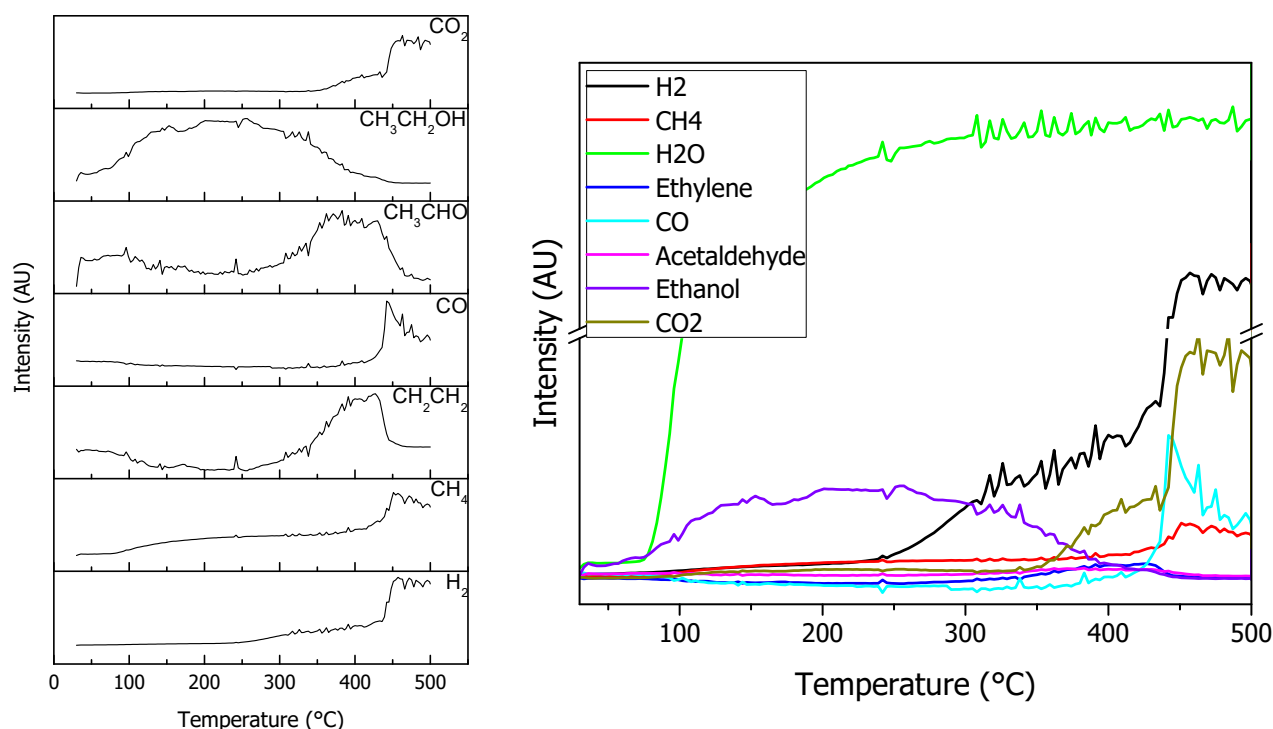


Figure A.10 MS feeding EtOH-H₂O for Ni-Lac-Zr.

All in all, it was demonstrated that NiO reducibility was enhanced by the presence of La₂O₃ on the catalyst surface. In fact, Ni-Lac-Zr was reduced within an 1h at 500 °C in presence of water while Ni-Zr was not reduced. An ethanol activation mechanism was proposed on the catalyst surface and it is reported in Figure A.17. In fact, ethanol can be adsorbed on these catalytic system as ethoxy (2) and undissociated ethanol (1). The experiment in presence of water evidenced that acetaldehyde tends to be formed successively (3 or 4). Therefore, it is likely that ethoxy species are oxidized to acetaldehyde on the catalyst surface. Then, acetaldehyde is transformed into acetate (7) with a successive temperature increase. Along with temperature increase they can be further oxidized to carbonates (7) or they can promote coke formation decomposing on the catalyst surface (6). At 500 °C all the reaction reported happened contemporarily producing preferentially hydrogen and coke. Unfortunately, with these experiments it was not possible to discriminate which intermediate promoted the carbon nanotube or graphitic coke.

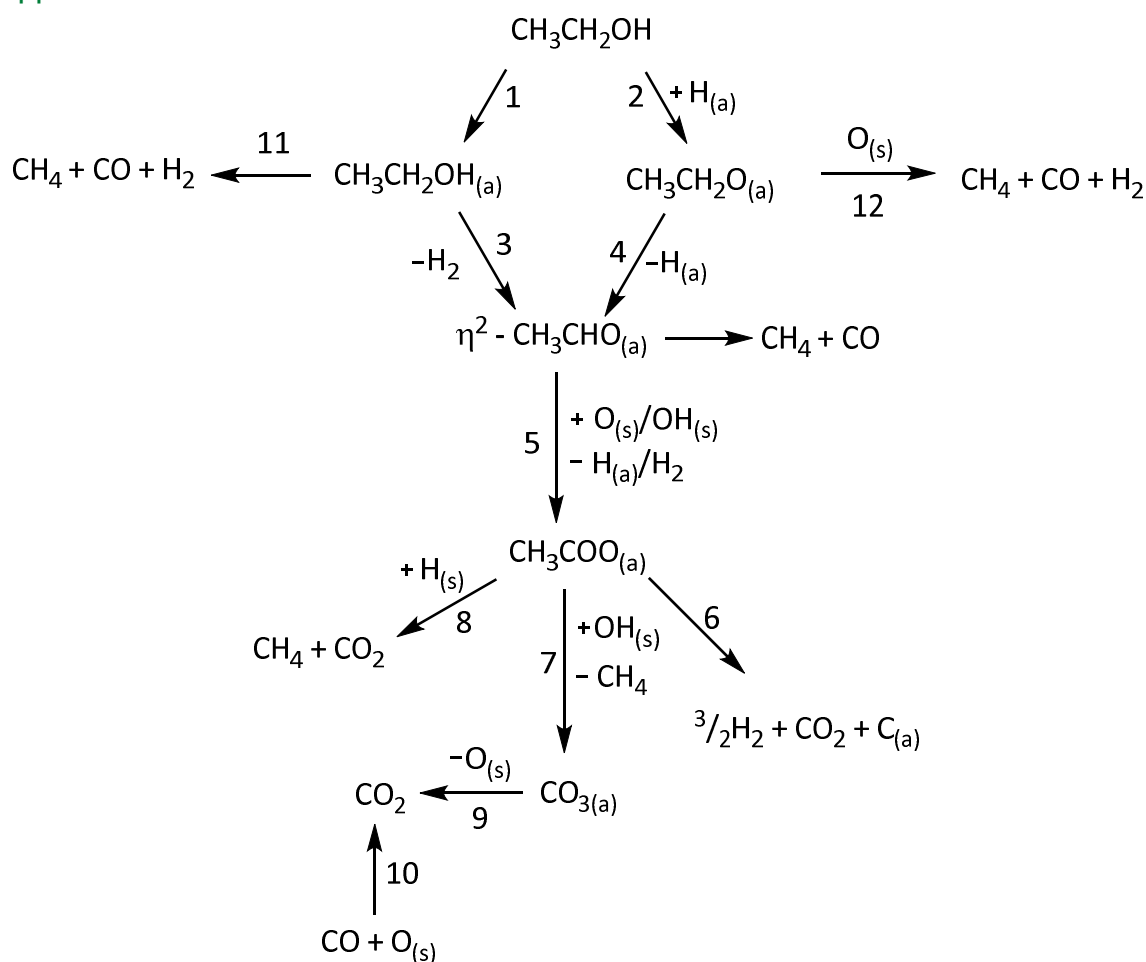


Figure A.11 Hypothesized surface reaction pathways for ZrO_2 based catalysts.

A.3 CeO_2 based catalysts

DRIFTS-MS feeding Ethanol on Ni-Ce

Figure A.12 showed DRIFTS spectra recorded while exposing continuously the Ni-Ce catalyst to pure ethanol at different temperatures. Ethanol was adsorbed as both undissociated (broad bands centred at 3344 cm^{-1} $\nu(\text{OH})$ and 1236 cm^{-1} $\delta(\text{OH})$) and ethoxide (2965 cm^{-1} , 2923 cm^{-1} , 2867 cm^{-1} , 1104 cm^{-1} and 1062 cm^{-1}) on the catalyst surface.^{78,89,90,191} The latter was adsorbed both as bidentate and monodentate as confirmed by the peaks corresponding to $\nu_{\text{bident}}(\text{CO})$ at 1062 cm^{-1} and $\nu_{\text{monodent}}(\text{CO})$ at 1104 cm^{-1} . The bands at 1445 cm^{-1} and 1381 cm^{-1} were due to $\delta_{\text{as}}(\text{CH}_3)$ and $\delta_{\text{s}}(\text{CH}_3)$, respectively. In the C-H stretching region the bands related to $\nu_{\text{as}}(\text{CH}_3)$ at 2970 cm^{-1} and $\nu_{\text{s}}(\text{CH}_3)$ at 2869 cm^{-1} were detected along with the $\nu_{\text{as}}(\text{CH}_2)$ at 2926 cm^{-1} and $\nu_{\text{s}}(\text{CH}_2)$ at 2898 cm^{-1} .⁸² The band at 889 cm^{-1} might be assigned to the convolution of $\nu_{\text{s}}(\text{CCO})$ of ethoxy species and $\delta(\text{Ni-OH})$.^{89,192} The hypothesis of a convolution is reasonable since ethanol adsorption on CeO_2 showed the same spectral feature but it presented a sharper shape, as shown in Figure A.15. The catalyst terminal OH group were characterized by the negative $\nu(\text{OH})$ at 3660 cm^{-1} . As far as the band at 1236 cm^{-1} is concerned, the assignation was not simple since H-bonded ethanol was detected up to 150°C . However, the intensity of this band decreased raising the temperature up to 300°C . At this temperature, the 1236 cm^{-1} band was affected by a quite strong shape change due to carbonates presence. Up to 250°C , the ethoxy bands slightly decreased along with the temperature increment. At 100°C , the bands at 1562 cm^{-1} and 1429 cm^{-1} started to raise and were assigned to $\nu_{\text{as}}(\text{OCO})$ and $\nu_{\text{s}}(\text{OCO})$ of acetate species, respectively. The acetate band

intensity increased raising the temperature and at 200 °C the acetate CH_3 bending transition appeared at 1338 cm^{-1} .¹⁹³ A further temperature increase led to partly acetate transformation into carbonates. This assumption is likely since acetates band shapes broadened while other two peaks at 928 cm^{-1} and 1021 cm^{-1} appeared and were ascribed to bridged and bidentate carbonates, respectively.¹⁹⁴

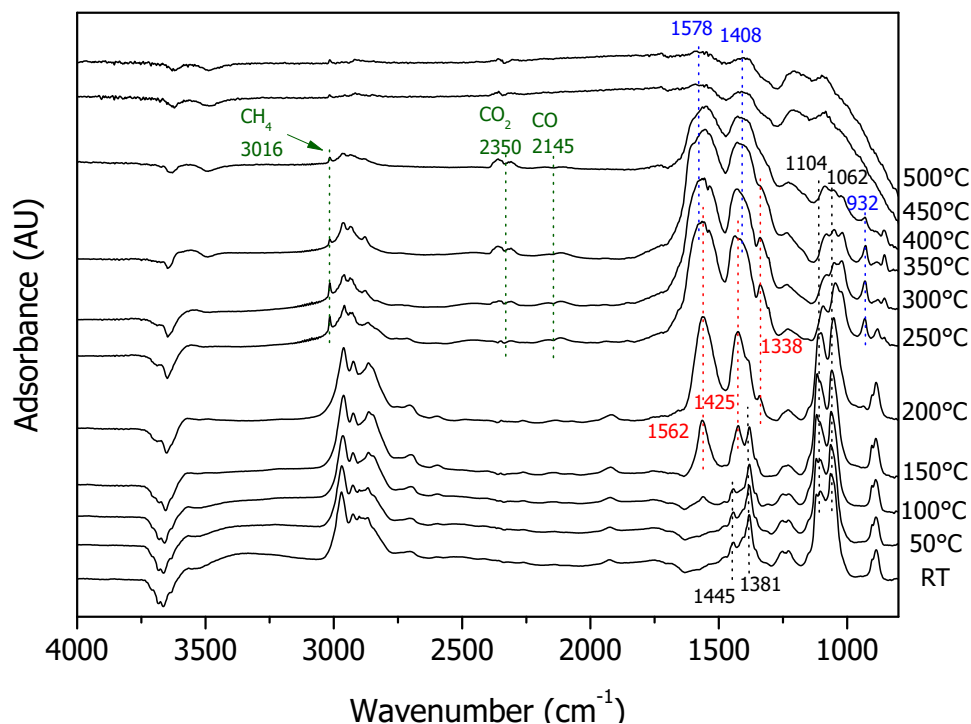
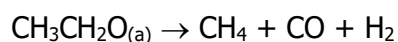
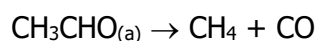
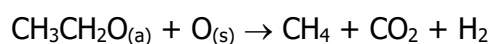


Figure A.12 DRIFTS of Ni-Ce feeding EtOH.

From 250 °C to 400 °C three gas phase bands were detected at 3018 cm^{-1} , 2338 cm^{-1} and 2140 cm^{-1} and related to the presence of CH_4 , CO_2 and CO according to the observations of Xu et al.¹⁹³. They observed also a decrement of acetate band intensity and ethoxy band disappearance. These last two observations were not appreciated in the present work because of the continuous ethanol stream. Furthermore, according to Xu et al.¹⁹³ the production of CH_4 , CO_2 and CO from 250 °C to 400 °C is associated to NiO reduction to Ni^0 . This observation was supported by in situ XRD.¹⁹³ In this experiment the reduction was evidenced even by the drastic change in the catalyst continuum line at 450 °C and 500 °C (Figure A.12). This change was already appreciable in the spectra recorded at 400 °C and it was associated to NiO reduction.¹⁹⁵ Moreover, the analysis of the mass trends, reported in Figure A.13 suggests that ethanol is the reducing agent. In fact, H_2 trend even if it was increasing from 200 °C, as soon as EtOH started to be consumed steeply increased reaching a maximum along with CH_4 and CO . The latter two compounds can be formed by both the following reactions:



Then, it is reasonable to hypothesize that the adsorbed EtO^- is responsible for the initial reduction of NiO and afterwards, H_2 presence helped to reduce it as suggested by the minimum detected at 250 °C in its mass trend. CO_2 was already produced from 250 °C and it can be formed by ethanol decomposition according to:



Anyway, since CO_2 reached a maximum between 350 °C and 400 °C, it is possible that it interacts with the catalyst to form carbonates.

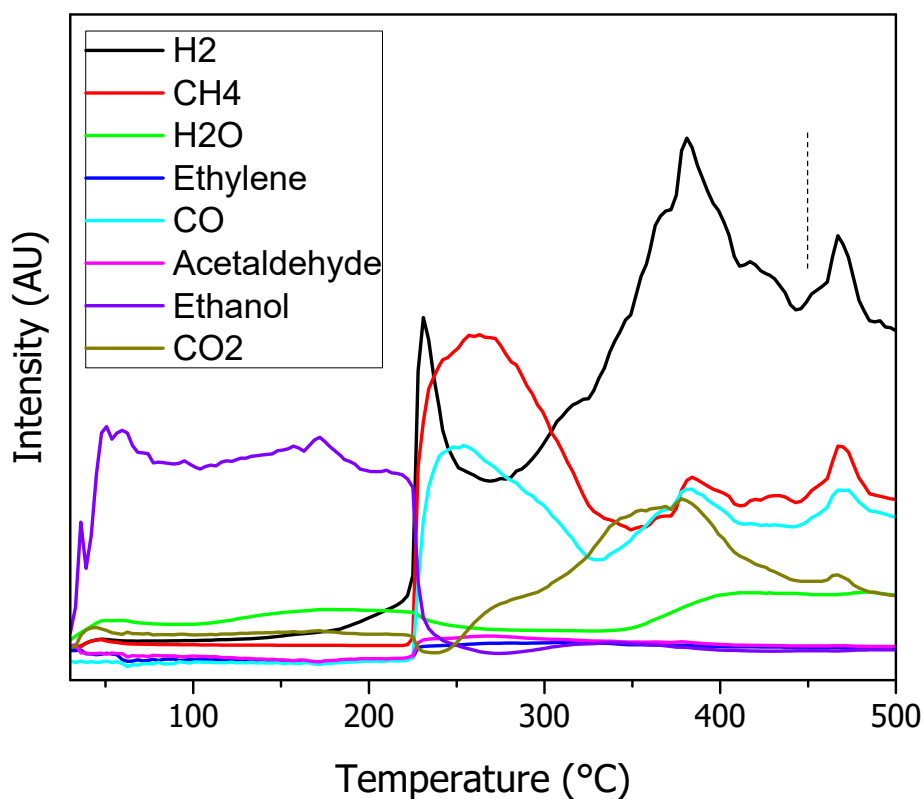


Figure A.13 Mass Ni-Ce feeding ethanol.

DRIFTS-MS feeding Ethanol on Ni-Lac-Ce

88

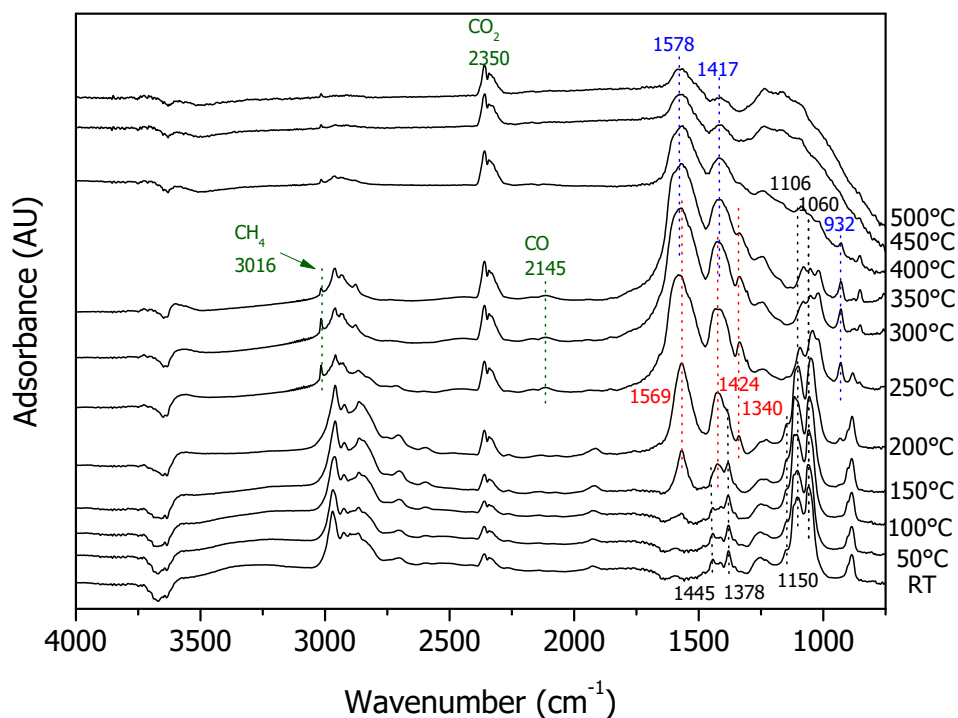


Figure A.14 DRIFTS Ni-Lac-Ce feeding EtOH.

Ni-Lac-Ce showed IR spectral features comparable with Ni-Ce, as shown in Figure A.14. At room temperature, it was possible to detect bands related to two different types of adsorbed ethanol. The bands at 1060 cm^{-1} and 1106 cm^{-1} might be reasonably assigned to $\nu_{\text{ident}}(\text{CO})$ and

$\nu_{\text{monodent}}(\text{CO})$, respectively (i.e. product of ethanol dissociative adsorption). The broad band at 1257 cm^{-1} might be assigned to $\delta(\text{OH})$ of un-dissociated ethanol. The broadness of this peak and the presence of the large adsorption from 3064 cm^{-1} to 3503 cm^{-1} let to hypothesize that ethanol was H-bonded to catalyst surface. This broad peak was present up to $150 \text{ }^{\circ}\text{C}$. Even in this experiment, ethanol was continuously fed, and this might explain the persistence of 1257 cm^{-1} band at higher temperature. Other ethoxy bands present at RT were: $\nu_{\text{as}}(\text{CH}_3)$ (2970 cm^{-1}), $\nu_{\text{as}}(\text{CH}_2)$ (2928 cm^{-1}), $\nu_{\text{s}}(\text{CH}_2)$ (2867 cm^{-1}), $\nu_{\text{as}}(\text{CH}_3)$ (shoulder at 2844 cm^{-1}), $\delta_{\text{as}}(\text{CH}_3)$ (1445 cm^{-1}), $\delta_{\text{s}}(\text{CH}_3)$ (1378 cm^{-1}) and $\nu_{\text{s}}(\text{CCO})$ (888 cm^{-1}).^{88,89} The latter peak might be affected by $\delta(\text{Ni-OH})$ contribution since it was present in the CeO_2 spectrum showing a sharper shape, as shown in Figure A.15.¹⁹² η^2 -acetaldehyde $\nu(\text{CO})$ (1150 cm^{-1} , shoulder) and $\nu(\text{CC})$ (1230 cm^{-1} , this spectral feature is convoluted with the $\delta(\text{OH})$ one) were detected on this catalyst. At $150 \text{ }^{\circ}\text{C}$, 1569 cm^{-1} and 1424 cm^{-1} acetate bands started to raise. At the same time, the broad band related to $\nu(\text{OH})$ vanished while the acetates $\delta(\text{CH}_3)$ started to be detectable at 1340 cm^{-1} . At $250 \text{ }^{\circ}\text{C}$, acetaldehyde bands disappeared, probably due to acetaldehyde conversion into acetates. Acetates began to be partially converted into carbonates at $300 \text{ }^{\circ}\text{C}$. In fact, at this temperature the acetate peaks became wider since they were overlapped with carbonates ones. The presence of this last species was further confirmed by the presence of the band at 932 cm^{-1} and the shape change of the band at 1340 cm^{-1} assignable to bridged and bidentate carbonates, respectively.¹⁹⁴ From $250 \text{ }^{\circ}\text{C}$ to $350 \text{ }^{\circ}\text{C}$, CH_4 (3016 cm^{-1}), CO_2 (2350 cm^{-1}) and CO (2145 cm^{-1}) gas phase transition were detected and they were correlated with NiO reduction, as explained for Ni-Ce.¹⁹³ Also in this case, at $400 \text{ }^{\circ}\text{C}$, a background change was detected, and it was considered a further proof of the metal reduction. The same mass trend for H_2 , CO , CH_4 and CO_2 were observed, as reported in Figure A.16. In fact, even on this catalyst, it is possible to hypothesize NiO reduction by ethanol enhanced by H_2 presence.

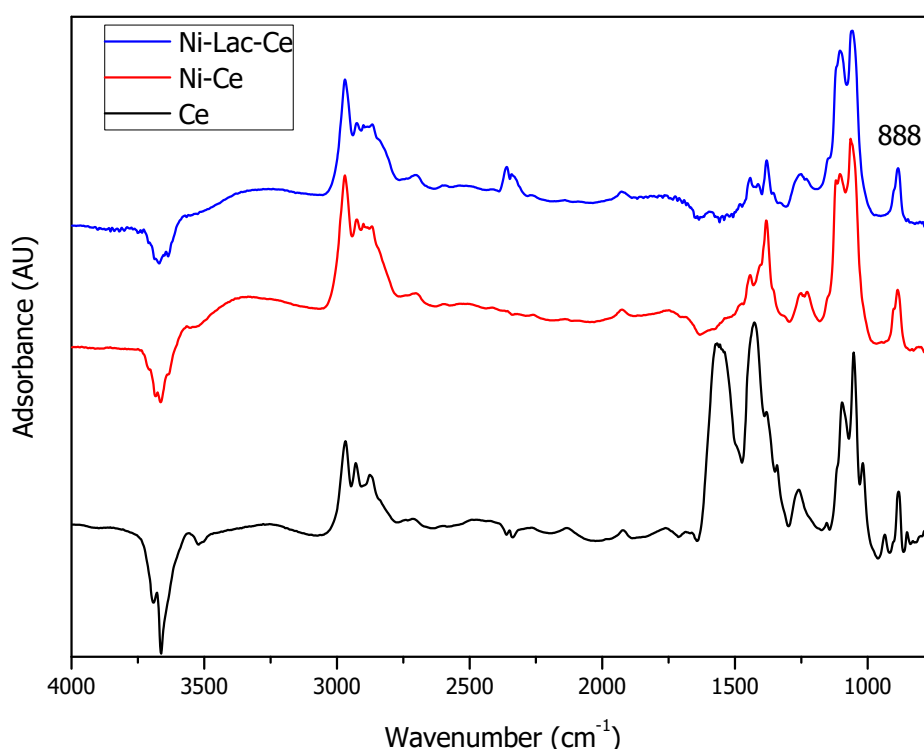


Figure A.15 comparison of the 888 cm^{-1} band shapes among Ce, Ni-Ce and Ni-Lac-Ce at $30 \text{ }^{\circ}\text{C}$ during ethanol feeding.

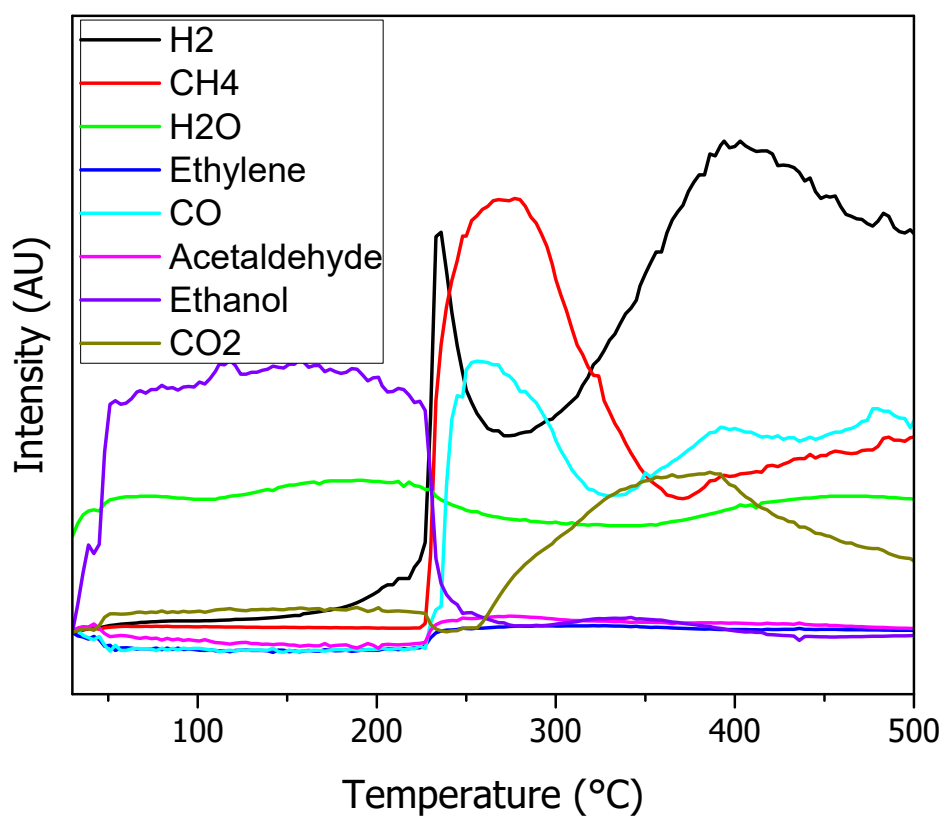


Figure A.16 Mass Ni-Lac-Ce feeding EtOH.

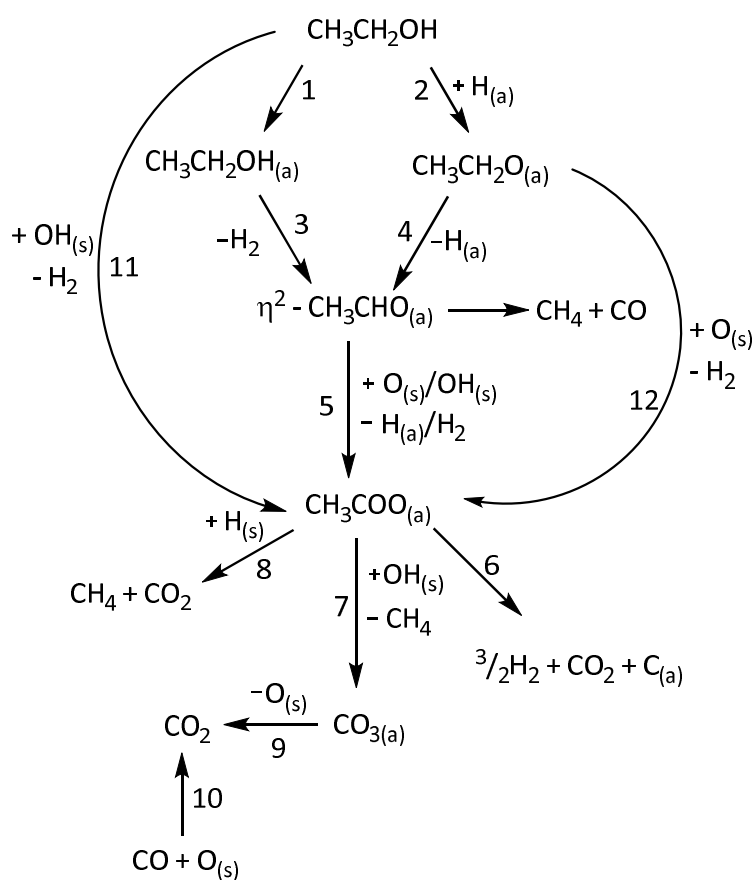


Figure A.17 Hypothesized surface reaction pathways on Ce based catalyst.

The surface reaction pathway for Ce based catalyst, reported in Figure A.17, is similar to the one observed for Zr based catalyst. In fact, ethanol can be adsorbed as ethoxy (4) or H-bonded ethanol (3). Acetaldehyde formation (3 and 4) was evidenced only on Ni-Lac-Ce suggesting that La_2O_3 played a beneficial role its formation. Acetaldehyde and ethoxy can be successively oxidized to acetate (5, 12 and 11) which can be further transformed into carbonates (7). Carbonates and acetate presence caused coke formation (6 and 7).

A.4 Conclusions

Ethanol steam reforming on Ce and Zr based catalyst was studied by means of DRIFTS-MS spectroscopy *in operando*. The experiments highlighted that La_2O_3 addition to the catalyst enhanced NiO reducibility in presence of ethanol. In fact, in the test in the presence of water, which compete for the adsorption on the active sites, it was observed a different reduction time. Ni-Zr was not reduced in presence of EtOH/ H_2O mixture neither after 1 h of reaction. On the contrary, Ni-Lac-Zr reduction was slower than in presence of only EtOH but complete within the same amount of time. Furthermore, significant evidences that ethanol is the reducing agent were gained in the tests performed on Ce based catalyst. In fact, the reduction occurred in a temperature range between 230 °C and 350 °C. Ethanol is the initiator of the reduction which, after, is probably carried out by both ethanol oxidation to CO_2 and H_2 for Ce based catalyst. On the contrary, it is likely that the reduction on Zr based catalyst is carried out by ethanol oxidation to acetaldehyde. In fact, in the MS trends for Zr based catalyst H_2 did not present a minimum but an increasing trend over the time (and temperature).

Acetaldehyde was thought to be a beneficial intermediate whose formation is favored by La_2O_3 addition. On the contrary, acetate and carbonate intermediates were associated with coke formation.

Anyway, to gain a better understanding of the actual ethanol activation on the catalyst surface some test in which ethanol is not continuously fed would be necessary. In fact, an experiment in which just a pulse of ethanol is adsorbed on the catalyst surface would allow to obtain more details about acetaldehyde and ethylene formation which is thought to be beneficial and detrimental, respectively, for ethanol steam reforming reaction.

Appendix B. Ethyl lactate oxidation into ethyl pyruvate

This work was done in collaboration with W. Zhang and S. Shiju in Rothenberg's research group in Amsterdam University. Two papers were published dealing with the data reported in this appendix in ACS Catalysis and in Catalysis Science & Technology.^{196,197}

The aim of this collaboration was to understand by means of DRIFTS-MS which was the V bond that was participating in the reaction, and which was not directly involved both in liquid and in gas phase. The reactivity results and the catalysts characterization are reported in the published papers.^{196,197}

B.5 Methods

A Bruker Vertex 70 equipped with a Pike DiffusIR cell attachment and in line with a mass spectrometer EcoSys-P from European Spectrometry System was used for the DRIFTS measurements. The cell window was made of ZnSe. An MCT detector after 128 scans and 4 cm⁻¹ resolution was used to record the spectra.

In each experiment the sample was pretreated at 450 °C in He for 30 min to obtain a clean catalyst surface. After, the carrier gas was switched to air for test in presence of oxygen. This last passage was omitted in the tests in absence of O₂. Then, IR backgrounds were collected every 50 °C from 450 °C to 50 °C. Afterwards, L-ethyl lactate (EL) pulse was done at 50 °C. Then, the catalyst was kept under the carrier gas flow for 30 min in order to eliminate physisorbed molecules. Afterwards, the sample temperature was increased by 5 °C min⁻¹ and the spectra were recorded every 50 °C. In the experiments done during the oxidation of ethyl lactate at 130 °C the background was taken at 130 °C. After, O₂ and Ethyl lactate were fed continuously, and their reaction was followed for 6 h collecting a spectrum every 20 min. During the overall IR analysis several mass signals (m/z) were monitored continuously: 4, 14, 15, 17, 18, 27, 28, 29, 31, 42, 43, 44, 45, 46, 58, 60, 61, 70, 74, 103, 116.

92

B.6 DRIFTS spectra of bare V₂O₅/TiO₂

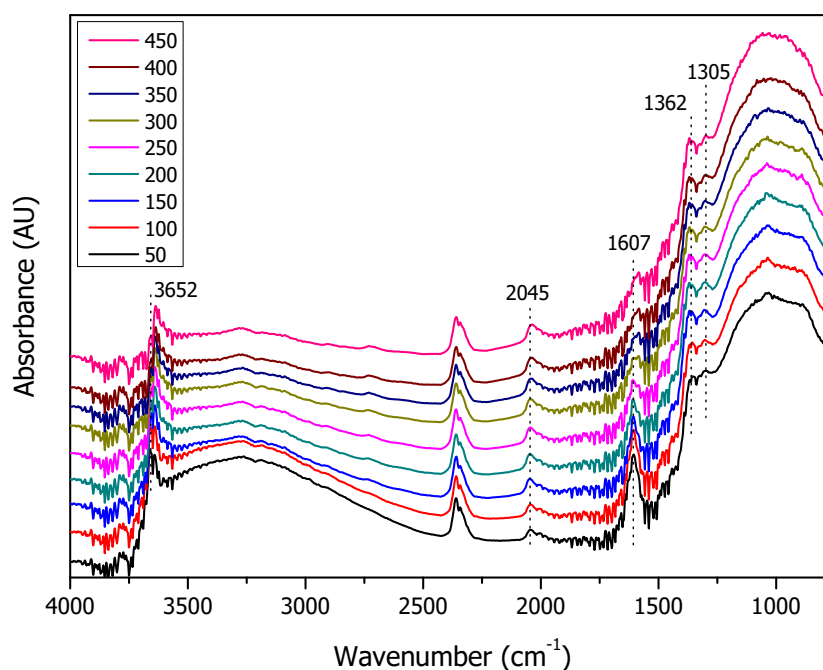


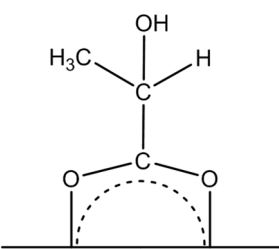
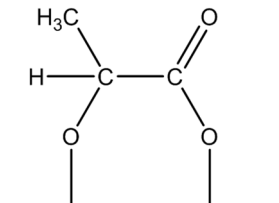
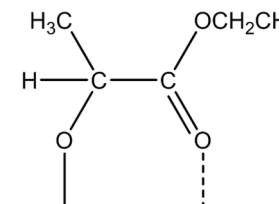
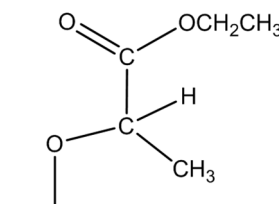
Figure B.1 VO_x-TiO₂ catalyst DRIFTS spectrum.

In *Figure B.1* are reported the DRIFTS spectra of bare $\text{VO}_x\text{-TiO}_2$ catalyst.

It is possible to appreciate three quite defined bands:

- 1347 cm^{-1} was attributed by Narayana et al¹⁹⁸ to the anatase phase, by Garcia et al¹⁹⁹ to the interaction of TiO_2 (anatase) with V-O bending modes and by Kantcheva²⁰⁰ to a combination of the symmetric stretching of the VO_4^{3-} ion with a deformation mode of V-O. Since the bare anatase spectrum, reported in the NIST database²⁰¹, does not show any signal in this region; it was reasonable to assign this transition to a combination bands due to V-O bonds;
- 2040 cm^{-1} assigned to the first overtone of V=O bond vibration;²⁰²
- 1607 cm^{-1} due to the V-O-V bond overtone or the presence of small amount of unreacted hydroxyl groups on the support.¹⁹⁹

Adsorption mode of ethyl lactate

Molecules	Vibrational mode	Wavenumber (cm^{-1})
	$\nu_{\text{as}}(\text{COO})$	1570
	$\nu_{\text{s}}(\text{COO})$	1450
	$\nu_{\text{AL}}(\text{C-O})$	1140
	$\delta_{\text{AL}}(\text{OH})$	1270
	$\nu(\text{C-O})$	1058
	$\nu(\text{C-O})$	1118
	$\nu(\text{C=O})$	1614
	$\nu(\text{C-O})$	1667
	$\delta_{\text{EL}}(\text{C-O})$	1220
	$\nu(\text{C-O})$	1730
	$\delta_{\text{EL}}(\text{C-O})$	1220

AL = Alcoholic functionalities, EL = Ethyl Lactate

Table B.1 Ethyl lactate adsorption modes and their vibration wavenumber.²⁰³

- $-\text{OCH}_2\text{CH}_3$ vibrational modes.

Wavenumber (cm^{-1})	Vibration type
2995-2930 (m)	$\nu_{\text{as}}(\text{CH}_3, \text{CH}_2)$
2930-2890 (w)	$\nu_{\text{s}}(\text{CH}_3)$
2920-2860 (w)	$\nu(\text{CH}_3)$
1490-1460 (m-w)	$\delta(\text{OCH}_2)$
1480-1435 (m)	$\delta_{\text{as}}(\text{CH}_3)$
1390-1360 (m-s)	$\delta_{\text{s}}(\text{CH}_3)$
1385-1335 (m-w)	CH_3 wagging
1325-1340 (m-w)	CH_2 twisting
1195-1135 (w)	CH_3 rocking
1150-1080 (w)	CH_3 rocking

w = weak, m = medium, s = strong

Table B.2 $-\text{OCH}_2\text{CH}_3$ vibrational modes.²⁰⁴

B.7 Ethyl Lactate (L) adsorption on VO_xTiO_2 in absence of O_2 .

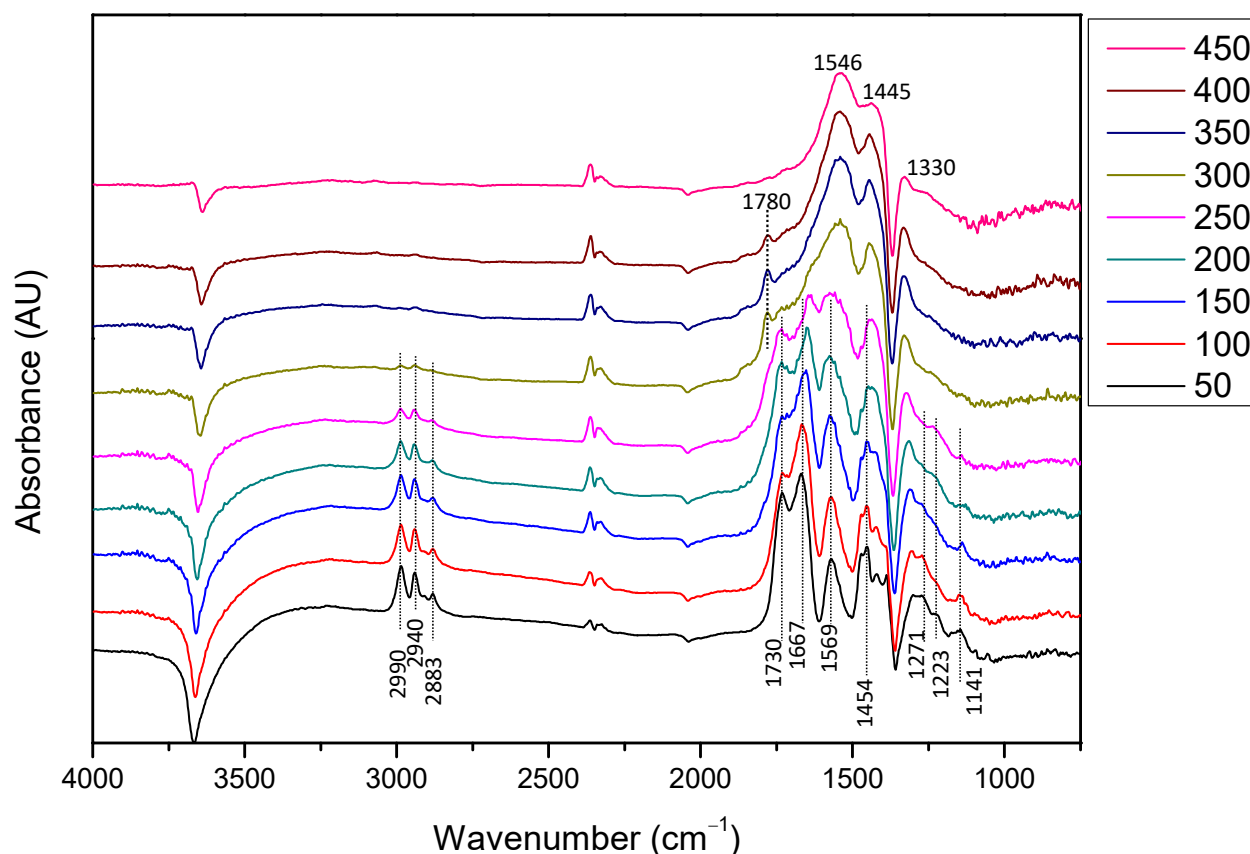


Figure B.2 Ethyl lactate (L) adsorption and TPD on $\text{VO}_x\text{-TiO}_2$ in absence of O_2 .

Figure B.2 shows the temperature-dependent DRIFT spectra for $\text{VO}_x\text{-TiO}_2$ in absence of O_2 . The negative bands that are detectable at 3669 cm^{-1} , 2040 cm^{-1} and 1360 cm^{-1} are due to the interaction of the catalyst functional group (OH, V=O and V-O, respectively) with the adsorbed EL. This molecule might be adsorbed on the catalyst surface as showed in Table B.1. These absorption modes differ from each other for $\nu(\text{C-O})$ wavenumber or the presence of $\nu(\text{COO})$ or $\nu(\text{C=O})$ vibration, as reported in Table B.1. In this case the bands due to adsorption mode (a), (c) and (d) were detected. On the contrary, the adsorption mode (b) was excluded to be formed on this catalyst surface. All of the three modes share some vibrations, such as $\nu_{\text{as}}(\text{CH}_3)$, $\nu_{\text{s}}(\text{CH}_3)$, $\nu(\text{C-H})$, $\delta_{\text{as}}(\text{CH}_3)$, $\delta_{\text{s}}(\text{CH}_3)$ and $\delta(\text{C-H})$ at 2990 cm^{-1} , 2940 cm^{-1} , 2883 cm^{-1} , 1473 cm^{-1} , 1388 cm^{-1} , 1302

cm^{-1} , respectively.^{203,205} The vibrational modes of the ester functionalities ethyl chain are usually weak in intensities and overlapped to the ones of the CH_3 group.²⁰⁴ The intensity of EL, adsorbed as (c) and (d), band diminished while the one of the bands due to (a) raised increasing the temperature. Ethanol mass signal, reported in Figure B.3, confirmed that a temperature increase favoured the lactate species adsorbed as (a). At 250 °C the CO_2 mass trend showed a maximum. Until this temperature, this molecule release might be associated to the decarboxylation of ethyl lactate or lactate. Alongside this molecule, ethanol or acetate might be produced. From 250 °C the EL bands started to shift towards lower wavenumber and the shape of the EL adsorbed as (a) become broader. Moreover, at this temperature, the V-O band underwent a blue shift, indicating a reinforcement of the interaction of this bond with the adsorbate molecule. It is even worth noting the formation of a small shoulder around 1780 cm^{-1} . This shoulder becomes a peak at 300 °C and its apparition corresponds to the alcoholic transition vanishing. This band might be assigned to the carbonyl stretching of the α -keto group of the pyruvate.^{206,207} At this temperature some band shift is detected, in fact the $\nu_{\text{as}}(\text{COO})$ and $\nu_{\text{s}}(\text{COO})$ moved to 1546 cm^{-1} and 1445 cm^{-1} , respectively, as the $\delta(\text{CH}_3)$ to 1330 cm^{-1} . A maximum in ethyl acetate mass signal was detected at 300 °C; its formation might be due to the interaction of ethanol in the gas phase (produced by the ethyl functionalities) and the acetate adsorbed onto the catalyst surface. A further temperature increase led to a pyruvate band decrement and an increase of the carboxylate band. This bands are stable even at 450 °C on the catalyst surface and they might be assigned to the acetate vibrational mode ($\nu_{\text{as}}(\text{COO})$, $\nu_{\text{s}}(\text{COO})$ and $\delta(\text{CH}_3)$). A further maximum of CO_2 mass signal was observed at 400 °C and it might be associated with the decarboxylation of pyruvate species that produces acetate alongside CO_2 . In fact, at 450 °C the pyruvate band completely vanished.

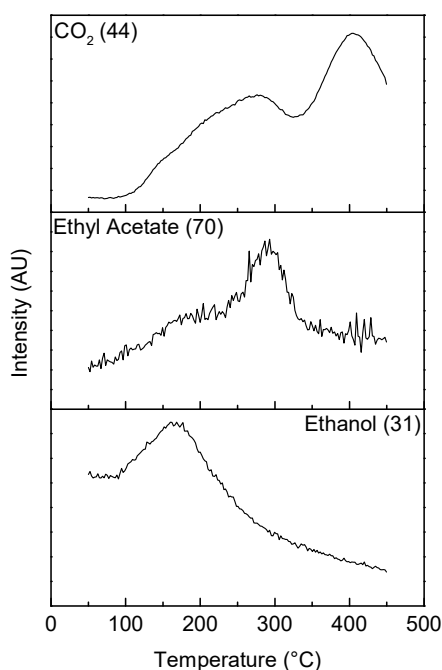
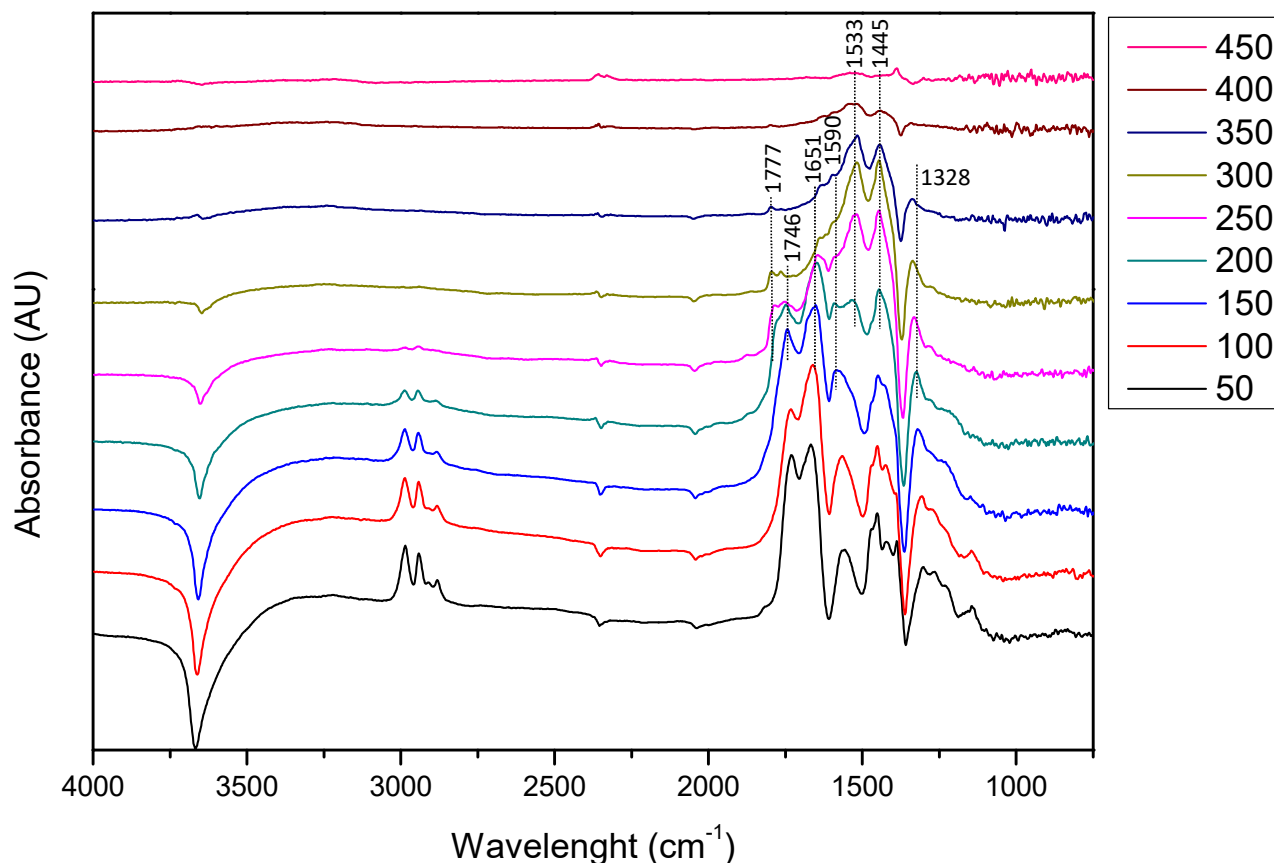


Figure B.3 Mass signal for EL adsorption on $\text{VO}_x\text{-TiO}_2$ in absence of O_2 .

B.8 Ethyl Lactate (L) adsorption on VO_xTiO_2 in presence of O_2 .Figure B.4 $\text{VO}_x\text{-TiO}_2$ DRIFTS after EL adsorption in presence of O_2

In Figure B.4, the temperature dependent DRIFTS spectra for $\text{VO}_x\text{-TiO}_2$ in presence of O_2 are reported. At low temperature, the vibrational band analysis is analogue to the one previously reported for the test in absence of O_2 . In fact, it was possible to observe the band related to the ethyl lactate adsorption modes. Even in this case, it was adsorbed only as the (a), (c) and (d) modes, as showed in Table B.1. Also in this experiment, ethanol mass signal, shown in Figure B.5, was observed at low temperature confirming that ethyl lactate is adsorbed on the catalyst surface both as dissociate and un-dissociated species. In the present experiment, the OH vibrational modes (1140 cm^{-1} , 1268 cm^{-1}) vanished at $150\text{ }^\circ\text{C}$ while a carboxylic acid C=O stretching shift toward 1750 cm^{-1} was observed. This wavenumber increment ($\Delta\nu = 20\text{ cm}^{-1}$) might be ascribed to a change in the surrounding environment of the C=O and this might be due to the formation of pyruvate. A shoulder at 1533 cm^{-1} started to raise and it was assigned to the $\nu_{\text{as}}(\text{COO})$ of the pyruvate adsorbed as carboxylate.²⁰³ CO_2 and ethanol mass signals showed a maximum around $200\text{ }^\circ\text{C}$ indicating that some lactate might decompose. At this temperature, the shoulder at 1533 cm^{-1} became a defined peak while a shoulder at 1777 cm^{-1} started to be detectable and it was assigned to the α -keto group of the pyruvate. A further temperature increase led to a complete disappearance of the lactate band (1651 cm^{-1}). In fact, at $300\text{ }^\circ\text{C}$ the only bands distinguishable on the surface were at 1777 cm^{-1} , 1746 cm^{-1} , 1533 cm^{-1} and 1445 cm^{-1} and were assigned to α -keto group $\nu(\text{C=O})$, carboxylate $\nu(\text{C=O})$, bidentate carboxylate $\nu_{\text{as}}(\text{COO})$ and $\nu_{\text{s}}(\text{COO})$, respectively. All of them were related to pyruvate specie.^{203,206,207} At $400\text{ }^\circ\text{C}$, the pyruvate peaks vanished completely, and only two large peaks in the $\nu(\text{COO})$ stretching region were detectable along with the physisorbed gas-phase CO_2 transitions at 2360 cm^{-1} , 2335 cm^{-1} . The $\nu_{\text{as}}(\text{COO})$ and $\nu_{\text{s}}(\text{COO})$ might be assigned to carbonates.⁹⁵ It is worth noticing that the V=O interaction

disappeared as the pyruvate bands, while the V-O one is still present with the carbonates transitions but shifted at higher wavenumbers.

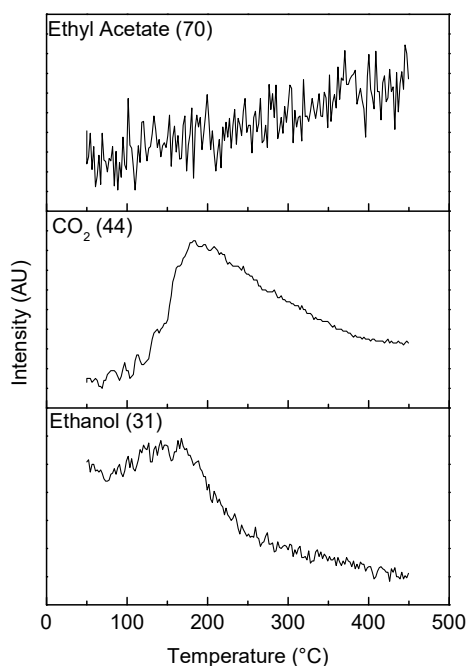


Figure B.5 Mass signal for EL adsorption on $\text{VO}_x\text{-TiO}_2$ in presence of O_2 .

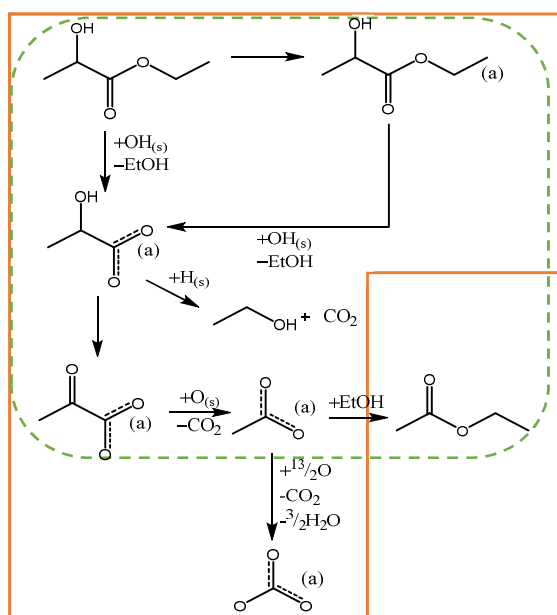


Figure B.6 Hypothesized reaction pathways. The reaction route surrounded by the green dashed line is for the experiments conducted in absence of O_2 while the one surrounded by the orange is for the test conducted in presence of O_2 .

All in all, it was possible to hypothesize that once ethyl lactate was adsorbed on the catalyst surface, it could decompose to ethanol and CO_2 or be oxidized by the V-O bond to pyruvaldehyde, as shown in Figure B.6. It is reasonable to hypothesize that the adsorption mode (c) and (d) favoured pyruvate formation while the mode (a) favoured the decomposition reaction. Once formed, Pyruvate can decarboxylate to form acetate which can successively be transformed into carbonates.

B.9 Aerobic oxidation of ethyl lactate on mesoV-TiO₂ at 130 °C

The results obtained at different reaction time during the DRIFT study of ethyl lactate oxidation on mesoV-TiO₂ are reported in Figure B.7. In the C-H stretching region, it was possible to detect the following bands: 2987, 2943, and 2885 cm⁻¹ assigned to $\nu_{as}(\text{CH}_3)$, $\nu_{as}(\text{CH}_2)$, and $\nu_s(\text{CH}_3)$, respectively.²⁰³ The bands at 1473 cm⁻¹, 1454 cm⁻¹ and 1324 cm⁻¹ were assigned to C-H bending modes.²⁰³ The bands detected at 1562 cm⁻¹, 1425 cm⁻¹ and 1740 cm⁻¹ are the fingerprint of adsorbed lactate and belonged to mode (a) $\nu_{as}(\text{COO})$, $\nu_s(\text{COO})$ and mode (d) $\nu(\text{C=O})$, respectively. Moreover, the two weak bands at 1130 cm⁻¹ and 1217 cm⁻¹ were assigned to the C-O vibration of $\nu(\text{C-O})$ and $\delta(\text{C-O})$ of ethyl lactate. The two peaks visible at 1678 cm⁻¹ and 1658 cm⁻¹ were ascribed to $\nu(\text{C=O})$ interacting with the catalyst surface (mode (c)).²⁰³ After 20 min, two new shoulders were detected at 1867 cm⁻¹ and 1780 cm⁻¹. These two were related to the α -keto group carbonyl stretching of pyruvate.²⁰⁶

It is important to notice that the V=O overtone band intensity at 2040 cm⁻¹ is not changing during the aerobic oxidation of ethyl lactate. On the contrary the V-O bond at 1370 cm⁻¹ is slightly diminished (since the oxygen is in defect).¹⁹⁹ These results suggest that the V-O bond is directly involved in the reaction while the V=O is an observer.

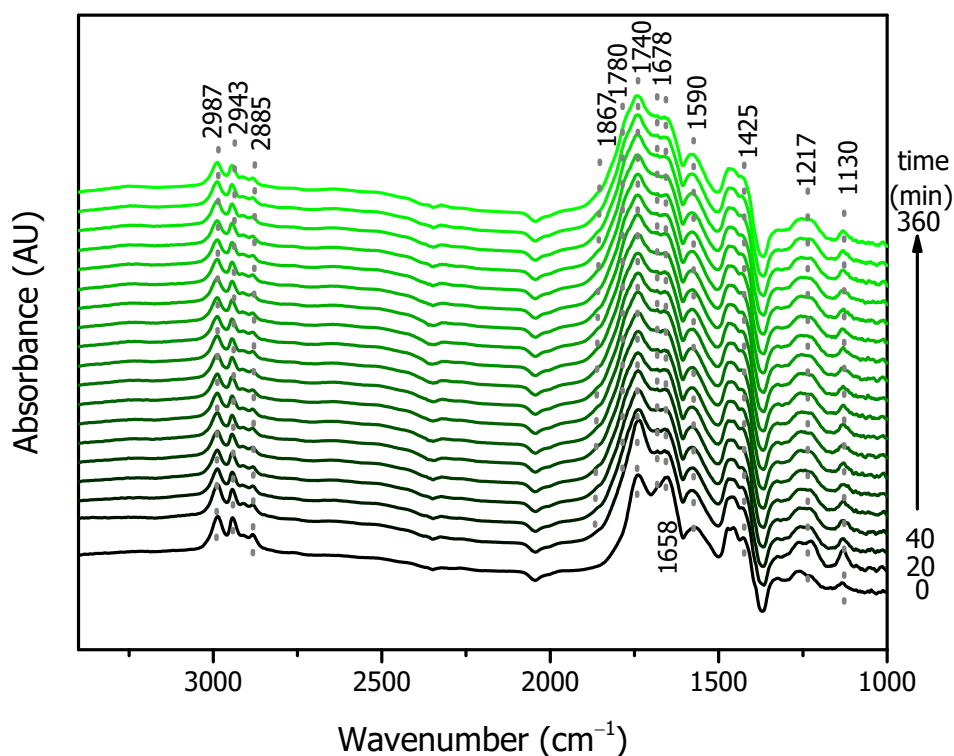


Figure B.7 In situ DRIFTS spectra recorded every 20 min during ethyl lactate aerobic oxidation on mesoV-TiO₂.

B.1 Conclusion

Thanks to the DRIFTS-MS experiments, it was possible to elucidate that both V-O and V=O bonds are involved in the interaction between the catalyst and the EL. Furthermore, V-O plays a key role for the reaction being the oxygen donor as shown by the test in absence and in presence of O₂. V=O might help to obtain the correct adsorption mode coordinating with the adsorbed molecule, but it is not directly involved in the reaction mechanism.

By the result analysis, it was possible to hypothesize a reaction mechanism for the EL oxidation. The hypothesized pathways are reported in Figure B.6. The reaction intermediates that might be

formed on the catalyst surface are the same. The main differences are that in presence of O_2 carbonates were formed on the catalyst surface, while O_2 free condition ethyl acetate production was promoted.

Publications

Journals:

1. Gyngazova M., Grazia L., Lolli A., Innocenti G., Tabanelli T., Mella M., Albonetti S., Cavani F.: *"Mechanistic insights into the catalytic transfer hydrogenation of furfural with methanol and alkaline earth oxides"* submitted to **Journal of Catalysis**
2. Pizzolitto C., Menegazzo F., Ghedini E., Innocenti G., di Michele A., Cruciani G., Cavani F., Signoretto M.: *"Ni based catalysts for ethanol DIR-SOFC applications: increase of ceria redox ability by La₂O₃ addition"*, *accepted manuscript*, **ACS Sustainable Chemistry & Engineering**, DOI: 10.1021/acssuschemeng.8b02103
3. Zhang W., Innocenti G., Ferbinteanu M., Ramos-Fernandez E.V., Sepulveda-Escribano A., Wu H., Cavani F., Rothenberg G., Shiju N.R.: *"Understanding the oxidative dehydrogenation of ethyl lactate to ethyl pyruvate over vanadia/titania catalysts"* **Catalysis Science & Technology**, 2018, Advance Article, DOI:10.1039/C7CY02309J
4. Zhang W., Innocenti G., Oulego P., Gitis V., Wu H., Ensing B., Cavani F., Rothenberg G., Shiju N. R.: *"Highly selective oxidation of ethyl lactate to ethyl pyruvate catalyzed by mesoporous vanadia-titania"*, **ACS Catalysis** **8**, **3**, **2365-2374**, DOI:10.1021/acscatal.7b03843

References

- (1) Roser, M. CO₂ and other Greenhouse Gas Emissions <http://ourworldindata.org/data/resources-energy/co2-and-other-greenhouse-gas-emissions/>.
- (2) Ragauskas, A. J.; Williams, C. K.; Davison, B. H.; Britovsek, G.; Cairney, J.; Eckert, C. A.; Frederick, W. J.; Hallett, J. P.; Leak, D. J.; Liotta, C. L.; Mielenz, J. R.; Murphy, R.; Templer, R.; Tschaplinski, T. *Science* (80-.). **2006**, *311* (5760), 484–489.
- (3) Shafiee, S.; Topal, E. *Energy Policy* **2009**, *37*(1), 181–189.
- (4) Vaccaro, L. *Biofuel Res. J.* **2017**, *4* (4), 713–714.
- (5) Anastas, P.T.; Warner, J. C. *Oxford Univ. Press* **1998**.
- (6) Anastas, P.; Eghbali, N. *Chem. Soc. Rev.* **2010**, *39*(1), 301–312.
- (7) Lee, R. A.; Lavoie, J.-M. *Anim. Front.* **2013**, *3* (2), 6–11.
- (8) EASAC (European Academies Science Advisory Council). *The current status of biofuels in the European Union, their environmental impacts and future prospects*, 2012.
- (9) Phillips, S.; Flach, B.; Lieberz, S.; Lappin, J.; Bolla, S. *EU Biofuels Annual 2018*; 2018; Vol. EU-28.
- (10) Aro, E.-M. *Ambio* **2016**, *45* (S1), 24–31.
- (11) Maity, S. K. *Renew. Sustain. Energy Rev.* **2015**, *43*, 1446–1466.
- (12) Kamm, B.; Kamm, M. *Chem. Biochem. Eng. Q.* **2004**, *18*(1), 1–6.
- (13) Kamm, B.; Gruber, P. R.; Kamm, M. In *Ullmann's Encyclopedia of Industrial Chemistry*, 2016; pp 1–38.
- (14) Maity, S. K. *Renew. Sustain. Energy Rev.* **2015**, *43*, 1427–1445.
- (15) Statistical, B. *67 th edition Renewable energy*, 2018.
- (16) U.S. Energy information administration. *Monthly biodiesel production report*, 2018.
- (17) Razali, N.; Abdullah, A. Z. *Appl. Catal. A Gen.* **2017**, *543* (December 2016), 234–246.
- (18) Ndaba, B.; Chiyanzu, I.; Marx, S. *Biotechnol. Reports* **2015**, *8*, 1–9.
- (19) Roozbehani, B.; Mirdrikvand, M.; Moqadam, S. I.; Roshan, A. C. *Chem. Technol. Fuels Oils* **2013**, *49*(2), 115–124.
- (20) Kosaric, N.; Duvnjak, Z.; Farkas, A.; Sahm, H.; Bringer-Meyer, S.; Goebel, O.; Mayer, D. In *Ullmann's Encyclopedia of Industrial Chemistry*, Wiley-VCH Verlag GmbH & Co. KGaA: Weinheim, Germany, 2011; Vol. 13, pp 1–72.
- (21) Ibrahim, M. F.; Kim, S. W.; Abd-Aziz, S. *Renew. Sustain. Energy Rev.* **2018**, *91* (March 2017), 1192–1204.
- (22) Bahrmann, H.; Lipps, W. **2005**.
- (23) Hahn, H.-D.; Dämbkes, G.; Rupprich, N.; Bahl, H.; Frey, G. D. *Ullmann's Encycl. Ind. Chem.* **2013**, 1–13.
- (24) Kujawska, A.; Kujawski, J.; Bryjak, M.; Kujawski, W. *Renew. Sustain. Energy Rev.* **2015**, *48* (August 2018), 648–661.

References

- (25) Yang, S.-T.; Jingbo Zhao. ADAPTIVE ENGINEERING OF CLOSTRIDIUM FOR INCREASED 1-BUTANOL PRODUCTION. US8450093, 2013.
- (26) Bagnato, G.; Iulianelli, A.; Sanna, A.; Basile, A. *Membranes (Basel)*. **2017**, 7(2).
- (27) Christoph, R.; Schmidt, B.; Steinberger, U.; Dilla, W.; Karinen, R. *Ullmann's Encycl. Ind. Chem.* **2012**, 67–82.
- (28) Kim, D. S.; Hanifzadeh, M.; Kumar, A. *Environ. Prog. Sustain. Energy* **2018**, 37(1), 7–19.
- (29) Komesu, A.; Allan, J.; Oliveira, R. De; Martins, S. **2017**, 2020 (2), 4364–4383.
- (30) Sin, L. T.; Rahmat, A. R.; Rahman, W. A. W. A. In *Plastics Design Library*, Sin, L. T., Rahmat, A. R., Rahman, W. A. W. A. B. T.-P. A., Eds.; William Andrew Publishing: Oxford, 2013; pp 1–70.
- (31) Sin, L. T.; Rahmat, A. R.; Rahman, W. A. W. A. In *Plastics Design Library*, Sin, L. T., Rahmat, A. R., Rahman, W. A. W. A. B. T.-P. A., Eds.; William Andrew Publishing: Oxford, 2013; pp 301–327.
- (32) Grand View Research. *Lactic Acid Market Analysis By Application (Industrial, F&B, Pharmaceuticals, Personal Care) & Polylactic Acid (PLA) Market Analysis By Application (Packaging, Agriculture, Transport, Electronics, Textiles), And Segment Forecasts, 2018 - 2025*; 2017.
- (33) Starr, J. N.; Westhoff, G. In *Ullmann's Encyclopedia of Industrial Chemistry*, Wiley-VCH Verlag GmbH & Co. KGaA: Weinheim, Germany, 2014; pp 1–8.
- (34) Cubas-Cano, E.; González-Fernández, C.; Ballesteros, M.; Tomás-Pejó, E. *Biofuels, Bioprod. Biorefining* **2018**, 12 (2), 290–303.
- (35) Li, S.; Deng, W.; Wang, S.; Wang, P.; An, D.; Li, Y.; Zhang, Q.; Wang, Y. *ChemSusChem* **2018**, 11 (13), 1995–2028.
- (36) Jantasee, S.; Kienberger, M.; Mungma, N.; Siebenhofer, M. *J. Chem. Technol. Biotechnol.* **2017**, No. March.
- (37) Sheldon, R. A. *ACS Sustain. Chem. Eng.* **2018**, 6(4), 4464–4480.
- (38) Posada, J. A.; Patel, A. D.; Roes, A.; Blok, K.; Faaij, A. P. C.; Patel, M. K. *Bioresour. Technol.* **2013**, 135, 490–499.
- (39) Vohra, M.; Manwar, J.; Manmode, R.; Padgilwar, S.; Patil, S. *J. Environ. Chem. Eng.* **2014**, 2(1), 573–584.
- (40) Swana, J.; Yang, Y.; Behnam, M.; Thompson, R. *Bioresour. Technol.* **2011**, 102 (2), 2112–2117.
- (41) Zhang, Q.; Dong, J.; Liu, Y.; Wang, Y.; Cao, Y. *J. Energy Chem.* **2016**, 25(6), 907–910.
- (42) Mohd Azhar, S. H.; Abdulla, R.; Jambo, S. A.; Marbawi, H.; Gansau, J. A.; Mohd Faik, A. A.; Rodrigues, K. F. *Biochem. Biophys. Reports* **2017**, 10, 52–61.
- (43) Alvira, P.; Tomás-Pejó, E.; Ballesteros, M.; Negro, M. J. *Bioresour. Technol.* **2010**, 101 (13), 4851–4861.
- (44) Li, K.; Liu, S.; Liu, X. *Int. J. Energy Res.* **2014**, 38 (8), 965–977.
- (45) Bibi, R.; Ahmad, Z.; Imran, M.; Hussain, S.; Ditta, A.; Mahmood, S.; Khalid, A. *Renew. Sustain. Energy Rev.* **2017**, 71, 976–985.
- (46) Acharya, B.; Roy, P.; Dutta, A. *Biofuels* **2014**, 5(5), 551–564.

References

- (47) Sun, J.; Wang, Y. *ACS Catal.* **2014**, *4* (4), 1078–1090.
- (48) Pavarelli, G.; Velasquez Ochoa, J.; Caldarelli, A.; Puzzo, F.; Cavani, F.; Dubois, J.-L. *ChemSusChem* **2015**, *8* (13), 2250–2259.
- (49) West, R. M.; Braden, D. J.; Dumesic, J. A. *J. Catal.* **2009**, *262* (1), 134–143.
- (50) Jin, C.; Yao, M.; Liu, H.; Lee, C. F. F.; Ji, J. *Renew. Sustain. Energy Rev.* **2011**, *15* (8), 4080–4106.
- (51) García, V.; Pääkilä, J.; Ojamo, H.; Muurinen, E.; Keiski, R. L. *Renew. Sustain. Energy Rev.* **2011**, *15* (2), 964–980.
- (52) Guerbet, M. *C. R. Hebd. Séances Acad. Sci.* **1899**, *128*, 511–513.
- (53) Gabriëls, D.; Hernández, W. Y.; Sels, B.; Van Der Voort, P.; Verberckmoes, A. *Catal. Sci. Technol.* **2015**, *5* (8), 3876–3902.
- (54) Ndou, A. S.; Plint, N.; Coville, N. J. *Appl. Catal. A Gen.* **2003**, *251* (2), 337–345.
- (55) Carvalho, D. L.; De Avillez, R. R.; Rodrigues, M. T.; Borges, L. E. P.; Appel, L. G. *Appl. Catal. A Gen.* **2012**, *415–416*, 96–100.
- (56) Pang, J.; Zheng, M.; He, L.; Li, L.; Pan, X.; Wang, A.; Wang, X.; Zhang, T. *J. Catal.* **2016**, *344*, 184–193.
- (57) Yang, K. W.; Jiang, X. Z.; Zhang, W. C. *Chinese Chem. Lett.* **2004**, *15* (12), 1497–1500.
- (58) Jiang, D.; Wu, X.; Mao, J.; Ni, J.; Li, X. *Chem. Commun.* **2016**, *52* (95), 13749–13752.
- (59) Silvester, L.; Lamonier, J. F.; Lamonier, C.; Capron, M.; Vannier, R. N.; Mamede, A. S.; Dumeignil, F. *ChemCatChem* **2017**, *9* (12), 2250–2261.
- (60) Quesada, J.; Faba, L.; Díaz, E.; Ordóñez, S. *Appl. Catal. A Gen.* **2017**, *542* (April), 271–281.
- (61) Hanspal, S.; Young, Z. D.; Prillaman, J. T.; Davis, R. J. *J. Catal.* **2017**, *352*, 182–190.
- (62) Earley, J. H.; Bourne, R. A.; Watson, M. J.; Poliakoff, M. *Green Chem.* **2015**, *17* (5), 3018–3025.
- (63) León, M.; Díaz, E.; Vega, A.; Ordóñez, S.; Auroux, A. *Appl. Catal. B Environ.* **2011**, *102* (3–4), 590–599.
- (64) Tsuchida, T.; Sakuma, S.; Takeguchi, T.; Ueda, W. *Ind. Eng. Chem. Res.* **2006**, *45* (25), 8634–8642.
- (65) Tsuchida, T.; Kubo, J.; Yoshioka, T.; Sakuma, S.; Takeguchi, T.; Ueda, W. *J. Catal.* **2008**, *259* (2), 183–189.
- (66) Ogo, S.; Onda, A.; Yanagisawa, K. *Appl. Catal. A Gen.* **2011**, *402* (1–2), 188–195.
- (67) Ogo, S.; Onda, A.; Iwasa, Y.; Hara, K.; Fukuoka, A.; Yanagisawa, K. *J. Catal.* **2012**, *296*, 24–30.
- (68) Ramasamy, K. K.; Gray, M.; Job, H.; Santosa, D.; Li, X. S.; Devaraj, A.; Karkamkar, A.; Wang, Y. *Top. Catal.* **2016**, *59* (1), 46–54.
- (69) Tesquet, G.; Faye, J.; Hosoglu, F.; Mamede, A. S.; Dumeignil, F.; Capron, M. *Appl. Catal. A Gen.* **2016**, *511*, 141–148.
- (70) Ramasamy, K. K.; Gray, M.; Job, H.; Smith, C.; Wang, Y. *Catal. Today* **2016**, *269*, 82–87.

References

- (71) Schlaf, M.; Editors, Z. C. Z. *Reaction Pathways and Mechanisms in Thermocatalytic Biomass Conversion I*.
- (72) Chieregato, A.; Ochoa, J. V.; Bandinelli, C.; Fornasari, G.; Cavani, F.; Mella, M. *ChemSusChem* **2015**, *8* (2), 377–388.
- (73) Scalbert, J.; Thibault-Starzyk, F.; Jacquot, R.; Morvan, D.; Meunier, F. *J. Catal.* **2014**, *311*, 28–32.
- (74) Young, Z. D.; Davis, R. J. *Catal. Sci. Technol.* **2018**, *8* (6), 1722–1729.
- (75) Brunauer, S.; Emmett, P. H.; Teller, E. *J. Am. Chem. Soc.* **1938**, *60* (2), 309–319.
- (76) Young, Z. D.; Hanspal, S.; Davis, R. J. *ACS Catal.* **2016**, *6* (5), 3193–3202.
- (77) Raskó, J.; Kiss, J. *Appl. Catal. A Gen.* **2005**, *287* (2), 252–260.
- (78) Moraes, T. S.; Rabelo Neto, R. C.; Ribeiro, M. C.; Mattos, L. V.; Kourtelesis, M.; Ladas, S.; Verykios, X.; Noronha, F. B. *Appl. Catal. B Environ.* **2016**, *181*, 754–768.
- (79) Hill, I. M.; Hanspal, S.; Young, Z. D.; Davis, R. J. *J. Phys. Chem. C* **2015**, *119* (17), 9186–9197.
- (80) Garbarino, G.; Sanchez Escribano, V.; Finocchio, E.; Busca, G. *Appl. Catal. B Environ.* **2012**, *113–114*, 281–289.
- (81) Rintramee, K.; Föttinger, K.; Rupprechter, G.; Wittayakun, J. *Appl. Catal. B Environ.* **2012**, *115–116*, 225–235.
- (82) Ochoa, J. V.; Trevisanut, C.; Millet, J.-M. M.; Busca, G.; Cavani, F. *J. Phys. Chem. C* **2013**, *117* (45), 23908–23918.
- (83) Taifan, W. E.; Yan, G. X.; Baltrusaitis, J. *Catal. Sci. Technol.* **2017**, *7* (20), 4648–4668.
- (84) Schmal, M.; Cesar, D. V.; Souza, M. M. V. M.; Guarido, C. E. *Can. J. Chem. Eng.* **2011**, *89* (5), 1166–1175.
- (85) de Lima, S. M.; Silva, A. M.; da Cruz, I. O.; Jacobs, G.; Davis, B. H.; Mattos, L. V.; Noronha, F. B. *Catal. Today* **2008**, *138* (3–4), 162–168.
- (86) Dömök, M.; Oszkó, A.; Baán, K.; Sarusi, I.; Erdo'helyi, A. *Appl. Catal. A Gen.* **2010**, *383* (1–2), 33–42.
- (87) Dömök, M.; Tóth, M.; Raskó, J.; Erdo'helyi, A. *Appl. Catal. B Environ.* **2007**, *69* (3–4), 262–272.
- (88) Yee, A.; Morrison, S. J.; Idriss, H. *J. Catal.* **1999**, *186* (2), 279–295.
- (89) Idriss, H. et al. *Juornal Catal.* **1995**, *155*, 219.
- (90) Mattos, L. V.; Noronha, F. B. *J. Catal.* **2005**, *233* (2), 453–463.
- (91) Yee, a.; Morrison, S. J.; Idriss, H. *Catal. Today* **2000**, *63* (2–4), 327–335.
- (92) Petitjean, H.; Chizallet, C.; Krafft, J.-M.; Che, M.; Lauron-Pernot, H.; Costentin, G. *Phys. Chem. Chem. Phys.* **2010**, *12* (44), 14740.
- (93) Petitjean, H.; Krafft, J. M.; Che, M.; Lauron-Pernot, H.; Costentin, G. *J. Phys. Chem. C* **2011**, *115* (3), 751–756.
- (94) Hattori, H. *Chem. Rev.* **1995**, *95* (3), 537–558.
- (95) Seiferth, O.; Wolter, K.; Dillmann, B.; Klivenyi, G.; Freund, H.; Scarano, D.; Zecchina, A.

- 1999**, 421, 176–190.
- (96) Carvalho, D. L.; Borges, L. E. P. P.; Appel, L. G.; Ramírez De La Piscina, P.; Homs, N. *Catal. Today* **2013**, 213, 115–121.
- (97) Idriss, H.; Seebauer, E. G. *J. Mol. Catal. A Chem.* **2000**, 152 (1–2), 201–212.
- (98) Termine, J. D.; Lundy, D. R. *Calcif. Tissue Res.* **1974**, 15 (1), 55–70.
- (99) Zhai, S.; Lin, C.-C.; Xue, W. *Vib. Spectrosc.* **2014**, 70, 6–11.
- (100) Popović, L.; Waal, D. de; Boeyens, J. C. A. *J. Raman Spectrosc.* **2005**, 36 (1), 2–11.
- (101) Antonakos, A.; Liarokapis, E.; Leventouri, T. *Biomaterials* **2007**, 28, 3043–3054.
- (102) Frost, R. L. *J. Raman Spectrosc.* **2011**, 42 (8), 1690–1694.
- (103) Frost, R. L.; López, A.; Xi, Y.; Granja, A.; Scholz, R.; Lima, R. M. F. *Spectrochim. Acta Part A Mol. Biomol. Spectrosc.* **2013**, 114, 309–315.
- (104) Klaewkla, R.; Arend, M.; Hoelderich, W. F. No. 3.
- (105) Zhang, W.; Desikan, A.; Oyama, S. T. *J. Phys. Chem.* **1995**, 99 (39), 14468–14476.
- (106) Chandrasekar, A.; Sagadevan, S.; Dakshnamoorthy, A. *Int. J. Phys. Sci.* **2013**, 8 (32), 1639–1645.
- (107) Popa, C.; Albu, M.; Costescu, A.; Luculescu, C.; Trusca, R.; Antohe, S. **2005**, 4 (2004), 137–150.
- (108) Busca, G. *Phys. Chem. Chem. Phys.* **1999**, 1 (5), 723–736.
- (109) Guisnet, M.; Magnoux, P. *Appl. Catal.* **2001**, 212, 83.
- (110) Eposition, C. O. K. E. D. *Stud. Surf. Sci. Catal.* **1989**, 51 (C), 339–346.
- (111) Angelici, C.; Weckhuysen, B. M.; Bruijninx, P. C. A. *ChemSusChem* **2013**, 6 (9), 1595–1614.
- (112) Ochoa, J. V.; Malmusi, A.; Recchi, C.; Cavani, F. *ChemCatChem* **2017**, 9 (12), 2128–2135.
- (113) Kyriienko, P. I.; Larina, O. V.; Soloviev, S. O.; Orlyk, S. M.; Calers, C.; Dzwigaj, S. *ACS Sustain. Chem. Eng.* **2017**, 5 (3), 2075–2083.
- (114) Mohsenzadeh, A.; Zamani, A.; Taherzadeh, M. J. *ChemBioEng Rev.* **2017**, 4 (2), 75–91.
- (115) Soh, J. C.; Chong, S. L.; Hossain, S. S.; Cheng, C. K. *Fuel Process. Technol.* **2017**, 158, 85–95.
- (116) Wu, C.-Y.; Wu, H.-S. *ACS Omega* **2017**, 2 (8), 4287–4296.
- (117) Rodrigues, E. G.; Keller, T. C.; Mitchell, S.; Pérez-Ramírez, J. *Green Chem.* **2014**, 16 (12), 4870–4874.
- (118) Hernández-Giménez, A. M.; Ruiz-Martínez, J.; Puértolas, B.; Pérez-Ramírez, J.; Bruijninx, P. C. A.; Weckhuysen, B. M. *Top. Catal.* **2017**, 60 (19–20), 1522–1536.
- (119) Hara, M.; Nakajima, K.; Kamata, K. *Sci. Technol. Adv. Mater.* **2015**, 16 (3), 1–22.
- (120) Dapsens, P. Y.; Menart, M. J.; Mondelli, C.; Pérez-Ramírez, J. *Green Chem.* **2014**, 16 (2), 589–593.
- (121) Feliczak-Guzik, A.; Sprynskyy, M.; Nowak, I.; Buszewski, B. *Catalysts* **2018**, 8 (1), 31.

References

- (122) Lux, S. *Chem. Biochem. Eng. Q.* **2016**, 29 (4), 575–585.
- (123) Clippel, F. De; Dusselier, M.; Rompaey, R. Van; Vanelderen, P.; Dijkmans, J.; Makshina, E.; Giebler, L.; Baron, G. V; Denayer, J. F. M.; Pescarmona, P. P.; Jacobs, P. A.; Sels, B. F. *J. Am. Chem. Soc.* **2012**, 134 (24), 10089–10101.
- (124) Nakajima, K.; Hirata, J.; Kim, M.; Gupta, N. K.; Murayama, T.; Yoshida, A.; Hiyoshi, N.; Fukuoka, A.; Ueda, W. *ACS Catal.* **2018**, 8 (1), 283–290.
- (125) Hayashi, Y.; Sasaki, Y. *Chem. Commun.* **2005**, No. 21, 2716–2718.
- (126) Rasrendra, C. B.; Fachri, B. A.; Makertihartha, I. G. B. N.; Adisasmito, S.; Heeres, H. J. *ChemSusChem* **2011**, 4 (6), 768–777.
- (127) Wang, X.; Liang, F.; Huang, C.; Li, Y.; Chen, B. *Catal. Sci. Technol.* **2015**, 5 (9), 4410–4421.
- (128) Assary, R. S.; Curtiss, L. A. *J. Phys. Chem. A* **2011**, 115 (31), 8754–8760.
- (129) Schlaf, M.; Editors, Z. C. Z.; Zhang, Z. C.; Faba, L.; Díaz, E.; Ordóñez, S.; Marcel Schlaf; Z. Conrad Zhang; Faba, L.; Díaz, E.; Ordóñez, S.; Marcel Schlaf; Z. Conrad Zhang; Faba, L.; Díaz, E.; Ordóñez, S.; Schlaf, M.; Editors, Z. C. Z.; Zhang, Z. C.; Faba, L.; Díaz, E.; Ordóñez, S.; Marcel Schlaf; Z. Conrad Zhang; Faba, L.; Díaz, E.; Ordóñez, S.; Marcel Schlaf; Z. Conrad Zhang; Faba, L.; Díaz, E.; Ordóñez, S. *Reaction Pathways and Mechanisms in Thermocatalytic Biomass Conversion I*; Schlaf, M., Zhang, Z. C., Eds.; Green Chemistry and Sustainable Technology; Springer Singapore: Singapore, 2016.
- (130) Ennaert, T.; Van Aelst, J.; Dijkmans, J.; De Clercq, R.; Schutyser, W.; Dusselier, M.; Verboekend, D.; Sels, B. F. *Chem. Soc. Rev.* **2016**, 45 (3), 584–611.
- (131) Pescarmona, P. P.; Janssen, K. P. F.; Delaet, C.; Stroobants, C.; Houthoofd, K.; Philippaerts, A.; De Jonghe, C.; Paul, J. S.; Jacobs, P. A.; Sels, B. F. *Green Chem.* **2010**, 12 (6), 1083.
- (132) Janssen, K. P. F.; Paul, J. S.; Sels, B. F.; Jacobs, P. A. *Stud. Surf. Sci. Catal.* **2007**, 170, 1222–1227.
- (133) West, R. M.; Holm, M. S.; Saravanamurugan, S.; Xiong, J.; Beversdorf, Z.; Taarning, E.; Christensen, C. H. *J. Catal.* **2010**, 269 (1), 122–130.
- (134) Okuhara, T. *Chem. Rev.* **2002**, 102 (10), 3641–3666.
- (135) Feliczak-Guzik, A.; Sprynskyy, M.; Nowak, I.; Jaroniec, M.; Buszewski, B. *J. Colloid Interface Sci.* **2018**, 516, 379–383.
- (136) Taarning, E.; Saravanamurugan, S.; Holm, M. S.; Xiong, J.; West, R. M.; Christensen, C. H. *ChemSusChem* **2009**, 2 (7), 625–627.
- (137) Yang, X.; Wu, L.; Wang, Z.; Bian, J.; Lu, T.; Zhou, L.; Chen, C.; Xu, J. *Catal. Sci. Technol.* **2016**, 6 (6), 1757–1763.
- (138) Cho, H. J.; Dornath, P.; Fan, W. *ACS Catal.* **2014**, 4 (6), 2029–2037.
- (139) Pighin, E.; Díez, V. K.; Di Cosimo, J. I. *Appl. Catal. A Gen.* **2016**, 517, 151–160.
- (140) Li, L.; Collard, X.; Bertrand, A.; Sels, B. F.; Pescarmona, P. P.; Aprile, C. *J. Catal.* **2014**, 314, 56–65.
- (141) Zhang, Z.; ZHAO (Kent), Z. *Chinese J. Catal.* **2011**, 32 (1–2), 70–73.
- (142) Wang, J.; Masui, Y.; Onaka, M. *Applied Catal. B, Environ.* **2011**, 107 (1–2), 135–139.
- (143) Wang, X.; Liang, F.; Huang, C.; Li, Y.; Chen, B. *Catal. Sci. Technol.* **2016**, 6 (17), 6551–

References

6560.

- (144) Petrov, I.; Michalev, T. *НАУЧНИ ТРУДОВЕ НА РУСЕНСКИЯ УНИВЕРСИТЕТ (Proceedings - Chem. Technol.)* **2012**, No. 51, Book 9.1, 30–35.
- (145) LI XUEHUI; ZHIXIANG, X.; HONGWEI, M.; JINXING, L.; FUKUN, L. CN107162892A. CN107162892A, 2017.
- (146) Zhang, Y.; Wang, J.; Ren, J.; Liu, X.; Li, X.; Xia, Y.; Lu, G.; Wang, Y. *Catal. Sci. Technol.* **2012**, 2(12), 2485–2491.
- (147) Rao, K. T. V.; Souzanchi, S.; Yuan, Z.; Ray, M. B.; Xu, C. (Charles). *RSC Adv.* **2017**, 7(76), 48501–48511.
- (148) Saravanan, K.; Park, K. S.; Jeon, S.; Bae, J. W. *ACS Omega* **2018**, 3(1), 808–820.
- (149) Dapsens, P. Y.; Mondelli, C.; Pérez-Ramírez, J. *ChemSusChem* **2013**, 6(5), 831–839.
- (150) Dapsens, P. Y.; Kusema, B. T.; Mondelli, C.; Pérez-Ramírez, J. *J. Mol. Catal. A Chem.* **2014**, 388–389, 141–147.
- (151) Wang, X.; Song, Y.; Huang, C.; Wang, B. *Sustain. Energy Fuels* **2018**, 2(7), 1530–1541.
- (152) Oberhauser, W.; Evangelisti, C.; Caporali, S.; Dal Santo, V.; Bossola, F.; Vizza, F. *J. Catal.* **2017**, 350, 133–140.
- (153) Mylin, A. M.; Levytska, S. I.; Sharanda, M. E.; Brei, V. V. *Catal. Commun.* **2014**, 47, 36–39.
- (154) Hartman, R. L.; McMullen, J. P.; Jensen, K. F. *Angew. Chemie Int. Ed.* **2011**, 50(33), 7502–7519.
- (155) Tanimu, A.; Jaenicke, S.; Alhooshani, K. *Chem. Eng. J.* **2017**, 327, 792–821.
- (156) Yue, J. *Catal. Today* **2018**, 308, 3–19.
- (157) Sievers, C.; Noda, Y.; Qi, L.; Albuquerque, E. M.; Rioux, R. M.; Scott, S. L. *ACS Catal.* **2016**, 6, 8286–8307.
- (158) Albuquerque, E. M.; Borges, L. E. P.; Fraga, M. A.; Sievers, C. *ChemCatChem* **2017**, 9(14), 2675–2683.
- (159) Albuquerque, E. M.; Borges, L. E. P.; Fraga, M. A. *Green Chem.* **2015**, 17(7), 3889–3899.
- (160) Santos, K. M. A.; Albuquerque, E. M.; Borges, L. E. P.; Fraga, M. A. *Mol. Catal.* **2018**.
- (161) Sushkevich, V. L.; Ordonsky, V. V.; Ivanova, I. I. *Appl. Catal. A Gen.* **2012**, 441–442, 21–29.
- (162) Kishor Mal, N.; Fujiwara, M. *Chem. Commun.* **2002**, No. 22, 2702–2703.
- (163) Kamiya, Y.; Sakata, S.; Yoshinaga, Y.; Ohnishi, R.; Okuhara, T. *Catal. Letters* **2004**, 94(1), 45–47.
- (164) Malmusi, A. *Sustainable Catalytic Processes for the Valorisation of Light Alcohols*, alma, 2016.
- (165) Barrett, E. P.; Joyner, L. G.; Halenda, P. P. *J. Am. Chem. Soc.* **1951**, 73(1), 373–380.
- (166) Tamura, M.; Shimizu, K. I.; Satsuma, A. *Appl. Catal. A Gen.* **2012**, 433–434, 135–145.
- (167) Davis, M. E., Davis, R. J. *Fundamentals of Chemical Reaction Engineering*, 2003.
- (168) Miyamoto, S.; Atsuyama, K.; Ekino, K.; Shin, T. *Chem. Pharm. Bull.* **2018**, 66(6), 632–636.

References

- (169) Jastrzbski, W.; Sitarz, M.; Rokita, M.; Bułat, K. *Spectrochim. Acta - Part A Mol. Biomol. Spectrosc.* **2011**, *79* (4), 722–727.
- (170) Fang, L.; Shi, Q.; Nguyen, J.; Wu, B.; Wang, Z.; Lo, I. M. C. *Environ. Sci. Technol.* **2017**, *51* (21), 12377–12384.
- (171) Hezel, A.; Ross, S. D. *Spectrochim. Acta* **1966**, *22* (11), 1949–1961.
- (172) Assaaoudi, H.; Ennaciri, A.; Rulmont, A.; Harcharras, M. *Phase Transitions* **2000**, *72* (1), 1–13.
- (173) Guzman, E. R.; Ordonez-regil, E. **2007**, No. October 2015.
- (174) Shmachkova, P.; Kotsarenko, N. S.; Mudrakovskii, I. L.; Shmachkova, V. P.; Kotsarenko, N. S.; Mastikhin, V. M. *J. Phys. Chem. Solids* **1986**, *47* (4), 335–339.
- (175) Hudson, M. J.; Workman, A. D.; Adams, R. J. W. *Solid state ionics* **1991**, *46*, 159–165.
- (176) Zah-Letho, J. J.; A., V.; A, J.; F., T.; Piffard, Y.; M., T. *J. Solid State Chem.* **1995**, *116* (2), 335–342.
- (177) Girard, G.; Vasconcelos, F.; Montagne, L.; Delevoye, L. *Solid State Nucl. Magn. Reson.* **2017**, *84*, 210–215.
- (178) Brown, I. D.; Skowron, A. *J. Am. Chem. Soc.* **1990**, *112* (9), 3401–3403.
- (179) Fogler, H. S. In *Elements of Chemical Engineering*; Pearson Education Inc., 2006; pp 813–866.
- (180) van Bokhoven, J. A.; Xu, B. In *From Zeolites to Porous MOF Materials - The 40th Anniversary of International Zeolite Conference*; Xu, R., Gao, Z., Chen, J., Yan, W. B. T.-S. in S. S. and C., Eds.; Elsevier, 2007; Vol. 170, pp 1167–1173.
- (181) Torres-Knoop, A.; Poursaeidesfahani, A.; Vlugt, T. J. H.; Dubbeldam, D. *J. Chem. Theory Comput.* **2017**, *13* (7), 3326–3339.
- (182) Iuga, A.; Ader, C.; Gröger, C.; Brunner, E. *Annu. Reports NMR Spectrosc.* **2006**, *60*, 145–189.
- (183) Pizzolitto, C.; Menegazzo, F.; Ghedini, E.; Innocenti, G.; Di Michele, A.; Cruciani, G.; Cavani, F.; Signoretto, M. *ACS Sustain. Chem. Eng.* **2018**, acssuschemeng.8b02103.
- (184) Pizzolitto, C. Sviluppo di catalizzatori nanostrutturati a base di Nichel per la produzione di idrogeno ., Università Ca' Foscari Venezia, 2016.
- (185) Kouva, S.; Honkala, K.; Lefferts, L.; Kanervo, J. *Catal. Sci. Technol.* **2015**, *5* (7), 3473–3490.
- (186) Busca, G. *Catal. Today* **1996**, *27* (3–4), 457–496.
- (187) Coskun, F.; Cetinkaya, S.; Eroglu, S. *Jom* **2017**, *69* (6), 987–992.
- (188) Diagne, C.; Idriss, H.; Kiennemann, A. *Catal. Commun.* **2002**, *3* (12), 565–571.
- (189) Sheng, P. Y.; Yee, A.; Bowmaker, G. A.; Idriss, H. *J. Catal.* **2002**, *208* (2), 393–403.
- (190) Sheng, P. Y.; Bowmaker, G. A.; Idriss, H. *Appl. Catal. A Gen.* **2004**, *261* (2), 171–181.
- (191) Sheng, P.-Y.; Yee, A.; Bowmaker, G. A.; Idriss, H. *J. Catal.* **2002**, *208* (2), 393–403.
- (192) Lucarelli, C.; Galli, S.; Maspero, A.; Cimino, A.; Bandinelli, C.; Lolli, A.; Velasquez Ochoa, J.; Vaccari, A.; Cavani, F.; Albonetti, S. *J. Phys. Chem. C* **2016**, *120* (28), 15310–15321.

References

- (193) Xu, W.; Liu, Z.; Johnston-Peck, A. C.; Senanayake, S. D.; Zhou, G.; Stacchiola, D.; Stach, E. A.; Rodriguez, J. A. *ACS Catal.* **2013**, *3* (5), 975–984.
- (194) Seiferth, O.; Wolter, K.; Dillmann, B.; Klivenyi, G.; Freund, H.-J.; Scarano, D.; Zecchina, a. *Surf. Sci.* **1999**, *421* (1–2), 176–190.
- (195) Busca, G. *Catal. Today* **1996**, *27* (3–4), 323–352.
- (196) Zhang, W.; Innocenti, G.; Oulego, P.; Gitis, V.; Wu, H.; Ensing, B.; Cavani, F.; Rothenberg, G.; Shiju, N. R. *ACS Catal.* **2018**, *8* (3), 2365–2374.
- (197) Zhang, W.; Innocenti, G.; Ferbinteanu, M.; Ramos-Fernandez, E. V; Sepulveda-Escribano, A.; Wu, H.; Cavani, F.; Rothenberg, G.; Shiju, N. R. *Catal. Sci. Technol.* **2018**, *8* (15), 3737–3747.
- (198) Rao, R. K.; K.V. Narayana, A. Venugopal, K.S. Rama Rao, S. Khaja Masthan, V. Venkat Rao, P. K. R. *Appl. Catal. A, Gen.* **1998**, *167*, 11–22.
- (199) Garcia, A.; Yan, N.; Vincent, A.; Singh, A.; Hill, J. M.; Chuang, K. T.; Luo, J.-L. *J. Mater. Chem. A* **2015**, *3* (47), 23973–23980.
- (200) Kantcheva, M. *Phys. Chem. Chem. Phys.* **2000**, *2*, 3043–3048.
- (201) Rumon, K. A. In *NIST Chemistry WebBook, NIST Standard Reference Database Number 69*, P.J. Linstrom and W.G. Mallard, Ed.; National Institute of Standards and Technology, Gaithersburg MD, 20899, 1989; Vol. 21, pp 74–86.
- (202) Borovkov, V. Y.; Mikheeva, E. P.; Zhidomirov, G. M.; Lapina, O. B. *Kinet. Catal.* **2003**, *44* (5), 710–717.
- (203) Chen, Y.-K. K.; Lin, Y.-F. F.; Peng, Z.-W. W.; Lin, J.-L. L. *J. Phys. Chem. C* **2010**, *114* (41), 17720–17727.
- (204) Socrates; Socrates, G. *Infrared and Raman characteristic group frequencies.*, third edit.; Wiley, 2004.
- (205) Cassanas, G.; Morssli, M.; Fabregue, E.; Bardet, L. *J. Raman Spectrosc.* **1991**, *22* (April), 409–413.
- (206) Wen, B.; Li, Y.; Chen, C.; Ma, W.; Zhao, J. *Chem. - A Eur. J.* **2010**, *16* (39), 11859–11866.
- (207) Kakihana, M.; Okamoto, M. *J. Phys. Chem.* **1984**, *88* (9), 1797–1804.